University of Alberta

Magnetotelluric imaging beneath the Taiwan orogen:
An arc-continent collision

by

Edward Alan Bertrand

A thesis submitted to the Faculty of Graduate Studies and Research
in partial fulfillment of the requirements for the degree of

Doctor of Philosophy
in
Geophysics

Department of Physics

Spring 2010
Edmonton, Alberta

Examining Committee

Dr. Martyn Unsworth, Department of Physics

Dr. John Waldron, Department of Earth and Atmospheric Sciences

Dr. Jeff Gu, Department of Physics

Dr. Claire Currie, Department of Physics

Dr. David Wiltschko, Department of Geology and Geophysics, Texas A&M University

DEDICATION

To the memory of Ruth Helen Norton (1915-2007), I think of you often.

ABSTRACT

Arc-continent collisions are a fundamental plate tectonic process that control continental growth, orogen development and the distribution of natural hazards and natural resources. This process actively occurs in Taiwan where the Luzon Volcanic Arc collides obliquely with the passive margin of the Eurasian Plate. An important characteristic of the arc-continent collision in Taiwan is that oblique convergence has produced an orogen that decreases in age from north to south. Investigation of the temporal evolution of the Taiwan orogen is therefore made possible through studies at different latitudes on the island.

The first long-period magnetotelluric (MT) measurements in Taiwan were recorded at 82 locations on three profiles across south, central and north Taiwan during 2006-2007. These MT data were collected as a component of the TAIGER (Taiwan Integrated Geodynamics Research) project and are analyzed and interpreted in this thesis. The TAIGER project was initiated to: 1) collect multi-technique high resolution geophysical data required to unambiguously distinguish between end-member tectonic models proposed for central Taiwan, and 2) to investigate the orogen evolution by comparison of data collected at latitudes ranging from south to north Taiwan.

In this thesis, the central Taiwan TAIGER MT data are shown to be inconsistent with orogen-scale thin-skinned tectonic models and instead support predictions of lithospheric-scale deformation (i.e. thick-skinned tectonics) beneath the Central Ranges. Similarity between resistivity models of central and southern Taiwan indicate that thick-skinned tectonics is occurring in both locations, and is therefore a persistent mode of deformation that operates as the orogen develops. The resistivity model for northern Taiwan is shown to be consistent with dewatering of the subducting Philippine slab, and with deformation described by the subducting indenter tectonic model.

A global context for the Taiwan results is provided by comparison to the South Island of New Zealand that shares many similarities with the tectonic setting in Taiwan. MT resistivity models support lithospheric deformation beneath the Southern Alps, and the occurrence of fluid-based conductors in the Marlborough region caused by dewatering of the Pacific slab.

ACKNOWLEDGEMENTS

I wish to express my thanks and gratitude to my supervisor, Professor Martyn Unsworth. I feel very fortunate to have been given the opportunity to contribute to an international research project that comprises a number of geophysical methods. I'm confident that the education and experience that I've gained while working with Martyn has prepared me well for a future career in Geophysics.

The first-step in this research project involved the collection of a large dataset of Magnetotelluric measurements across the densely populated and rugged island of Taiwan. I am therefore indebted to those who participated in the fieldwork component of this research – Chih-Wen Chiang, Erşan Türkoğlu, Han-Lun Hsu, Martyn Unsworth, Graham Hill and Meg Bertrand. In particular, without the efforts of Chih-Wen Chiang, the MT data acquisition would not have been such a success. Additionally, assistance from Professor's Chow-Son Chen and Chien-Chih Chen at National Central University is greatly appreciated.

I wish to also thank the members of my committee, Professor's John Waldron, Jeff Gu, and Claire Currie for their insight on this research and helpful comments on my thesis. In addition, I benefitted greatly from comments and discussion with Professor David Wiltschko, and thank him for his time in traveling to the University of Alberta for my PhD defence.

Lastly, I am grateful for the continued support from my friends and family. My parents always encourage and support me in whatever I choose to pursue, and for that, they are deeply thanked. And to my wife, simply put, this degree could not have been completed without you!

TABLE OF CONTENTS

LIST OF TABLES

LIST OF FIGURES

LIST OF ABBREVIATIONS AND SYMBOLS

1-D	One-Dimensional
2-D	Two-Dimensional
3-D	Three-Dimensional
BATS	Broadband Array for Taiwan Seismology
CF	Chuchih Fault
CP	Coastal Plain
CPU	Central Processing Unit
CR	Coastal Range
CWB	Central Weather Bureau
ECR	Eastern Central Range
EM	Electromagnetic
EUP	Eurasian Plate
FBC	Foreland Basin Conductor
GPS	Global Positioning System
HL	Hualien
HSR	Hseuhshan Range
INDEPTH	International Deep Profiling of Tibet and the Himalaya
IP	Ilan Plain
KS	Kaohsiung
KYH	Kuanyin Basement High
LF	Lishan Fault
LFC	Lishan Fault Conductor
LH	Lanhsu
LT	Lutao
LV	Longitudinal Valley
LVA	Luzon Volcanic Arc
LVC	Longitudinal Valley Conductor
LVF	Longitudinal Valley Fault
Ma	Million years ago
Moho	Mohorovičić Discontinuity: Crust-Mantle Boundary
MT	Magnetotellurics
Myr	Million years
NCU	National Central University
NIMS	Narod Intelligent Magnetotelluric System
NLCG	Non-linear Conjugate Gradients
PB	Puli Basin
PH	Penghu Archipelago

PKH	Peikang Basement High
PNG	Papua New Guinea
PP	Pingtung Plain
PSP	Philippine Sea Plate
r.m.s.	Root Mean Square
RT	Ryukyu Trench
SCS	South China Sea
SIGHT	South Island Geophysical Transect
TAIGER	Taiwan Integrated Geodynamics Research
TC	Taichung
TE	Transverse Electric
TM	Transverse Magnetic
TETMHZ	Transverse Electric, Transverse Magnetic and Tipper data
TP	Taipei
WCR	Western Central Range
WF	Western Foothills

α	Geoelectric strike
	Topographic slope
B	Magnetic induction
β	Basal dip
	Phase tensor invariant: indicator of 3-D induction
E	Electric field strength
ε	Dielectric permitivitty: Free space value: 8.854×10^{-12} C^2/Nm^2
D	Electric displacement
	Distortion tensor
δ	Skin depth
f	Frequency
Φ	Magnetotelluric phase tensor
Φ_{max}	Phase tensor invariant
Φ_{min}	Phase tensor invariant
ϕ	Magnetotelluric phase
	Porosity
	Critical taper angle
H	Magnetic field strength
η	Density of free charge
J	Electric current density
k	Wave number
M_w	Moment Magnitude
m	Cementation exponent
μ	Magnetic permeability: Free space value: $4\pi \times 10^{-7}$ N/A^2
P	Pressure Wave
ρ	Electrical resistivity
ρ_a	Apparent resistivity

S_h	Shear distortion matrix
S	Shear Wave
ScS	Shear Wave Reflected from the Core-Mantle Boundary
SKS	Shear Wave Refracted by the Outer Core
SV	Vertically Polarized Shear Wave
T	Period
	Tipper magnitude
T_w	Twist distortion matrix
σ	Electrical conductivity
v_p	P-wave velocity
v_s	S-wave velocity
ω	Angular frequency
x,y,z	Cartesian coordinate axes, z positive downwards
Z	MT impedance tensor

Note that symbols commonly used to represent various quantities are adopted, and that this results in multiple definitions for some symbols. However, within the text it is clear which definition applies.

1. INTRODUCTION

Arc-continent collisions are an important plate tectonic process that has contributed to the growth of the continents. In the Archean and Proterozoic, the growth of cratons occurred in part through the accretion of terranes by arc-continent collisions. This process also led to the formation of major Phanerozoic orogens such as the Appalachian and Cordilleran margins of North America (Condie, 1997). Arc-continent collisions cause deformation of the continents, control the distribution of natural resources, and also represent natural hazards from associated earthquakes and landslides (Okaya et al., 2007). Understanding these collisions is thus important to gain insight into a fundamental plate tectonic process.

Arc-continent collisions have occurred since the Archean and are ubiquitous in the Earth's record of continental assembly (Wu F.T. et al., 2007a). However, the study of these collisions in ancient orogens is hindered by post-orogenic tectonic overprinting, which obscures the syn-orogenic plate geometries, kinematics and tectonic setting. Thus, studies of active collisions are required for detailed and well constrained analysis of the mechanics of mountain building and associated deformation processes (Malavieille et al., 2002).

At present, active arc-continent collisions are occurring in East Timor, Papua New Guinea, and Taiwan (Huang et al., 2000). The island of East Timor formed when the continental shelf of the Indo-Australian plate came into contact with the westernmost Banda Arc. The introduction of continental shelf material forced a transition from subduction to collision and the subsequent creation of East Timor in the late Miocene (Charlton, 1991). Similarly, in eastern Papua New Guinea, the

Finisterre Range records a Pliocene arc-continent collision between the Bismarck Arc and the Indo-Australian plate (Abbott et al., 1994). Thirdly, the island of Taiwan was formed by collision between the Luzon Volcanic Arc (LVA) on the western edge of the Philippine Sea Plate (PSP) and the continental margin of the Eurasian Plate (EUP). An important characteristic of the Taiwan arc-continent collision is that convergence between the LVA and the passive margin of the EUP is oblique. This obliquity has resulted in a propagating suture, which has developed a mature orogen in north Taiwan that becomes younger to the south (Suppe, 1981). The collision is estimated to have commenced in the late Miocene (5-6 Ma) in northern Taiwan and is in very early stages in southern Taiwan (Huang C.Y. et al., 2006). Since the orogen is now collapsing in the north (Teng, 1996), the tectonic system exhibits the full range of processes from pre-collision offshore southern Taiwan, to active collision in central Taiwan and post-collision in the north. Taiwan thus provides an ideal location to study the time-evolution of processes involved in arc-continent collision from beginning to end. Additional factors that make Taiwan a suitable location for study include the following:

(1) Extensive geoscientific research has been conducted in Taiwan since first being recognized as an arc-continent collision (Chai, 1972). Taiwan is now widely considered as a classic example of an arc-continent collision (Twiss and Moores, 2007). This previous work has established a well constrained geologic framework and plate tectonic kinematics, required to launch more detailed orogen investigations.

(2) Oblique plate convergence can produce an extreme seismic hazard (Grevemeyer and Tiwari, 2006; Cheng, 2009). In this past century, nearly a dozen $M_w > 7.0$ earthquakes have occurred in the Taiwan region (Huang et al., 1999), the most recent being the September 21, 1999 $M_w = 7.6$ Chi-Chi earthquake (Kao and Chen, 2000; Yue et al., 2005; Ma et al., 2006), which took the lives of over 2400 people and caused over US$20 billion in economic losses (Schiff, 2000). The Chi-Chi earthquake produced a coseismic slip of up to 12 m at the surface,

along 80 km of the Chelungpu Fault (Dominguez et al., 2003). This devastating event brought to the forefront the importance of understanding the tectonic and deformation processes caused by an arc-continent collision.

(3) Lastly, Taiwan is relatively small in spatial extent and has a modern transportation infrastructure. These features facilitate access to remote areas and make orogen-scale studies possible at reasonable expense.

Previous research in Taiwan has led to the development of several tectonic models which aim to explain the collision related tectonic processes and deformation. However, these models exhibit major differences in lithospheric structure beneath central Taiwan; it has long been contested whether the collision of the LVA with the continental margin of the EUP was followed by eastward subduction of the continental lithosphere. This debate divides the numerous models proposed into two end-members: (1) thin-skinned tectonics (Suppe, 1987), and (2) thick-skinned lithospheric deformation (Wu et al., 1997). As the name implies, the thin-skinned model predicts that all collision related deformation occurs within a thin wedge of the upper crust, soled by a basal décollement. Below this deforming wedge, the Eurasian lithosphere is thought to subduct to the east. In contrast, the thick-skinned model predicts deformation and progressive thickening of the crust to occur within the entire continental lithosphere beneath the core of the orogen. This model is consistent with the presence of a décollement beneath western Taiwan, but does not predict that such a feature extends across the entire island. A debate has continued about which of these models is applicable to Taiwan because, until recently, insufficient geophysical data were available to unequivocally resolve the lithospheric structure beneath the island.

In 2004, an international study of the Taiwan arc-continent collision was initiated to address these questions. The TAIGER (Taiwan Integrated Geodynamics Research) project was designed to collect the high resolution, multi-disciplinary

lithospheric scale data set required to distinguish between the proposed tectonic models, and to investigate fundamental processes associated with arc-continent collisions. To achieve this goal, the TAIGER project proposed the acquisition of seismic data (active and passive, onshore and offshore, reflection and refraction), petrophysical lab measurements, geodynamic modeling and magnetotelluric (MT) data collection. The field campaign was designed to build upon existing research and to exploit the north-south variation in the age of the orogen to study the full range of mountain building and collision related processes.

In 2006-2007, the first long-period MT data were recorded at 82 stations across Taiwan as part of the TAIGER project. The TAIGER MT data were acquired by the University of Alberta, in collaboration with National Central University in Taiwan, and form the basis of this thesis. Measurements were made on cross-island transects in north, central and south Taiwan to study the temporal evolution of the orogen; comparison of transect models permits investigation of along-strike variation in the orogen development. To reduce the high levels of cultural EM noise on the densely populated island, a remote reference station was operated on the Penghu archipelago during measurements on the island proper.

Magnetotellurics is a passive geophysical imaging technique that measures time variations of natural electromagnetic (EM) fields at the surface of the Earth. Measurements of these fields are used to generate models of subsurface electrical resistivity as a function of depth; longer period signals sample greater volumes of the Earth as governed by the skin depth phenomena (Simpson and Bahr, 2005). The electrical resistivity models are interpreted and used to infer geological and rheological properties of interest.

Sources of low electrical resistivity (high conductivity) in the subsurface include metallic minerals, graphite, partial melt and aqueous fluids (Jones, 1992). Given a number of possible sources, interpretations of anomalous regions of low resistivity in MT models must include a justification of the inferred cause. In

active tectonic environments, aqueous fluids or partial melt are the most likely contributor to large-scale zones of low resistivity (Jiracek et al., 2007, and references therein). Thus, lithospheric scale MT models of the active arc-continent collision in Taiwan effectively map fluids and/or melts. Despite representing a volumetrically minor constituent of the Earth's crust and mantle, fluids and partial melts can dramatically lower the strength of crustal and upper mantle materials (Cox, 2005; Rosenberg and Handy, 2005). Such low resistivity anomalies may therefore indicate mechanically weak zones where deformation is localized (Wannamaker et al, 2008).

Within the past decade, MT has made major contributions to multidisciplinary international research projects (e.g. INDEPTH, SIGHT) aimed at investigating the lithospheric deformation associated with convergent margins (Wei et al., 2001; Wannamaker et al., 2002). Through data integration, these projects reduce inherent non-uniqueness in individual techniques and result in well constrained tectonic interpretations. For example, seismology can identify structural discontinuities; however, evidence of fluid content and thermal conditions are better resolved by electrical methods. Since MT is the only EM exploration technique capable of imaging to depths greater than 10 km (Unsworth, 1999), and is very sensitive to the presence of minor constituents that can profoundly influence crustal rheology (Karato and Wenk, 2002), MT has proven to be a valuable addition to lithospheric scale studies of convergent margins.

This thesis describes the acquisition, analysis and interpretation of the TAIGER long-period MT data. These data are shown to successfully image lithospheric scale features of the Taiwan orogen and support the thick-skinned lithospheric deformation model for central Taiwan. Along-strike differences in features observed in adjacent profiles are explained in terms of the northwards age-progression of mountain building. The multidisciplinary research benefits interpretations through quantitative comparison with complementary data sets,

and indicate that orogen related deformation beneath the Central Ranges in Taiwan occurs under ductile conditions and on a lithospheric scale.

In Chapter 2 the tectonic and geological setting of Taiwan is discussed, followed by a critical review of the tectonic models that have been proposed for Taiwan. These previous studies reveal the lack of geophysical data capable of resolving the deeper structure of the Taiwan orogen, and which are essential to unequivocally distinguish between the proposed end-member models.

The theoretical basis of MT is summarized in Chapter 3. Additional information can be found in Simpson and Bahr (2005) and in the numerous references provided in this chapter.

Details of the TAIGER project and associated magnetotelluric (MT) data acquisition are described in Chapter 4. This discussion includes time series processing and a study of the overall dimensionality of the MT data.

Chapter 5 describes the inversion of the MT data collected in central Taiwan and shows that the resistivity models support the lithospheric deformation (thick-skinned) tectonic model. The MT resistivity model is compared with seismicity and quantitatively correlated with a seismic P-wave velocity model to further constrain this interpretation[1].

The MT data collected in southern Taiwan are described in Chapter 6. An identical analysis approach as applied to the central Taiwan MT data was undertaken and indicates that these data also support the thick-skinned model of tectonics in the developing orogen. Comparison with the central Taiwan model yields variations that are linked to the evolution of the orogen.

---

[1]A version of this chapter has been published. Bertrand et al., 2009, *Geology*, 37: 711-714.

In Chapter 7, the MT data collected in northern Taiwan are described. The resistivity model of northern Taiwan shows distinct features in comparison with the models of southern and central Taiwan. Variations are explained in terms of the subducting indenter model; contact between the obliquely converging PSP and EUP occurs at progressively greater depths beneath northern Taiwan.

Lastly, Chapter 8 contains a synthesis of the TAIGER MT data interpretation. The main aspects of the resistivity models of southern, central and northern Taiwan are summarized. In addition, global context of these results are provided through a comparison with MT resistivity models from the transpressional collision that formed the Southern Alps, New Zealand.

2. GEOLOGY, TECTONICS AND GEOPHYSICS OF TAIWAN

The island of Taiwan (Figure 2-1) is located in a region whose geological structure and history has been controlled by the interactions of the Philippine Sea Plate (PSP) and the Eurasian Plate (EUP). Taiwan is currently bracketed by subduction zones of opposite polarity. Offshore southern Taiwan, the Eurasian oceanic lithosphere subducts eastwards beneath the PSP along the Manila trench. Northeast of Taiwan the PSP subducts northwards beneath the EUP at the Ryuku trench. Back-arc extension has formed the Okinawa trough, which extends into northern Taiwan as the Ilan Plain. In between these two subduction zones, Eurasian continental lithosphere (that is too buoyant to subduct) has collided with the Luzon Volcanic Arc and formed the Taiwan orogen since the late Miocene. This collision is oblique and has resulted in an orogen that becomes progressively older from south to north Taiwan (Byrne and Liu, 2002).

2.1 Cenozoic Tectonics of Southeast Asia

Tectonic events of relevance to the evolution of the Taiwan orogen began near the end of the Eocene (35 Ma). At this time, rifting of the passive continental margin of the EUP resulted in the formation of horsts and grabens bounded by normal faults in the pre-Tertiary basement of the Eurasian continental crust (Malavieille et al., 2002). This rifting led to the opening of the South China Sea (SCS) in the early Oligocene (30 Ma, Sun, 1985; Hall, 1997). Opening of the SCS was coincident with closure of the proto-SCS, due in part to the southeast extrusion of Indochina related to the India-Asia continent-continent collision (Tapponnier et al., 1982). In the late Oligocene (~25 Ma; Hall, 1997), the development of the

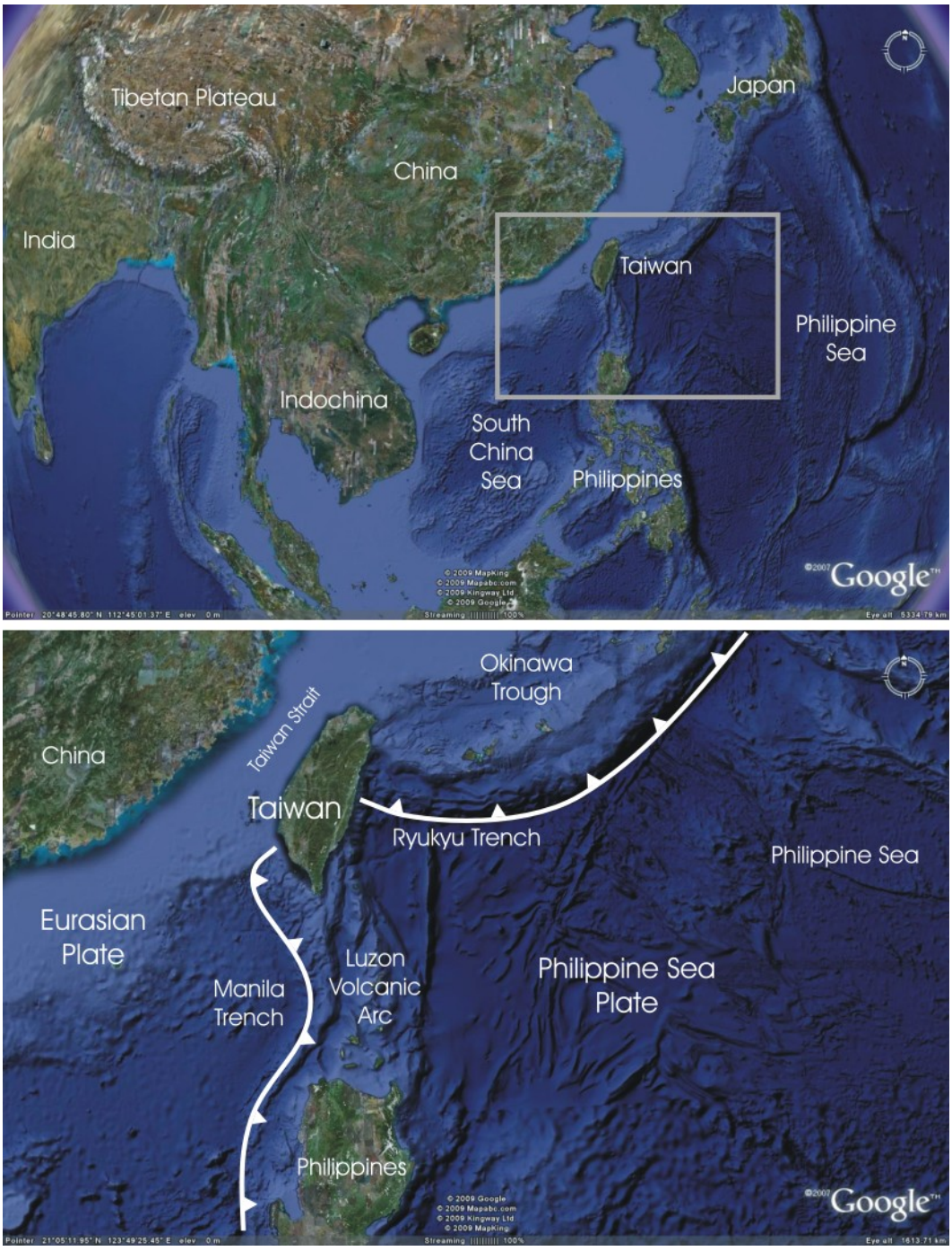

Figure 2-1. Top Panel: Regional map of East Asia showing major geographical areas. Bottom Panel: Regional map of Taiwan showing major geographical and tectonic features. The Eurasian and Philippine Sea Plates are separated by the Ryukyu and Manila Trenches. Maps were generated using Google Earth 4.0.2737 software, freely available at http://earth.google.com/.

sinistral Sorong strike-slip fault system at the Indo-Australian margin facilitated clockwise rotation of the PSP and initiated changes to plate boundaries throughout Southeast Asia (Hall, 1997; 2002). Of significance to Taiwan, this clockwise rotation shut off spreading in the SCS (Sibuet et al., 2002) and initiated east-dipping subduction of the newly formed oceanic crust along the Manila trench (Huang C.Y. et al., 2006). Subduction facilitated metamorphic dehydration of the downgoing slab and subsequent magmatism at the surface that formed the Miocene Luzon Volcanic Arc (LVA) on the western margin of the PSP (Malavieille et al., 2002). Fission-track dating of andesitic volcanics, in what is now the Coastal Range geological province of eastern Taiwan (Figure 2-2), indicates that the LVA began to form at 16 to 15 Ma in the middle Miocene (Yang et al., 1988; 1995).

The northward propagation of the PSP via subduction at the Ryukyu trench brought the LVA into contact with the southwest trending EUP continental margin at the end of the Miocene (Hall, 1997; Byrne and Liu, 2002). The introduction of the Eurasian shelf material into the convergent plate boundary caused a change from subduction to collision. A general buoyancy analysis indicates that continental and oceanic island arc crust resist subduction (Cloos, 1993). Thus, convergence in the late Miocene initiated a transition to collisional tectonics, and subsequent formation of the Taiwan orogen.

The timing of the arc-continent collision in Taiwan has been indirectly estimated by several methods. (1) A change in the source of sediments filling the foreland basin from the western continental margin of Eurasia to the eastern Taiwan orogen; the first appearance of slate in lower Pliocene sequences marks the initiation of uplift in the Central Ranges (Lundberg and Dorsey, 1990; Chou and Yu, 2002). The initial collision must have occurred before this time. (2) The age of subsidence in the foreland basin; interpreted to be the result of orogenic loading (Lin and Watts, 2002; Simoes and Avouac, 2006) (3) Cessation of andesitic volcanism in the Coastal Range; the last volcanic activity indicates the

onset of collision and occurred at 5 to 6 Ma in northern Taiwan (Chi et al., 1981; Lo et al., 1994). Offshore southeastern Taiwan, volcanism on Lanhsu and Lutao islands (Figure 2-2) terminated at 0.5 to 1.5 Ma, respectively (Yang et al., 1988; Lo et al., 1994). At present, Mount Iraya located at 20.5°N on Batan Island marks the northernmost extremity of active volcanism along the Luzon Arc (Malavieille et al., 2002). These methods and others are discussed in Huang C.Y. et al. (2006) and suggest that arc-continent collision began in northern Taiwan at 5-6 Ma in the late Miocene. (4) Estimates from plate reconstruction models (Seno et al., 1993) and geodetic data (Yu et al., 1997) are consistent with the initiation of collision in the late Miocene.

2.2 The Taiwan Arc-Continent Collision

The island of Taiwan has long been recognized as the type locality for studying an active arc-continent collision (Chai, 1972; Suppe, 1987; Lallemand et al., 1997; Wu et al., 1997; Byrne and Liu, 2002; Twiss and Moores, 2007; Wu F.T. et al., 2007a; Bertrand et al., 2009). A number of factors make Taiwan the best location to study an active arc-continent collision and include the following.

1. Since recognition of Taiwan as an active arc-continent collision (Chai, 1972), extensive geoscientific research has established the present plate geometries and tectonic kinematics. Seno (1993) determined the best fitting rotation pole that describes the relative motion between the PSP and EUP to be located near the Kuril Islands, at 48.2°N and 157.0°E. This location predicts plate motions consistent with those from the global relative plate model NUVEL-1, and suggests relative convergence at Taiwan along an azimuth of N51°W, at a rate of 70 mm/yr. Despite the PSP being surrounded by subduction zones, analysis of geodetic data has largely confirmed the predictions of Seno (1993). Using GPS measurements, Yu et al. (1997) determined the relative motion between the Penghu Islands on the EUP and Lanhsu Island on the PSP as convergent motion along an azimuth of N54°W, at a rate of 82 mm/yr (Figure 2-2).

2. The high rate of plate convergence coupled with the sub-tropical climate (average rainfall is 300 cm/yr; Nezat, 2001), produces one of the most rapidly evolving locations on Earth. Uplift rates of coastal terraces around Taiwan are ~5.5 mm/yr (Li, 1976), and in the areas of highest topography, uplift of ~30 mm/yr relative to the Longitudinal Valley is recorded (Liu and Yu, 1990; Yu and Kuo, 2001). Erosion rates in the mountainous regions based on fission track data and incised fluvial terraces are in the range 2-10 mm/yr (Hartshorn et al., 2002; Hsieh and Knuepfer, 2002; Fuller et al., 2003; Willet et al., 2003), and sedimentation rates in the coastal plains are as high as 20 mm/yr (Shyu et al. 2005). The Liwu River alone transports ~10^7 tons of sediment to the Philippine Sea each year, accounting for ~0.1% of the global sediment supply to the worlds seas (Harthshorn et al., 2002). Furthermore, evidence exists for synorogenic normal faulting in the hinterland, which plays an important role in the reduction of topography and the exhumation of high-grade metamorphic rocks (Crespi, 1996). The combination of rapid rates of uplift and denudation produce steep topography with deeply incised valleys resulting in the exposure of high-grade metamorphic rocks in the Taiwan hinterland. These exposures permit the study of tectonic deformation in a zone of active and rapidly evolving transpression.

3. Approximately 20° of obliquity exists between the plate convergence vector and the normal to the EUP margin (Pulver et al., 2002). As a result, collision with the north-south trending LVA has propagated southwestward at a rate of ~60 mm/yr, from initial contact in north Taiwan (Byrne and Liu, 2002). Convergence has thus formed an orogen that is mature in north Taiwan and becomes progressively younger to the south. In essence, every 60 km in distance traveled from south to north Taiwan is equivalent to 1 Myr of mountain building. Thus, latitude is linked to orogenic maturity, allowing the present-day study of south Taiwan to yield insight into the past of locations farther north. Facilitating this approach is the small spatial extent of the island (380 km long and 140 km across at its widest point; Suppe, 1981). The small size permits studies of the whole orogen evolution at a realistic cost.

The significance of the oblique convergence is enhanced by the fact that sufficient time has passed since initial collision for Taiwan to display the entire evolution of an arc-continent collision, from initiation to collapse (Shyu et al., 2005). Taiwan now occupies a pivotal position along the boundary of the Eurasian and Philippine Sea Plates. Offshore southern Taiwan, subduction of oceanic lithosphere results in the formation of a submarine accretionary prism and an active magmatic arc (Reed et al., 1992; Yu et al., 1999). Onshore southern Taiwan, the emerging mountain belt reflects the transition from subduction to collision as the arc encroaches onto the continental margin. In contrast, post-collisional collapse and extension occur progressively northwards of 23.7°N as the orogen transfers to a region of back-arc extension (Bos et al., 2003; Wu et al., 2009). The Ilan Plain in northeastern Taiwan represents the onshore extension of the actively spreading Okinawa trough (Lallemand and Liu, 1998; Sibuet et al., 1998). In central Taiwan, where collision began ~3 Ma (Teng, 1990), recent thermochronology (Fuller et al., 2002) confirms earlier predictions that the orogen has reached a steady state, where uplift is balanced by erosion (Suppe, 1981).

In summary, the obliquity of collision and the well constrained geology and tectonic kinematics make Taiwan an ideal natural laboratory to study the evolution of an arc-continent collision from beginning to end.

2.3 Geological Provinces and Major Tectonic Features of Taiwan

Eight primary geological provinces have formed in response to the arc-continent collision and are oriented parallel to the island axis (Figure 2-2). Boundaries of these tectonostratigraphic units were refined in 1986 with the release of the second edition of the geological map of Taiwan (Ho, 1986) and explanatory text (Ho, 1988). In general, the Longitudinal Valley separates rocks of EUP affinity to the west from the accreted Luzon Volcanic Arc rocks on the PSP to the east. The sub-units of EUP affinity are bounded mainly by faults (Figure 2-3), and generally increase in age and metamorphic grade to the east (Ernst et al., 1985).

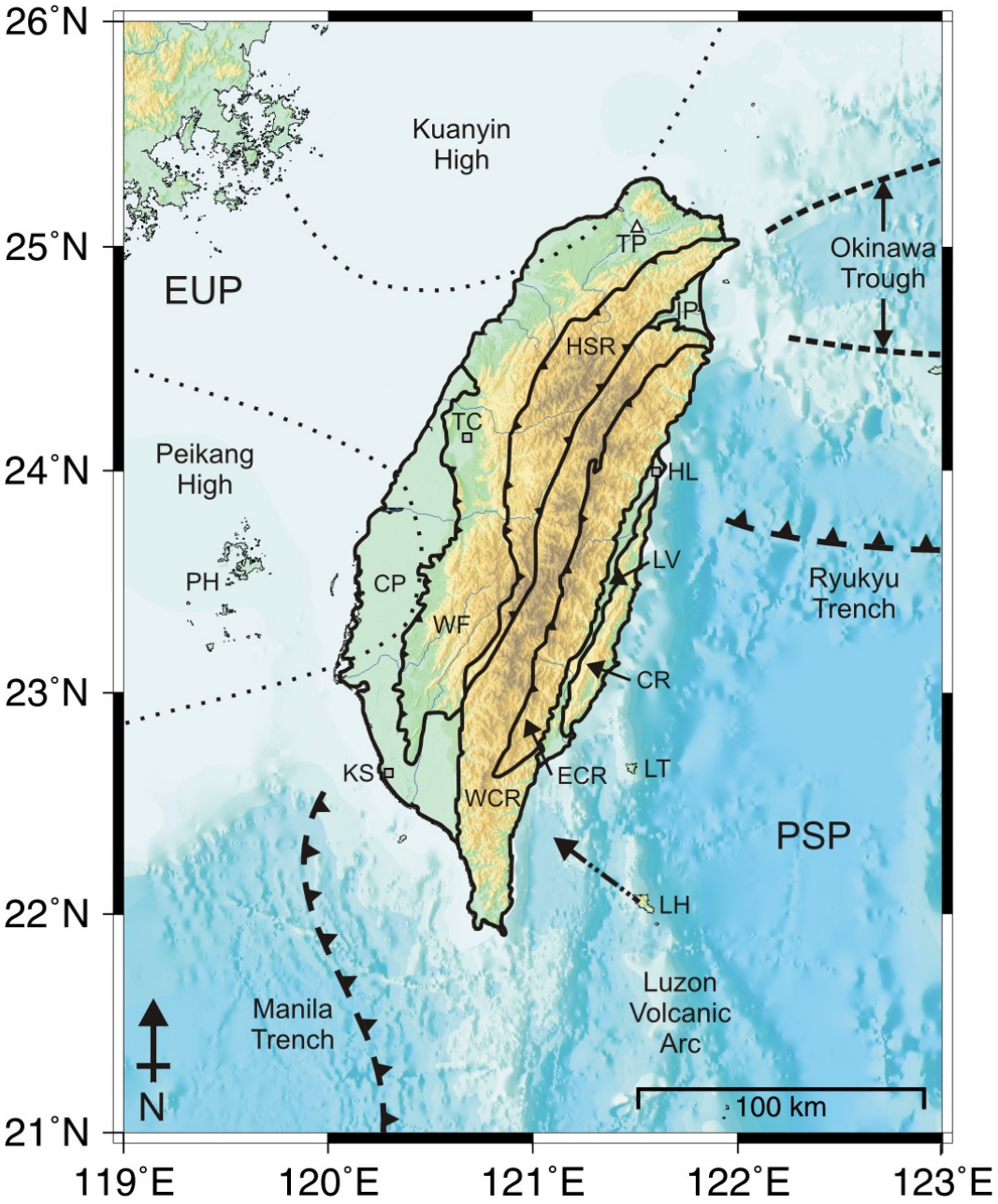

Figure 2-2. Geologic and tectonic map of Taiwan and surrounding regions. Main geological provinces: Coastal Plain CP, Western Foothills WF, Hseuhshan Range HSR, Western/Eastern Central Range W/ECR, Longitudinal Valley LV, Coastal Range CR and Ilan Plain IP. Relative convergence between the PSP and EUP is indicated by the dashed arrow (82 mm/yr, N54°W; Yu et al., 1997). Major cities: Taipei TP, Taichung TC, Hualien HL and Kaohsiung KS. Islands surrounding Taiwan are: Penghu Archipelago PH, Lutao LT and Lanhsu LH. Dashed lines delineate estimated boundaries of the Peikang and Kuanyin basement highs (Mouthereau et al., 2002).

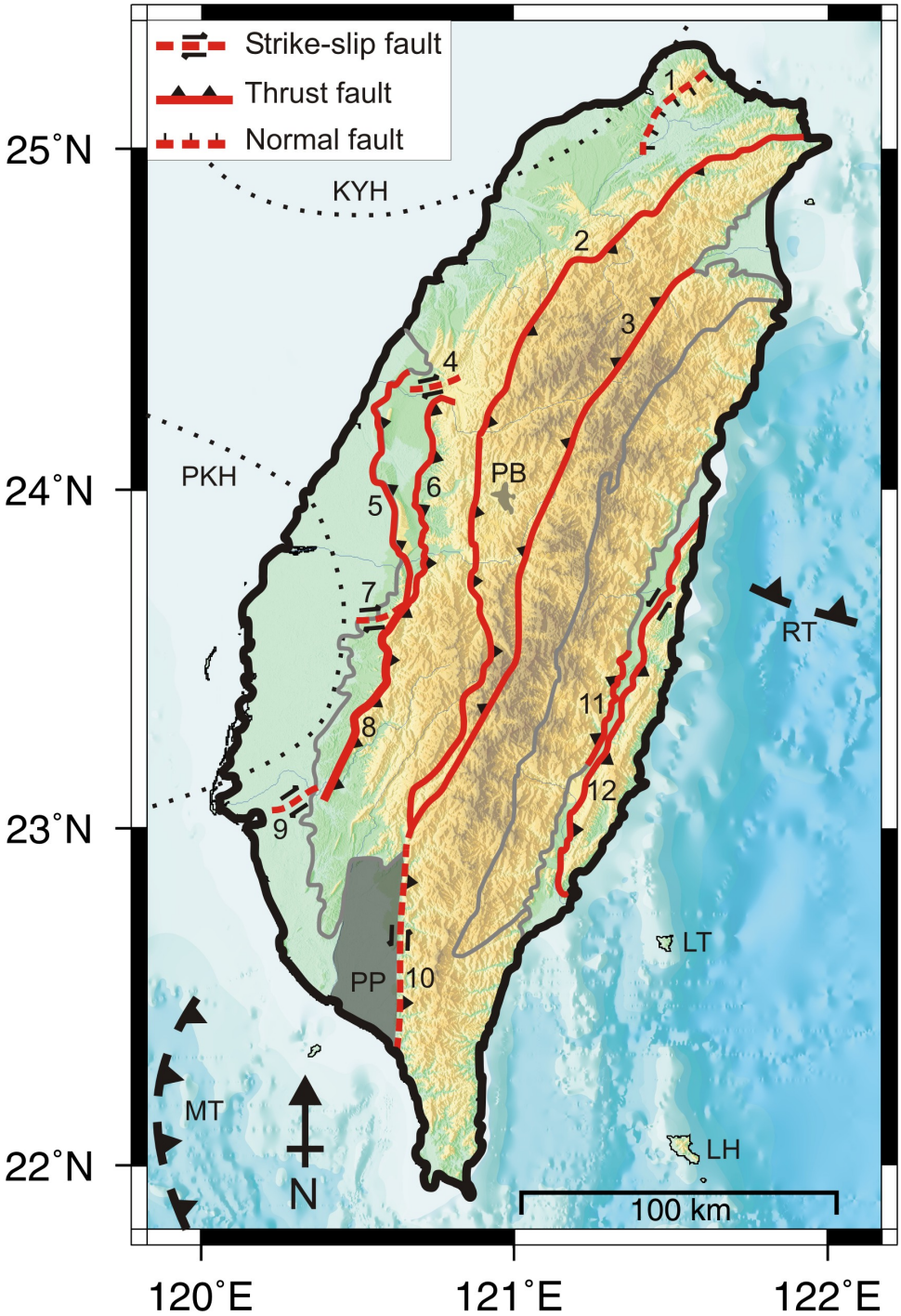

Figure 2-3. Major faults and tectonic features of Taiwan. Subduction trenches: Manila Trench MT and Ryukyu Trench RT. Basement highs: Peikang High PKH and Kuanyin High KYH. Sedimentary basins in grey: Puli Basin PB and Pingtung Plain PP. Islands surrounding Taiwan: Lutao LT and Lanhsu LH. Major faults: 1. Shanchiao Fault, 2. Chuchih Fault, 3. Lishan Fault, 4. Tuntzuchiao Fault, 5. Changhua Fault, 6. Chelungpu Fault, 7. Meishan Fault, 8. Chukou Fault, 9. Hsinhua Fault, 10. Chaochou Fault, 11. Central Range Fault, 12. Longitudinal Valley Fault. (Based on Shyu et al., 2005 and Ng et al., 2009).

2.3.1 Coastal Plain (CP)

On the west, the relatively undeformed, low relief Coastal Plain (CP) consists of poorly consolidated sedimentary deposits derived from the mountain ranges to the east (Hickman et al., 2002). These basin sediments uncomformably overlie basement rocks of the Eurasian continental margin, which regionally dip to the east from flexure and downwarping in response to orogenic loading by the Taiwan hinterland (Chou and Yu, 2002). Accompanying orogen uplift, flexural subsidence and rapid sedimentation have resulted in two intrabasinal highs and an intermediate foredeep (Mouthereau et al., 2002). The Penghu archipelago, a region of 64 islands in the Taiwan Strait is covered by Pleistocene flood basalts and located near the crest of the central Peikang basement high. The Kuanyin basement high is located just offshore northwestern Taiwan. The intervening foredeep is filled with up to 5 km of Pliocene-Pleistocene clastic sediments that thicken eastward and emerge above sea level to form the Coastal Plain (Mouthereau et al., 2002). Significant deposition occurs in the foreland basin (up to 20 mm/yr; Shyu et al., 2005) and the Taiwan Strait rarely exceeds 100 m depth (Malavieille et al., 2002). Geological and geophysical models have confirmed the importance of the Peikang High in the deformation of the Taiwan orogen (Lu and Malavieille, 1994; Lacombe et al., 2001; Byrne et al., 2005). The stable Peikang and Kuanyin structures resist deformation and force the overall S-shape of the orogen (Figure 2-2; Yu et al., 1997).

In southern Taiwan, the Chaochou Fault separates the Pingtung Plain from the Western Central Range (WCR) province (Figure 2-3). This fault juxtaposes Miocene age metamorphic rocks of the WCR with Quaternary strata in the Pingtung Plain, signifying a large component of vertical slip in addition to left-lateral strike-slip (Hickman et al., 2002). The rapidly subsiding Pingtung Plain (up to 13 mm/yr) is extruding to the southwest and is inferred to exist above the final piece of subducting Eurasian oceanic lithosphere (Shyu et al., 2005). The northern tip of the Pingtung Plain corresponds to the northern limit of the seismically defined Wadati-Benioff zone associated with subduction at the Manila trench

(Kao et al., 2000; Lacombe et al., 2001). On the surface, this latitude corresponds to the impingement of the Western Foothills (WF) on the WCR, signifying the transition from subduction of oceanic lithosphere to collision with the continental margin. North of the Pingtung Plain, a topographic break associated with the deformation front defines the eastern boundary of the CP with the adjacent WF.

2.3.2 Western Foothills (WF)

The Western Foothills province comprises shallow marine to shelf clastic sediments of Oligocene (30 Ma) to Quaternary age (Huang, 1978; Teng, 1990). These sediments are essentially unmetamorphosed and imbricated along numerous active folds and thrust faults trending mainly north or northeast and dipping east or southeast (Tillman and Byrne, 1995; Yu et al., 1997). The Western Foothills province is considered a classic example of a fold-and-thrust belt (Suppe, 1980; Clark et al., 1993; Twiss and Moores, 2007).

Fold-and-thrust belts are common at the external edges of orogens, such as the WF province of Taiwan where shallow marine rocks are piling up onto the Eurasian continental shelf (Shyu et al., 2005). The thin-skinned tectonic model has successfully explained many features of fold-and-thrust belts, treating the deforming material as a critically tapering Coulomb wedge (Davis et al., 1983). A Coulomb material is defined as an aggregate of grains that frictionally slide past one another; at the orogen-scale, upper crustal rocks behave as a Coulomb material and actively deform to maintain a critical taper ($\phi = \alpha + \beta$) defined by the basal dip, β, and the topographic slope, α, (Davis et al, 1983). By analogy, this model predicts that deformation occurs in the same manner as a wedge of sand in front of a moving bulldozer (Figure 2-4). As material is added or removed from the wedge, the entire wedge deforms by thrust-sheet imbrication to maintain critical taper (Tillman and Byrne, 1995).

Chapple (1978) noted that most fold-and-thrust belts posses a detachment surface

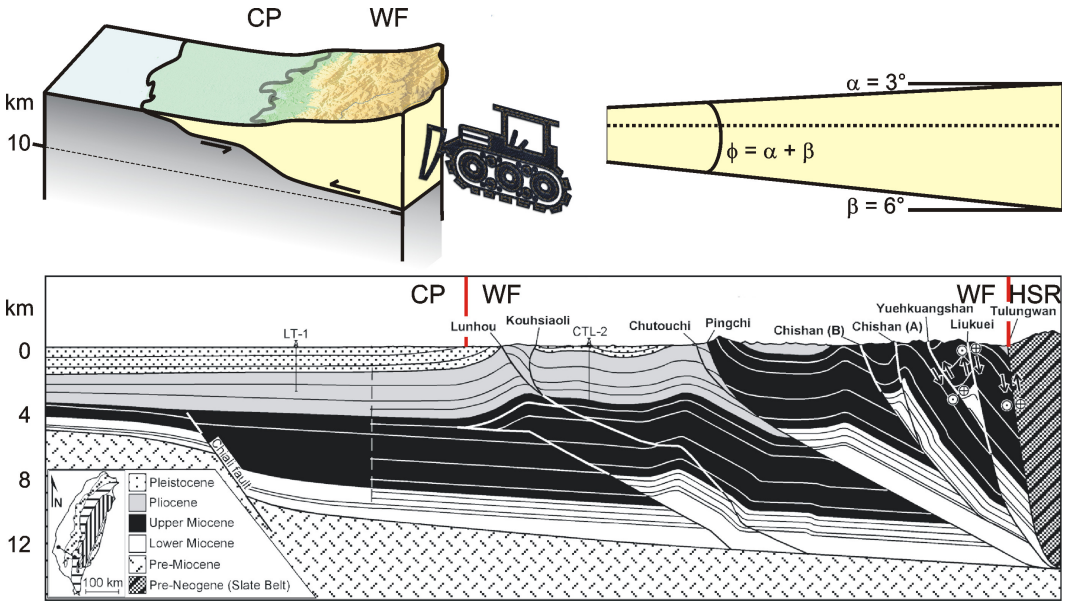

Figure 2-4. Top left: Illustration of the critical taper model for the Taiwan fold-and-thrust belt. Top right: Schematic showing the basal dip β, topographic slope α, and critical taper angles ϕ (Suppe, 1981). Bottom: Balanced cross section (no vertical exaggeration) through southwestern Taiwan terminating to the east at the Hseuhshan range (modified from Hickman et al., 2002).

(basal décollement) that gradually dips towards the hinterland. These detachments are often localized in relatively weak layers (e.g. salt or shale) and permit slip (Hubbard and Shaw, 2009), since the coefficient of sliding friction (inferred to be 0.5 for the Taiwan décollement; Barr and Dahlen, 1990) is less than the internal friction in the overlying wedge (0.6-0.8; Byerlee, 1978). The basal décollement beneath the WF of Taiwan dips moderately (β = 6°) within the upper crust (Figure 2-4) and is well defined by extensive drilling, seismic reflection profiling and detailed surface mapping (Suppe, 1980; 1981; 1987).

In central Taiwan, near Taichung, the Changhua Fault represents the western limit of active deformation (Shyu et al., 2005). However, total slip on the Changhua Fault (a few hundred metres; Chen, 1978) is far less than on the interior Chelungpu Fault, which ruptured most recently in the 1999 Chi-Chi earthquake (Kao and Chen, 2000). To the south, these faults terminate at the strike-slip Meishan Fault. Further south, a blind thrust is inferred beneath the Chiayi Hills (Figure 2-4) and marks the boundary of the WF and CP (Suppe 1980; Hung et al.,

1999). In the north, the Changhua and Chelungpu Faults end in a complex transition zone at the Tuntzuchiao Fault with along-strike pairs of anticlines and synclines. Although no major thrust outcrops in the north, these folds are likely due to a blind thrust (Suppe and Namson, 1979; Hung and Wiltschko, 1993).

2.3.3 The Taiwan Slate Belt (HSR and WCR)

The east-dipping Chuchih thrust fault bounds the WF from the Taiwan slate belt, which comprises the Hseuhshan Range (HSR) and the Western Central Range (WCR) that are separated by the Lishan Fault (Figure 2-2 and 2-3). These provinces exhibit structural variations and differ in age and lithology, suggesting deposition in distinct structural settings on the passive margin of Eurasia.

Hseuhshan Range (HSR)

The HSR consists of Eocene-Oligocene shallow marine successions of sandstone, quartzite and argillite, metamorphosed at prehnite-pumpellyite facies in the west, and increasing to lower greenschist facies in the east (Clark et al., 1993; Fisher et al., 2002; Gourley et al., 2007). Structural studies of the HSR suggest that it formed as a regional-scale pop-up structure, bounded by steeply dipping thrust faults (Fisher et al., 2007). Specifically, rocks of the HSR are thrust over the WF along the east-dipping Chuchih Fault. The eastern boundary is marked by the steeply west-dipping Lishan Fault, which is now widely accepted to be an inverted passive margin growth fault initially formed during Oligocene rifting of the Eurasian margin (Clark et al., 1993; Fisher et al., 2002; McIntosh et al., 2005). The thick Oligocene sequences exposed in the HSR are thus inferred to represent deposition in a northeast trending half-graben, existing on the continental margin prior to collision (McIntosh et al., 2005). East-dipping cleavage in the west, and west-dipping cleavage in the east, support interpretation of the HSR as an inverted graben (Clark et al., 1993; Tillman and Byrne, 1995). The HSR tapers-out in southern Taiwan as the orogen continues off the southwest trending continental shelf and onto the continental slope (Lacombe et al., 1999; Wu et al., 2004).

In central Taiwan, the Puli piggy-back basin is located just east of the WF–HSR contact within the hinterland thrust belts (Figure 2-3). Quaternary strata thicken to over 150 m (Zhang and Huang, 2004) and form smooth terrace surfaces elevated up to 500 m above the present river channels (Powell et al., 2002). Mueller et al. (2002) propose that a shallow décollement inferred beneath the WF dips steeply eastwards at the Puli Basin to maintain critical taper of the orogen.

Western Central Range (WCR)

The WCR rocks are finer grained and inferred to have been deposited closer to the continental slope than rocks in the HSR (Wu et al., 1997). The thick Oligocene strata of the HSR are not present in the WCR, which consists of only Eocene and Micoene slates and minor interbedded sandstones with southeast dipping structural fabric (Fisher et al., 2002; 2007). In southern Taiwan, the slate belt consists of only the WCR as the Chuchih and Lishan Faults merge (Figure 2-3).

Lishan Fault (LF)

Interpretation of the Lishan Fault (LF) as a growth fault, with little sediment accumulation in the footwall (WCR) and thick accumulation in the hanging-wall (HSR), can explain the absence of Oligocene strata in the WCR (McIntosh et al., 2005). However, incremental strain histories near this contact now indicate a top-to-the east sense of shear, suggesting that the LF is a reactivated passive margin growth fault with oblique thrust movement (Angelier et al., 1990; Clark et al., 1993; Lee et al., 1997). The LF juxtaposes greenschist grade Eocene-Oligocene rocks of the eastern HSR against prenhite-pumpellyite grade Miocene rocks of the western WCR. Except for this small break in trend directly across the fault, age and metamorphic grade otherwise increases eastwards across Taiwan (Ernst et al., 1985; Clark et al., 1993; Wu et al., 1997).

The Lishan Fault is a major structural boundary that spans the length of the island (Figure 2-3). In central Taiwan, the LF coincides with the western edge of an aseismic zone beneath the Central Ranges (Wu et al., 2004). This fault provides

an example for inversion of a rift-related structure and highlights the importance of pre-existing features in the development of the orogen (Gourley et al., 2007).

2.3.4 Eastern Central Range (ECR)

East of the slate belt are the exposed pre-Tertiary metamorphic rocks of the Eastern Central Range (ECR). The ECR consists of a complex of high grade, multi-deformed schists, gneisses and some marble that are grouped under the general stratigraphic term, Tananoa Schist (Ho, 1988; Tillman and Byrne, 1995; Hickman et al., 2002). These rocks have been exposed after deep burial (> 10 km) and represent mid-crustal depths (Wu et al., 1997). The Tananoa Schist corresponds to exhumed Eurasian continental basement (Tillman and Byrne, 1995; Lan et al., 1996), but interpretation is complicated by Mesozoic deformation and metamorphism obscuring features related to the ongoing collision (Pulver et al., 2002). The ECR exposes rocks of the highest metamorphic grade in the orogen, and defines the eastern boundary of rocks with EUP affinity.

2.3.5 Longitudinal Valley (LV)

East of the Central Ranges lies the narrow, NNE trending Longitudinal Valley (LV) filled with 1-2 km of coarse, clastic sediments (Tsai et al., 1974). The LV is a fault-bounded depression that overlies the suture zone between the PSP and the EUP (Yu and Kuo, 2001; Hickman et. al., 2002). The eastern boundary of the valley is defined by a highly-active, sinistral west-vergent oblique thrust, the Longitudinal Valley Fault (LVF) (Barrier and Angelier, 1986; Shyu et al, 2008). The western boundary is marked by the west-dipping Central Range Thrust, mapped only along a small segment of the valley (Shyu et al., 2008).

Geodetic measurements in the southern LV indicate that convergence of ~30 mm/yr is accommodated across the LVF (Angelier et al., 1997; Yu et al., 1997; Lee et al., 2001; Cheng et al., 2002). Farther north, near the city of Hualien, only

~5 mm/yr of shortening occurs as the converging plates transition to subduction of the PSP at the Ryukyu trench north of 23.7°N (Wu et al., 2009).

2.3.6 Coastal Range (CR)

East of the LVF lies the Coastal Range (CR) comprising the remnant telescoped Luzon Volcanic Arc and forearc basin that have collided with and accreted to the Eurasian continental margin. The CR is comprised of a volcanic basement of Miocene–Pliocene andesitic composition, uncomformably overlain by ~5 km of collisional Plio-Pleistocene sedimentary sequences derived from the west (Barrier and Angelier, 1986; Dorsey, 1992). Elevated Holocene shorelines along the CR indicate rapid active uplift at rates of ~2.5 to >8 mm/yr (Liew et al., 1993). The rapid uplift could reflect the accretion and shortening of an arc-forearc basin complex similar to ongoing deformation offshore southeastern Taiwan (Shyu et al., 2005). Several studies have proposed tectonic models involving arc-forearc detachment, followed by partial subduction of the forearc block (Chemenda et al., 2001; Malavieille et al., 2002; Tang et al., 2002).

2.3.7 Ilan Plain (IP)

In northern Taiwan (north of 23.7°N), horizontal extension occurs as the orogen is transferred to the hanging wall of the Ryukyu subduction zone. The Ilan Plain (IP) represents the onshore extension of the Okinawa Trough (Figure 2-2); the back-arc basin associated with subduction at the Ryukyu trench (Teng, 1996). The normal faults that bound the Ilan plain are generally considered to be the southwest extension of the faults that bound the offshore Okinawa trough (Shyu et al., 2005). The westward propagation of the trough causes north-south extension of the NE Taiwan orogen (Suppe, 1987; Teng 1996). Collapse of northern Taiwan is indicated by the following observations. (1) The northern crests of the HSR and WCR are appreciably lower than crests farther south, and (2) the margins of the northern crests are being buried by alluvial deposition on the east coast and in the

Taipei basin (Shyu et al., 2005). The spreading rate in the Okinawa trough determined from seafloor magnetic anomalies is ~46 mm/yr (Letouzey and Kimura, 1985), which is consistent with the geodetic estimate of 56.2 mm/yr along an azimuth of N156°E from GPS data (Yu et al., 1997). The Lishan Fault that divides the HSR and WCR runs along the Lanyang river valley and terminates in the Ilan Plain (Figure 2-3).

2.4 Tectonic Models

Several models have been proposed to explain the tectonics that give rise to the topography and geology observed across the Taiwan orogen. In general, all models agree on the following aspects of the collision (Hickman et al., 2002):

1. The orogen is due to collision of the Luzon Volcanic Arc and the Eurasian continental margin.
2. The collision is propagating to the south, with south Taiwan undergoing the majority of present compressional deformation.
3. The boundary between the PSP and the EUP lies beneath the LV.

However, despite consensus on these points, major disagreement between existing models lies in their treatment of the Eurasian continental lithosphere. Specifically, the primary difference between models is focused on the involvement of the continental lithosphere in the collision; it is debated whether collision of the Luzon Volcanic Arc with the Eurasian continental margin permitted continued subduction of the Eurasian continental lithosphere during orogen formation. This debate divides the numerous models proposed into two end-members: (1) thin-skinned tectonics (Suppe, 1987), which predicts a detachment within the upper crust, below which subduction of the undeformed continental lithosphere occurs (Figure 2-5), and (2) thick-skinned lithospheric deformation (Wu et al., 1997), which infers vertically continuous deformation of the entire crust and upper mantle, resulting in a thickened crustal root (Figure 2-6).

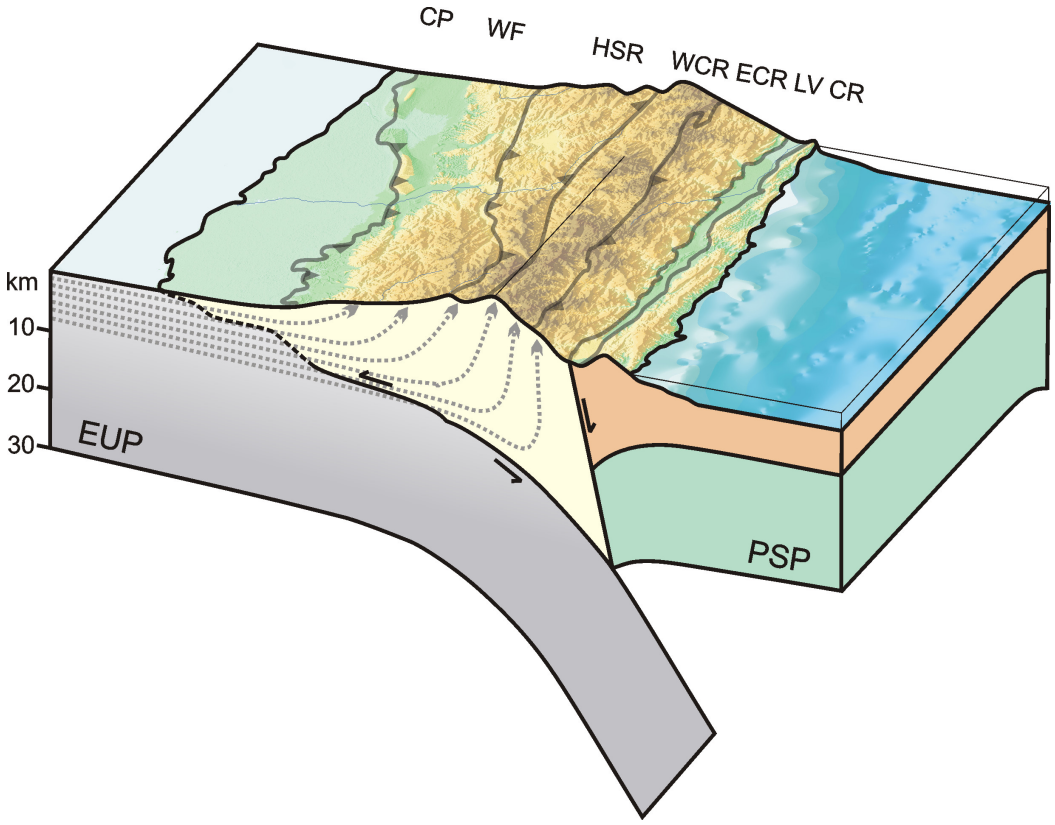

Figure 2-5. Schematic of the thin-skinned tectonic model. Vertical exaggeration is 1.5x. Particle paths are drawn assuming a fixed PSP reference frame.

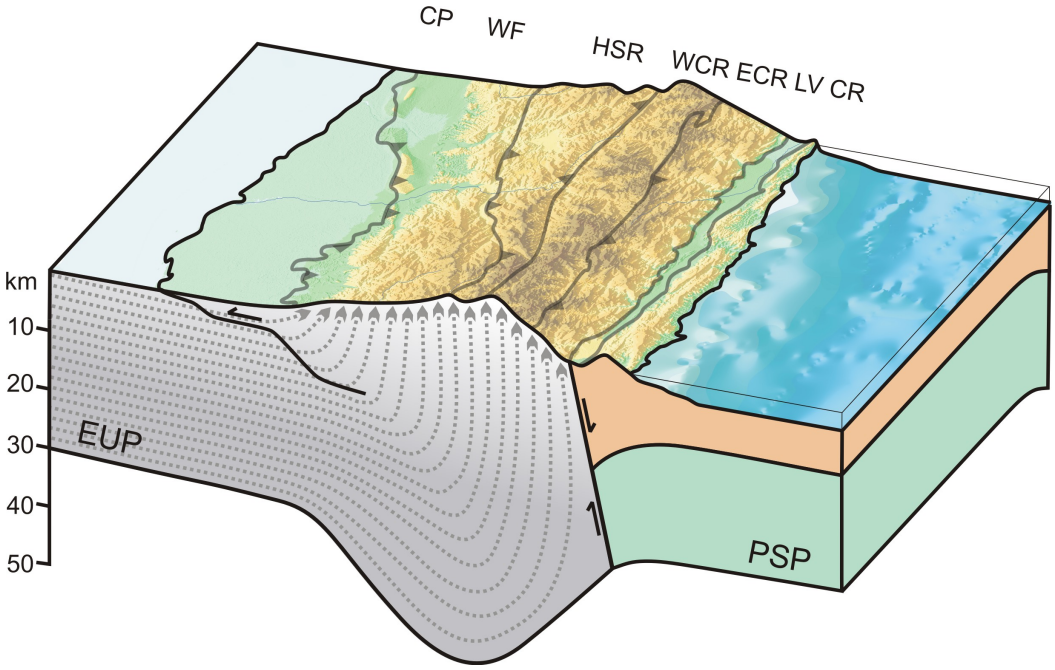

Figure 2-6. Schematic of the thick-skinned lithospheric deformation model. Vertical exaggeration is 1.5x. Particle paths are drawn assuming a fixed PSP reference frame.

2.4.1 Thin-Skinned Tectonics

Development of the thin-skinned tectonic model in Taiwan began with the application of critical wedge models to the Western Foothills fold-and-thrust belt (e.g. Suppe, 1976; 1980). Shallow seismic reflection and well log data collected in the CP and WF for hydrocarbon exploration were used to constrain balanced cross-sections, which revealed a shallow ($\beta = 6°$) east-dipping décollement in the upper crust (Suppe, 1981). The discovery of a décollement prompted further studies that modeled the WF as a critical wedge deforming by thrust imbrication to maintain a critical taper (Dahlen and Suppe, 1988; Dahlen and Barr, 1989). In these papers, the Central Ranges are treated as a rigid backstop, which scrape off sediments of the WF above the basal décollement (Figure 2-4). The thin-skinned structure of the WF fold-and-thrust belt is well established from hydrocarbon exploration that includes extensive borehole data, seismic reflection profiling and detailed surface mapping (Suppe, 1987).

Over time, the application of thin-skinned tectonics in Taiwan progressed into treating the entire orogen as a critically deforming wedge. Although less constrained, simplified cross-sections were extended eastwards to include the Central Ranges (Figure 2-7; Suppe, 1987), and numerous studies were undertaken applying thin-skinned tectonics on the orogen-scale (Barr and Dahlen 1990; Willet, 1999; Willet and Brandon, 2002; Fuller et al., 2006; Simoes and Avouac, 2006; Simoes et al., 2007). Paramount to these models is the assumption that the shallow décollement imaged beneath the WF extends eastward beneath the Central Ranges. By clustering $M_w > 1$ hypocentres onto perceived planar structures, Carena et al. (2002) imaged a sub-horizontal band of seismicity at 8-10 km depth beneath central Taiwan, which was inferred to be the décollement.

Figure 2-7. Simplified cross-section of the Taiwan orogen deformed via thin-skinned tectonics. Redrawn from Suppe, 1987.

The development of thin-skinned type models for the Taiwan orogen has evolved as new geological/geophysical data become available. Model variants all share a common characteristic (i.e. subduction of Eurasian lithosphere beneath an upper crustal décollement) but differ in their specifics. For example, based on results of a mechanical model, Chemenda et al. (1997; 2001) proposed that subduction of the continental crust triggered detachment of the Eurasian slab beneath Taiwan. Slab break-off was linked to exhumation of Eurasian crust in the Central Ranges and to inferred westward subduction of the PSP beneath the CR. Eurasian slab break-off and a flip of subduction polarity is also suggested by Teng et al. (2000) and Pysklywec (2001) as a response to buoyant continental crust entering the collision zone. From results of global seismic tomography (Bijwaard et al., 1998) and offshore bathymetry, Lallemand et al. (2001) interpreted a relatively weak high seismic velocity anomaly east of Taiwan to be the subducting Eurasian slab. Furthermore, as no deep (> 100 km) seismicity is associated with this anomaly, Lallemand et al. (2001) support the prediction of a detached Eurasian slab.

In addition to slab break-off, several models propose detachment and subduction of the forearc block beneath the remnant LVA (Chemenda et al., 1997; 2001; Malavieille et al., 2002). Since only the narrow LV now separates the remnant arc from the uplifted Eurasian basement in the ECR, this seems a likely scenario. However, these models also invoke eastward thrusting of the CR over the PSP, a prelude to reversal of the subduction polarity. Tang et al. (2002) performed 2-D geodynamical modeling to study the deformation and failure pattern of the PSP. Results support failure at the arc to occur along an east-dipping fault, resulting in subduction of the forearc block, rather than failure along a west-dipping fault that would lead to a subduction reversal. These results are supported by active-source seismic data that show no evidence for eastward thrusting of the CR and westward subduction of the PSP in southern Taiwan (McIntosh et al., 2005).

The thin-skinned model successfully accounts for the general topography and overall eastward increase in metamorphic grade across Taiwan. For example, with

erosion and uplift rates balanced, the wedge maintains a steady-state cross section as is observed in central Taiwan (Suppe, 1987; Fuller et al., 2002). In addition, as material enters from the west on depth-dependent paths, exhumation of higher grade materials is predicted to occur farther into the hinterland (Figure 2-5). However, the extension of thin-skinned models to the orogen scale occurred when few constraints on deep crustal structure were available beneath the Central Ranges. As new data are acquired, the principal assumption that subduction of continental lithosphere extends eastwards beneath the majority of Taiwan must be tested. Major implications of orogen-scale thin-skinned models are:

1. A shallow dipping décollement must exist within the upper crust and extend across the island beneath the Central Ranges.
2. Passive subduction of the Eurasian lithosphere occurs below the décollement (i.e. below ~10 km depth; Carena et al., 2002) and all deformation associated with the collision is confined to the upper crust.

2.4.2 Thick-Skinned Lithospheric Deformation

The thick-skinned tectonic model predicts that the entire Eurasian lithosphere is involved in the collision and deforms in a vertically contiguous system (Wu et al., 1997). This model is consistent with evidence for a shallow décollement beneath western Taiwan, but not with the assumption that a sub-horizontal detachment extends eastward beneath the Central Ranges. Rather, deformation and progressive thickening of the continental crust beneath the core of the orogen are proposed (Figure 2-6). The lithospheric deformation model for the Taiwan orogen (Wu et al., 1997) is analogous to that developed to explain observations of thickened lithosphere beneath the South Island in New Zealand (Molnar et al., 1999). Magnetotelluric (MT) data collected on a transect across the South Island showed evidence for deformation within a crustal root, supporting thick-skinned tectonics (Wannamaker et al., 2002). Recent MT data collected in central Taiwan yield similar results (Bertrand et al., 2009).

In the thick-skinned model, buoyant Eurasian continental crust resists subduction as it is dragged into the Manila trench by the attached downgoing oceanic slab. The resistance to subduction drives the collapse of the forearc basin and subsequent collision with the volcanic arc. As convergence continues, decoupling of the Eurasian continental lithosphere from the down-going oceanic lithosphere triggers flexural rebound and uplift of the Taiwan orogen (Lin, 2000). This uplift drives the exhumation of the metamorphic rocks exposed in the hinterland.

The thick-skinned model satisfies indications from geophysical data for deep collision-related deformation. For example, seismicity extends below the level of any proposed décollement in central and western Taiwan (McIntosh et al., 2005). Further, an aseismic zone beneath the Central Ranges may indicate ductile deformation and crustal thickening (Lin, 2000; Wu et al., 2004; Gourley et al., 2007). Crustal thickening is also invoked to explain low seismic velocities modeled at depth beneath the Central Ranges (Rau and Wu, 1995; Ma et al., 1996; Kim et al., 2005; Wu Y.M. et al., 2007). In addition, the reactivation of Paleogene rift-related basement features (e.g. the Lishan Fault; Gourley et al., 2007) highlights the importance of pre-existing structure (Lee et al., 2002). Reactivation provides evidence for deep collision-related deformation. Major implications of the thick-skinned lithospheric deformation model are:

1. Deformation involves the entire crust and upper mantle.
2. A shallow décollement does not extend across the entire orogen.

2.4.3 Model Uncertainty

The two end-member models described above predict different structures at mid and lower crustal depths. However, the debate over which is correct has persisted for two main reasons: (1) both models satisfactorily explain the geology and morphology of the Taiwan orogen, and (2) until recently, insufficient geophysical data were available to unequivocally resolve the deep crustal structure beneath

Taiwan. In the following sections, constraints from geophysical methods are summarized and discussed in light of the two end-member tectonic models. However, the persistence of both models must not be overlooked; a single thin or thick-skinned model may be too limiting for a full understanding of the Taiwan orogen (Lee et al., 2002; Mouthereau et al., 2001; 2002).

2.5 Geophysical Constraints on Proposed Models

2.5.1 Geodesy

Measurements of short-term, relative deformation rates can be obtained by repeated surveying of fixed landmarks using the Global Positioning System (GPS). In 1989, 140 surveying monuments, including 9 permanent stations were installed in Taiwan (Yu and Chen, 1994). The network was surveyed annually between 1990 and 1996 and baseline lengths computed daily for the permanent stations all showed linear trends, despite some earthquakes of $M_w > 5$. Therefore, steady-state motion was assumed (Yu et al., 1997). Figure 2-8 shows the relative horizontal motion vectors with respect to Penghu Island. South of 23.7°N, a south to north decrease in velocities is evident as crustal shortening decreases with the maturity of collision (Gourley et al., 2007). This trend is particularly clear along the active LVF, which accounts for up to 25-30% of the total plate convergence (Bos et al., 2003). North of 23.7°N, surface deformation is small as subduction at the Ryukyu trench causes the collision to occur at depth (Wu et al., 2009). Substantial along-strike extrusion is evident in southwest Taiwan and occurs in response to both ongoing collisional shortening and indentation by the Peikang basement high (Lacombe et al., 2001; Hickman et al., 2002; Hsu et al., 2009).

The GPS measurements show how the 82 mm/yr of total plate convergence is partitioned across Taiwan. In addition to shortening accommodated by the LVF, several authors have suggested that ~30-45 mm/yr is transferred to the WF through a subhorizontal detachment beneath the Central Ranges (Loevenbruck et al., 2001; Dominguez et al., 2003; Hsu et al., 2003). However, this interpretation

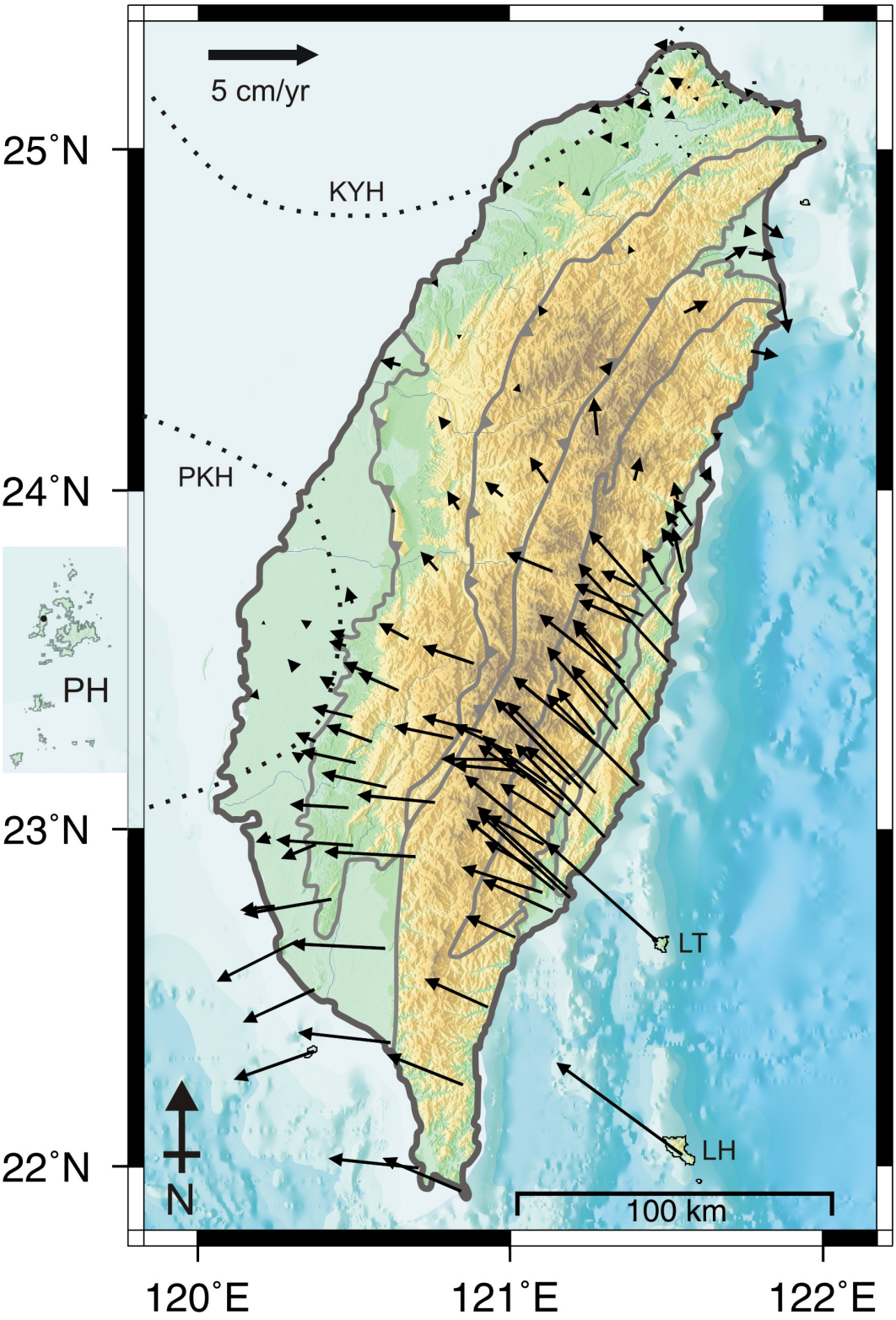

Figure 2-8. Horizontal velocities of GPS stations relative to Penghu Island PH. Data from Yu et al., 1997 – data errors are generally less than 2 mm/yr and 2°. Scale arrow in upper left. Islands: Lutao LT and Lanhsu LH. Peikang PKH and Kuanyin KYH basement highs.

is poorly constrained as measurements are sparse in the Central Ranges. Additional GPS data are needed to identify which faults accommodate active deformation in the orogen (Yu and Kuo, 2001). As of 2006, there are now more than 290 continuously recording GPS stations in Taiwan (Wu F.T. et al., 2007b) with network details available at: http://gps.earth.sinica.edu.tw.

2.5.2 Gravity

Measurements of the Earth's gravitational potential field can provide information about the density structure of the crust and mantle. In addition, gravity anomalies are often used to determine if an area is in isostatic equilibrium (Fowler, 2005). In Taiwan, 603 gravity measurements were made with fairly uniform coverage on an island-wide survey between 1980 and 1987 (Yen et al., 1998). Recently, an airborne gravity survey was conducted over Taiwan and results generally agree with the surface data (Hwang et al., 2007).

Figure 2-9 shows the Bouger anomaly map determined from the surface gravity data. In western Taiwan, negative anomalies are due to a mass deficit from downwarping and low density sediments in the foreland basin (Chou and Yu, 2002). In the Taiwan Strait, positive anomalies are due to the Peikang and Kuanyin basement highs. Beneath the Hengchung peninsula, positive values are caused by dense underlying oceanic crust. The large negative anomaly offshore eastern Taiwan results from thick sediments and downwarped crust in the Hoping basin (Hwang et al., 2007). However, the most striking feature of the Bouger anomaly map is the significant lack of correlation with the surface topography that implies dynamic rather than isostatic support of the young Taiwan orogen (Wu et al., 1997; Yen et al., 1998). Further, synthetic gravity data computed for an isostatically compensated model of Taiwan's topography does not adequately reproduce the measured data (Yen et al., 1998). The Taiwan orogen is thus undercompensated, implying that there is an insufficient low-density crustal root beneath the island to maintain the present topography.

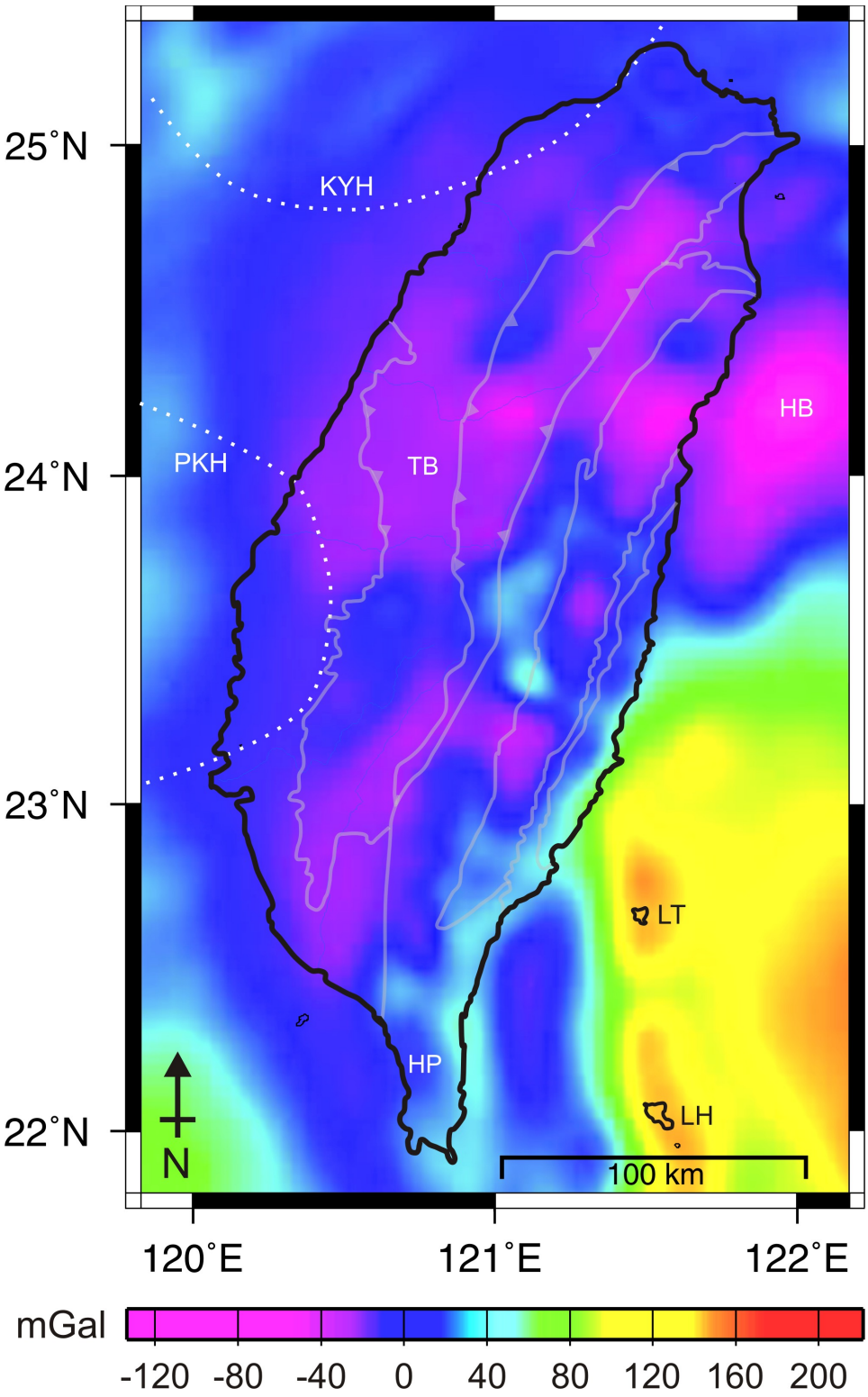

Figure 2-9. Bouger gravity anomaly map of Taiwan. Data from Yen et al., 1998. Significant anomalies are: Taichung Basin TB, Hoping Basin HB, Hengchung Peninsula HP. Islands: Lutao LT and Lanhsu LH. Peikang PKH and Kuanyin KYH basement highs.

The gravity data can provide insight to the end-member tectonic models. For example, assigning densities to the predicted structures in the thin-skinned model does not predict Bouger anomalies that match the observations (Yen et al., 1998). In contrast, good agreement with the measured data is obtained for a model with thickened crust beneath the Central Ranges (Wu et al., 1997). Recently, Zhang et al. (2004) inverted these gravity data to obtain a 3-D density model of Taiwan that supports the existence of a crustal root extending to depths of 50-60 km beneath the Central Ranges. To fit these gravity data required a density contrast at the Moho in the range 400-500 kg/m^3, that is consistent with density estimates of the lower crust and upper mantle from petrophysical data (Christensen and Mooney, 1995). However, gravity modeling is non-unique and cannot unambiguously distinguish between the proposed tectonic models.

2.5.3 Magnetics

A second geophysical potential-field method involves measurements of the Earth's magnetic field. These data are sensitive to the concentration of magnetic minerals and provide information on the crustal structure. Although not published for Taiwan, these data can also provide constraints on crustal temperature from calculation of the Curie depth (Negi et al., 1987). From July 2003 to February 2004, 6063 measurements of the Earth's magnetic field were made on the first ever island-wide survey of Taiwan (Yen et al., 2009). Previously, magnetic anomaly maps of Taiwan were restricted to exploration surveys by the Chinese Petroleum Corporation (Hsieh and Hu, 1972; Chang and Hu, 1981) and a sparsely instrumented survey by Hsu et al., 1998. These new magnetic data are sensitive to shallow basalts and outline the structure of the Peikang and Kuanyin basement highs, and reveal positive magnetic lineaments aligned parallel to the orogen (Figure 2-10). In particular, a northeast trending lineament is observed beneath the Lishan Fault, with Pleistocene-Pliocene Au-Cu mineralization (Lewis et al., 2007) occurring in regions of intersecting anomalies. These ore deposits are likely related to fluid flow driven by the convergent tectonics (Craw et al., 2002).

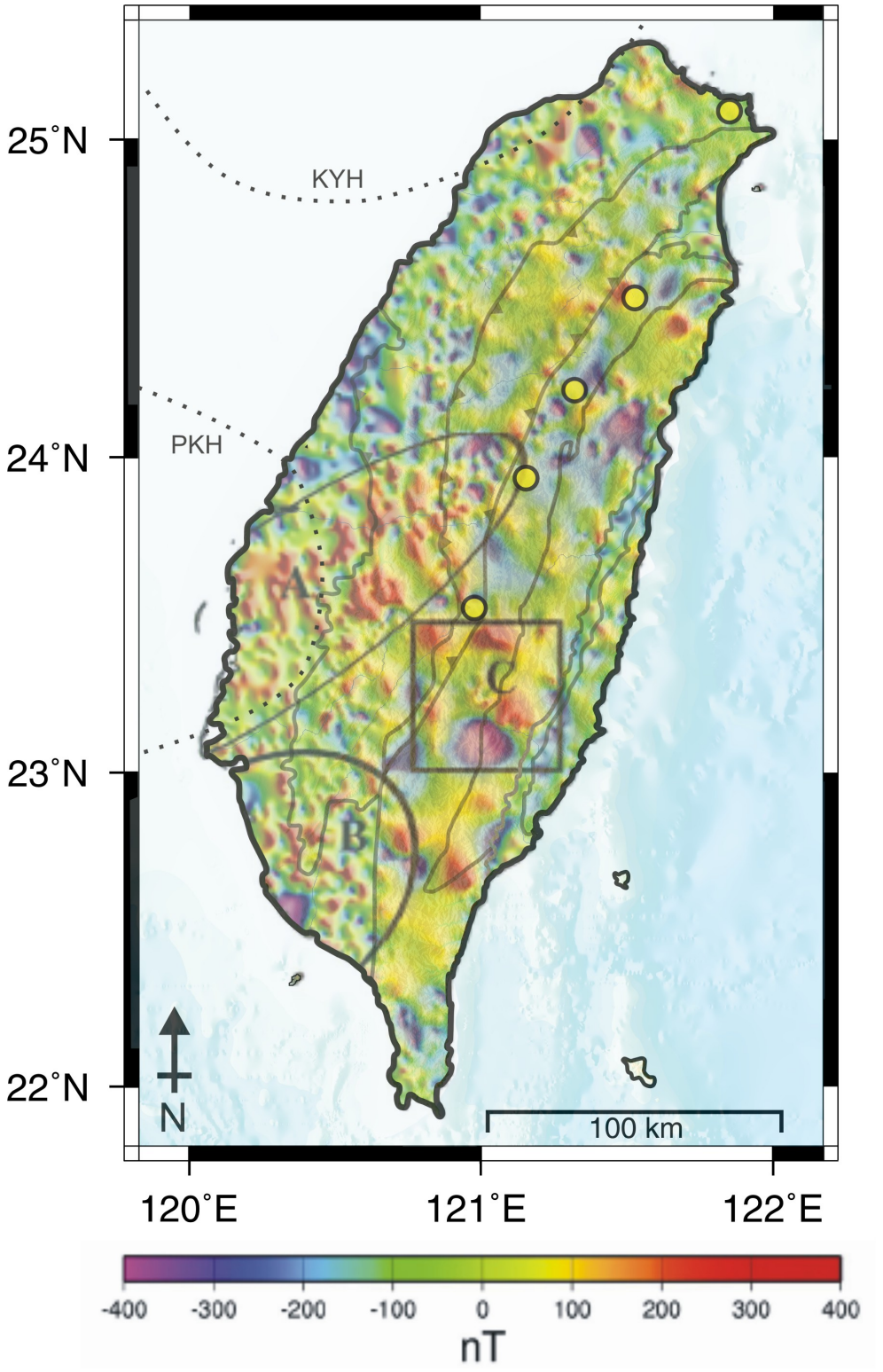

Figure 2-10. Magnetic anomaly map of Taiwan. Modified from Yen et al. (2009). A: Shallow basement, B: Iron-bearing sediments, C: Inferred ultramafic body. Yellow circles indicate locations of Au-Cu deposits (Lewis et al., 2007). Peikang PKH and Kuanyin KYH basement highs.

2.5.4 Seismicity

Earthquakes represent a response to tectonic stress and hypocentre locations and focal mechanisms provide insight on the internal deformation of the orogen. In 1991, the quality of local earthquake data in Taiwan improved with the expansion of the short-period seismic network to 72 stations. These data are complemented by 50 stations within the Broadband Array for Taiwan Seismology (BATS), and 1 Global Seismic Network station (TATO). Taiwan is very seismically active (Figure 2-11); the Central Weather Bureau catalog records over 15,000 events each year (Wu et al., 2004).

In southern Taiwan, a Wadati-Benioff zone associated with eastward subduction of the EUP at the Manila trench is visible south of 23°N (profile 9 in Figure 2-12; Kao et al., 2000; Lacombe et al., 2001). Similarly, in northern Taiwan dipping seismicity denotes northward subduction of the PSP at the Ryukyu trench (profile 10 in Figure 2-12; Lin, 2000). In contrast, there is no seismic evidence for an active subduction zone in central Taiwan (profiles 1-8 in Figure 2-12). Rather, an aseismic gap with sub-vertical boundaries exists beneath the Central Ranges (Lin, 2000; Wu et al., 2004). The lack of seismicity may either indicate weak strain or that this area experiences ductile deformation (Lin et al., 1998). Wu et al. (2004) attribute the aseismic gap to an enhanced ductility of rocks caused by an increased thermal gradient. The high thermal gradient could result from decoupling between the continental and oceanic lithosphere, resulting in rapid exhumation.

The 1999 $M_w = 7.6$ Chi-Chi earthquake (Figure 2-11) was followed by more than 20 $M_w > 6$ and over 20,000 $M_w > 2$ aftershocks. These events provided a new dataset for central Taiwan (Kao and Chen, 2000; Wu et al., 2004) and illuminated several previously quiescent steeply-dipping clusters of seismicity. For example, a planar cluster of events that dips steeply to the west was observed beneath the Lishan Fault extending to depths of 40 km (Gourley et al., 2007). These events occur at the western boundary of the aseismic zone and focal mechanism solutions reveal thrust faulting with the Central Ranges on the footwall side (Wu

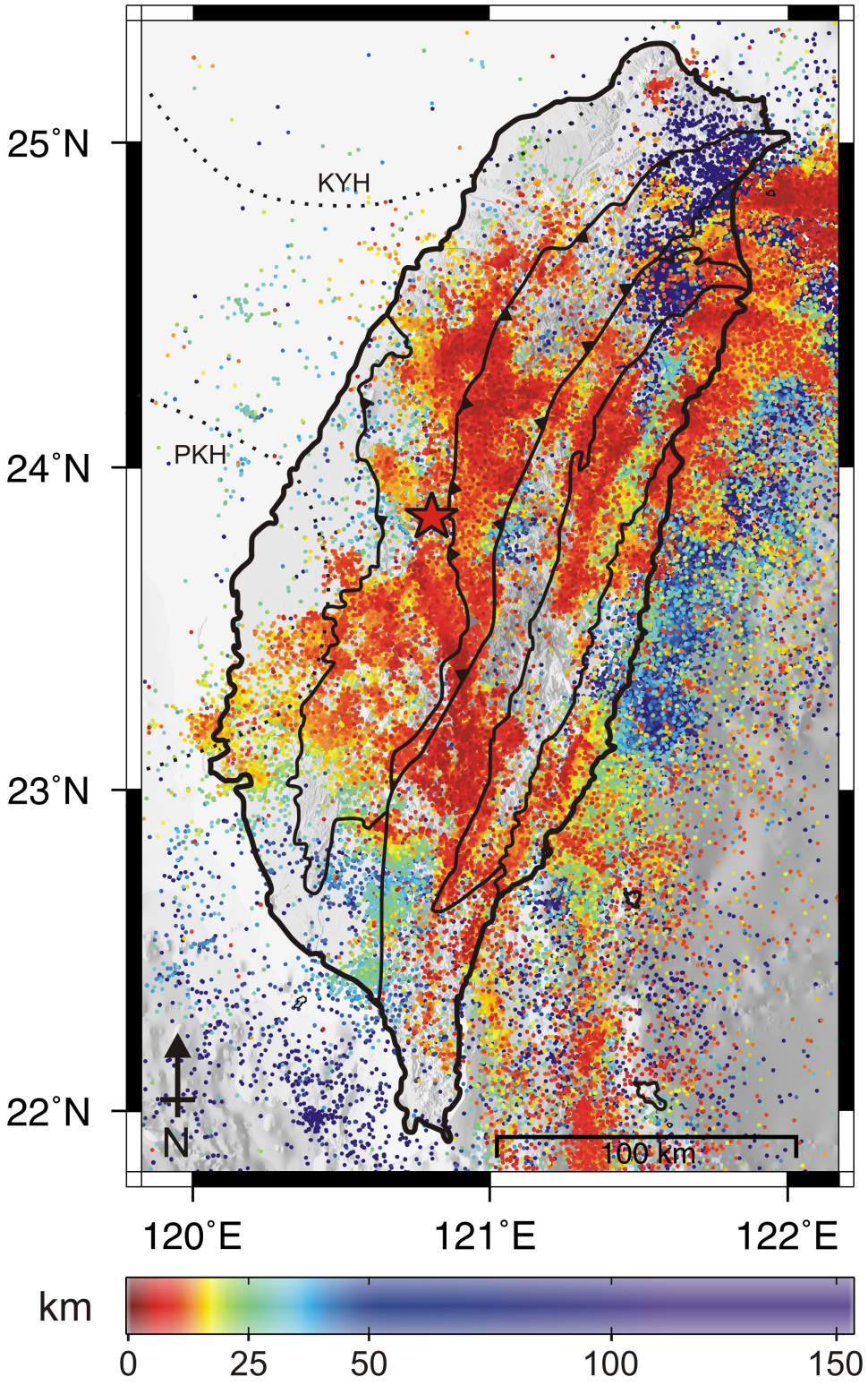

Figure 2-11. Seismicity of Taiwan. Hypocentre data for 267211 $M_w > 2$ events from 1991 to 2005, relocated by Wu et al., 2008. Colourbar denotes depth beneath sea level. The star marks the epicenter of the 1999 $M_w = 7.6$ Chi Chi earthquake. Peikang PKH and Kuanyin KYH basement highs.

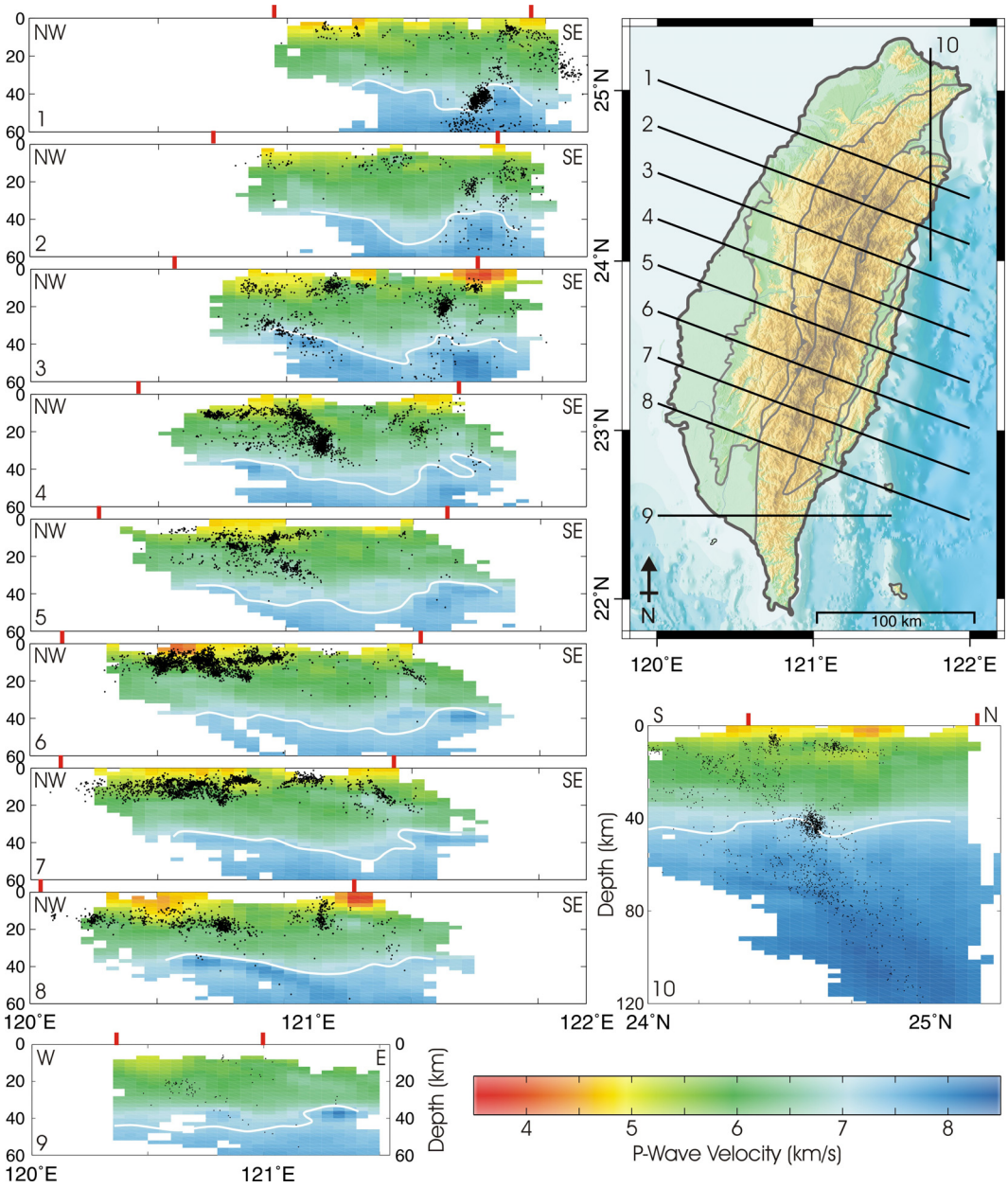

Figure 2-12. Cross sections of Taiwan seismicity (Wu et al., 2008 – only events with the highest quality relocation (A) are shown) and P-wave velocity (courtesy of Francis Wu – white areas indicate poor raypath coverage). Profile locations are shown in the inset map. Red bars denote where the profiles intersect the coasts of Tawain. No vertical exaggeration.

et al., 2004). Gourley et al. (2007) suggest these deep events, located below the brittle-ductile transition (~10-15 km depth) indicate the presence of strong materials at depth. With the Central Ranges forming the footwall, deformation recorded by these events would aid in the development of a crustal root.

The observation of an aseismic gap beneath the Central Ranges is opposed by Carena et al. (2002) who relocated and collapsed hypocentres on to inferred planar surfaces. These authors suggest that a continuous band of sub-horizontal seismicity exists at a depth of ~10 km and extends from the WF to the CR beneath central Taiwan (Figure 2-13). This band is inferred to be the décollement predicted by the thin-skinned tectonic model, but is not consistent with the aseismic gap observed beneath the Central Ranges by several other authors (e.g. Wu et al., 1997; Lin, 2000; Wu et al. 2004; Gourley et al., 2007; Wu et al., 2008).

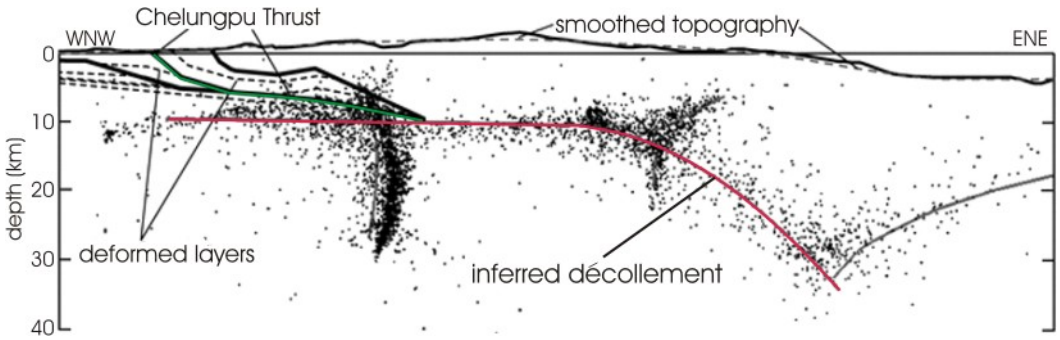

Figure 2-13. Cross section showing projected earthquakes together with inferred fault traces. Modified from Carena et al., 2002. No vertical exaggeration.

In general, earthquake location errors for stations recorded on islands are relatively large compared to continental settings (Gourley et al., 2007). This increased error, especially in depth location, results from spatial limitations of the seismic station distribution, and resulting seismic velocity models.

2.5.5 Seismic Tomography

Seismic tomography inverts measured traveltimes from seismic events to surface receivers in order to deduce variations in the subsurface seismic velocity. However, model resolution beneath Taiwan is poor, due to both the narrow width of the island and to a lack of deep local earthquakes. Until recently, only small-scale regional data and low resolution global measurements (Bijwaard et al., 1998) have been used to image the upper mantle velocity structure. Figure 2-12 shows cross-sections of a tomographic model consisting of P-wave velocity

estimates on an x = y = 5, z = 2 km grid and was obtained from first arrival data from TAIGER active seismic transects in 2007-2008. This model and others have revealed the following features of the crustal structure beneath Taiwan:

1. A low velocity zone exists beneath the Ilan Plain that is due to the onshore extension of the Okinawa trough (profile 10 in Figure 2-12; Rau and Wu, 1995).

2. Beneath the CP and WF, a low velocity wedge is consistent with sedimentary rocks in the foreland basin (profiles 1-9 in Figure 2-12; Wu Y.M. et al., 2007).

3. A deep high velocity zone beneath the LV and CR is interpreted to be oceanic crust of the Luzon forearc sliver (profiles 4-7 in Figure 2-12; Cheng et al., 2009). This zone is associated with high seismicity, yet resolution is insufficient to reveal forearc structure (Cheng et al., 2002).

4. High velocities exist at shallow depths (2-15 km) beneath the Central Ranges (profiles 3-4 in Figure 2-12; Wu Y.M. et al., 2007). These high velocities contradict the thin-skinned model, which predict the thickest sequence of sedimentary and upper crustal rocks to exist in the back of the wedge. Rau and Wu (1995) proposed that the high velocities result from exhumation due to decoupling and uplift in a thick-skinned regime.

5. A low velocity root (0.1-0.6 km/s slower than average) occurs beneath the aseismic Central Ranges to a depth of ~50 km at 24°N (profiles 2-4 in Figure 2-12; Roecker et al., 1987; Wu et al., 1997; Wu Y.M. et al., 2007). The correlation of low velocities within the aseismic zone implies that this region responds to the collision by ductile deformation and crustal thickening (Wu et al., 1997).

Both the seismicity and tomographic model results show significant variations in lithospheric structure that are inconsistent with the critical wedge model. Further, evidence for a deep Moho (~50km; Lin, 2005; Wu Y.M. et al., 2007) beneath the Central Ranges supports the development of a crustal root predicted by the thick-skinned model. However, only an orogen-scale densely instrumented seismic

tomography study using combinations of active and passive sources will significantly improve the resolution of structural features beneath Taiwan. Note that the tomographic model in Figure 2-12 represents a preliminary version of this required orogen-scale model that includes TAIGER active source seismic data.

2.5.6 Shear Wave Splitting Measurements

Finite strain in the mantle can produce an anisotropic fabric that is revealed by anisotropic shear wave propagation. This anisotropy is manifested at the surface by a time-delay observed between the arrivals of vertically propagating orthogonal shear wave modes, and is termed shear wave splitting. Strain induced lattice preferred orientation of upper mantle minerals results in faster propagation for waves polarized parallel to the plane of shear, than for those with cross-polarization (Molnar et al., 1999). Thus, the orientation and magnitude of shear wave splitting anomalies can reveal deformation properties of the mantle. However, it cannot be determined where the anisotropy occurs along the seismic travelpath. While splitting is commonly attributed to anisotropy in the upper mantle (Silver, 1996), ancient lithospheric deformation, or contributions from multiple regions of anisotropy (including the crust) could also contribute to the overall splitting observed.

In Taiwan, Rau et al., (2000) published shear wave delay times for S and ScS phases that increase from south to central Taiwan, and were interpreted to reflect the transition from subduction to collision (Figure 2-14). More striking is that the orientation of the fast direction was observed to be aligned parallel to the orogen. Recent measurements of SKS and SKKS phases confirm both the magnitude of the delay times and the pervasive orogen-parallel pattern of the fast axis (Hao et al., 2009; Huang B.S. et al., 2006). Since laboratory measurements of crustal rocks in Taiwan yield S-splitting delay times of less than 0.1 s (Kuo et al., 1994), and delay times at Penghu are less than 0.5 s (Wu F.T. et al., 2007a), the large magnitude S-splitting can at least in part be attributed to upper mantle anisotropy.

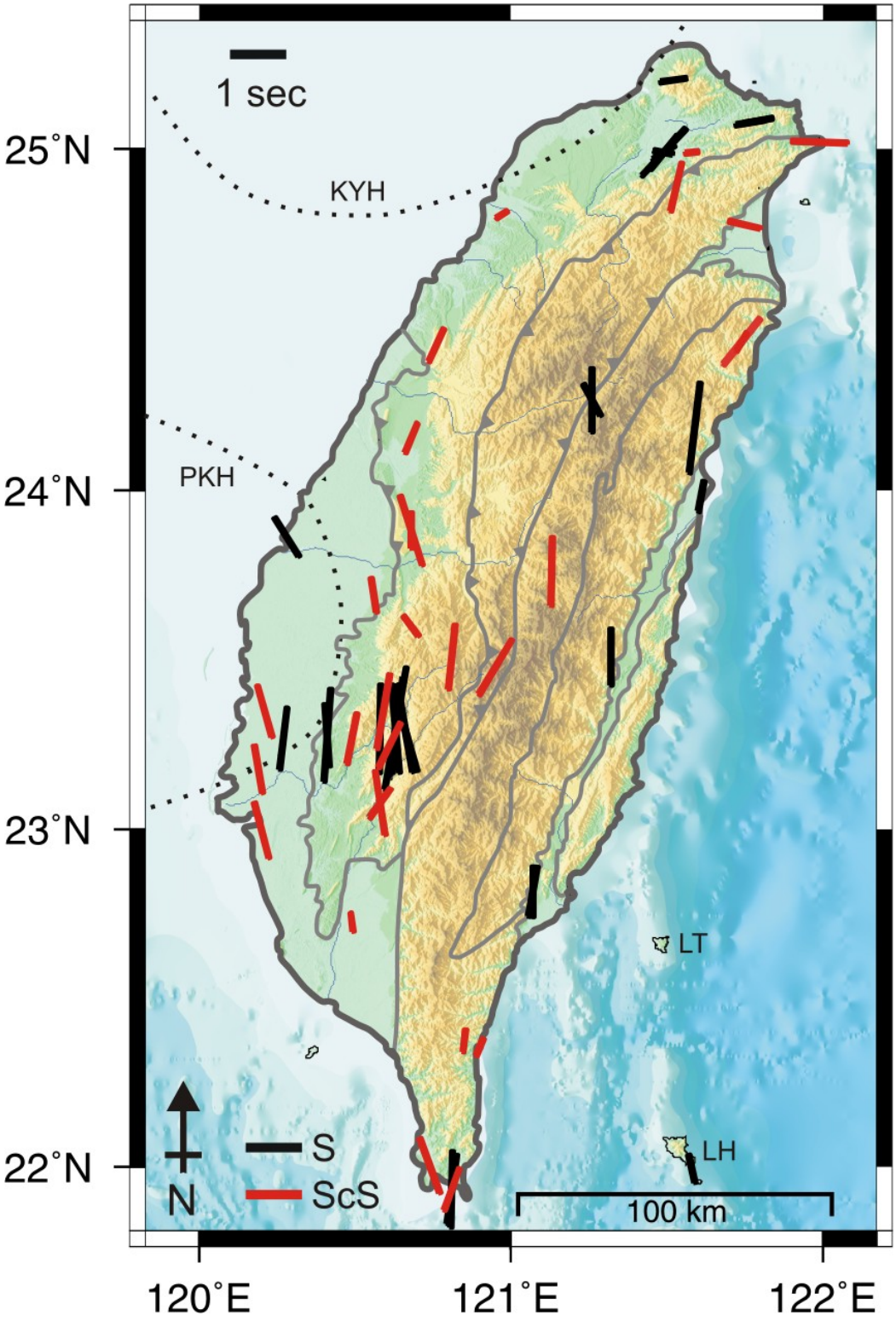

Figure 2-14. Shear wave splitting parameters for S and ScS phases plotted at station sites. The bar azimuth denotes the direction of fast polarization, with delay time proportional to bar length. Data from Rau et al., 2000. Islands: Lutao LT and Lanhsu LH. Peikang PKH and Kuanyin KYH basement highs.

The orogen-parallel orientation of the fast axis is therefore inferred to indicate that the lithosphere is reacting coherently with the upper crust in response to tectonic stress, as predicted by the thick-skinned model (Wu et al., 1997). In contrast, the downgoing lithosphere is assumed to be decoupled from the upper crust in the thin-skinned model, and is not expected to resemble the overlying orogen.

On the South Island of New Zealand, S-splitting data also show a fast axis that is parallel to the orogen structure in the Southern Alps (Molnar et al., 1999). Traveltime delays of 1-2 s are observed, similar to those measured in Taiwan (Wu F.T. et al., 2007a). These data suggest widespread deformation in the underlying mantle beneath the Southern Alps (Molnar et al., 1999).

2.5.7 Receiver Functions

When a seismic wave is incident on an interface, mode conversion may occur, partitioning the transmitted energy. For example, a P-wave incident on the Moho will split into a transmitted P-wave and a vertically polarized shear (SV) wave (Fowler, 2005). Since the SV-wave travels slower than the P-wave, the difference in arrival times between these waves at the surface can be used to determine the depth of the interface.

The most comprehensive receiver function analysis of Taiwan was performed by Kim et al. (2004) and indicates Moho depths beneath eastern Taiwan of 50-52 km, thinning towards the west to 28-32 km. However, complications of receiver function analysis permitted the use of data from only 7 BATS stations sparsely distributed throughout Taiwan. Strong azimuthal variations of the receiver functions were noted at most stations which could indicate dipping interfaces or anisotropy. Neither the study by Kim et al. (2004), nor earlier work (Ma and Song, 1997; Tomfohrde and Nowack, 2000) accounted for the effects of dipping layers or anisotropy, which have been documented by Rau et al. (2000). Nonetheless, receiver function estimates of thickened crust beneath the Central

Ranges support the thick-skinned lithospheric deformation model. However, these results do not rule out thin-skinned tectonics beneath the WF and CP.

2.5.8 Active Source Seismology

Active source reflection and refraction experiments are some of the best tools for imaging crustal scale structure. However, active source seismic data have almost exclusively been collected in western Taiwan by the Chinese Petroleum Corporation for hydrocarbon exploration (Suppe and Namson, 1979; Chi et al., 1981; Suppe, 1980; 1981; 1987). An exception was the TAICRUST project, which was primarily marine-based, but produced three onshore/offshore transects (McIntosh et al., 2005). Unfortunately, due to a typhoon, profiles were only shot in one direction, and depth resolution was limited to ~20 km. These data are thus not sufficient to define the lower crustal structure beneath the Central Ranges. However, interpretation of these data by McIntosh et al. (2005) and Hetland and Wu (1998) suggests a northwards evolution from thin-skinned tectonics in southernmost Taiwan to lithospheric collision in central Taiwan.

2.5.9 Thermal Structure

Thermal conditions are important for understanding crustal rheology and can aid interpretation of geophysical data, such as seismic velocity and seismicity (Song and Ma, 2002). For example, the coincidence of low velocity and low seismicity beneath the Central Ranges may be due to a high temperature and geothermal gradient (Wu, 1978; Wu et al., 1997). However, the surface heat flow in Taiwan has been measured only in shallow (<150 m) drill holes for hot spring exploration (Lee and Cheng, 1986). Further, since few observations were made in the Central and Coastal Ranges, contour maps are imprecise (Figure 2-15; Lin, 2000).

The surficial heat flow of Taiwan roughly mimics the topography, with a thermal high coincident with the aseismic zone observed beneath the Central Ranges (Lin,

2000). Several authors have analysed these heat flow data to place constraints on thin-skinned tectonic models of the orogen (Dahlen and Barr, 1989; Barr and Dahlen, 1990; 1989; Hwang and Wang, 1993). However, modeling by Lin et al. (1998) and Lin (2000) requires a late stage of rapid exhumation in the Central Ranges to fit the observed data. A possible mechanism for this inferred uplift is detachment and exhumation of subducted continental crust from the down-going oceanic slab in a thick-skinned regime. Analyses of fission track ages indicate that the ECR is experiencing greater uplift than the slate belt provinces, suggesting a distinct exhumation history (Liu et al., 2001; Willett et al., 2003). Further, present uplift rates measured by leveling data indicate rates of ~30 mm/yr (Liu and Yu, 1990), greater than the average rates of 7.5-15 mm/yr for the last million years determined by fission-track and K-Ar dating (Tsao et al., 1992).

Unfortunately, the measured heat-flow data are somewhat unreliable as the effects of local groundwater circulation were not accounted for, which can result in misleading values (Lachenbruch et al., 1995). Anomalously high and low heat flow data were thus eliminated prior to modeling by Song and Ma (2002), and their results suggest a modest geothermal gradient of 17 °C/km in the depth range 10-30 km. This estimate agrees well with integrated kinematic and thermal models of fission track ages from the Central Ranges that suggest a geothermal gradient in the range 20-25 °C/km (Willett et al., 2003). In contrast, Wu et al. (1997) have suggested a higher geothermal gradient (up to 50 °C/km) may exist due to inferred exhumation of the Central Ranges and strain heating in the orogen. However, in their thick-skinned model, while erosion and exhumation would increase the geothermal gradient, crustal thickening would compete to decrease it.

Despite efforts made to understand the thermal structure of Taiwan, an unavoidable obstacle remains in that heat flow measurements are difficult to make and interpret in areas of extreme relief. An alternative approach could be to determine electrical conductivities from magnetotelluric measurements, and interpret these data in terms of the thermal structure (Wu et al., 1997).

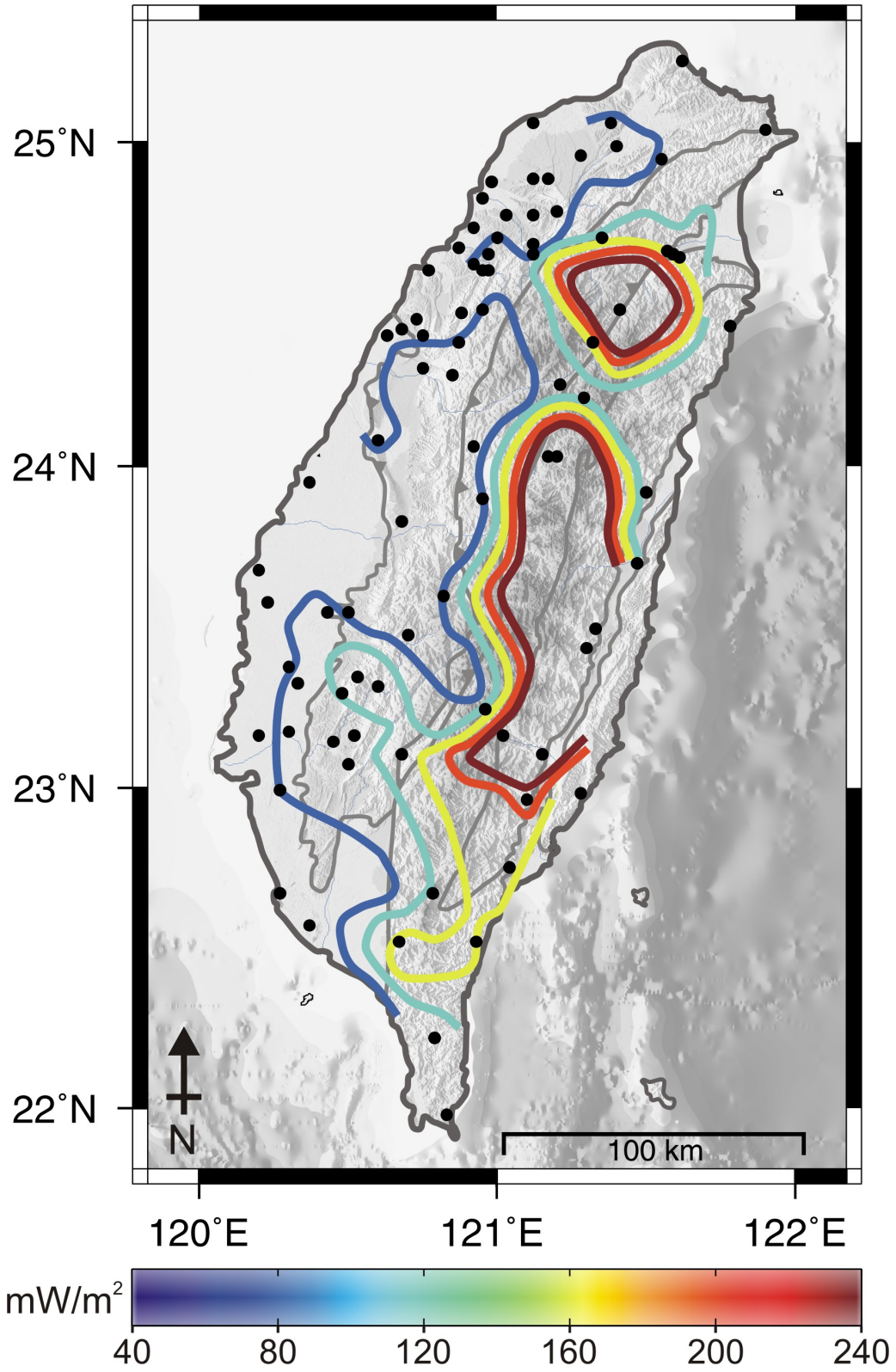

Figure 2-15. Contour map of observed surface heat flow in Taiwan. Measurement locations are indicated by black dots. Data from Lee and Cheng, 1986. Note that sparse data leads to imprecise surface heat flow contours in the Central Ranges.

2.5.10 Electromagnetic Studies

Electromagnetic (EM) geophysical methods image subsurface properties of the Earth from the measurement and analysis of natural or induced electromagnetic fields at the surface or within boreholes. Various EM techniques exist that are suitable to specific applications, such as resource exploration, near-surface mapping or deep tectonic studies. In Taiwan, EM methods have been employed for studying tectonic models of the island, and on a local scale for investigation of specific structure, such as groundwater characterization and geothermal exploration.

Time Domain EM

Time Domain surveys generate artificial EM fields that penetrate the subsurface. These primary fields generate secondary electric currents in conductive structures through the process of electromagnetic induction. These secondary currents create a secondary magnetic field that is measured by a surface receiver. Properties of the secondary magnetic field are used to map the electrical resistivity structure of the Earth (Telford et al., 1990). In the Longitudinal Valley, analysis of 350 Time Domain EM soundings reveals that conductive sediment thickens towards the south (Chen, 1998a), as previously indicated by seismic refraction data (Tsai et al., 1974). This observation suggests that the LV is closing in response to the oblique plate convergence (Chen, 1998a).

Magnetotellurics

In contrast to Time Domain EM, Magnetotellurics (MT) is a passive geophysical method; natural electromagnetic fields that diffuse in the Earth are measured to image the subsurface resistivity structure. MT is the only EM technique capable of imaging to depths greater than 10 km (Unsworth, 1999), and is thus very useful in lower crustal and upper mantle tectonic investigations. Electrical resistivity is particularly sensitive to temperature and electrically conductive materials (e.g. saline fluid, partial melt, sulphides and graphite), which can significantly affect crustal strength (Karato and Wenk, 2002; Wannamaker et al., 2002).

Early magnetotelluric studies in Taiwan employed 1-D analysis and inversion of broadband (0.001 – 1000 s) MT data to map conductivity anomalies in the upper crust (Chen 1998b; 1998c). Observed conductivity anomalies were inferred to be caused by aqueous fluids released by dehydration reactions in the crust, and were discussed in relation to known seismogenic zones. Later investigation focused on local conductive anomalies near the Sanyi-Puli seismic zone (Chen and Chen, 2000a; Chen and Chen, 2002) and beneath the Chi-Chi earthquake hypocentre (Chen and Chen, 2000b; Chen et al., 2002; Chen C.C. et al., 2007). These papers correlate deep crustal resistivity structure with these seismogenic zones, as high-pressure fluids in fault zones have been suggested to influence earthquake occurrence (Zhao et al., 1996; Ague et al., 1998). More recently, broadband MT data collected in central Taiwan through a collaborative field effort between National Central University, Taiwan and the University of Alberta were added to the existing MT database (~200 stations) and used to generate a 2-D inversion model across central Taiwan (Chen C.S. et al., 2007). Inversions of these MT data showed evidence of anomalous crustal conductors. However, the overall data quality and spatial coverage were insufficient to constrain model features. To adequately image the lithospheric-scale resistivity structure beneath Taiwan requires a much higher quality and spatially comprehensive dataset.

2.6 Summary of Previous Geophysical Research

Extensive well log data, exploration seismics and geological mapping have long established that a shallow-dipping décollement exists within the upper crust beneath the Western Foothills of Taiwan (Suppe, 1987). On the basis of this basal detachment, the Western Foothills fold-and-thrust belt was successfully modeled as a critically tapering accretionary wedge (Suppe 1976, 1980), that notably yielded the geological concepts of fault-bend and fault-propagation folding (Suppe, 1983, Suppe and Medwedeff, 1984). Over time, the application of thin-skinned tectonic models was extended to the orogen scale. Underlying this progression was the assumption that the basal décollement continued eastwards

beneath the Central Ranges. Since little constraint on the deep crustal structure beneath central Taiwan was available, this assumption was reasonable at the time.

As new geophysical data became available, the extension of the sub-horizontal detachment beneath the Central Ranges was questioned. Based on patterns of seismicity and other geophysical evidence, Wu et al. (1997) proposed the thick-skinned lithospheric deformation model that predicts the entire Eurasian lithosphere is involved in the collision and deformed in a vertically continuous system. This model contrasts with the thin-skinned theory that only permits collisional deformation within the upper-crustal accretionary wedge.

Despite obvious differences in the predicted lithospheric structure beneath central Taiwan, debate between these models has persisted due to inherent uncertainties in geophysical data. For example, while most earthquake relocation models indicate an aseismic region beneath the WCR, and clusters of deep-crustal seismicity (e.g. Wu et al., 2004; Gourley et al., 2007; Wu et al., 2008), a seismically defined upper-crustal sub-horizontal décollement was interpreted by Carena et al. (2002) beneath the Central Ranges. Partly contributing to this discrepancy is the difficulty in relocating events beneath a narrow island (Gourley et al., 2007).

An interesting first-order observation of the references organized in Table 2-1 reveals that the majority of recent results support the thick-skinned tectonic model for the Taiwan orogen. Further, no data are shown to be compatible solely with the thin-skinned model. However, the observation that some data have been interpreted to support either end-member model suggests that the cautionary remarks of Lee et al. (2002) and Mouthereau et al., (2001; 2002) should be heeded; namely that a single-minded thin or thick-skinned approach may limit a full understanding of the Taiwan orogen. Reality may lie within a combination of these end-member models, and additionally could vary with location along the orogen strike as inferred by McIntosh et al. (2005).

Method	Thin-Skinned	Thick-Skinned
Geodesy	Loevenbruck et al., 2001 Dominguez et al., 2003 Hsu et al., 2003	Hickman et al., 2002 Hsu et al., 2009
Gravity		Yen et al., 1998 Zhang et al., 2004
Seismicity	Carena et al., 2002	Wu F.T. et al., 1997; 2004 Lin, 2000 Gourley et al., 2007 Wu, Y.M. et al., 2007, 2008
Seismic Tomography	Lallemand et al., 2001	Roecker et al., 1987 Rau and Wu, 1995 Wu, Y.M. et al., 2007
Shear Wave Splitting		Rau et al., 2000 Huang C.Y. et al., 2006 Hao et al., 2009
Receiver Functions		Ma and Song, 1997 Tomfohrde and Nowack, 2000 Kim et al. 2004
Active Source Seismology		Hetland and Wu, 1998 McIntosh et al. 2005
Thermal Structure	Hwang and Wang, 1993 Barr and Dahlen, 1989; 1990 Dahlen and Barr, 1989	Lin, 2000
Magnetotellurics		Chen C.S. et al., 2007 Bertrand et al., 2009

Table 2-1. Summary of published geophysical studies supporting the end-member tectonic models for the Taiwan orogen.

Inherent uncertainties present in any individual geophysical technique require that a detailed multi-disciplinary approach be undertaken to unambiguously resolve the deep crustal structure beneath the Taiwan orogen. For example, Bertrand et al. (2009) quantitatively correlated a seismic velocity model with a magnetotelluric resistivity model to increase constraints on evidence for lithospheric deformation beneath the Central Ranges. This thesis describes the first-ever long-period MT data collected across the Taiwan orogen and their implications to the style of tectonics in this active arc-continent collision.

3. THE MAGNETOTELLURIC METHOD

Magnetotellurics (MT) is a passive geophysical imaging technique that records the time variation of natural electric and magnetic fields at the surface of the Earth. The amplitude and phase of these field components at the surface are dependent on the subsurface electrical structure. Specifically, the ratios of simultaneous electric and magnetic field measurements are used to image spatial variations of the electrical resistivity in the Earth. The electrical resistivity ρ (or its reciprocal quantity, the electrical conductivity σ) is sensitive to the fluid content of crustal and upper mantle rocks.

The electromagnetic behaviour of a medium is generally expressed in terms of three parameters. The electrical conductivity σ, dielectric permittivity ε and magnetic permeability μ describe the conductive, capacitive and inductive properties of the substance, respectively (Stratton, 1941). For linear isotropic materials, these quantities are defined by the following constitutive relationships

$$\mathbf{J} = \sigma \mathbf{E} \tag{3.1}$$

$$\mathbf{D} = \varepsilon \mathbf{E} \tag{3.2}$$

$$\mathbf{B} = \mu \mathbf{H} \tag{3.3}$$

where **J**, **E**, **D**, **B** and **H** represent the electric current density, electric field strength, electric displacement, magnetic induction and magnetic field strength, respectively (Griffiths, 1999). However, variations from the free space value of permeability $\left(\mu_{\circ} = 1.2566x10^{-6}\ \mathrm{N/A^2}\right)$ are minor for Earth materials (Zhdanov and Keller, 1994). In addition, at the low frequencies measured by magnetotelluric instruments, variations in dielectric permittivity can be neglected (see equations 3.15 and 3.16 below). In contrast, the electrical resistivity varies over 4 orders of

magnitude on lithospheric length-scales (Figure 1.5 in Simpson and Bahr, 2005). This wide variability makes electrical resistivity a useful property for determining the fluid content and mechanical properties of the crust and mantle.

Many descriptions of the MT method have been limited to sections within broader texts on electromagnetic methods in geophysics (e.g. Telford et al., 1990; Vozoff, 1991; Reynolds, 1997). In addition, many technical aspects of MT theory are spread over various volumes of Elsevier's *Methods in Geochemistry and Geophysics*, which is a broad-based series of texts (e.g. Kaufman and Keller, 1981; Berdichevsky and Zhdanov, 1984; Zhdanov and Keller, 1994; Spichak, 2006). Fortunately, Simpson and Bahr (2005) have recently published a text devoted solely to describing the practical aspects of MT. This book provides a comprehensive overview of MT theory and applications, consolidated in an easily accessible single volume (Türkoğlu and Bertrand, 2007).

3.1 Historical Development

The MT method was first proposed in 1950 with a brief description of how the frequency-dependent ratio of orthogonal electric and magnetic field components at the surface could be used to measure the resistivity structure of the Earth (Tikhonov, 1950). Specifically, Tikhonov showed that a proportionality and phase shift should exist between perpendicular components of the horizontal fields at the surface. The method was independently discovered by Cagniard (1953), who published the theoretical basis of MT in more detail, and is now commonly credited with pioneering the technique. A critical underlying assumption in MT is that the incident EM fields satisfy a plane wave approximation at the surface. Initially, the validity of this assumption was challenged (Wait, 1954; Price, 1962) and the technique was in doubt. More than a decade passed before Madden and Nelson (1964) convincingly showed that for a realistic Earth resistivity model the source fields can be adequately characterized as spatially uniform at the surface. MT then became established as a valid exploration technique.

3.2 Energy Sources for MT Exploration

The MT method requires measurements of the time variations of electric and magnetic fields at the surface of the Earth, that are made in the presence of the Earth's internal static magnetic field. Remnant magnetization of crustal rocks and dynamo action in the Earth's core comprise the internal part. However, time-variations of these fields are small, and it is the external fields that provide the energy source for MT. The external fields are generated by two mechanisms that operate within distinct frequency regimes (Heise et al., 2006). Above f = 1 Hz, signals originate from worldwide lightning activity and traverse the globe within a leaky waveguide bounded by the relatively conducting Earth and ionosphere. The ionosphere is a region of plasma with high electrical conductivity. The energy for fields with f < 1 Hz originates from the solar wind, which is a stream of H and He ions emitted radially outwards from the surface of the sun. The Earth's magnetic field deflects these charged particles along magnetic field lines towards the polar regions. However, temporal changes in the solar wind due to sunspot activity and other phenomena excite harmonics of the Earth's magnetosphere and induce large-scale electric currents in the ionosphere. These induced currents generate changes in the magnetic field that can be measured at the surface of the Earth and comprise the natural source exploited by long-period MT.

3.3 Electromagnetic Diffusion in the Earth

Equations describing the propagation of EM fields in the Earth can be derived from Maxwell's equations (Maxwell, 1873), which form a set of four fundamental partial differential equations that completely describe the behaviour of EM fields:

$$\nabla \times \mathbf{E} = -\frac{\partial \mathbf{B}}{\partial t} \qquad \text{(Faraday's Law)} \qquad (3.4)$$

$$\nabla \times \mathbf{H} = \mathbf{J} + \frac{\partial \mathbf{D}}{\partial t} \qquad \text{(Ampère's Law)} \qquad (3.5)$$

$$\nabla \cdot \mathbf{E} = \frac{\eta}{\varepsilon} \qquad (3.6)$$

$$\nabla \cdot \mathbf{B} = 0 \qquad (3.7)$$

where η is the density of free electric charges. Using the vector identity,

$$\nabla \times \left(\nabla \times \mathbf{A}\right) = \nabla\left(\nabla \cdot \mathbf{A}\right) - \nabla^2 \mathbf{A} \tag{3.8}$$

(Stratton, 1941), and taking the divergence of Faraday's Law gives,

$$\nabla\left(\nabla \cdot \mathbf{E}\right) - \nabla^2 \mathbf{E} = -\frac{\partial \mathbf{B}}{\partial t}. \tag{3.9}$$

Assuming that there are no free electric charges in the Earth (i.e. $\eta = 0$), and using Ampère's law in equation (3.8) with the constituent relationships yields,

$$\nabla^2 \mathbf{E} = \mu\sigma \frac{\partial \mathbf{E}}{\partial t} + \mu\varepsilon \frac{\partial^2 \mathbf{E}}{\partial t^2}. \tag{3.10}$$

Starting with the curl of Ampère's law results in the analogous equation for **B**,

$$\nabla^2 \mathbf{B} = \mu\sigma \frac{\partial \mathbf{B}}{\partial t} + \mu\varepsilon \frac{\partial^2 \mathbf{B}}{\partial t^2}. \tag{3.11}$$

Assuming that the time variations of the natural electric and magnetic fields at the surface have a harmonic time dependence (i.e. $e^{-i\omega t}$), equations (3.10) and (3.11) can be expressed as functions of angular frequency ($\omega = 2\pi f$),

$$\nabla^2 \mathbf{E} + \mu\omega^2 \varepsilon\left(1 + i\frac{\sigma}{\omega\varepsilon}\right)\mathbf{E} = 0 \tag{3.12}$$

$$\nabla^2 \mathbf{B} + \mu\omega^2 \varepsilon\left(1 + i\frac{\sigma}{\omega\varepsilon}\right)\mathbf{B} = 0 \tag{3.13}$$

which satisfy the form of Helmholtz equations with propagation constant,

$$k = \omega\sqrt{\mu\varepsilon\left(1 + i\frac{\sigma}{\omega\varepsilon}\right)}. \tag{3.14}$$

For MT measurements, data are acquired within the frequency range $10^{-5} < f < 10^{3}$ Hz, or equivalently within the period range $10^{-3} < T < 10^{5}$ s. Taking the free space values of permeability and permittivity, the second term that describes conduction current in equation (3.14) dominates, even with a lower limit for the conductivity of the continental crust (e.g. $\sigma = 0.0001$ S/m). Thus, neglecting the first term that represents the displacement current, the Helmholtz equations simplify to

$$\nabla^2 \mathbf{E} + i\omega\mu\sigma \mathbf{E} = 0 \tag{3.15}$$

$$\nabla^2 \mathbf{B} + i\omega\mu\sigma \mathbf{B} = 0. \tag{3.16}$$

Therefore within the spectral band sampled by MT, the electric and magnetic fields propagate via diffusion within the Earth. In contrast, in the insulating air the fields travel via wave propagation. Note that since the magnetic permeability is assumed constant, **B** and **H** are interchangeable.

3.4 Apparent Resistivity, Skin Depth and Phase

The simple analysis of MT data depends on the assumption of uniform incident EM fields. Therefore, assuming a vertically incident (z-direction) plane wave requires that **E** and **H** are constant on surfaces normal to incidence. Arbitrarily taking **E** to be polarized in the x-direction requires **H** polarization in the y-direction to achieve normal incidence; the Poynting vector $(\mathbf{P} = \mathbf{E} \times \mathbf{H})$ defines the direction of energy propagation (Griffiths, 1999). In component form, equation (3.15) simplifies to,

$$\frac{d^2 \mathrm{E_x}}{dz^2} + i\omega\mu\sigma \mathrm{E_x} = 0 \tag{3.17}$$

which is a homogeneous linear second-order differential equation with constant coefficients. General solutions satisfy the form (Zill, 1997),

$$\mathrm{E_x} = \mathrm{E_1} e^{-i\omega t} e^{-kz} + \mathrm{E_2} e^{-i\omega t} e^{+kz} \tag{3.18}$$

where $\mathrm{E_1}$ and $\mathrm{E_2}$ are constants and $k^2 = i\omega\mu\sigma$ is the wave number. Recognizing that at infinite depth the incident field must decay to zero amplitude, and that at the surface the amplitude is defined to be $\mathrm{E_\circ}$, yields the final solution

$$\mathrm{E_x} = \mathrm{E_\circ} e^{-i\omega t} e^{-(1-i)\sqrt{\frac{\omega\mu\sigma}{2}} z}. \tag{3.19}$$

Expanding Faraday's law into component form and simplifying terms in accordance with the assumption of plane polarized waves yields the expression,

$$\mathrm{H_y} = -\frac{1}{i\omega\mu} \frac{\partial \mathrm{E_x}}{\partial z}. \tag{3.20}$$

Taking the ratio of equations (3.19) and (3.20) and isolating for the electrical resistivity yields

$$\rho_{xy} = \frac{1}{\omega\mu}\left|\frac{\mathrm{E_x}}{\mathrm{H_y}}\right|^2 = \frac{1}{\omega\mu}\left|\mathrm{Z_{xy}}\right|^2. \tag{3.21}$$

Equation (3.21) mathematically describes the fundamental basis of MT as discovered by Tikhonov (1950) and Cagniard (1953), relating the ratio EM fields measured at the surface (defined as the EM impedance, Z) to the subsurface electrical resistivity. For a homogeneous half-space, this measurement of resistivity is equal to the actual bulk resistivity of the subsurface. However, over a non-uniform Earth, this estimate is more correctly referred to as an apparent resistivity ρ_a, defined as the average resistivity over a hemisphere of radius equal to one skin depth (equation 3.23). Thus, equation (3.21) is commonly expressed in the more general form,

$$\rho_a = \frac{1}{\omega\mu}\left|\mathrm{Z}\right|^2. \tag{3.22}$$

The skin depth is a frequency-dependent measure of the distance that EM fields diffuse into a conductive medium, such as the Earth. The skin depth is defined as the distance where the surface amplitude of the EM fields is reduced by a factor of $1/e$ (Griffiths, 1999). From equation (3.19), the skin depth is expressed as,

$$\delta = \sqrt{\frac{2}{\omega\mu\sigma}} = \sqrt{\frac{\rho T}{\pi\mu}} \tag{3.23}$$

indicating that longer period EM signals penetrate deepest in resistive media. In contrast, reducing signal period and increasing conductivity decrease the skin depth. The skin depth relates resistivity to subsurface depth via signal frequency, or equivalently, period. MT is therefore a sounding technique.

Variations in the subsurface resistivity also influence the phase difference between the measured electric and magnetic fields. Note that in a non-insulating medium (i.e. $\sigma \neq 0$), the propagation constant is complex (equation 3.14) and a phase-shift will exist between the electric and magnetic components of an EM wave (Figure 3-1). This phase shift is defined by

$$\phi_{xy} = \tan^{-1}\left[\mathrm{Im}\left(\mathrm{Z_{xy}}\right)/\mathrm{Re}\left(\mathrm{Z_{xy}}\right)\right]. \tag{3.24}$$

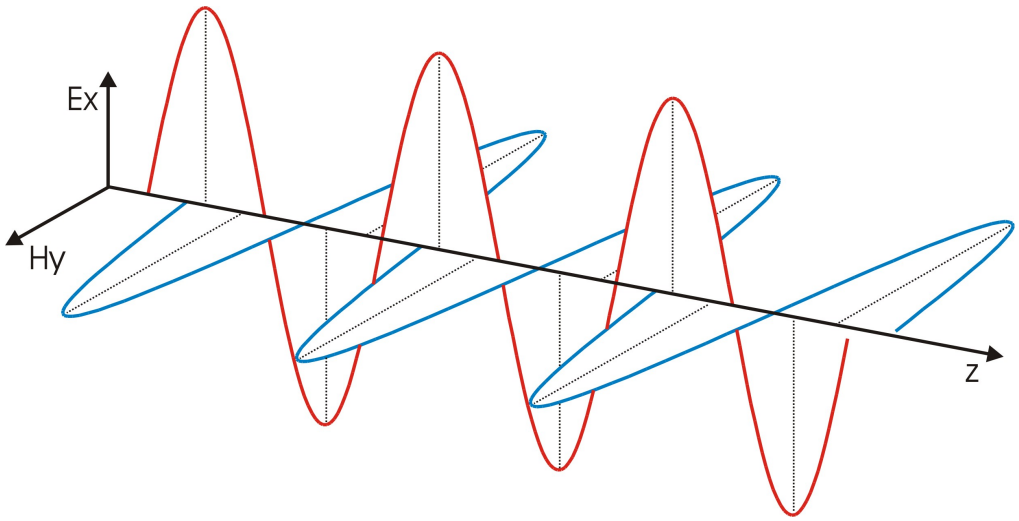

Figure 3-1. Transverse electromagnetic wave with a 60° phase shift between the electric and magnetic components. Note that for the low frequencies measured in MT, the displacement current is neglected and EM fields propagate via diffusion. However, the concept of phase is most easily illustrated for transverse waves.

For a half-space of constant resistivity, components of the electric and magnetic fields are equal and the phase becomes 45°. The phase is sensitive to changes in resistivity with depth; when resistivity increases, the phase becomes less than 45°, and vice versa. This relationship is approximated to first-order as (Vozoff, 1990),

$$\phi(\mathrm{T}) = \frac{\pi}{4}\left(1 - \frac{d\log_{10}\rho}{d\log_{10}\mathrm{T}}\right). \tag{3.25}$$

Note that the absolute amplitude of the incident EM fields is not required in equation 3.21 and 3.22 since only the ratio of the electric and magnetic components is used. Further, it can be shown that EM waves incident at all angles will refract vertically in the Earth due to the extreme contrast in electrical resistivity that occurs at the Earth's surface (Vozoff, 1991).

3.5 MT Impedance of a One-Dimensional Earth

A typical 1-D Earth model consists of variations with depth only. For this multi-layered model, Wait (1954) derived a recursion formula to analytically calculate the surface impedance in an iterative process starting from the lowermost layer, a

homogeneous half-space. This simplified model is useful for demonstrating the principles of the MT method but is often not applicable to data interpretation. Wait's recursion formula is,

$$Z_n = \frac{\omega\mu}{k_n}\left[\frac{k_n Z_{n+1} + \omega\mu \tanh(k_n l_n)}{\omega\mu + k_n Z_{n+1} \tanh(k_n l_n)}\right] \tag{3.26}$$

where from equation (3.19),

$$k_n = (1-i)\sqrt{\frac{\omega\mu\sigma_n}{2}} \tag{3.27}$$

and the thickness of nth layer is $l_n = z_n - z_{n-1}$. A two-layer model (Figure 3-12) is sufficient to illustrate key concepts and equation (3.26) simplifies to,

$$Z_S = \frac{\omega\mu}{k_1}\left[\frac{k_1 + k_2 \tanh(k_1 z_1)}{k_2 + k_1 \tanh(k_1 z_1)}\right]. \tag{3.28}$$

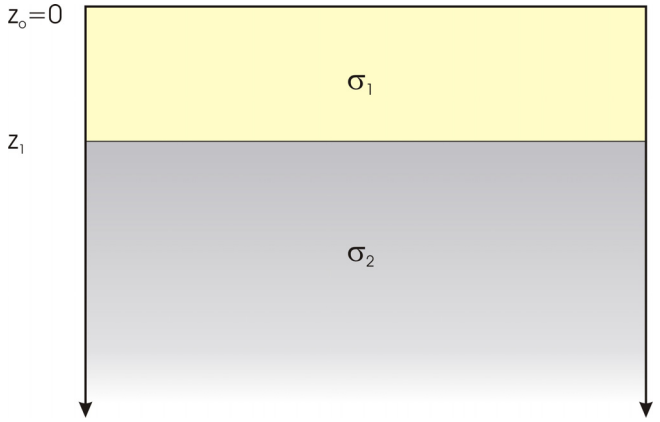

Figure 3-2. Two-layer half-space resistivity model.

High Frequency Limit

In this case, $\tanh(k_1 z_1) \to 1$, equation (3.28) reduces to $Z_S = Z_1$ and $\rho_{aS} = \rho_1$. Therefore, at high frequency MT is sensitive to the upper layer only, since the skin depth (equation 3.23) is small.

Low Frequency Limit

In this case, $\tanh(k_1 z_1) \to 0$, equation (3.28) reduces to $Z_S = Z_2$ and $\rho_{aS} = \rho_2$. At low frequency, the skin depth is large and the MT response is dominated by the resistivity of the lower half-space.

To explore variations of the bottom layer properties requires that these frequency effects be avoided. A thin-layer approximation is enforced by setting $\lambda_1 >> z_1$, which implies that $k_1 z_1 << 1$ and thus, $\tanh(k_1 z_1) \rightarrow k_1 z_1$ giving,

$$Z_S = \omega\mu\left(\frac{1 + k_2 z_1}{k_2 + k_1^2 z_1}\right). \tag{3.29}$$

Conductive Basement $(\sigma_2 >> \sigma_1)$

In this case, $k_2 >> k_1$, equation (3.29) reduces to $Z_S = \omega\mu z_1$ and $\rho_{aS} = \omega\mu z_1^2$. The apparent resistivity depends only on the thickness of the resistive layer, illustrating that MT is very sensitive to the depth to the top of a conductive layer.

Resistive Basement $(\sigma_2 << \sigma_1)$

In this case, $k_2 << k_1$, equation (3.29) reduces to $Z_S = \omega\mu / k_1^2 z_1$ and $\rho_{aS} = \left[\omega\mu(\sigma_1 z_1)^2\right]^{-1}$. Therefore, the apparent resistivity depends on the product of the conductivity and thickness of the upper layer, termed the conductance. This case reveals an inherent non-uniqueness of the method. MT cannot independently resolve the conductivity and thickness of a layer. Rather, measurements are sensitive only to the product of these quantities. Independent information is required to overcome this uncertainty if either parameter is desired individually.

3.6 MT Impedance of a Two-Dimensional Earth

A 2-D Earth contains resistivity variations in only one horizontal direction (y-direction), in addition to depth. In this case, expanding Ampère's and Faraday's laws, and eliminating partial derivatives with respect to x (the invariant geoelectric strike direction), allows the subsequent equations to be coupled into two independent modes containing only mutually orthogonal field components:

$$\frac{\partial B_z}{\partial y} - \frac{\partial B_y}{\partial z} = \mu\sigma E_x \quad \frac{\partial E_x}{\partial z} = i\omega B_y \quad -\frac{\partial E_x}{\partial y} = i\omega B_z \qquad \textbf{TE Mode} \tag{3.27}$$

$$\frac{\partial E_z}{\partial y} - \frac{\partial E_y}{\partial z} = i\omega B_x \quad \frac{\partial B_x}{\partial z} = \mu\sigma E_y \quad -\frac{\partial B_x}{\partial y} = \mu\sigma E_z \qquad \textbf{TM Mode} \tag{3.28}$$

The TE (transverse electric) mode contains only measurements of the strike-parallel electric fields and strike-perpendicular magnetic fields. In contrast, the TM (transverse magnetic) mode is comprised of strike-parallel magnetic fields and strike-perpendicular electric fields (Figure 3-3).

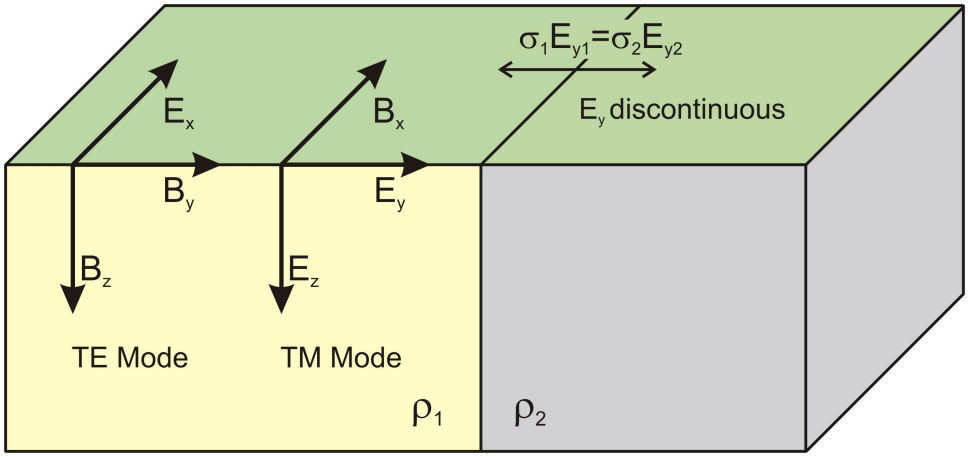

Figure 3-3. Two-dimensional quarter-space model. Resistivity structure is invariant parallel to the geoelectric strike (x-direction).

3.6.1 The Transverse Electric (TE) Mode

The TE mode comprises the field components E_x, B_y and B_z. Since E_x flows parallel to geoelectric strike, and magnetic fields normal to an interface are continuous, these field components are all continuous and related by inductive effects. It follows that estimates of the apparent resistivity (ρ_{xy}) and phase (ϕ_{xy}) are spatially continuous. The presence of thin conductors oriented parallel to geoelectric strike is well resolved by the TE mode, but depth resolution is limited. However, vertical magnetic fields are generated in the TE mode due to lateral gradients in conductivity. These vertical fields mainly help to resolve lateral variations, but also possess some vertical resolution (Unsworth et al., 2000).

3.6.2 The Transverse Magnetic (TM) Mode

The TM mode is comprised of the components E_y, B_x and E_z and includes both inductive and galvanic (frequency independent) effects. The galvanic effects arise

from charge accumulation on conductive boundaries required to satisfy the conservation of current density law as E_y flows perpendicular to strike. These effects cause estimates of ρ_{yx} and ϕ_{yx} to be discontinuous across an interface giving the TM mode enhanced sensitivity to lateral conductivity variations. Note that since air is assumed to be a perfect insulator, E_z at the surface tends to zero.

3.7 The Electromagnetic Impedance Tensor

The amplitude and phase relationships between ratios of horizontal orthogonal electric and magnetic fields at the Earth's surface are represented by the electromagnetic impedance that is defined to be,

$$Z = \frac{E}{H}. \tag{3.29}$$

The impedance is known as a transfer function, since it describes the frequency dependent connection between the input (magnetic field) and output (electric field) of a linear and time-invariant system. In general, the impedance represents a tensor quantity and is expressed as (Sims et al., 1971),

$$\begin{bmatrix} E_x \\ E_y \end{bmatrix} = \begin{bmatrix} Z_{xx} & Z_{xy} \\ Z_{yx} & Z_{yy} \end{bmatrix} \begin{bmatrix} H_x \\ H_y \end{bmatrix}. \tag{3.30}$$

The impedance tensor contains information on the geoelectric directionality and dimensionality of the Earth, and simplifies in the limiting cases of one- and two-dimensions. To illustrate these forms requires the definition of two orthogonal coordinate frames (Figure 3-4).

3.7.1 One-Dimensional Earth

For the multi-layered Earth model, surface measurements of the impedance are independent of the azimuth of the measured orthogonal electric and magnetic fields. The impedance tensor contains a single value and simplifies to,

$$\mathbf{Z_{1D}} = \begin{bmatrix} 0 & Z_{xy} \\ -Z_{xy} & 0 \end{bmatrix}. \tag{3.31}$$

The diagonals are zero, since Faraday's law describes magnetic field variations to induce only orthogonal electric fields; parallel components are uncorrelated.

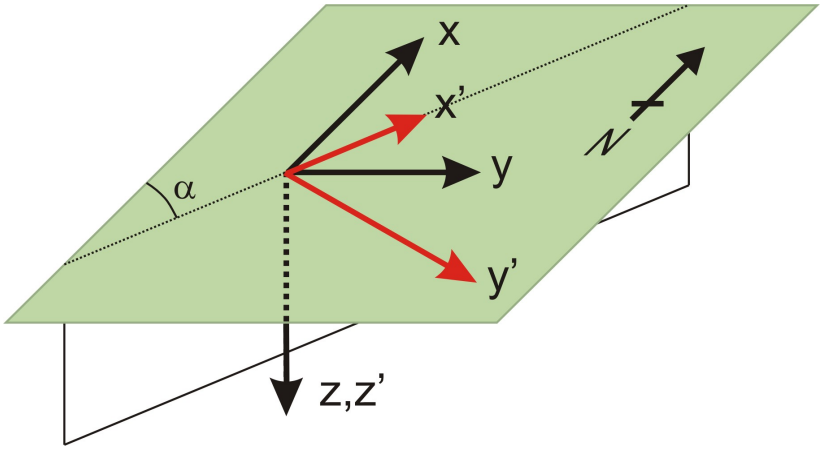

Figure 3-4. Orthogonal coordinate systems. Field coordinate frame (x,y,z) aligned to geomagnetic north, and the geoelectric coordinate frame (x',y',z') aligned to geoelectric strike α.

3.7.2 Two-Dimensional Earth

In the 2-D case, the surface impedance is dependent on the azimuth of the orthogonal field measurements. In the special case that the field and geoelectric frames are aligned, the impedance tensor reduces to,

$$\mathbf{Z_{2D}} = \begin{bmatrix} 0 & Z_{xy} \\ Z_{yx} & 0 \end{bmatrix}. \tag{3.32}$$

In general, the geoelectric strike direction is unknown prior to data acquisition and the measured tensor will contain non-zero diagonal entries. For perfectly 2-D data, mathematical rotation reduces the measured impedance tensor to the form in equation (3.32). The rotation matrix is,

$$\mathbf{R} = \begin{bmatrix} \cos\alpha & \sin\alpha \\ -\sin\alpha & \cos\alpha \end{bmatrix} \tag{3.33}$$

and operates to give $Z_{2D} = RZR^t$, where ^{t} denotes the transpose. However, the strike angle cannot be determined from the impedance tensor elements alone. Since rotation by 90° simply switches the modes, two orthogonal directions are possible. Induction vectors (see below) are often used to overcome this ambiguity.

3.7.3 Three-Dimensional Earth

The most general case is when resistivity varies in three-dimensions. In practice, measured MT data are never entirely 1-D or 2-D, and diagonal elements of the impedance tensor are always non-zero. However, in many cases the Earth response is dominated by an overall 1-D or 2-D structure, permitting data analysis within these lower dimensions. Detailed assessment of the dimensionality of MT data is therefore required to determine if 3-D effects are sufficiently present to preclude a simpler 1-D or 2-D analysis.

3.8 Induction Vectors and the Coast Effect

The impedance tensor does not capture the full information available from MT data since it comprises only the horizontal field components; lateral variations in conductivity induce non-zero vertical magnetic fields. Analogous to the EM impedance, ratios of the vertical to horizontal magnetic fields are linked by the magnetic transfer function, commonly known as the tipper function T (Parkinson, 1959; 1962; Wiese, 1962),

$$\left[\mathrm{H}_z\right] = \begin{bmatrix} T_x & T_y \end{bmatrix} \begin{bmatrix} \mathrm{H}_x \\ \mathrm{H}_y \end{bmatrix}. \tag{3.34}$$

The tipper magnitude is given by,

$$|T| = \sqrt{|T_x|^2 + |T_y|^2} \tag{3.35}$$

and is proportional to the intensity of anomalous current concentrations that result in the vertical fields (Jones and Price, 1970). The tipper is so named because it tips the horizontal magnetic fields into the vertical plane. This phenomenon is visualized through vector representations of the tipper functions, referred to as induction vectors (Figure 3-5).

Similar to the phase shift that exists between the horizontal EM fields, the tipper quantity also includes in-phase (real) and out-of-phase (imaginary) components. This phase-lag results from the finite time required to induce vertical fields at

conductive boundaries in the subsurface. For strong conductors the tipper response is dominantly in-phase (Telford et al., 1990), and when plotted as induction vectors (Figure 3-5), these arrows point towards areas of anomalous current concentrations (in the Parkinson convention). These induction arrows are therefore sensitive to lateral conductivity variations and in addition can provide insight on the dimensionality of the Earth; in a 2-D model these vectors should align perpendicular to geoelectric strike.

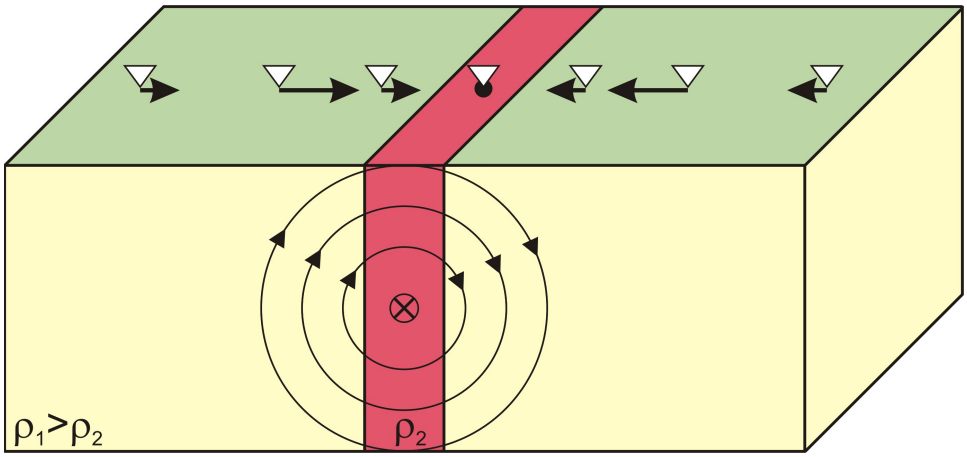

Figure 3-5. Induction vectors (real component, Parkinson convention) plotted on a profile across geoelectric strike for a 2-D Earth model. White triangles denote MT stations and black arrows the induction vectors. The circular rings show magnetic field lines at a point in time when current is into the page.

One of the largest contrasts in electrical conductivity at the Earth's surface occurs along the coasts (Lilley, 2007) where induced vertical magnetic fields rotate nearby induction vectors to point towards the conductive ocean (Parkinson, 1959; 1962). Since the skin depth is much shallower in the sea than on land, electric currents spread out to depth beneath the continents (Park et al., 1991). The length over which these currents vertically diffuse is termed the adjustment distance and defines the region influenced by the coast effect (Ranganayaki and Madden, 1980; Weaver and Dawson, 1992). Seawater also influences the TE and TM mode impedances observed in coastal regions (Fischer, 1979). Along-strike electric currents will preferentially flow within the conductive seawater; thus the TE mode will record low electric field and ρ_{TE} will be down-biased. In contrast, the

increased current flowing onshore in the near-surface will lead to higher values of ρ_{TM}. MT data analysis from coastal areas must therefore account for the presence of surrounding seawater. Figure 3-6 shows synthetic MT data that were 2-D forward modeled at locations in a coastal region. The bias towards higher TM mode and lower TE mode resistivity is clearly observed, with the effect increasing with proximity to the coast. In addition, the large in-phase tipper response in comparison to the imaginary component response reflects the strong conductivity of the seawater and causes the induction vectors to point towards the coast.

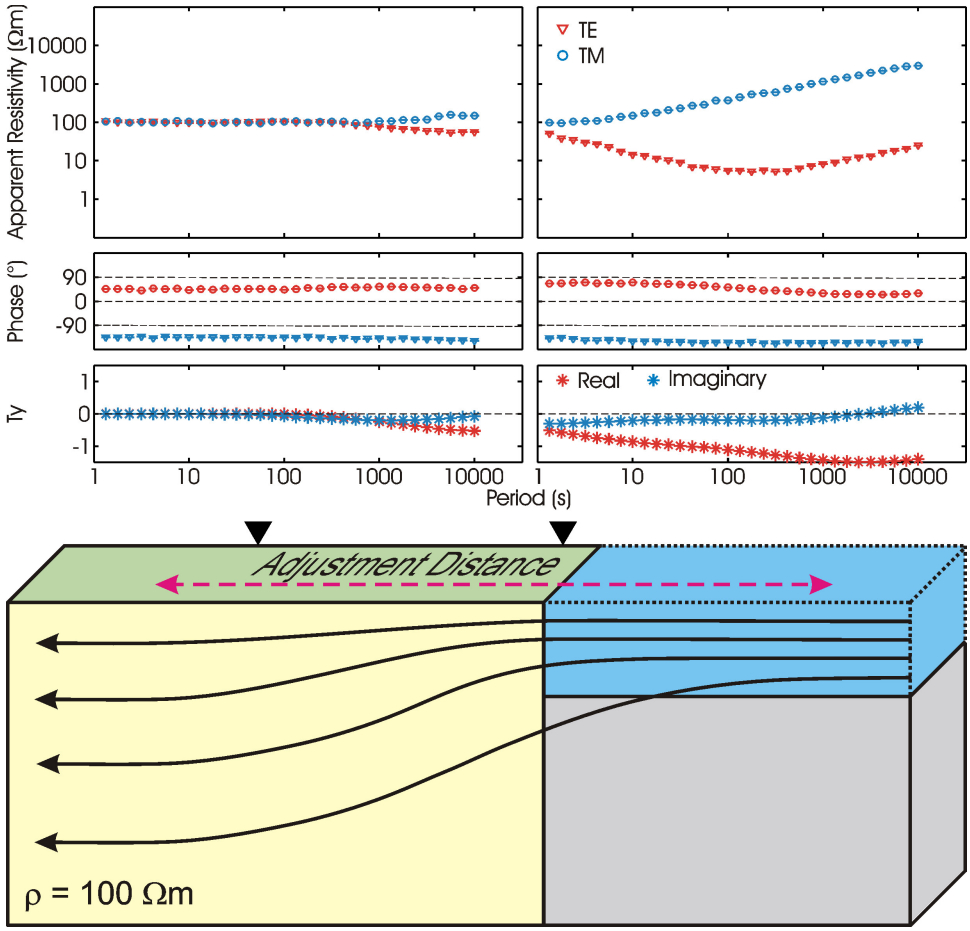

Figure 3-6. Geomagnetic coast effect. Top panels show synthetic MT data 2-D forward modeled at measurement locations (black triangles) on land near (2 km) and far (100 km) from the coast. Note that the coast effect diminishes with distance from the seawater (ρ = 0.3 Ωm). Black arrows denote electric current lines for the TM mode. Red dashed arrow indicates the adjustment distance.

3.9 Dimensionality and Distortion

Localized conductivity heterogeneities beneath an MT site can alter the direction and magnitude of the regional electric fields (Bibby et al., 2005). At long-periods (i.e. skin depth greater than the dimensions of local heterogeneities), inductive effects within these conductive heterogeneities become negligible compared to the inductive response of the regional structure (Jiracek, 1990). Therefore, MT data comprise a superposition of the inductive (frequency dependent) signature of the regional structure and the galvanic (frequency independent) distortion from any localized near-surface heterogeneities (Wannamaker et al., 1984). The distortion masks the response of the regional structure and analysis may be required to eliminate the galvanic effects. In tensor notation,

$$\mathbf{D} = \begin{bmatrix} D_{11} & \mathrm{D}_{12} \\ \mathrm{D}_{21} & D_{22} \end{bmatrix} \tag{3.36}$$

defines the distortion tensor whose elements are real and frequency independent (Groom and Bahr, 1992; Chave and Smith, 1994). The relationship between the regional ($\mathbf{Z}_\mathrm{R}$) and observed ($\mathbf{Z}$) impedance tensors becomes,

$$\mathbf{Z} = \mathbf{D}\mathbf{Z}_\mathrm{R} \,. \tag{3.37}$$

To eliminate the galvanic distortion requires the determination of $\mathbf{Z}_\mathrm{R}$ from the measured tensor $\mathbf{Z}$. However, equation (3.37) defines an underdetermined set of eight equations with twelve unknowns, requiring further constraints to obtain a solution.

3.9.1 Rotation and Decomposition Methods

Several techniques have been developed to extract the regional impedance tensor based on the underlying assumption that the subsurface resistivity structure is two-dimensional. In this case, the impedance tensor simplifies to the form in equation (3.32), in the unknown geoelectric strike coordinate frame. Early models (e.g. Swift, 1967; reprinted 1986; Zhang et al., 1987; Bahr, 1988) estimate the geoelectric strike from a minimization criterion through rotation of the observed impedance tensor. However, rotational methods are unstable for measured data

containing noise and/or strong distortion and can lead to poor estimates of α. Groom and Bailey (1989) proposed a tensor decomposition model that uses an inversion scheme to remove the non-inductive responses from the impedance tensor. The algorithm was extended by McNeice and Jones (2001) to statistically fit an entire data set simultaneously, and is based on factoring the distortion tensor into determinable (twist and shear) and non-determinable (anisotropy and site gain) components. Including the real valued gain and anisotropy parameters into the regional impedance yields,

$$\mathbf{Z} = \mathbf{R}\mathbf{T}_{\mathbf{w}}\mathbf{S}_{\mathbf{h}}\mathbf{Z}_{\mathbf{2D}}\mathbf{R}^{\mathbf{T}} \tag{3.38}$$

where, $\mathbf{T_w}$ represents a rotation of the telluric vectors to align with the local strike, and $\mathbf{S_h}$ denotes an angular deflection of the telluric vectors to non-orthogonal orientation. Equation (3.38) describes a set of 8 equations and 7 unknowns (the geoelectric strike α, the twist and shear angles, and the 4 components of the 2-D impedance tensor) that is solved using a least-squares approach. Tensor decomposition is commonly used for distortion removal and to determine the geoelectric strike for assumed two-dimensional MT data.

3.9.2 The MT Phase Tensor

Equation (3.37) is underdetermined and necessarily requires constraints to obtain a solution. However, the assumptions made by Groom and Bailey (1989) reduce the problem to a degree where it becomes over-determined. This reduction suggests that too many constraints have been applied (Bibby et al., 2005). Caldwell et al. (2004) showed that a partial solution is possible without any assumptions regarding the dimensionality of the regional conductivity structure. Separating the impedance tensor into real (**X**) and imaginary (**Y**) parts,

$$\mathbf{Z} = \mathbf{X} + i\mathbf{Y} \, . \tag{3.39}$$

The MT phase tensor is defined to be,

$$\mathbf{\Phi} = \mathbf{X}^{-1}\mathbf{Y} = \begin{bmatrix} \Phi_{11} & \Phi_{12} \\ \Phi_{21} & \Phi_{22} \end{bmatrix}. \tag{3.40}$$

It follows from equation (3.37) that $\mathbf{\Phi} = \mathbf{\Phi}_{\mathbf{R}}$. Therefore, the observed and regional phase tensors are identical and independent of galvanic distortion (Caldwell et al., 2004; Bibby et al., 2005). The four elements of the phase tensor are the only uniquely determinable portion of the regional impedance tensor and themselves yield information on the dimensionality of the regional conductivity structure (Bibby et al., 2005). This information can be visualized by representing the phase tensor as an ellipse (Figure 3-7) that is completely characterized by one direction α, and three coordinate invariants, Φ_{max}, Φ_{min}, and β (e.g. Heise et al., 2007; 2008; Hill et al., 2009).

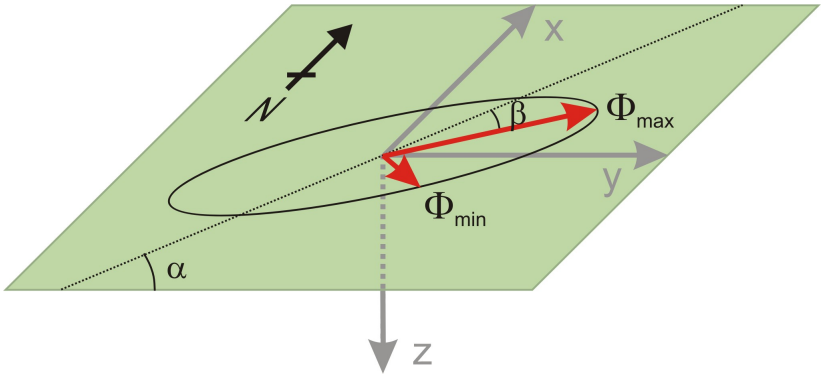

Figure 3-7. Graphical representation of the phase tensor. Coordinate invariants Φ_{max} and Φ_{min} define the magnitudes of the major and minor axes, the skew angle β measures the tensor's asymmetry. The angle α indicates the tensor's dependence on the coordinate system.

For the special case of a 1-D Earth, $\Phi_{max} = \Phi_{min}$ and the ellipse reduces to a circle. The angle $\beta = 0$ and α becomes undefined, which is simply a statement that geoelectric strike is not defined for 1-D resistivity structure. In 2-D, $\beta = 0$ and one principal axis of the ellipse aligns with α. In 3-D, all invariants are non-zero and the magnitude of β measures deviation from the 2-D case. The principal axis of the ellipse aligns to the direction $\alpha - \beta$, defining the direction of greatest inductive response, the closest equivalent of a strike direction (Bibby et al., 2005).

The phase tensor provides a guide to the dimensionality of the regional impedance without introducing any assumptions. The conjecture that too many constraints

are applied by earlier methods based on 2-D structure is indisputable; restricting to two-dimensions inadvertently sets the otherwise determinable quantity β to 0, the very indicator of 3-D structure (Caldwell et al., 2004; Bibby et al., 2005). However, for small values of β, conventional methods (i.e. tensor decomposition) will not introduce significant error (Bibby et al., 2005).

3.9.3 Static Shifts

Galvanic distortions result from charge accumulation on the surface of small-scale local heterogeneities due to the conservation of electric current (Price, 1973). Since MT theory assumes no free charges exist (i.e. $\eta = 0$), and the conservation of current is time-independent, these boundary charges distort the regional electric fields and manifest as a constant shift (static shift) of the impedance amplitudes (Smith, 1995). By extension, static shifts scale the apparent resistivity estimates but do not affect the phase of the impedance nor the magnetic fields.

Static shifts can introduce artifacts in MT inversion models if not corrected (Sternberg et al., 1988). Unfortunately, it is impossible to determine these scaling factors from the measured impedance at a single site. Various schemes have been developed that are discussed in detail by Jiracek (1990) and references therein. More recently, developments in iterative inversion algorithms that model apparent resistivity and static shift coefficients simultaneously (de Groot-Hedlin 1991; Rodi and Mackie 2001) have led to these methods being commonly employed to mitigate the effects of static shifts.

Of note, topography can generate effects that are essentially static shifts due to the conductivity contrast between land and air (Wannamaker et al., 1986; Jiracek, 1990). Electric current lines concentrate beneath valley bottoms (increasing electrical resistivity), and spread out below high elevations (down-biasing electrical resistivity). Therefore, surface elevations must be modeled when analyzing MT data in regions with significant topographic variation (Figure 3-8).

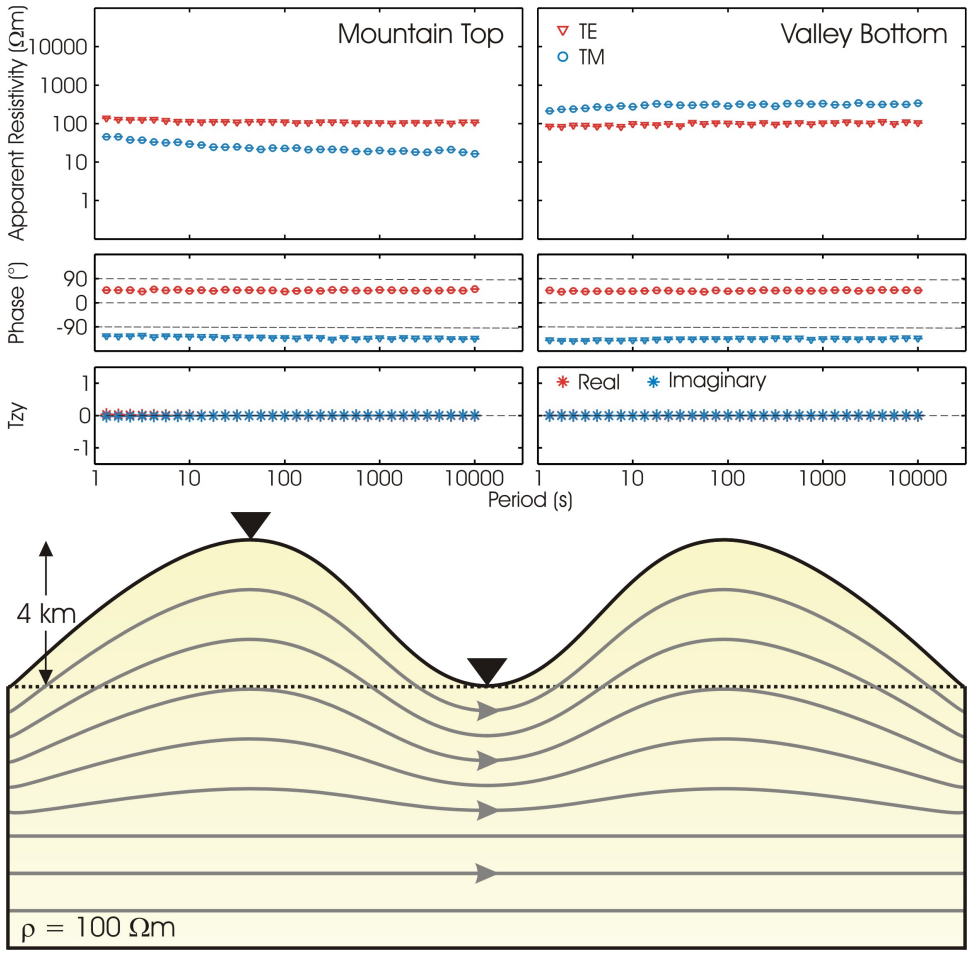

Figure 3-8. Galvanic topographic effect. Top panels show synthetic MT data 2-D forward modeled at measured locations (black triangles) on a mountain top and in a valley bottom. The static shift induced by the topography is clear in the TM mode; grey arrows show TM mode electric current lines. Note that no effect occurs for the tipper components and that the TE mode is almost unaffected.

3.10 Magnetotelluric Data Modeling and Inversion

MT measurements of apparent resistivity as a function of signal period are converted into models of true resistivity as a function of depth by (1) forward modeling and (2) inversion. While forward modeling by trial and error has advantages (Simpson and Bahr, 2005), inversion algorithms are automated and generate resistivity models that statistically fit the measured MT data by iterative procedures. Thus, inversion schemes are routinely used in MT data analysis. However, cavalier usage can lead to misleading results since the inversion

problem is non-unique and equally satisfied by an infinite number of models (Simpson and Bahr, 2005).

Any general inverse problem can be expressed as,

$$\mathbf{d} = \mathrm{G}(\mathbf{m}) \tag{3.41}$$

where, $\mathbf{d} = d^1, d^2, \ldots, d^N$ represents the data (impedance), G is the forward modeling function (Wait's recursion formula in 1-D) and $\mathbf{m} = m^1, m^2, \ldots, m^M$ defines the model parameters sought (subsurface resistivity). For sparsely sampled MT data (i.e. M > N), equation (3.41) is ill-conditioned and regularization is required to impose stability. Tikhonov regularization (Tikhonov and Arsenin, 1977) is used to condition the inversion towards smooth or minimum structure models. Since EM energy propagates diffusively within the Earth, MT data resolve conductivity gradients rather than sharp discontinuities (Simpson and Bahr, 2005). Further, since MT measurements sample hemispherical volumes of skin depth radii, like structures influence adjacent measurements when the inductive length-scale increases beyond the site spacing. Thus, smooth models are appropriate and obtained by minimization of the objective function (Mackie, 2001),

$$\mathbf{J}(\mathbf{m}_{k+1}) = \left[\mathbf{d} - \mathrm{G}(\mathbf{m}_{k+1})\right]^T R_{dd}^{-1}\left[\mathbf{d} - \mathrm{G}(\mathbf{m}_{k+1})\right] + \tau \left\| L\left(\mathbf{m}_{k+1} - \mathbf{m}_k\right)\right\|^2 \tag{3.42}$$

where, R_{dd}^{-1} is the error covariance matrix, L is an operator specifying the type of norm, $\mathbf{m_k}$ is the *a priori* model and τ is the regularization or trade-off parameter that controls the balance between data fit and obtaining a smooth model. In practice, due to the non-linearity of the MT inverse problem, the model response function is approximated by Taylor series expansion

$$\mathrm{G}(\mathbf{m}_{k+1}) = \mathrm{G}(\mathbf{m}_{k+1}) + \left.\frac{\partial \mathrm{G}}{\partial \mathbf{m}}\right|_{\mathbf{m_k}} \left(\mathbf{m}_{k+1} - \mathbf{m}_k\right) \tag{3.43}$$

and equation (3.42) is solved iteratively until convergence to the minimum structure model is achieved.

A 1-D interpretation of MT data is rarely applicable. However, the D^+ algorithm of Parker (1980) is important as it showed that a finite number of infinitely thin,

infinitely conducting layers gives the best fit to any 1-D MT dataset. While unrealistic, this model illustrates that MT data are sensitive to conductance.

2-D inversion is currently the standard approach for modeling MT data and a number of algorithms have been developed (e.g. Constable et al., 1987; Wannamaker et al., 1987; de Groot-Hedlin and Constable, 1990; Smith and Booker, 1991; Oldenburg and Ellis, 1993; Uchida 1993; Siripunvaraporn and Egbert 2000; Rodi and Mackie 2001). In this thesis, 2-D inversion models are generated using the NLCG6 algorithm (Rodi and Mackie, 2001), which uses non-linear conjugate gradients to solve for the least structure model. Two regularization parameters control the overall model smoothness τ, and the degree of horizontal smoothing α. The root-mean-square (r.m.s.) misfit measures the fit between the predicted model response and the observed data.

In cases where MT data display 3-D effects but maintain an overall 2-D characteristic, inversion using a 2-D algorithm can be valid (Wannamaker, 1999; Ledo, 2005). However, since the public release of the 3-D inversion algorithm WS3DINVMT (Siripunvaraporn et al., 2005), 3-D interpretation of MT data is becoming more common (e.g. Tuncer et al., 2006; Heise et al., 2008; Patro and Egbert, 2008; Türkoğlu et al., 2008; 2009; Hill et al., 2009) and has been used to generate models for this thesis. Despite progress to 3-D, WS3DINVMT currently inverts only the MT impedance elements and discards the tipper data. Further, the extensive computational demands are limiting the routine application of 3-D inversion modeling (Siripunvaraporn et al., 2005).

Regardless of dimensionality, MT inversion models are inherently non-unique. Model features therefore require careful analysis to ensure that they are required by the measured data. Many inversion models using a wide range of control parameters must be generated to ensure structures are robust. In addition, *a priori* knowledge about the existence of structure (e.g. seawater) can be introduced to constrain the range of physically acceptable models that fit a given dataset.

4 ACQUISITION AND DIMENSIONALITY OF TAIGER MT DATA

4.1 TAIGER Project

The TAIGER (Taiwan Integrated Geodynamics Research) project was funded by the Continental Dynamics Program of the National Science Foundation in 2004. This project proposed a multi-disciplinary investigation to understand the process of arc-continent collision in Taiwan and the surrounding ocean, and to address questions common to arc-continent collisions worldwide. The team of 10 principal investigators proposed a campaign of active and passive seismic studies on strategically placed transects (Figure 4-1), supplemented by petrophysical measurements, geodynamical modeling and magnetotelluric data acquisition. The six data transects were designed to investigate the evolution of the orogen; from south to north they traverse the full spectrum of pre- to post-collisional settings. Key questions proposed to be addressed by the TAIGER project include:

1. Does continental subduction play an important role in arc-continent collision? This feature is a key element in the thin-skinned orogenic model and distinguishes between the two end-member tectonic models.
2. How does an orogen evolve through time? By exploiting the north-south age variation of collision along the island, the transition from a young to mature orogen can be investigated within Taiwan.

The TAIGER project was initiated when no high-resolution geophysical data were available to unequivocally resolve the lithospheric structure beneath the Taiwan orogen. A comprehensive field campaign was proposed to provide the necessary data to address these fundamental questions. Similar multi-disciplinary projects have demonstrated success using an integrated geophysical approach to tectonic

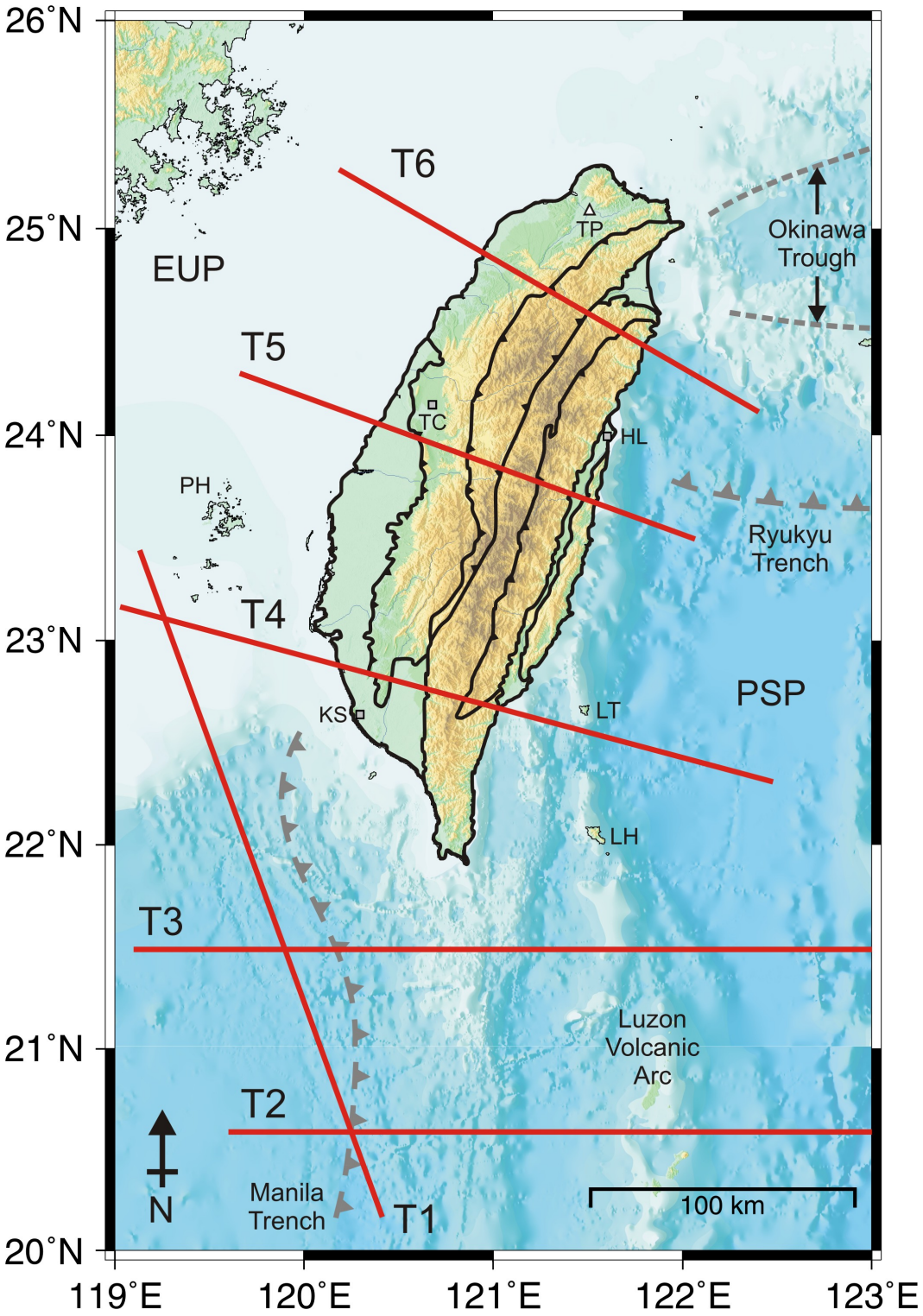

Figure 4-1. Proposed TAIGER transects for data acquisition. T1 – Continental margin benchmark, T2 – Pre-collision, T3 – Initial collision, T4 – Developing orogen, T5 – Mature orogen, T6 – Post collision, subduction and extension. Major cities: Taipei TP, Taichung, TC, Haulien HL and Kaohsiung KS. Islands surrounding Taiwan are: Penghu Archipelago PH, Lutao LT and Lanhsu LH.

studies. For example, in 1992 project INDEPTH (International Deep Profiling of Tibet and the Himalaya) was launched to develop a better understanding of the deep structure and mechanics of the India-Asia continent-continent collision (Zhao et al., 1993). While the first phase of the INDEPTH project used only deep seismic reflection profiling, subsequent phases (II and III) carried out between 1994 and 1999 collected coincident seismic and magnetotelluric data. Together these data suggest a layered model of aqueous fluids and partial melt best explains an extensive zone of coincident low velocity and resistivity in the mid-crust (Wei et al., 2001; Li et al., 2003). In addition, the SIGHT (South Island Geophysical Transect) project included coincident active source seismic and magnetotelluric data collected on a profile across the Southern Alps, New Zealand (Stern et al., 1997; Davey et al., 1998; Wannamaker et al., 2002). The SIGHT MT data revealed a broad region of low resistivity that was inferred to be caused by fluids released from metamorphism within a thickened crust (Wannamaker et al., 2002). Being situated on a transpressional boundary between two tectonic plates, the Southern Alps share many similarities to the tectonic setting of the Taiwan orogen.

Inherent non-uniqueness in individual geophysical methods can be reduced through a multi-disciplinary approach. Specifically, MT data have been shown effective at constraining rheological conditions required for interpretation of low seismic velocities and strong reflectivity within the middle to lower crust (Marquis and Hyndman, 1992; Marquis et al., 1995; Nelson et al., 1996; Li et al., 2003). In turn, seismic velocity models can provide further constraints on interpretations of MT data (Bedrosian et al., 2004; 2007; Bertrand et al. 2009). Recently, multidimensional joint inversion algorithms have been developed to simultaneously invert MT and seismic data (Meju et al., 2003; Gallardo and Meju, 2007; Moorkamp et al., 2007).

The TAIGER project proposed the collection of long-period MT data on the three land-based transects (T4, T5 and T6 in Figure 4-1) to yield models of electrical resistivity and provide constraints on the lithospheric composition and strength

beneath the orogen. In particular, the central transect crosses the mature orogen where differences in lithospheric structure between the end-member tectonic models are expected to be the greatest. Thus, there was a particular need to collect high quality deep sounding MT data in this region. The existence of a décollement, predicted to lie beneath the central ranges in the thin-skinned model (Carena et al., 2002), can be tested with MT data in central Taiwan.

In addition to distinguishing between the end-member tectonic models, MT data have the potential to provide constraints on the structure of the contact between the Western Foothills and the Hseuhshan Range. If sedimentary rocks of the fold-and-thrust belt have underthrust the more resistive slates to the east, MT data could potentially resolve the extent and geometry of this contact. In contrast, the underthrust low-velocity sedimentary rocks would pose a problem for seismic imaging methods (Unsworth, 2005). Along-strike variation in this contact would be revealed by changes in the adjacent transect models.

Detailed MT studies of the San Andreas Fault and other major faults (e.g. Unsworth and Bedrosian 2004; Bedrosian et al., 2007) have shown that MT data can image important details of fault zone structure. It is therefore plausible that structural details of the major faults in Taiwan could be interpreted with high resolution MT data collected on these proposed profiles.

4.2 Long Period MT Data Collection

Since 1995, over 200 broadband ($0.001 < \text{period} < 1000$ s) MT measurements have been made in Taiwan by the National Central University, prior to the TAIGER project (Chen et al., 1998b; Chen and Chen, 2002; Chen C.C. et al., 2007). While these data have been made available to us, their non-uniform spatial coverage and quality require that additional MT measurements be made to investigate the lithospheric structure on the orogen scale. In total, 82 long-period ($0.1 < \text{period} < 10000$ s) MT measurements were made on four transects across

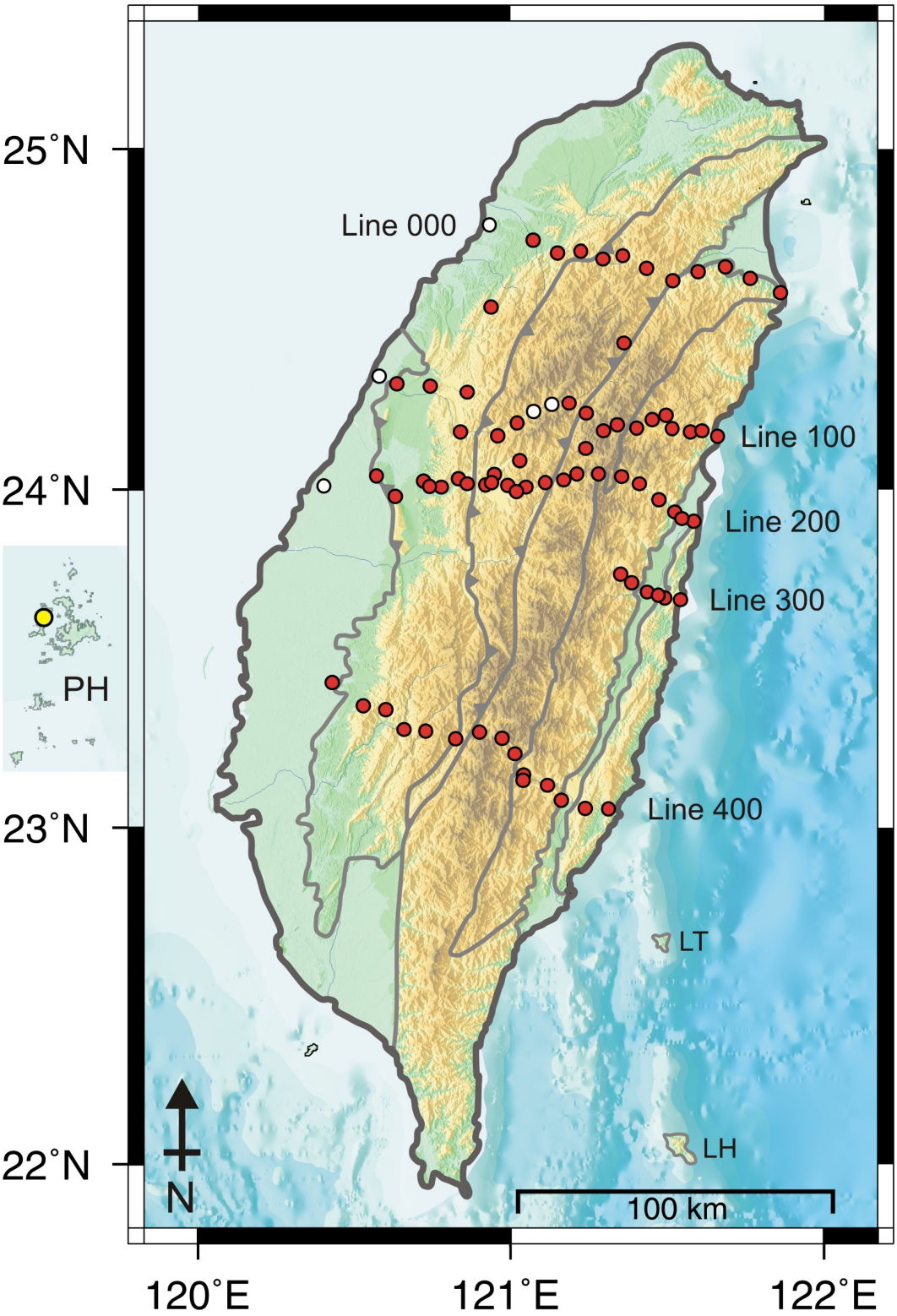

Figure 4-2. Location map of 82 long-period Magnetotelluric data measurements (red circles) in Taiwan. White circles indicate where only magnetic fields were recorded. Yellow circle denotes the remote reference station on the Penghu archipelago (PH).

Taiwan and on a short profile across the Longitudinal Valley (Figure 4-2). These data were collected during two separate field campaigns over the Fall of 2006 and Spring of 2007, in joint fieldwork by the University of Alberta and National Central University, Taiwan. The two survey periods allowed for processing and modeling of the initial measurements to guide the later data acquisition.

4.2.1 Fall 2006 MT Data Collection

Between April 25 and May 15 of 2006 a scouting trip to Taiwan was made for two main purposes: (1) to investigate the level of cultural electromagnetic noise present, and (2) to choose locations for the first deployment of 15 long-period instruments in the fall of that year. To accomplish the first task, 9 broadband MT stations were deployed using Phoenix V5-2000 instruments owned by NCU. Given the high population density in the low lying areas (Figure 4-3a) and the rugged topography and dense vegetation in the mountainous regions (Figure 4-3b), considerable effort was required to find locations appropriate for MT measurements. However, with resolve and determination, MT data processed using a remote reference and collected away from obvious sources of noise (power lines, highways, etc.) resulted in high quality soundings. These data contributed to 2-D inversion models of central Taiwan published by Chen et al., (2007a). This success and experience helped to guide the later half of this trip which involved scouting in central Taiwan for sites for future long-period MT measurements. Additionally, a quiet remote reference MT site was found on the Penghu archipelago that effectively reduced cultural noise biases in the Taiwan MT data (see section 4.3.3; Gamble et al., 1979).

Fifteen NIMS (Narod Intelligent Magnetotelluric Systems) instruments owned by the University of Alberta were shipped to Taiwan and the first TAIGER long-period MT station was installed on the Penghu archipelago on October 12, 2006. A total of 32 NIMS measurements were made in central Taiwan before the field crew returned to Canada on December 22, 2006. NIMS stations were installed on

profiles with a nominal spacing of 5 km and serviced on a weekly basis to check data quality and battery voltage. Stations that showed high levels of cultural electromagnetic noise after servicing were relocated to nearby sites to try to improve data quality. Each station recorded data for 3-4 weeks; time between installations was spent servicing and relocating poor quality stations, and scouting for locations for subsequent deployments. The Penghu remote reference station was serviced every 2.5 weeks.

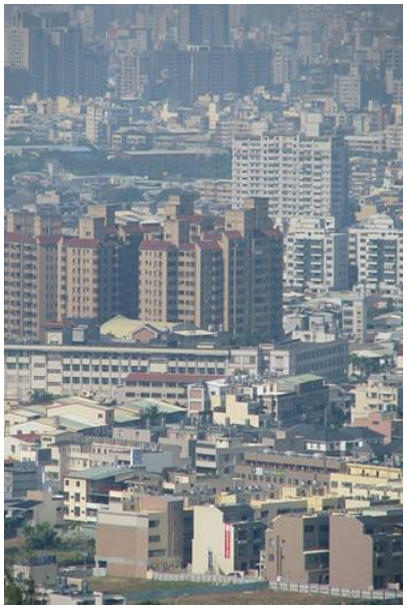

Figure 4-3a. City of Taichung. Bracketed by Lines 100 and 200 in western central Taiwan.

Figure 4-3b. Central cross-island highway through Taroko Gorge on the eastern portion of Line 100.

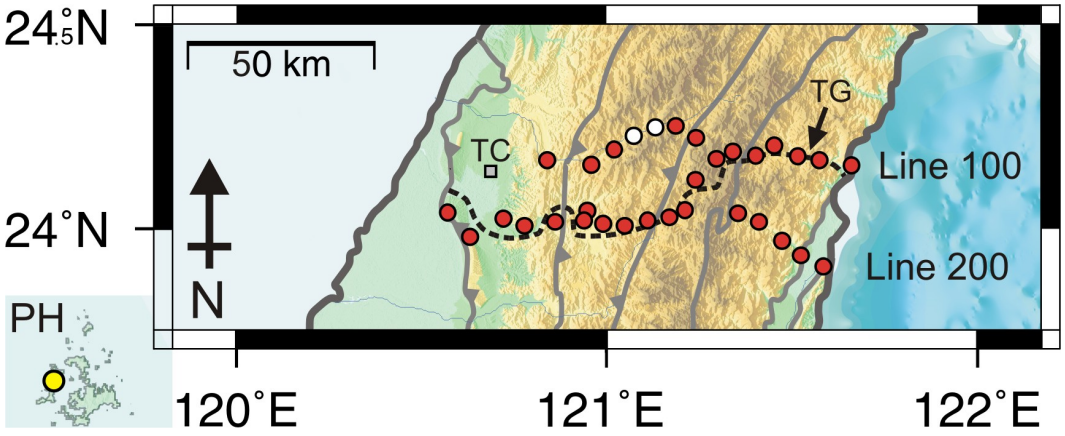

Figure 4-4. Long-period MT stations (red circles) deployed in the Fall of 2006. Yellow circle denotes the remote reference station on the Penghu archipelago. White circles indicate where only magnetic fields were recorded. Central cross-island highway (dashed black line). TC – Taichung, TG – Taroko Gorge.

Deployment across the high mountain ranges in central Taiwan followed the Central Cross-island Highway to permit easy access. Stations on Line 200 in west central Taiwan and on Line 100 in east central Taiwan were deployed on locations accessed from this highway (Figure 4-4). However, to obtain an array of data in central Taiwan, considerable effort was made to collect additional NIMS measurements in adjacent areas. Unfortunately, a gap in MT data on Line 100 could not be filled as there was no suitable location to deploy telluric wires near a major landslide caused by the 1999 M_w = 7.6 Chi-Chi earthquake. Therefore, two magnetometer-only stations were installed on steep slopes on either side of this gap (white circles in Figure 4-4). In addition, as there is no road across the high Central Ranges on Line 200, a wide gap remained on this profile.

The first few months of 2007 were spent processing and analyzing these initial MT data. Poor quality stations were identified and regions of interest were determined for collection of additional NIMS data during the second field campaign.

4.2.2 Spring 2007 MT Data Collection

Between March 4 and June 8, 2007 an additional 50 long-period MT measurements were made in Taiwan. As before, MT data collection commenced with installation of the remote reference station on the Penghu archipelago. NIMS measurements were then made on a profile across southern Taiwan, accessed by the south cross-island highway (Line 400). Fourteen NIMS were deployed along this highway extending from the east coast to the edge of the heavily populated Coastal Plain near Chiayi. After 3-4 weeks recording, these stations were relocated to northern Taiwan; 12 stations were deployed on a profile along the north cross-island highway (Line 000), and 2 between the north and the central lines (Figure 4-2). It was planned that off-profile stations could be useful to constrain along-strike features in a possible 3-D MT inversion model of northern Taiwan. After approximately 2 weeks, one station with high quality MT data was

redeployed on April 19, 2007 at Tianshih to fill the gap in the high Central Ranges on Line 200. This station required considerable effort as field personnel hiked 13 km from the nearest road access to reach the site. However, deployment at this location was crucial as it marked the only remaining gap in the spatial data coverage across central Taiwan.

Following the deployment in northern Taiwan, 6 NIMS were installed on a profile across the Longitudinal Valley on May 11 and May 12, 2007. The remaining 9 instruments were deployed at locations in east central Taiwan to improve the overall data coverage in this region. These locations were guided by the processing of the 2006 field data during January and February, 2007. A final deployment was made in early May, 2007 at additional locations in central Taiwan. Again, by processing the data collected to date, locations were chosen to improve the overall data quality and to minimize gaps in the spatial coverage. To extend the profiles laterally, 2 magnetometer-only stations were installed on the west coast on Lines 100 and 200, where it was not possible to deploy telluric wires (Figure 4-2).

In total, the TAIGER long-period MT data collection spanned 194 days over 3 trips to Taiwan and the first ever long-period MT data were collected at 82 locations across the island. Despite many difficulties in collecting MT data in Taiwan, the vast majority of the measurements were of good quality (Appendix A), and all stations recorded excellent magnetic field data. Note that while seafloor MT data would be a useful addition, this is likely not essential as demonstrated in the similar setting of New Zealand (Wannamaker et al., 2002).

4.2.3 NIMS Instrumentation

Long-period MT data were recorded using the 15 NIMS instruments owned by the University of Alberta (Figure 4-5). These systems record time-series data of orthogonal horizontal electric (Ex, Ey) and magnetic (Hx, Hy) field variations at

the Earth's surface. Variations in the vertical magnetic fields (Hz) are also recorded, and all data are stored on flash cards. The measurement sampling rate is 8 Hz and timing of the data collection is accurately determined from GPS signals.

Figure 4-5. NIMS (Narod Intelligent Magnetotelluric System). From left to right: solar panel, fluxgate magnetometer (white cylinder), magnetometer cable (red), data logger (grey box), electrode wire (black), grounding stake, four lead chloride electrodes (black cylinders) and a car battery.

Long-period magnetic fields are measured using a fluxgate magnetometer that records the total Earth's field at a precision of $7\,\mathrm{pT}/\sqrt{\mathrm{Hz}}$ over a dynamic range of ±83886 nT (Barry Narod, personal communication). Fluxgate magnetometers consist of three small ring-core magnets oriented in orthogonal Cartesian axes and each wrapped with two coils of wire – an input and receiver. AC current passed through the input coils drives the ring-cores through alternating cycles of magnetic saturation that induce current in the respective receiver coils. The finite time required to drive a ring-core to saturation is asymmetric in the presence of an external magnetic field and is manifested as variations in the currents recorded by the receiver coils. These variations are calibrated and used to determine the total external magnetic field (Primdahl, 1979). To give thermal stability and minimize movement, the magnetometer is buried in a shallow hole.

Electric field measurements are made by measuring the potential difference between orthogonal pairs of non-polarisable electrodes that form dipoles of typical length 75 – 100 m. NIMS instruments deployed in Taiwan used porous-pot electrodes consisting of a small piece of lead wire embedded in a solution of lead-chloride (Petiau, 2000). A porous ceramic base permits electrical contact between the ground and internal solution. To avoid thermal effects, electrodes were buried at a minimum depth of 30 cm. In addition, a suspension of wet bentonite mud was placed in the electrode holes to maintain good electrical contact for 3-4 weeks recording time. The NIMS instruments record the potential difference between orthogonal electrodes to an accuracy of 100 $\mathrm{nV}/\sqrt{\mathrm{Hz}}$, over a range of ±204 mV (Barry Narod, personal communication).

4.3 Time Series Data Processing

4.3.1 Time Series Data

Time series measurements of electric and magnetic field variations on the Earth's surface yield sample records due to stochastic ionospheric processes. Fortunately, averages of these random processes are stationary in time. Therefore, provided there are no local variations, MT data recorded at any given location are time-independent. This stationary behaviour permits large MT datasets to be acquired over a number of field campaigns (Egbert, 2002).

Figure 4-6 displays one hour of typical time series data recorded simultaneously at a location in central Taiwan (TGR235) and on Penghu (TGR000). Note the similarity of the orthogonal horizontal magnetic fields recorded at these stations, even though they are separated by over 100 km. This similarity occurs because the magnetic fields originate within the ionosphere, far from the Earth's surface. In contrast, the electric and vertical magnetic fields show much greater variation, since they reflect differences in the subsurface electrical resistivity structure.

Time series data recorded by NIMS instruments are high-pass (T_c = 30,000 s) and

low-pass (T_c = 0.25 s) filtered within the data logger to avoid non-uniform source field and aliasing effects, respectively. Note that data are collected for 3-4 weeks to ensure a good statistical sampling of the longest period signals.

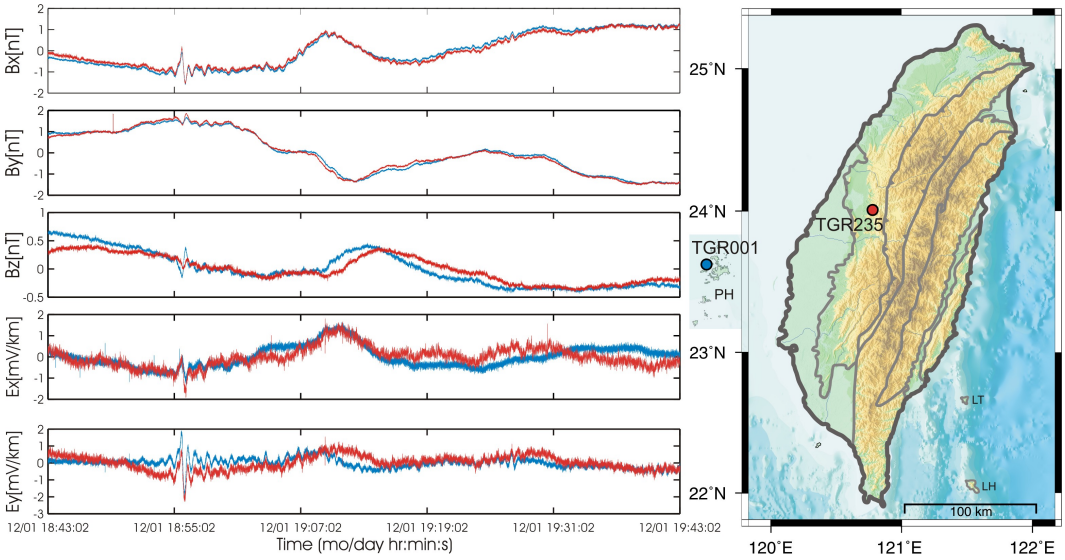

Figure 4-6. Simultaneous time series data (60 min) of magnetic and electric fields at station TGR235 (red) in the Western Foothills and at the remote reference station TGR000 on the Penghu archipelago (blue).

4.3.2 Converting Time Series to Frequency Domain Transfer Functions

The reduction of measured time-series data to estimates of the electromagnetic impedance transfer functions in the frequency domain is referred to as time series processing. The EM impedance describes the Earth's response (time-varying electric fields) to an input process (time-varying magnetic fields). However, since measured MT data contain noise, equation (3.29) is approximate and several methods have been developed for obtaining accurate estimates of the impedance.

Historically, numerical estimates of transfer functions were based on least-squares methods that assume that the statistical errors follow a Gaussian distribution (Swift, 1967; Rankin and Reddy, 1969; Sims et al., 1971). However, outliers that commonly occur in MT data generally follow a non-Gaussian distribution, and least-squares estimates can be misleading (Egbert and Booker, 1986). Manual

screening of time series was thus required to eliminate outliers, a lengthy, non-rigorous and error-prone approach. An important improvement in MT time-series processing involved the development of an automated, statistically robust scheme for transfer function estimation. Egbert and Booker (1986) published a robust alternative to the simple least squares method that uses an iteratively re-weighted least squares algorithm. This technique scales the field components by their errors and does not permit outliers to contaminate the impedance estimates. In addition, this automatic procedure has been shown to efficiently yield stable estimates of the transfer function with realistic errors (Egbert and Booker, 1986). All time-series processing of MT data for this thesis used the statistically robust software EMTF (Electromagnetic Transfer Function), developed by Gary Egbert (1997).

4.3.3 Remote Reference Processing

Multiplying equation (3.30) by $\left[\mathrm{H}_x^* \quad \mathrm{H}_y^*\right]$, where * denotes the complex conjugate, and solving for the impedance elements yields the following:

$$Z_{xx} = \frac{\left\langle \mathrm{E}_x\mathrm{H}_\mathrm{x}^* \right\rangle \left\langle \mathrm{H}_y\mathrm{H}_\mathrm{y}^* \right\rangle - \left\langle \mathrm{E}_x\mathrm{H}_\mathrm{y}^* \right\rangle \left\langle \mathrm{H}_y\mathrm{H}_\mathrm{x}^* \right\rangle}{\left\langle \mathrm{H}_x\mathrm{H}_\mathrm{x}^* \right\rangle \left\langle \mathrm{H}_y\mathrm{H}_\mathrm{y}^* \right\rangle - \left\langle \mathrm{H}_x\mathrm{H}_\mathrm{y}^* \right\rangle \left\langle \mathrm{H}_y\mathrm{H}_\mathrm{x}^* \right\rangle} = 0 \tag{4.1}$$

$$Z_{xy} = \frac{\left\langle \mathrm{E}_x\mathrm{H}_\mathrm{y}^* \right\rangle \left\langle \mathrm{H}_x\mathrm{H}_\mathrm{x}^* \right\rangle - \left\langle \mathrm{E}_x\mathrm{H}_\mathrm{x}^* \right\rangle \left\langle \mathrm{H}_x\mathrm{H}_\mathrm{y}^* \right\rangle}{\left\langle \mathrm{H}_x\mathrm{H}_\mathrm{x}^* \right\rangle \left\langle \mathrm{H}_y\mathrm{H}_\mathrm{y}^* \right\rangle - \left\langle \mathrm{H}_x\mathrm{H}_\mathrm{y}^* \right\rangle \left\langle \mathrm{H}_y\mathrm{H}_\mathrm{x}^* \right\rangle} = \frac{\left\langle \mathrm{E}_x\mathrm{H}_\mathrm{y}^* \right\rangle}{\left\langle \mathrm{H}_y\mathrm{H}_\mathrm{y}^* \right\rangle} \tag{4.2}$$

$$Z_{yx} = \frac{\left\langle \mathrm{E}_x\mathrm{H}_\mathrm{x}^* \right\rangle \left\langle \mathrm{H}_y\mathrm{H}_\mathrm{y}^* \right\rangle - \left\langle \mathrm{E}_y\mathrm{H}_\mathrm{y}^* \right\rangle \left\langle \mathrm{H}_y\mathrm{H}_\mathrm{x}^* \right\rangle}{\left\langle \mathrm{H}_x\mathrm{H}_\mathrm{x}^* \right\rangle \left\langle \mathrm{H}_y\mathrm{H}_\mathrm{y}^* \right\rangle - \left\langle \mathrm{H}_x\mathrm{H}_\mathrm{y}^* \right\rangle \left\langle \mathrm{H}_y\mathrm{H}_\mathrm{x}^* \right\rangle} = \frac{\left\langle \mathrm{E}_y\mathrm{H}_\mathrm{x}^* \right\rangle}{\left\langle \mathrm{H}_x\mathrm{H}_\mathrm{x}^* \right\rangle} \tag{4.3}$$

$$Z_{yy} = \frac{\left\langle \mathrm{E}_y\mathrm{H}_\mathrm{y}^* \right\rangle \left\langle \mathrm{H}_x\mathrm{H}_\mathrm{x}^* \right\rangle - \left\langle \mathrm{E}_y\mathrm{H}_\mathrm{x}^* \right\rangle \left\langle \mathrm{H}_x\mathrm{H}_\mathrm{y}^* \right\rangle}{\left\langle \mathrm{H}_x\mathrm{H}_\mathrm{x}^* \right\rangle \left\langle \mathrm{H}_y\mathrm{H}_\mathrm{y}^* \right\rangle - \left\langle \mathrm{H}_x\mathrm{H}_\mathrm{y}^* \right\rangle \left\langle \mathrm{H}_y\mathrm{H}_\mathrm{x}^* \right\rangle} = 0 \tag{4.4}$$

where it is assumed that the fields are not linearly polarized, implying $\left\langle \mathrm{E}_x\mathrm{E}_\mathrm{y}^* \right\rangle$, $\left\langle \mathrm{E}_x\mathrm{H}_\mathrm{x}^* \right\rangle$, $\left\langle \mathrm{H}_x\mathrm{H}_\mathrm{y}^* \right\rangle$, $\left\langle \mathrm{E}_y\mathrm{E}_\mathrm{x}^* \right\rangle$, $\left\langle \mathrm{E}_y\mathrm{H}_\mathrm{y}^* \right\rangle$ and $\left\langle \mathrm{H}_y\mathrm{H}_\mathrm{x}^* \right\rangle$ all equal 0, where $\langle\ \rangle$ denotes an average over a finite bandwidth (Sims et al., 1971). It was realized, however, that these estimates would be downward-biased by data errors in the autopowers

of the magnetic fields (Sims et al., 1971). Specifically, in the presence of noise,

$$\mathrm{H}_{x\mathrm{obs}} = \mathrm{H}_{x} + \mathrm{H}_{x\mathrm{noise}} \qquad \mathrm{H}_{y\mathrm{obs}} = \mathrm{H}_{y} + \mathrm{H}_{y\mathrm{noise}} \tag{4.5}$$

which after multiplication by respective complex conjugates yields

$$\begin{aligned} \left\langle \mathrm{H}_{x\mathrm{obs}} \mathrm{H}^{*}_{x\mathrm{obs}} \right\rangle &= \left\langle \mathrm{H}_{x} \mathrm{H}^{*}_{\mathrm{x}} \right\rangle + \left\langle \mathrm{H}_{x\mathrm{noise}} \mathrm{H}^{*}_{x\mathrm{noise}} \right\rangle \\ \left\langle \mathrm{H}_{y\mathrm{obs}} \mathrm{H}^{*}_{y\mathrm{obs}} \right\rangle &= \left\langle \mathrm{H}_{y} \mathrm{H}^{*}_{\mathrm{y}} \right\rangle + \left\langle \mathrm{H}_{y\mathrm{noise}} \mathrm{H}^{*}_{y\mathrm{noise}} \right\rangle \end{aligned} . \tag{4.6}$$

Using equations (4.6), the off-diagonal impedances are re-expressed as

$$\mathrm{Z}_{xy\,\mathrm{obs}} = \mathrm{Z}_{xy} \left(1 + \frac{\left\langle \mathrm{H}_{y\mathrm{noise}} \mathrm{H}^{*}_{y\mathrm{noise}} \right\rangle}{\left\langle \mathrm{H}_{y} \mathrm{H}^{*}_{\mathrm{y}} \right\rangle} \right)^{-1} \tag{4.7}$$

$$\mathrm{Z}_{yx\,\mathrm{obs}} = \mathrm{Z}_{\mathrm{yx}} \left(1 + \frac{\left\langle \mathrm{H}_{x\mathrm{noise}} \mathrm{H}^{*}_{x\mathrm{noise}} \right\rangle}{\left\langle \mathrm{H}_{x} \mathrm{H}^{*}_{\mathrm{x}} \right\rangle} \right)^{-1} \tag{4.8}$$

and it becomes clear that noise in the magnetic field autopowers will downward-bias the observed impedances. To remove this bias the remote reference method (Gamble et al., 1979) was proposed that involves replacing the conjugate terms in equations (4.7) and (4.8) with additional data collected simultaneously at a remote site. The basic idea is that at the remote location the MT signal will be the same, but the noise will be uncorrelated and the bias therefore removed (Simpson and Bahr, 2005). The remote reference technique led to a major improvement in MT data quality and is now routinely used in most MT measurement campaigns.

All TAIGER MT data were collected with a remote reference station operating on the Penghu archipelago. Located within the Taiwan Strait, the conductive seawater attenuates the cultural EM noise present in the mainland MT data. Thus, noise on either side of the Taiwan Strait is not expected to be correlated. Coherent magnetic field signals were recorded on Penghu and Taiwan (e.g. Figure 4-6), making this an excellent site for a remote reference station. Figure 4-7 illustrates the improvement in MT data quality obtained with remote reference processing. In the left panel, the apparent resistivity estimates rapidly decay within the period band 10-100 s, due to magnetic noise. On the right panel, the data in this decade are corrected by using the reference fields collected simultaneously on the Penghu

archipelago. Note that noise at short periods results from the insensitivity of fluxgate magnetometers below 10 s (Primdahl et al., 1987).

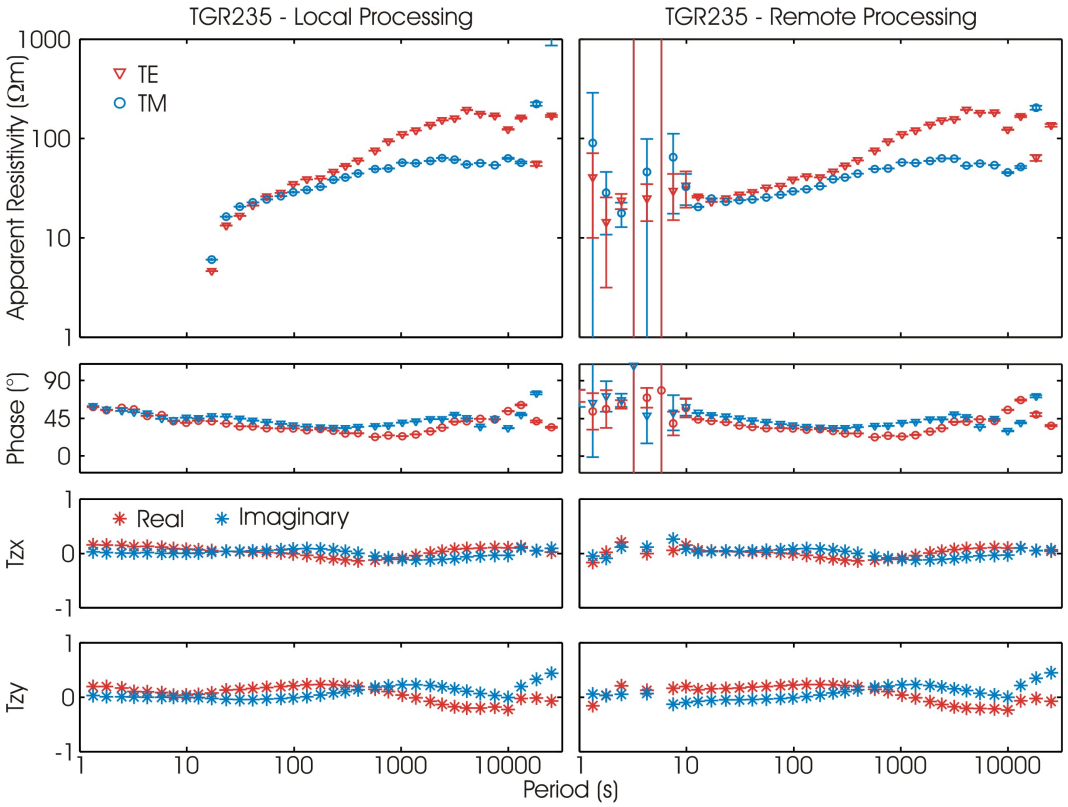

Figure 4-7. Local robust processing (left panel) and remote reference processing (right panel) for MT station TGR235 located in the Western Foothills of central Taiwan. Remote reference station is TGR000 on the Penghu archipelago.

4.4 MT Data Dimensionality

Prior to modeling, careful dimensionality analysis must be completed to determine if these MT data will require a 1-D, 2-D or 3-D interpretation. Simplified analysis of MT data in dimensions lower than required can lead to artifacts in inversion models and erroneous interpretations (Simpson and Bahr, 2005; Unsworth, 2007). Most often a 1-D approach is insufficient, and MT data are routinely modeled using a 2-D approximation. For MT data that display overall 2-D characteristics despite some 3-D effects, results obtained using 2-D inversion algorithms can be valid (Wannamaker, 1999; Ledo, 2005). In Taiwan,

geologic structures are largely 2-D and generally parallel the island long-axis with length scales nearly four-times their cross-island extent (Yen et al., 1998). However, the island of Taiwan is located in a region of complex tectonics and is surrounded by seawater of variable depths (Figure 2-1). These factors will contribute to 3-D induction and require a careful data analysis to determine if overall 2-D behaviour persists, or if 3-D interpretation is needed.

4.4.1 Tensor Decomposition – Strike Angles

The tensor decomposition method (Groom and Bailey, 1989; McNeice and Jones, 2001) is commonly used to determine the best fitting geoelectric strike direction for MT data that are assumed to be regionally 2-D. Figure 4-8 shows the results of the tensor decomposition algorithm (McNeice and Jones, 2001) applied to each MT station individually, and averaged over the period bands indicated. Note that a 90° ambiguity exists in these directions and external information must be used to determine the correct strike direction. The azimuth that is closest to the average island-strike has been chosen for display. It is clear from the consistent orientation of the bar azimuths that an overwhelming orogen-parallel geoelectric strike direction is determined for these MT data. Furthermore, despite some divergence, at the majority of sites the geoelectric strike remains consistent over all period bands shown. This consistency is an important indication that the MT data on these profiles can be considered 2-D. Closer observation of the strike directions reveals that the dominant azimuth for each profile subtly rotates clockwise from south to north Taiwan. This rotation matches the overall S-shape curvature of the island (Yu et al., 1997) and indicates that the geoelectric strike is consistent with the large-scale 2-D orogen structure and ocean bathymetry.

4.4.2 Induction Vectors

Induction vectors can provide an independent constraint on dimensionality assessment, because these vectors do not have the same 90° ambiguity as tensor

decomposition. For a 2-D approach to be valid, the real components of the induction vectors should point orthogonal to the geoelectric strike direction. Figure 4-9 shows the real components of the induction vectors plotted in the Parkinson convention averaged over the period bands indicated. It is clear that these vectors point towards conductors. Note that as the period increases, all induction vectors point towards the conductive Philippine Sea. This phenomenon has long been recognized in coastal regions (Parkinson, 1959; 1962; Lilley, 2007).

For MT stations located in western Taiwan (CP and WF), induction vectors are dominantly perpendicular to orogen structure at all periods. In contrast, significant along-strike components of these vectors occur for many stations collected in the Central Ranges. The maximum along-strike components occur over the period band 100-1000 s, which would be sensitive to depths between 50 and 160 km, assuming a 100 Ωm half-space. These along-strike components (that are largest at sites located in northeastern Taiwan) indicate 3-D conductivity structure. If these data are included in 2-D inversion models, very careful assessment of resistivity model features is needed to determine if they are required by the data, rather than artifacts due to the violation of model assumptions.

4.4.3 Phase Tensor Azimuth – Alpha-Beta Angles

As described in Chapter 3, the tensor decomposition method assumes a 2-D Earth model and subsequently determines the best-fitting geoelectric strike direction. More generally, Caldwell et al. (2004) showed that the MT phase tensor can provide a guide to the dimensionality of the regional impedance tensor without imposing any assumptions. Specifically, when graphically represented as an ellipse, one of the principal axes aligns to the direction of greatest inductive response that indicates the closest equivalent to a 2-D geoelectric strike direction (Bibby et al., 2005). Maps of the phase tensor ellipses averaged over the period bands indicated are shown in Figure 4-10. These ellipses are filled with colour that indicates the azimuth of the ellipsoidal major axes.

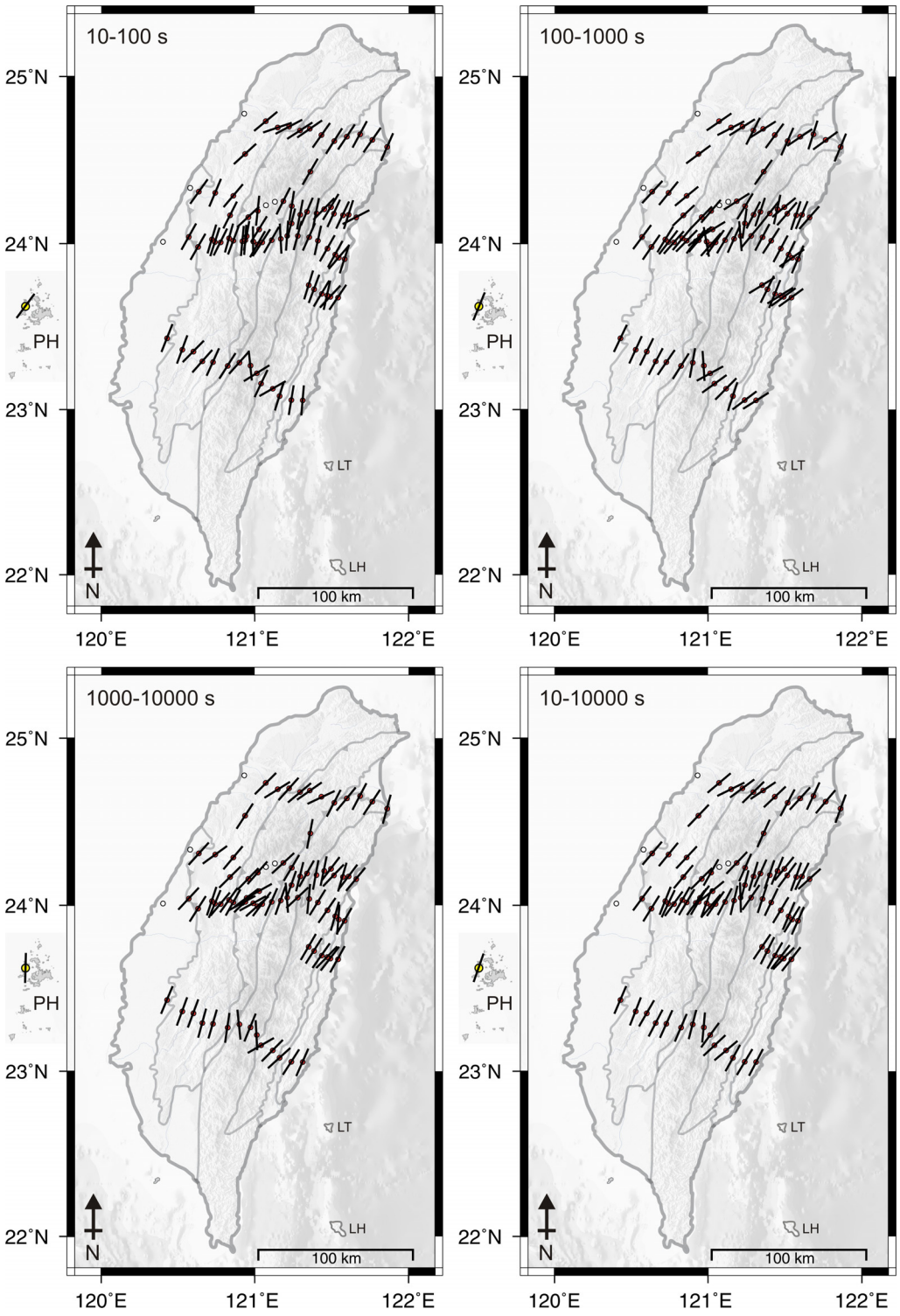

Figure 4-8. Geoelectric strike from tensor decomposition (McNeice and Jones, 2001) averaged over the labeled period decades. Bar azimuth denotes the strike direction. Overall, the geoelectric strike estimates parallel structure along the long-axis of the island. Note that scatter occurs mainly near the Lishan Fault. Red dots are MT stations and white dots show where only magnetic fields were recorded.

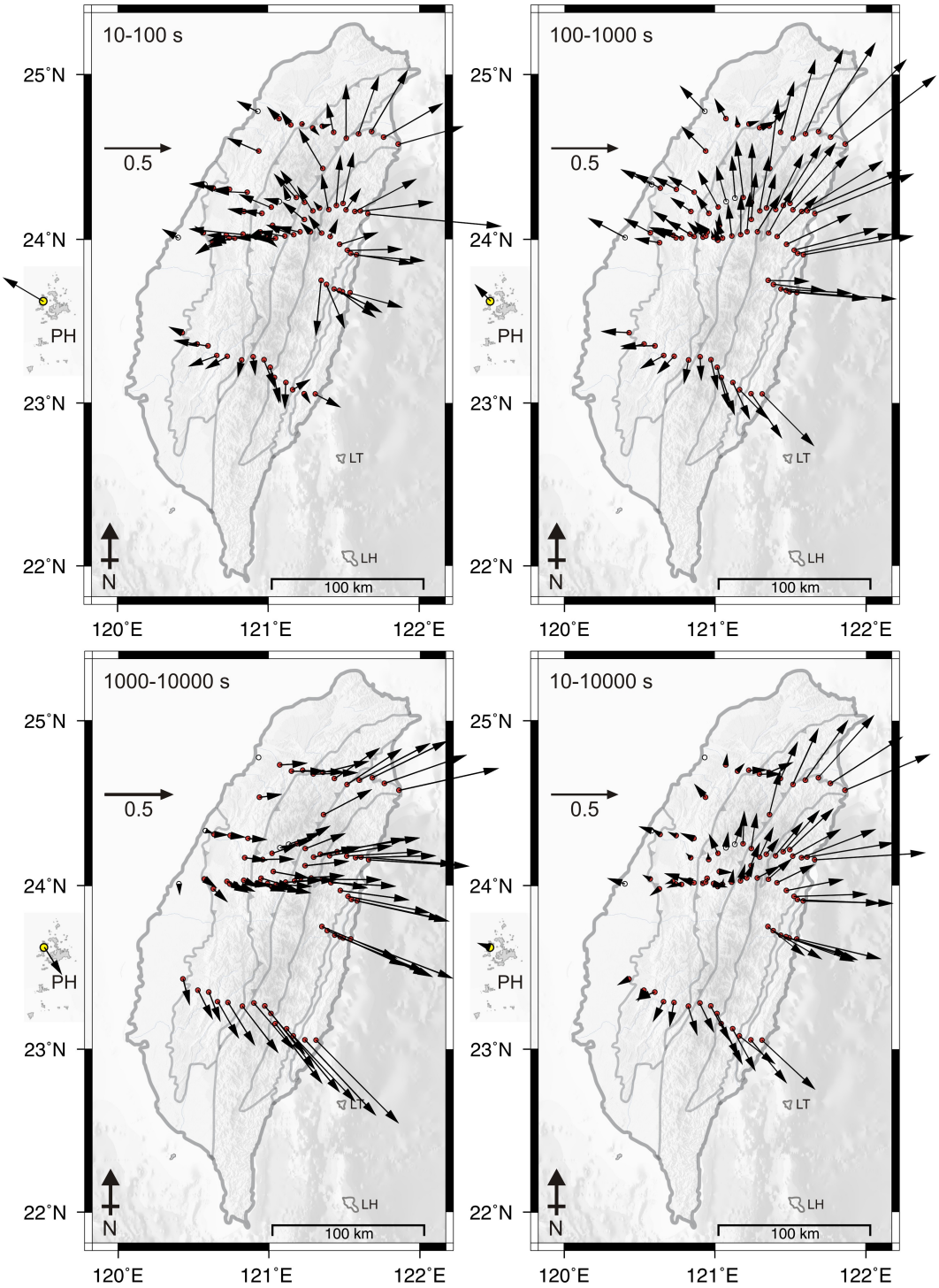

Figure 4-9. Induction vectors (real component, Parkinson convention) averaged over the labeled period decades. Scale arrow of magnitude 0.5 is shown. Despite an along-strike component at locations mainly east of the LF, indicating 3-D electrical structure, the dominant strike-perpendicular behaviour at the majority of stations throughout Taiwan indicates an overall 2-D electrical structure. Red dots are MT stations and white dots show where only magnetic fields were recorded.

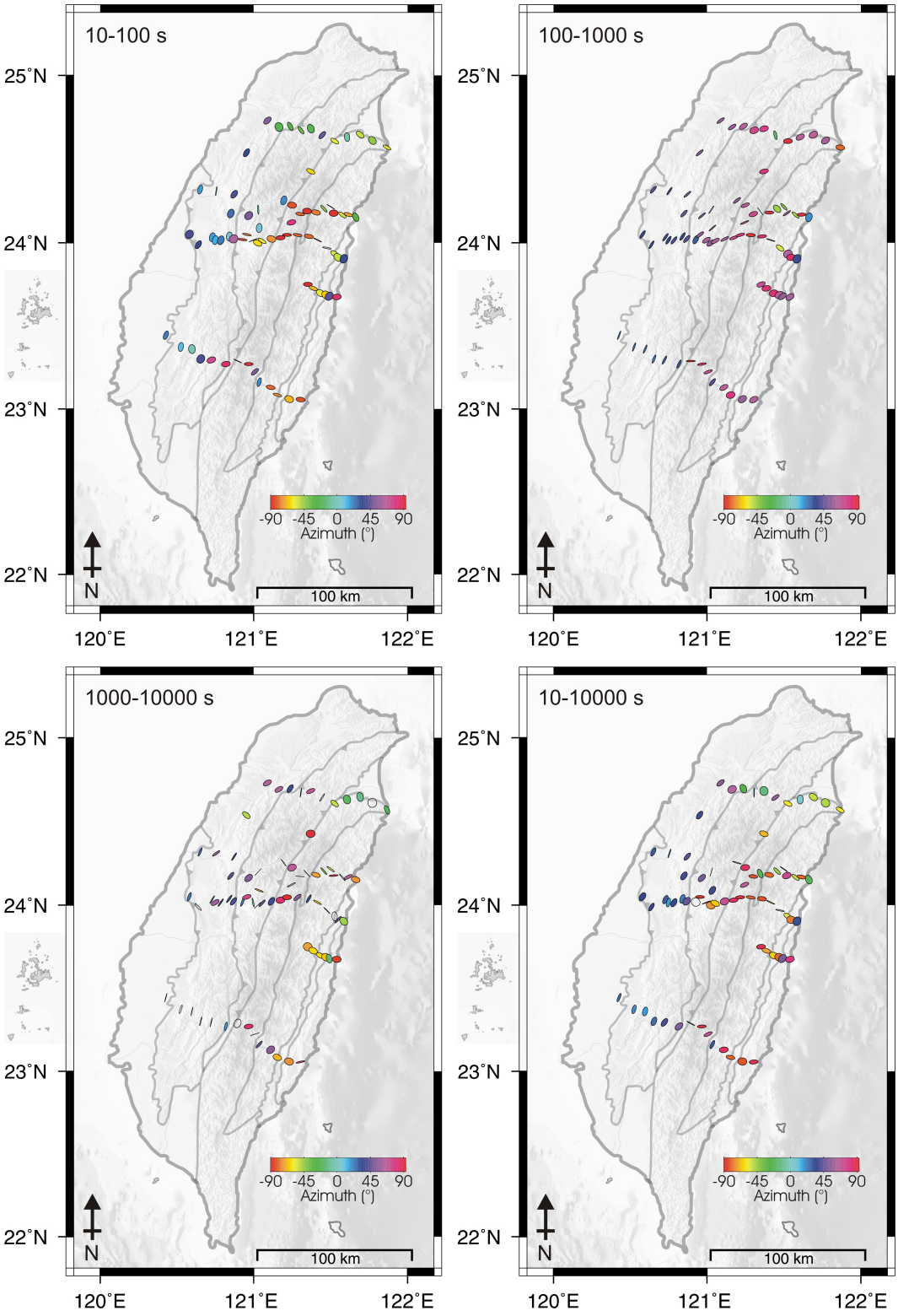

Figure 4-10. Phase Tensor azimuth (Caldwell et al., 2004) averaged over the labeled period decades. One ellipsoidal principal axes indicates the direction of maximum induction, which overall parallels the island structure. Note that a rotation in ellipse orientation is visible across the Lishan Fault.

In broad respect, the majority of the phase ellipses align parallel to the known geologic structure throughout Taiwan. However, as indicated by the along-strike induction vector components, significant deviation of the ellipse orientation occurs at stations located predominantly in the northeastern central ranges. Of note, a change in ellipsoidal orientation is observed across the Lishan Fault, suggesting that this boundary marks a significant feature in the island's conductivity structure.

4.4.4 Rose Diagrams

While the previous map-view plots illustrate the dimensionality of individual MT stations, rose diagrams are advantageous for revealing average data trends. In Figure 4-11, rose diagrams are shown that consolidate the results displayed in Figures 4-8 to 4-10, for data collected on linear profiles.

For the main profiles that traverse Taiwan (Lines 000, 100, 200 and 400) the rose diagrams of strike and alpha-beta effectively reveal that a dominant 2-D geoelectric strike direction exists collinear to the island long-axis and major geologic features in Taiwan. That these independent methods yield consistent results strengthens the conjecture that Taiwan displays an overall 2-D electrical structure. Further, the alignment of the real induction vectors is largely perpendicular to the profile geoelectric strike directions.

The greatest deviation from the overall 2-D behaviour occurs for Line 000 in northern Taiwan, where MT data were collected near a region of 3-D bathymetry and along the southern margin of the Ilan Plain. The Ilan Plain represents the onshore extension of the Okinawa trough, the back-arc basin associated with subduction at the Ryukyu trench (Teng, 1996). Despite a fairly dominant 2-D geoelectric strike obtained from tensor decomposition, the dichotomy observed in the induction vector responses for the western and eastern sides of this profile is

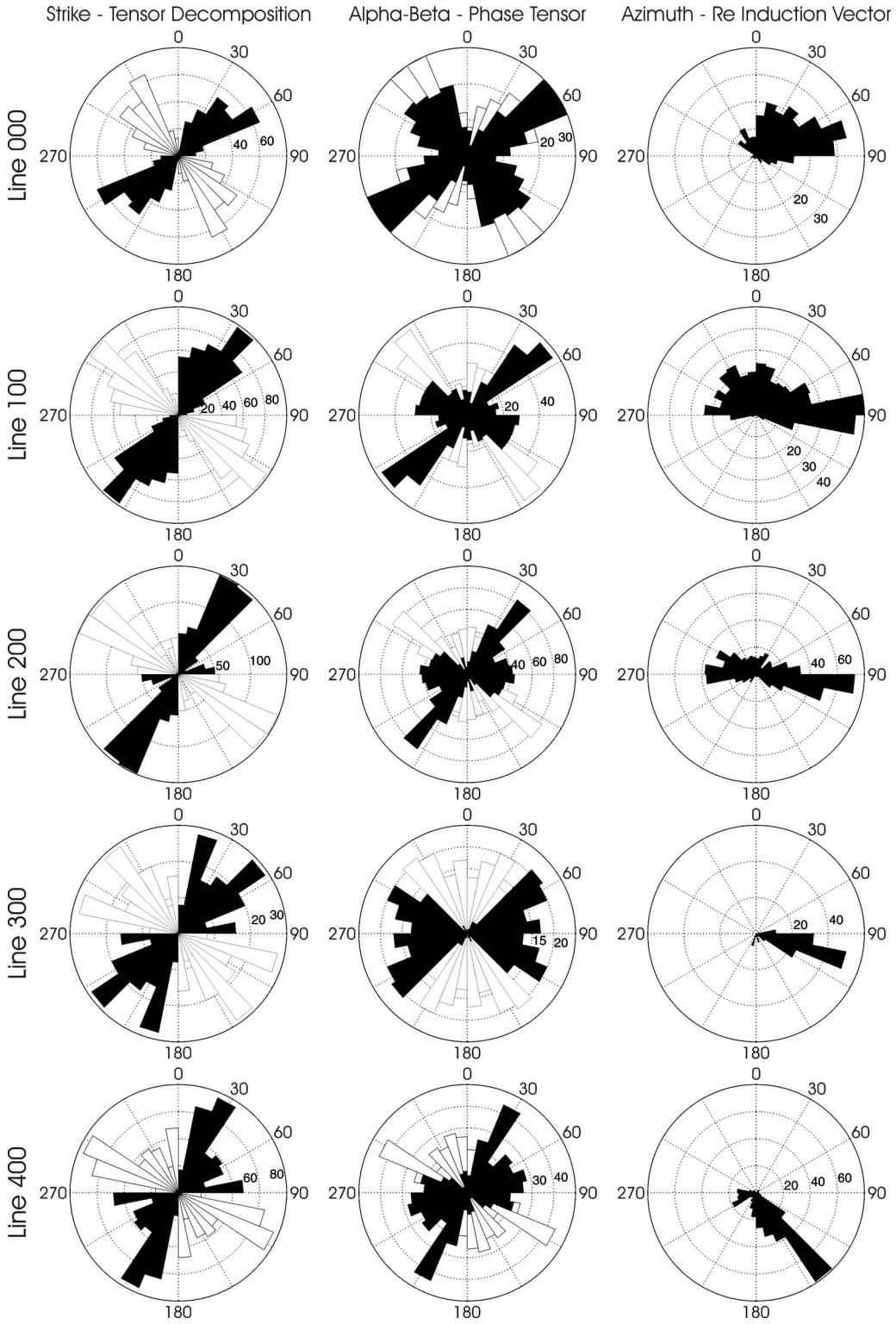

Figure 4-11. Rose diagrams for labeled dimensionality techniques for each TAIGER profile. Results include data for the period range 10-10000 s. Despite some 3-D indication, an overall 2-D geoelectric strike is observed. Black and white sectors are orthogonal and indicate the 90° strike ambiguity inherent in the tensor decomposition and phase tensor methods.

well captured by the phase tensor azimuth. Since the determinable parameter beta (which indicates 3-D structure) is inherently set to zero in the tensor decomposition approach, the phase tensor azimuth is more sensitive to the 3-D effects indicated by the along-strike induction vector components in northeastern Taiwan.

For the six long-period stations collected across the Longitudinal Valley on Line 300, the results of tensor decomposition and phase tensor analysis agree poorly, and do not indicate a dominate 2-D geoelectric strike direction. More detailed analysis of these data is thus required before they can be used for 2-D modeling. The consistent induction vector azimuths from these stations indicate their close proximity to the east coast of Taiwan, and the strong effects of the conductive Philippine Sea.

4.4.5 Summary – TAIGER MT Data Dimensionality

In summary, it is shown that the majority of MT data collected reflects dominant 2-D behaviour and indicates an orogen-parallel geoelectric strike direction. This overall behaviour permits the application of 2-D MT inversion and analysis of data collected along the main profiles across central, southern and northern Taiwan. However, caution must be exercised as significant indications of 3-D conductivity structure are observed at many sites. In particular, data in northeastern Taiwan show large amplitude along-strike real induction vector components and deviations from orogen-strike in the phase tensor azimuth. Detailed analysis of the dimensionality of MT stations included in inversion models of profiles in central, southern and northern Taiwan are contained in the subsequent chapters.

5 EVIDENCE FOR THICK-SKINNED TECTONICS IN CENTRAL TAIWAN

A number of tectonic models have been proposed to explain the collision tectonics of central Taiwan and include both thin-skinned and thick-skinned lithospheric deformation. These models predict very different structures at middle and lower crustal depths beneath the Central Ranges. Prior to TAIGER, insufficient geophysical data were available to unequivocally distinguish between them. This chapter presents the first magnetotelluric evidence for the occurrence of thick-skinned tectonics in central Taiwan (Bertrand et al., 2009).

5.1 Tectonic Models

In the thin-skinned model (Figure 2-5), a shallow décollement is predicted to dip eastwards within the upper continental crust. Orogen-related deformation is localized above this surface while the Eurasian continental lithosphere subducts below. The thin-skinned model was motivated by geological and shallow seismic exploration in the WF fold-and-thrust belt (Suppe, 1981). Near-surface deformation in the WF (Yue et al., 2005) and surface heat flow (Bahr and Dahlen, 1990) are consistent with predictions from critical wedge theory employing a shallow décollement. In addition, fitting subsets of inferred coplanar earthquakes to optimized 3-D surfaces has been used to show that a band of seismicity exists at 8–10 km depth, extending continuously from western Taiwan to the Coastal Range. This sub-horizon of seismicity was interpreted to be the décollement (Carena et al., 2002), but differs from several other relocation studies that show an aseismic gap beneath the WCR in central Taiwan (Wu et al., 1997; 2004; Gourley et al., 2007; Wu et al., 2008).

In contrast, the thick-skinned model (Figure 2-6) predicts continuous deformation throughout the lithosphere, with prograde metamorphism occurring within a thickened crust beneath the Central Ranges (Wu et al., 1997). This model is supported by observation of a crustal root in seismic tomography models (Wu Y.M. et al., 2007) and by an aseismic gap beneath the WCR and clusters of deep crustal seismicity observed in precisely relocated hypocentres (Wu et al., 2004). Receiver function analysis (Kim et al., 2004), TAICRUST active source seismic data (McIntosh et al., 2005), shear wave splitting (Rau et al., 2000) and gravity data (Yen et al., 1998) also support the thick-skinned model in central Taiwan. However, these existing geophysical data cannot unequivocally distinguish between these end-member models and additional constraints are needed.

5.2 MT Data: Collection and Analysis

As part of the TAIGER project, the first long-period (10–10000 s) MT data were collected in Taiwan. These measurements included 47 stations deployed on two closely spaced parallel transects across central Taiwan (Figure 4-2). As described in Chapter 4, these data indicate an overall 2-D geoelectric structure (Figure 4-11). However, 3-D effects are observed at some MT sites in central Taiwan and this is as expected in a region of complex geology that is surrounded by seawater of variable depths. Careful MT data analysis was undertaken to select a subset of 21 high quality MT stations that showed minimum 3-D behaviour. These stations were chosen to form a continuous profile across central Taiwan (Figure 5-1).

5.2.1 MT Data Dimensionality

The dimensionality and geoelectric strike direction of these 21 stations were investigated using tensor decomposition (McNeice and Jones, 2001) and phase tensor analysis (Caldwell et al., 2004). A consistent strike direction of N37°E was found by these techniques, and is parallel to the major geological boundaries in central Taiwan (Figure 5-2). The minimal scatter in these rose plots and the low

r.m.s. misfit (< 1.5) from tensor decomposition (Figure 5-3) indicate that the 2-D strike direction obtained is well constrained. In addition, values of twist and shear are mainly lower than ~30° and indicate that only minor galvanic distortion is present in these MT data, especially at the shorter periods (i.e. < 100 s) that are sensitive to the upper and middle crust (Figure 5-3). Values of twist and shear greater than ~30° indicate significant electric field distortion.

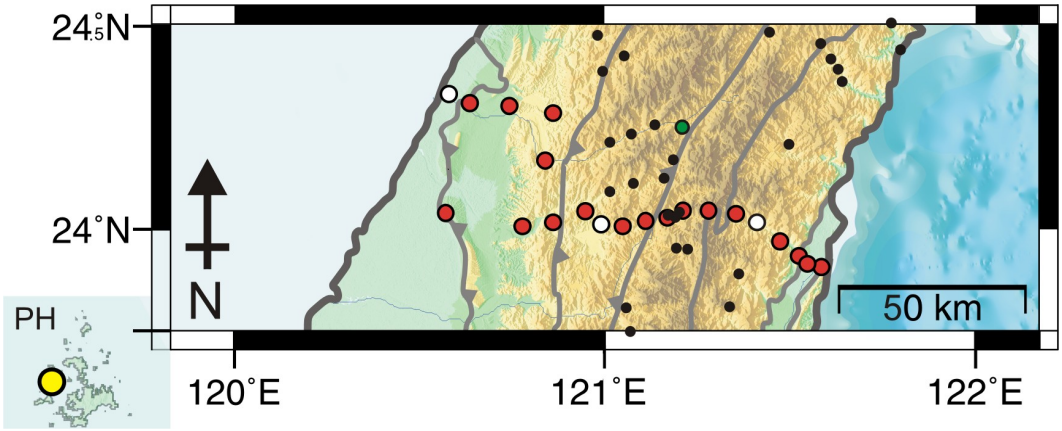

Figure 5-1. Long-period MT stations (red circles) used for 2-D modeling in central Taiwan. White circles indicate where only magnetic fields data were used due to high levels of noise and/or severe distortion. Yellow circle denotes the remote reference station on the Penghu archipelago PH. Green dot shows the location of a heat flow measurement adjacent the LF (Lee and Cheng, 1986). Black dots indicate hot spring locations.

The induction vectors were also analyzed to investigate the dimensionality of these MT data and for selecting stations optimum for 2-D analysis. As shown in Chapter 4, the induction vectors in northeastern Taiwan display significant northwards components that indicate 3-D electrical structure in the crust and upper mantle. However, in central Taiwan, these along-strike components are smallest at stations on Line 200 (Figures 4-9 and 4-11) and these data were favoured over the poorer quality data collected on Line 100 through Taroko Gorge. The rose diagrams in Figure 5-2 reveal overall minimal scatter for the selected stations and indicate a dominant strike-perpendicular trend for the induction vectors. In more detail, Figure 5-4 reveals that within the period band 10-100 s, the induction vectors point predominantly perpendicular to the geoelectric strike direction, indicating a 2-D conductivity structure. EM signals at

these periods are sensitive to mid-crustal depths where major differences are predicted between the end-member tectonic models. For periods greater than 1000 s, the induction vectors point east due to the large conductance of the Philippine Sea. However, at intermediate periods 100–1000 s, induction vectors in eastern Taiwan display an along-strike component, indicating 3-D conductivity structure. Despite this evidence for 3-D behaviour, 2-D analysis is justified by (a) the consistent geoelectric strike obtained from phase tensor analysis and tensor decomposition, and (b) the 2-D nature of the induction vectors at periods most sensitive to the upper and middle crust (Bertrand et al., 2009).

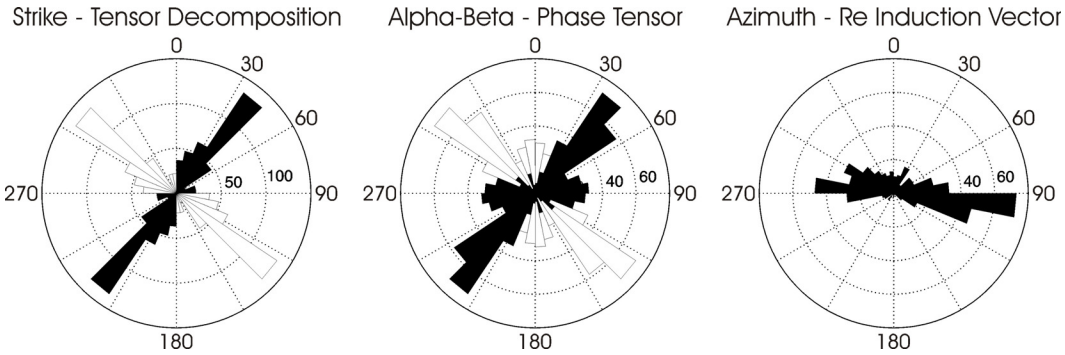

Figure 5-2. Rose diagrams showing results of dimensionality analysis. Results include MT data for the period range 10-10000 s and indicate a dominate 2-D orogen-parallel geoelectric strike direction for the 21 stations chosen (Figure 5-1).

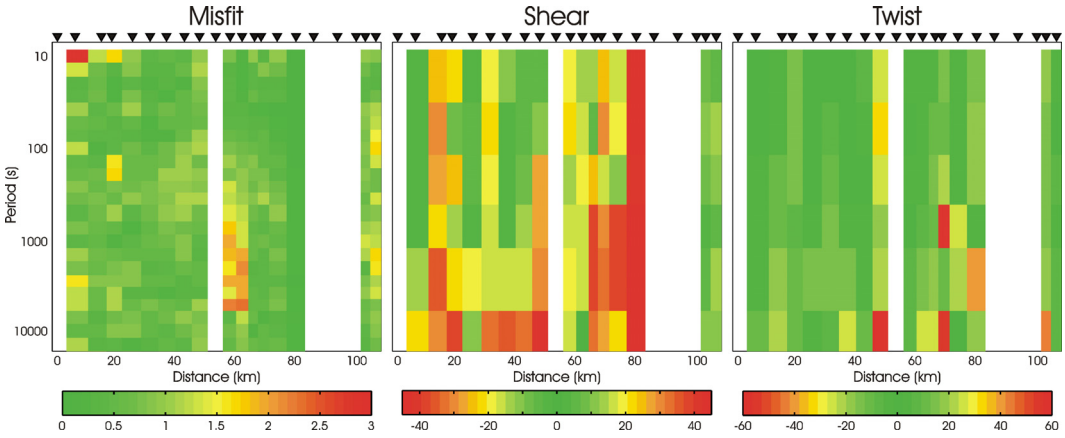

Figure 5-3. Results from tensor decomposition. The low r.m.s. misfit values indicate that the 2-D strike is well constrained (a value of 1 is ideal). Values of the shear and twist angles indicate minor galvanic distortion. White bands indicate where electric field data were excluded from 2-D analysis due to strong distortion.

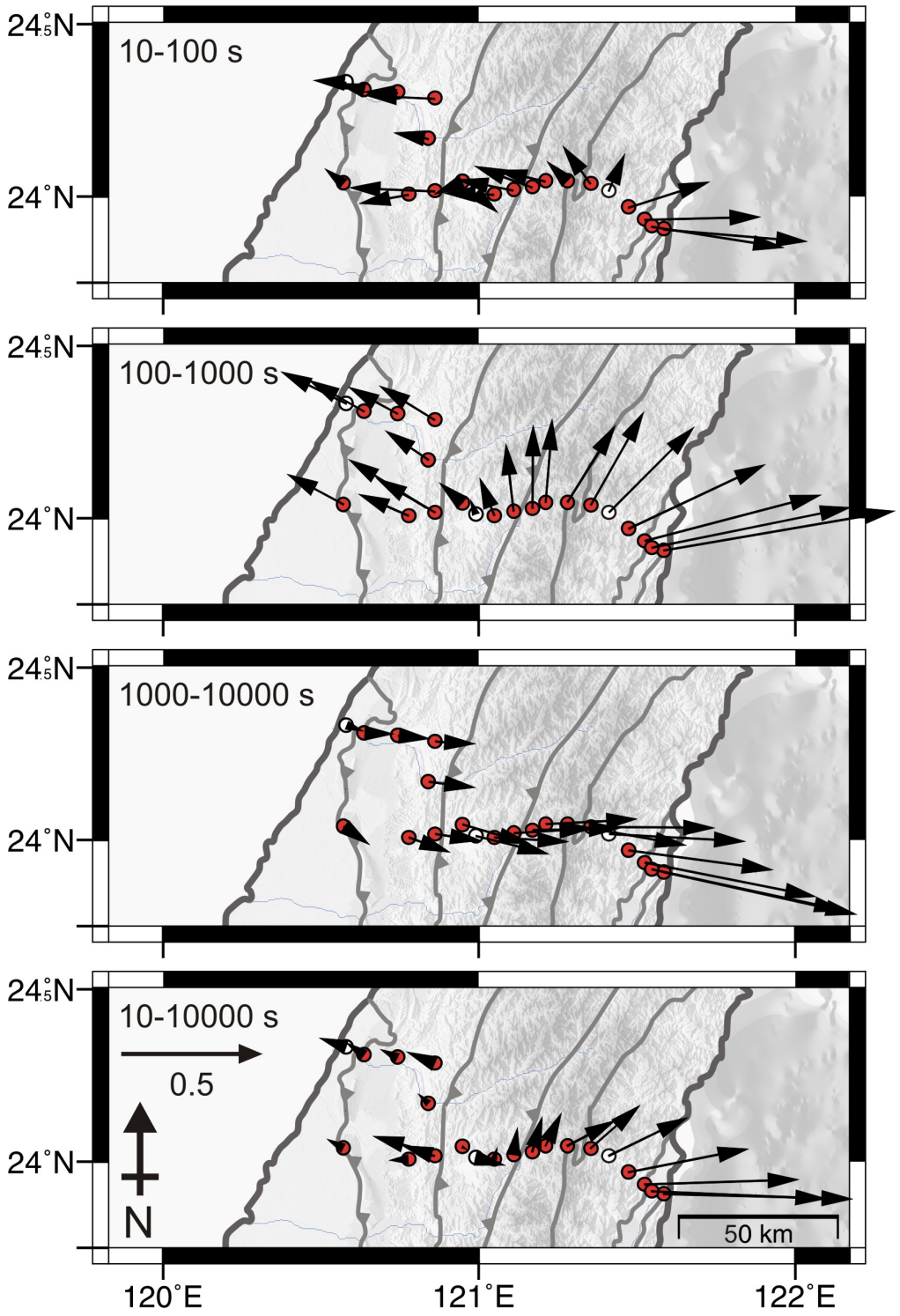

Figure 5-4. Real induction vector components averaged over the labeled period decades and plotted in the Parkinson convention. Scale arrow of magnitude 0.5 is shown. Despite along-strike components east of the LF at mid-periods, the overall strike-perpendicular behaviour indicates overall 2-D electrical structure in central Taiwan. The cross-orogen orientation of vectors adjacent the LF at short periods (10-100 s) sensitive to mid-crustal depths indicates 2-D structure at this location.

5.2.2 MT Data Observations

Before inversion it is useful to display the raw MT data in the frequency domain as pseudosections. Significant features present in an inversion model should be associated with features observed in the raw MT data; otherwise their presence in the model may not be required and could be the result of noise, distortion or the non-unique nature of the ill-posed inverse problem. The MT data were rotated to the geoelectric strike (N37°E) coordinate system and four sample MT data curves are shown in Figure 5-5 that demonstrate the high-quality of the long-period MT data recorded in central Taiwan. The apparent resistivity and phase curves shown for stations adjacent the LF reveals a discontinuous change in the TM mode response across this feature. At long-periods, low apparent resistivity is observed to the west of the fault (TGR260) and high apparent resistivity to the east (TGR265). This discontinuity could be due to vertical current channeling as excess near surface currents generated in the Philippine Sea dissipates downwards into the mantle beneath Taiwan, a phenomenon known as the coast effect (Figure 3-6; Lilley, 2007). If the LF were a sub-vertical conductive fault, it would provide a conductive window that would increase the dissipation of electric current to depth and cause abrupt changes in the slope and phase of the TM mode response (Park et al., 1991).

The coast effect and its influence on the vertical magnetic fields data is also evident in the lower panels of Figure 5-5, which display pseudosections of the in-phase (real) and out-of-phase (imaginary) tipper components. Decreasing values of the real component reflect the influence of the conductive Philippine Sea. Since the skin-depth phenomenon governs the sensitivity of MT periods at depth (i.e. longer period signals sample greater volumes of the Earth), at station TGR235 in western Taiwan, the decrease to negative in-phase tipper values occurs for periods greater than 2000 s. In contrast, in central Taiwan near the LF, negative values occur for periods greater than 1000 s, and on the east coast all in-phase tipper data are negative (TGR295), reflecting the close proximity to the Philippine Sea.

The near-surface (shortest periods) apparent resistivity measurements increase across Taiwan from west to east, associated with the overall increase in metamorphic grade across the island. Since an increase in metamorphic grade results in a reduction of porosity, a consequent increase in the electrical resistivity is observed (Hacikoylu et al., 2006). The easternmost station (TGR295) was installed in the Longitudinal Valley and shows relatively low near-surface resistivity as expected for Quaternary sediments in this area.

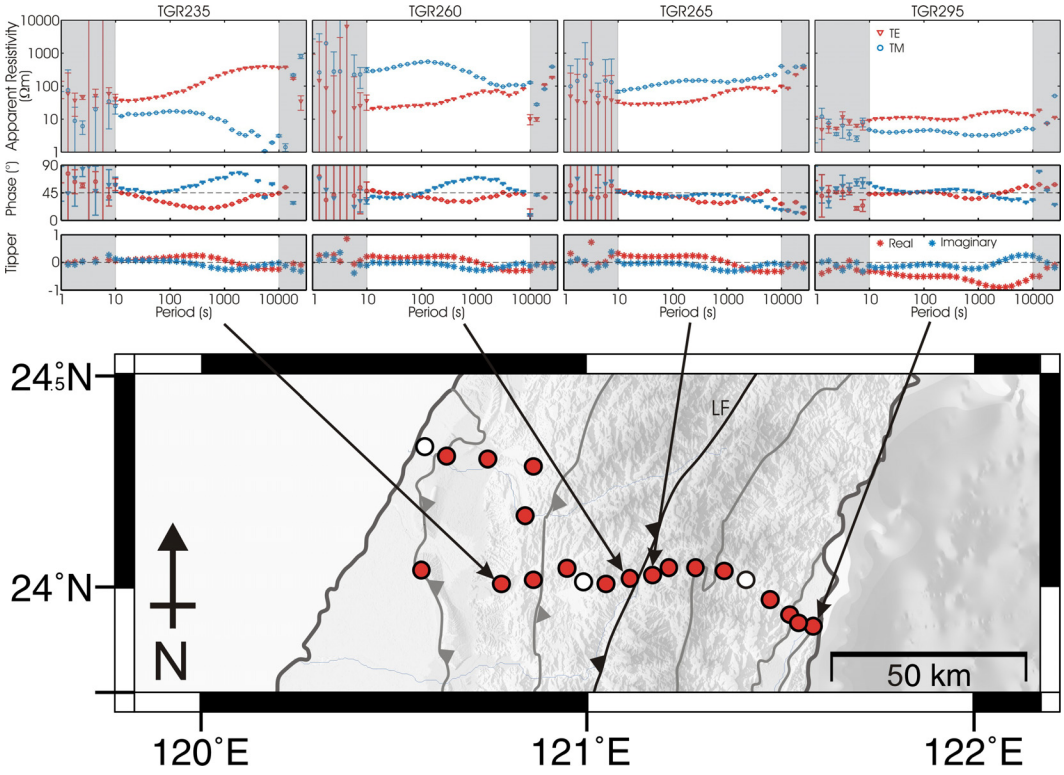

Figure 5-5. Sample long-period MT data from central Taiwan, rotated to the geoelectric strike (N37°E) coordinate frame. Data curves in the two middle-panels are adjacent the Lishan Fault and a significant change in the TM mode apparent resistivity and phase is observed at long-periods across this feature. Poor quality MT data within the shaded regions were not used in the inversion modeling.

Note that these raw MT apparent resistivity curves are affected by static shifts. A useful property of the phase and of the MT phase tensor invariants is that these parameters are unaffected by galvanic distortion and permit visualization of the measured data without influence from static shifts (Simpson and Bahr, 2005; Heise et al., 2006). Figure 5-6 contains pseudosections of the TE and TM mode

phase data, and of the phase tensor ellipses coloured with the geometric mean (ϕ_2) of the maximum (ϕ_{max}) and minimum (ϕ_{min}) phase difference between the magnetic source fields and the induced orthogonal electric currents. These parameters are all sensitive to the vertical resistivity gradient, values greater than 45° indicating decreasing resistivity with depth, and vice versa.

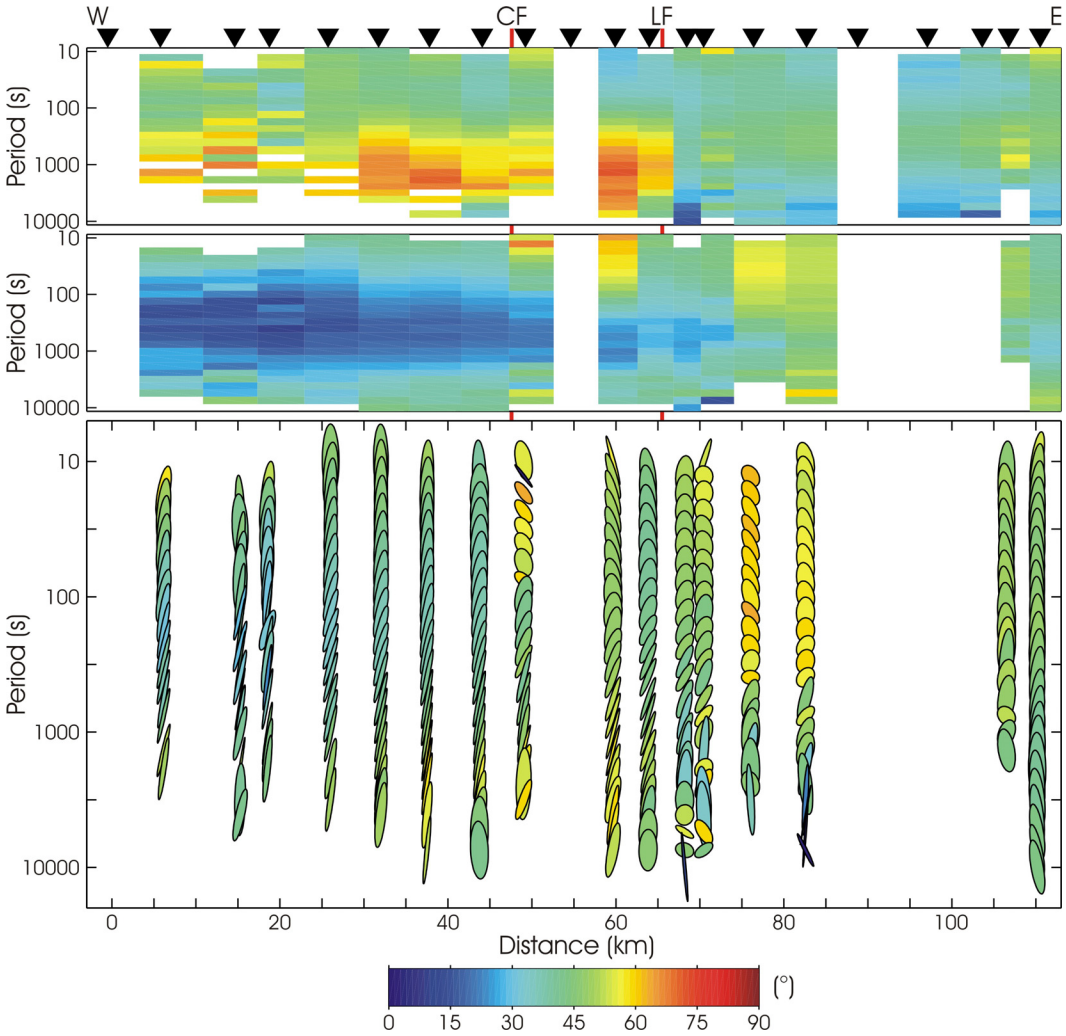

Figure 5-6. Pseudosections of long-period MT phase data in central Taiwan. Top Panel: TM mode phase. Middle Panel: TE mode phase. Bottom Panel: MT phase tensor invariant ϕ_2. White areas indicate where data have been masked in the following 2-D inversion modeling due to high levels of noise and/or severe distortion. Since ϕ_2 is an average, results are not shown where either the TM or TE mode phase has been masked. Profiles are oriented perpendicular to the geoelectric strike (N37°E). Faults are: Chuchih Fault CF and Lishan Fault LF.

At long periods in central Taiwan, high phases (> 45°) indicate the presence of a deep conductor that terminates abruptly in the TM mode and ϕ_2 responses at the Lishan Fault. The TM mode is particularly sensitive to lateral changes in electrical resistivity. These plots indicate a significant transition in the electrical structure across the LF, coincident with a change in orientation of the phase tensor ellipsoids. Figure 5-6 confirms the trend observed across the Lishan Fault in the raw MT data apparent resistivity curves (Figure 5-5), free from the influence of static shift effects.

5.2.3 2-D Inversion of MT Data

The NLCG6 2-D inversion algorithm of Rodi and Mackie (2001) was used to generate smooth resistivity models that fit the MT data collected in central Taiwan. Error floors of 20%, 7.5% and 0.03 were used for the apparent resistivity, phase and tipper data, respectively. Unlike the phase, the apparent resistivity data are susceptible to galvanic distortion. Setting a larger error floor for the phase down-weights these effects and mitigates any distortion effects (Li et al., 2003). In addition, inversion models included the known topography and bathymetry along the profile, and the algorithm was set to solve for the static shift coefficients at each site during late-stage iterations.

Many inversion models were computed for a range of control parameters and from a variety of starting models to ensure that significant resistivity features are robust and required by these MT data (Figure 5-7). The consistent structures observed in these inversion models reveal that these resistivity features are robust and are not strongly dependent on the particular regularization parameters (1-6 in Figure 5-7) or starting model resistivity (7-8 in Figure 5-7). In addition, since the TE mode data are most sensitive to off-profile (3-D) structure (Wannamaker et al., 2002), it is common to down-weight these data by increasing the error floors in comparison to the TM mode values (Heise et al., 2007; Hill et al., 2009). However, an inversion model generated with the TE mode error floors doubled in

comparison to the TM mode values resulted in little change in the final resistivity structures imaged (9 in Figure 5-7).

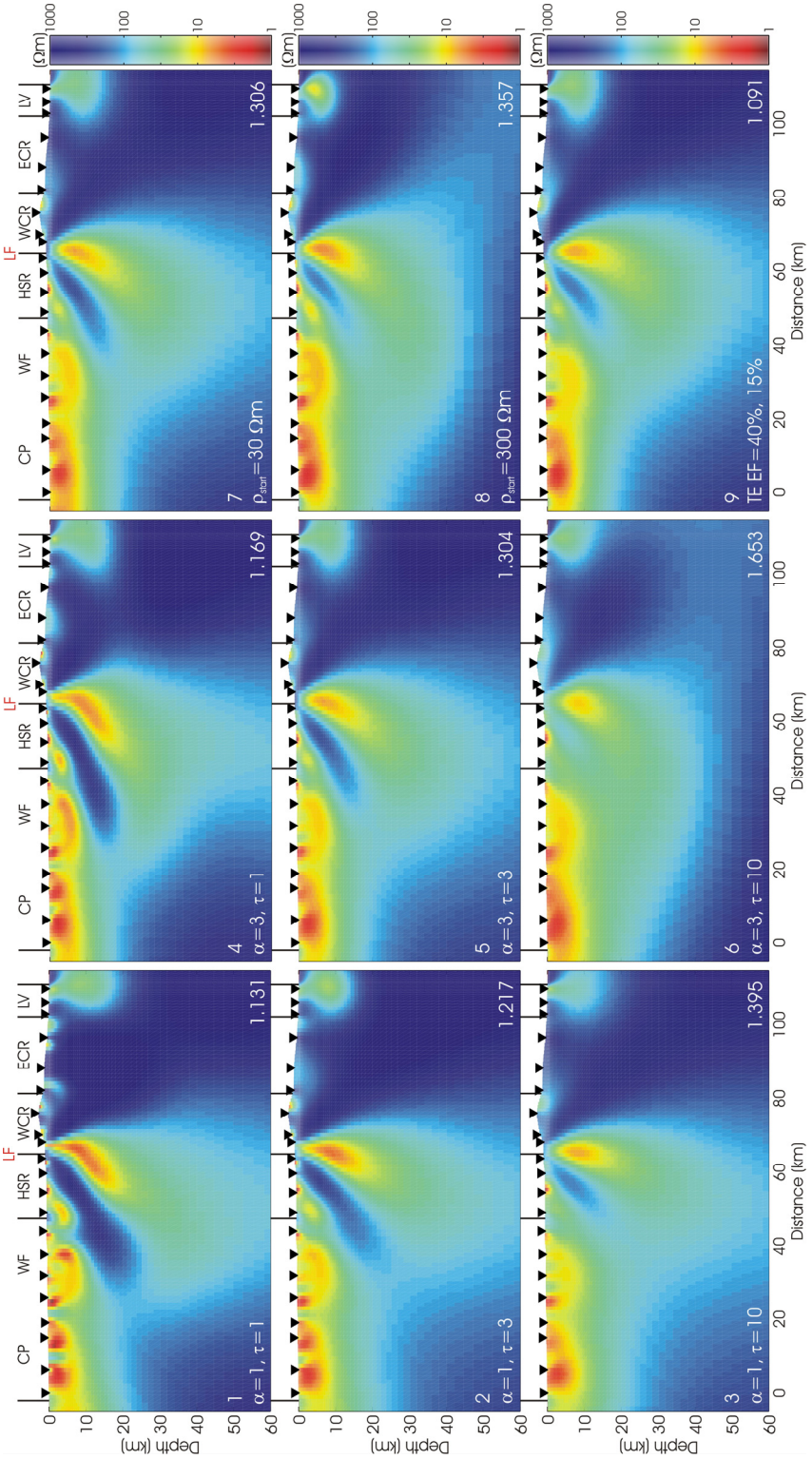

Figure 5-7. 2-D TETMHZ inversion models of central Taiwan. Inversions solved for the smoothest variations away from an *a priori* starting model that included the Philippine Sea and Taiwan Strait. Models 1-6 and 9 used 100 Ωm as the starting subsurface resistivity. Models 7-9 used smoothing parameters $\alpha = 3$ and $\tau = 3$. Error floors of 20% and 7.5% for the resistivity and phase were used for models 1-8. An absolute error floor of 0.03 was used for the tipper data in all inversion models. R.M.S. data misfit is shown in the bottom right corner of each model.

Further, inversion models generated with and without the entire TE mode apparent resistivity and phase data resulted in similar resistivity structures (not shown). This similarity indicates that the influence of 3-D effects on the final model is minor for these MT data in central Taiwan.

Since seawater is a stronger conductor than most subsurface Earth structures, the surrounding bathymetry must be included in the inversion models. Two methods were investigated for including the conductive seawater of the surrounding Philippine Sea and Taiwan Strait:

1. The resistivity of cells containing seawater was fixed and the inversion algorithm was forced to solve for the smoothest model in the spatial domain.
2. The resistivity of seawater cells was allowed to change, but subject to partial constraint by solving for the spatially smoothest model away from the *a priori* starting model.

The final resistivity models in (1) and (2) are generally similar (Figure 5-8), but the second approach was preferred as this avoids enforcing a fixed bathymetry that cannot be accurately modeled as the mesh becomes increasingly coarse at depth and away from the land-based measurements. With a fixed bathymetry, inaccuracies in the modeled seafloor cannot be smoothed by the inversion and result in the rougher resistivity structure observed beneath the island. The latter approach was found to yield stable models for MT data collected on Amchitka Island in the Aleutian Arc (Unsworth et al., 2007).

Smooth inversion models were sought that also fit the measured MT data to within an acceptable level. However, these are opposing requirements and the balance between them is controlled by the regularization parameter τ. To select the optimum value of τ, an L-curve (Figure 5-9) was constructed and the location of maximum curvature identified. This point balances the requirements for a spatially smooth resistivity model that also produces an acceptable r.m.s. data

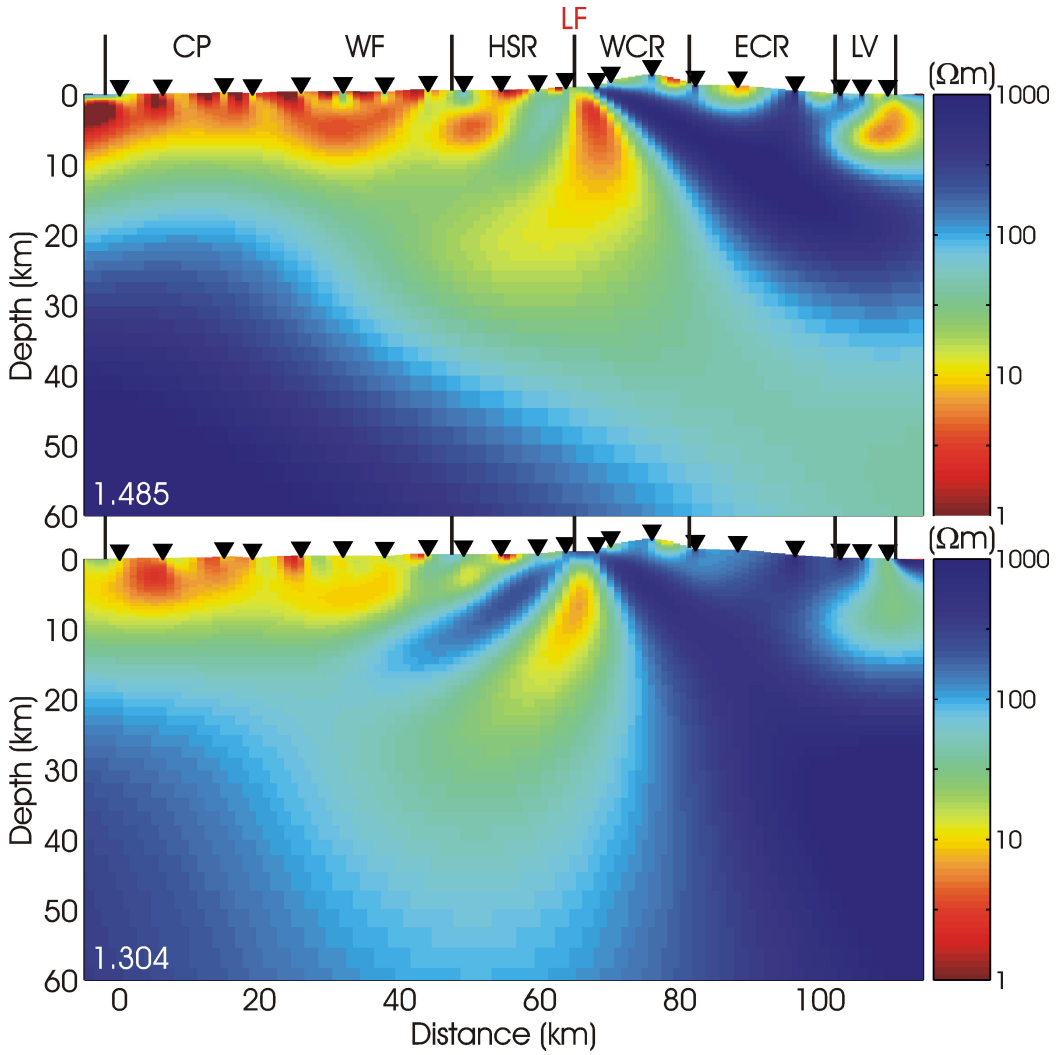

Figure 5-8. TETMHZ inversion models of MT data in central Taiwan. Top panel: Seawater cells fixed. Bottom Panel: Algorithm solved for the smoothest model away from the *a priori* starting model. Both models used $\alpha = 3$ and $\tau = 3$. The r.m.s. data misfit is shown in the bottom left corner of each model.

misfit (Hansen et al., 1992). The ratio of horizontal to vertical smoothing is defined by α, and models with $\alpha = 3$ were favoured to slightly emphasize lateral continuity (4-6 in Figure 5-7). Significant model structures were observed to persist over a wide range of smoothing parameters (1-6 in Figure 5-7), indicating a stable model with robust features that are required by these measured MT data.

A final inversion of the MT impedances and induction vector data produced a resistivity model that fit the observed MT data to within an acceptable r.m.s. misfit of 1.304 (Figure 5-10). Note that MT data showing high levels of distortion

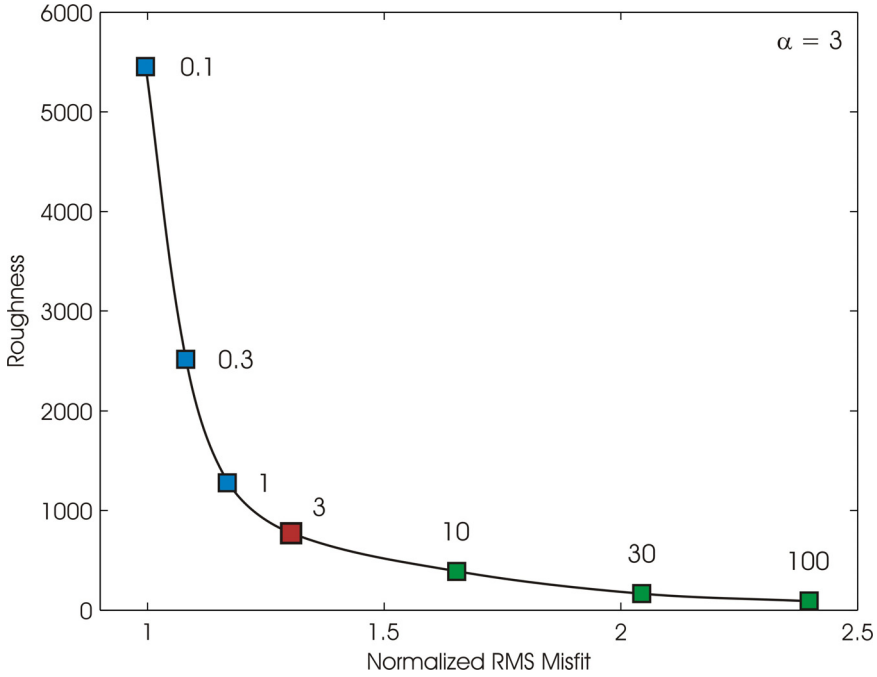

Figure 5-9. L-curve for 2-D TETMHZ inversion models of central Taiwan. τ for each model is shown, all models used α = 3. The maximum curvature occurs at τ = 3, and balances the tradeoff between data fit (decreasing misfit – blue squares) and obtaining a smooth model (decreasing roughness – green squares).

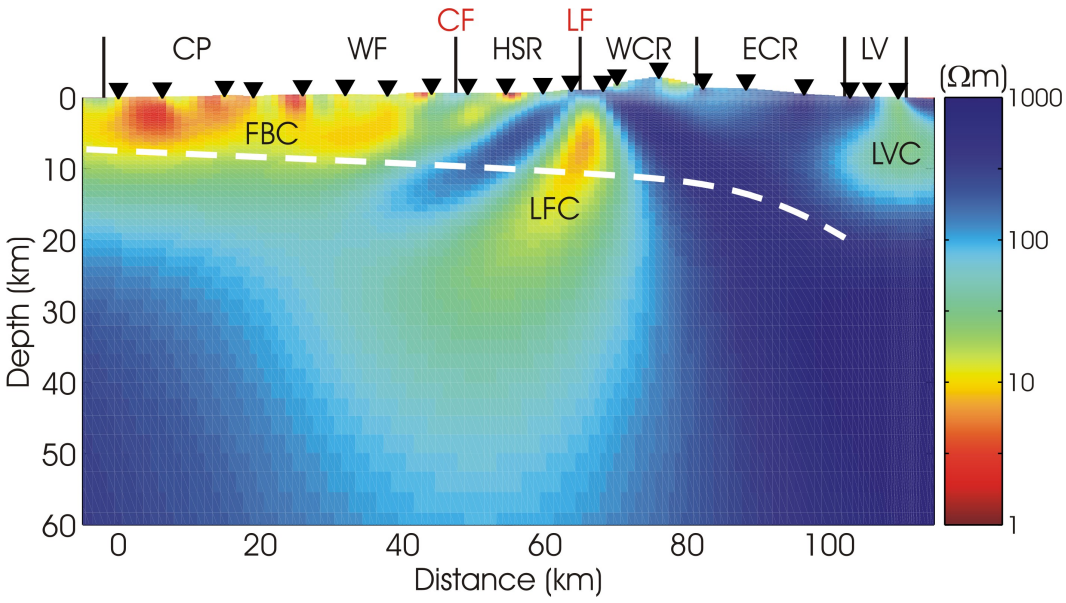

Figure 5-10. TE, TM and tipper, 2-D MT resistivity inversion model of central Taiwan. Model conductors: FBC – Foreland Basin Conductor; LFC – Lishan Fault Conductor; LVC – Longitudinal Valley Conductor. Dashed white line shows the décollement from Carena et al. (2002). Abbreviations above the model indicate the geological provinces (black), the Chuchih Fault CF and the Lishan Fault LF (red).

and/or noise were excluded from the modeling to allow a good fit to be achieved by the inversion. Pseudosections of the data and inversion model responses for these stations show good agreement (Figure 5-11). The increase in resistivity eastwards across Taiwan, observed in the sample data curves (Figure 5-5) and the final resistivity model (Figure 5-10), is clearly visible in the apparent resistivity pseudosections, especially for the TM mode that is most sensitive to lateral variations in resistivity (Figure 5-11). Further, the effect of the conductive Philippine Sea, which decreases the in-phase tipper data, is clearly observed at progressively shorter periods at stations collected nearer the east coast of Taiwan (Figure 5-11). As indicated by observation of the measured MT data apparent resistivity and phase (Figures 5-5 and 5-6), a significant transition occurs in the electrical structure beneath central Taiwan at the Lishan Fault. A sub-vertical conductor is imaged, which produced the discontinuity in the TM mode response at stations collected adjacent to this fault (Figure 5-5).

5.2.4 3-D Inversion of MT Data

Several indicators that the subset of 21 MT stations selected for 2-D analysis of central Taiwan displays dominant 2-D behaviour have been demonstrated. These indicators include:

1. A consistent, well-defined geoelectric strike direction obtained by both the tensor decomposition and phase tensor analysis techniques.
2. The strike-perpendicular rotation of the real component of the induction vectors at periods most sensitive to the upper and middle crust.
3. The low r.m.s. data misfits and stable 2-D inversion models that yield robust resistivity features over a wide range of control parameters.

However, Taiwan is undoubtedly a 3-D orogen. The plate boundary varies along the island-strike from northwards subduction of the Philippine Sea Plate north of 23.7°N latitude, to eastwards subduction of the Eurasian Plate beneath southern

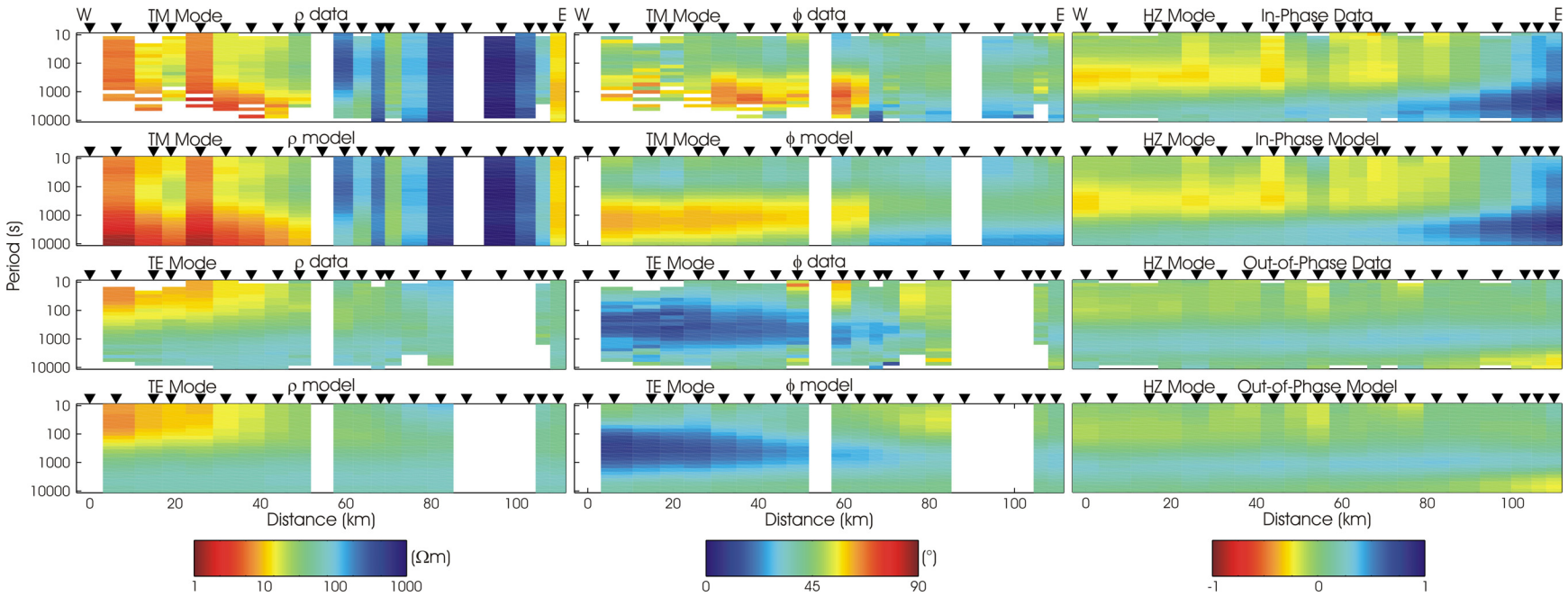

Figure 5-11. Pseudosections of the long-period MT data 2-D modeled in central Taiwan. The left and middle panels display the measured and modeled resistivity and phase data for the TM (Transverse Magnetic) and TE (Transverse Electric) modes. The right panel shows the measured and modeled in-phase (real) and out-of-phase (imaginary) tipper data. White regions indicate data that were excluded from the 2-D inversion modeling because of high levels of noise and/or severe distortion.

Taiwan, south of 23°N latitude. These opposite polarity subduction zones that bracket the island generate orogen parallel variation. In addition, the obliquity of the Luzon Volcanic Arc with respect to the passive Eurasian margin introduces along-strike structural variation. Lastly, while the bathymetry surrounding Taiwan may be considered approximately 2-D in central Taiwan, it is clearly not 2-D near the ends of the island where the shallow Taiwan Strait transitions to the deep water in the Philippine Sea. These factors could all induce significant 3-D induction effects that may influence the onshore MT data.

To ultimately determine if the resistivity structures imaged in the 2-D model of central Taiwan are robust, these same MT data were inverted using the 3-D inversion algorithm, WS3DINVMT (Siripunvaraporn et al., 2005). While this inversion code does not include the tipper data, an inversion model of the full 3-D impedance tensor resulted in a model of central Taiwan (Figure 5-12) that shows similar resistivity structures to those observed in the 2-D model (Figure 5-10).

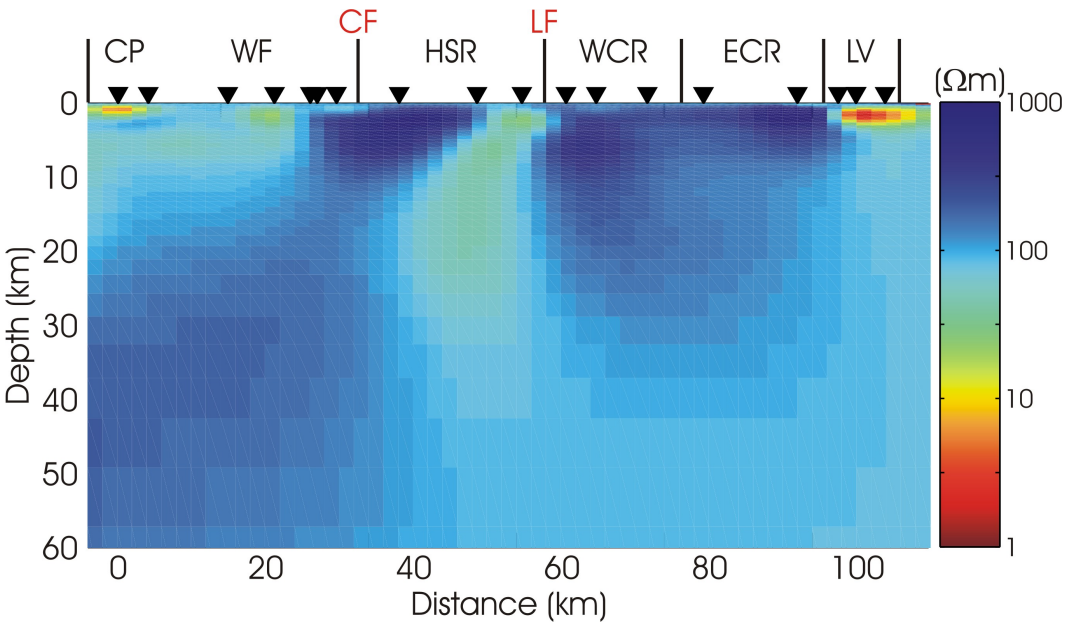

Figure 5-12. 2-D slice of a 3-D inversion model of the full MT impedance data in central Taiwan. Error floors of 20% and 10% were used for the diagonal and off-diagonal elements of the impedance tensor, respectively. Profile rotation is N20°E in order to minimize the number of cells required in the core of the model mesh. The r.m.s. data misfit is 2.061 after 3 iterations and 38 days of CPU time.

Note that due to the extensive computational requirements involved in inverting the full 3-D MT impedance tensor data, the numbers of model and data parameters were reduced in comparison to the 2-D analysis. For example, the model mesh used in the 2-D inversions contained 221 rows, and 177 columns that were spaced 1 km apart between the station locations. In contrast the mesh used for 3-D inversion was limited in size to 84 by 48 horizontal cells spaced 2 km apart between stations, and 63 rows at depth. In addition, while the 2-D models inverted MT data at 8 periods per decade between 10 and 10000 s, the 3-D inversions used only 4 periods per decade over this same period range. These reductions are required; 200 iterations of the 2-D NLCG6 algorithm took 6 hours of CPU time to invert 8 periods per decade of the TE, TM and tipper data in central Taiwan. In contrast, after running for 38 days, 3 iterations were completed for the 3-D inversion model of the reduced dataset. However, these reductions are justified since MT data vary smoothly in both the spatial and frequency domains (Simpson and Bahr, 2005).

Despite differences between the 2-D (NLCG6) and 3-D (WS3DINVMT) inversion algorithms, the 3-D inversion model in Figure 5-12 displays obvious similarity to the resistivity structures observed by 2-D inversion (Figure 5-10). This similarity strongly indicates that the resistivity features present in the 2-D inversion model of central Taiwan are robust and required by these MT data. Note that the 2-D model is used for the subsequent detailed analysis in this chapter, since the 3-D model can only represent the Earth with a coarse mesh.

5.3 Interpretation

5.3.1 Resistivity Model Interpretation

In the 2-D inversion model, a conductive (low resistivity) anomaly is imaged in the foreland basin of western Taiwan (FBC in Figure 5-10) that can be explained by interconnected fluids within the porous sedimentary rocks that comprise the CP and WF provinces. East of this zone, resistivity increases and is consistent

with a reduction in porosity where the sedimentary rocks contact the crystalline metamorphic rocks of the HSR. While limited in near-surface resolution, and traversing the conductive Puli basin, this model does not support underthrusting of the conductive WF rocks beneath the HSR at the Chuchih Fault. The steep contact imaged between these provinces is not consistent with the shallow dipping (i.e. 30°) thrust faults predicted by deformation within a critical wedge. Rather, this model suggests reactivation of a pre-existing structure (possibly a rift-related normal fault) and favours the thick-skinned tectonic model (Gourley et al., 2007). For example, the west-dipping Lishan Fault between the HSR and WCR may have formerly marked the eastern edge of an Oligocene half-graben (Clark et al., 1993).

In eastern Taiwan, a near-surface conductor (LVC in Figure 5-10) occurs beneath the LV. This conductor may be related to fluids within the Longitudinal Valley Fault, an active, high-angle oblique thrust fault that overlies the suture zone between the Eurasian Plate and the Philippine Sea Plate (Fig. 2 in Yu and Kuo, 2001). However, this feature is poorly constrained, owing to its location at the profile end, and the insensitivity of long-period MT data to near surface structure.

A prominent feature of the resistivity model is the mid-crustal conductor (LFC in Figure 5-10) located beneath the Lishan Fault. Partial melts and/or aqueous fluids have been proposed to explain similar crustal conductors elsewhere (Wannamaker et al., 2002, Unsworth et al., 2005). While temperatures greater than 1000 °C are required to melt dry crustal rocks, the presence of aqueous fluids can induce partial melting of felsic material at 650 °C (Vanyan and Gliko, 1999), and significantly reduces the electrical resistivity (Partzsch et al., 2000). However, heat-flow data from a well adjacent the LF in central Taiwan (Figure 5-1) indicate a geothermal gradient of 22 °C/km, limiting partial melting to depths below 30 km. Thus, given the relatively shallow depth of the LFC, a distributed zone of saline fluids in the middle to lower crust is the most likely cause of the low resistivity observed.

The Lishan Fault Conductor appears to cross the location of the décollement proposed by Carena et al. (2002). If the LFC is caused by a zone of interconnected aqueous fluids, then this is significant in terms of the depth extent of crustal deformation in central Taiwan. The presence of such a feature is consistent with a thick-skinned model since interconnected fluids would be released below 10–15 km depth from prograde metamorphism in the thickening crust (Wannamaker et al., 2002). The geometry of the Lishan Fault Conductor presents two challenges to the thin-skinned model.

1. With minimal deformation below the décollement, it is difficult to envision a mechanism to generate fluids at shallow depths within the subducting Eurasian Plate.
2. If a décollement were present, it might be expected to disrupt upward fluid migration.

Clearly, identifying whether the LFC extends into the mid-crust has significant tectonic implications. However, resolving the depth extent presents a challenge, since MT data are primarily sensitive to the depth to the top of a conductor. Smooth inversions of MT data often smear conductive features to depth (Chen et al., 2007a); thus a series of constrained inversions were implemented with models fixed to be resistive below a given depth. The fit to the observed tipper data (ratio of vertical to horizontal magnetic fields) adjacent the Lishan Fault is illustrated in Figure 5-13. Note that these inversions also fit the MT impedances; however, only the tipper responses are shown as these data are most sensitive to vertical structure (Unsworth et al., 2000). Progressively decreasing the depth to the resistive basement causes an increase in the data misfit; the depth at which this occurs indicates the shallowest conductor permitted by the data (Li et al., 2003). The F30 model fits the measured data very well. The misfit is higher in the F20 model, but is still acceptable. In contrast, the F10 model does not adequately fit the measured data, indicating that the Lishan Fault Conductor extends beyond a depth of 10 km.

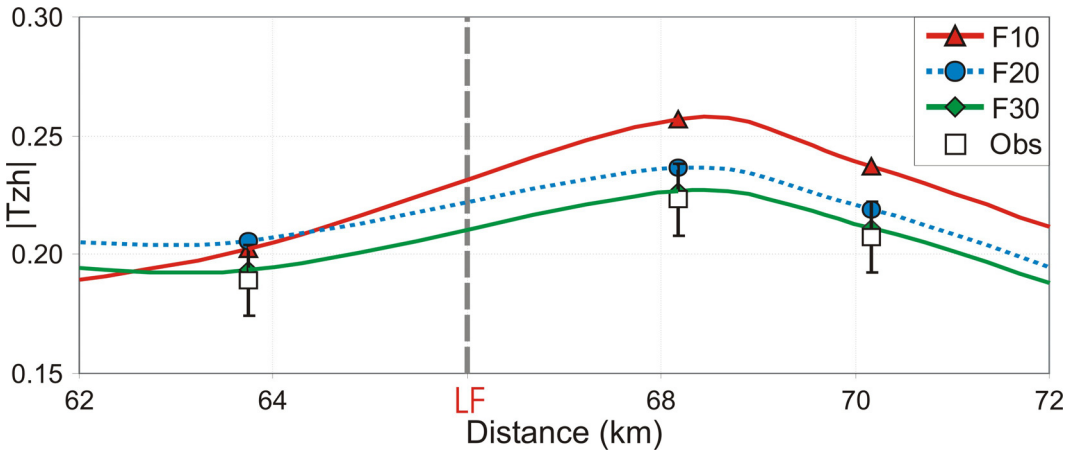

Figure 5-13. Tipper data parallel to profile at a period of 100 s for stations adjacent the Lishan Fault. Open squares denote measured data with absolute error floor of 0.03. Smooth curves are responses of constrained inversion models with a resistive (300 Ωm) basement fixed at depths of 10, 20 and 30 km; models F10, F20 and F30, respectively.

MT data are sensitive to the conductance (integrated conductivity) of a layer. Therefore, conductance plots of the fixed inversion models can further illustrate whether the inversion algorithm is able/unable to fit the data subject to the imposed constraints. The top panel in Figure 5-14 illustrates that for the F20 and F30 models, the integrated conductance to a depth of 60 km beneath the profile is similar to that for the free inversion model, where the basement depth was unconstrained. In contrast, with a resistive basement fixed at 10 km, the model conductance shows oscillatory behaviour beneath the LF. This behaviour illustrates that the F10 inversion model is forced to over-emphasize shallow (< 10 km) features of alternating high-low conductivity in order to fit the data. To show that the inability of the inversion algorithm to fit the measured MT data with the F10 model is robust, the same fixed inversion models were generated using regularization values of $\alpha = 1$ and $\tau = 1$. These values will give more weight to fitting the measured MT data and relax the smoothing constraint compared to the previous model results that used $\alpha = 3$ and $\tau = 3$. Generating the same conductance plot for these rougher inversion models indicates that the inversion algorithm is still unable to fit the F10 model (bottom panel in Figure 5-14).

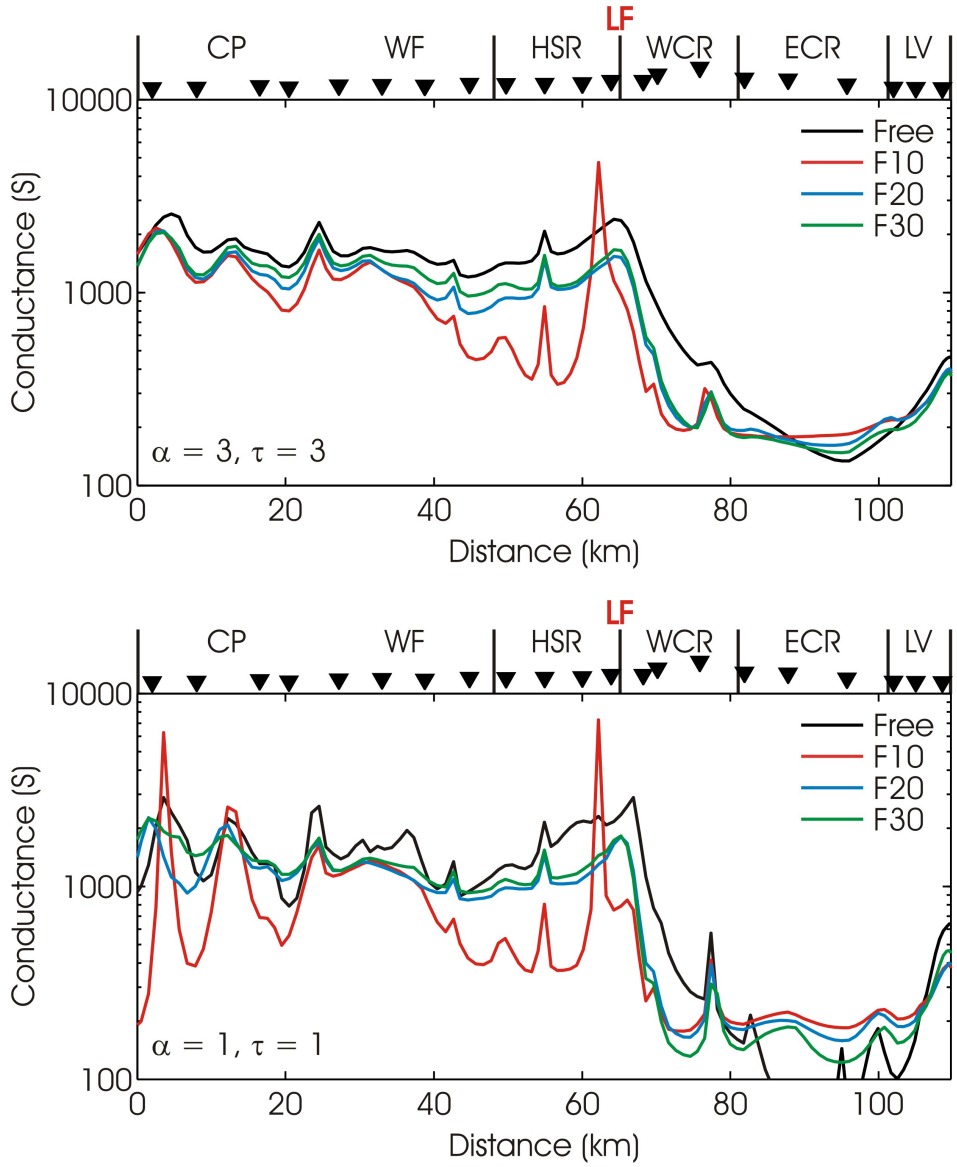

Figure 5-14. Integrated conductance to 60 km depth for the constrained 2-D inversion models of central Taiwan. Top Panel: Smoothing parameters: $\alpha = 3$ and $\tau = 3$. Bottom Panel: Smoothing parameters: $\alpha = 1$ and $\tau = 1$. The F10 model is oscillatory near the LF indicating that the inversion algorithm is unable to generate a spatially smooth model with a resistive basement fixed at 10 km depth.

Model	r.m.s. Misfit $\alpha = 3, \tau = 3$	Difference	r.m.s. Misfit $\alpha = 1, \tau = 1$	Difference
F10	2.114	0.246	1.980	0.187
F20	1.868	0.098	1.794	0.130
F30	1.770		1.664	

Table 5-1. Normalized r.m.s. misfit for the constrained inversion models of central Taiwan.

Reductions in the r.m.s. data misfit provide quantitative insight to the ability of the inversion algorithm to fit the constrained inversion models. As summarized in Table 5-1, the reduction in r.m.s. misfit between the F10 and F20 models is much greater than that between the F20 and F30 models. The significant reduction in misfit between the F10 and F20 models indicates the inability of the inversion algorithm to fit these MT data with a resistive basement fixed at 10 km depth.

These MT data clearly indicate the presence of a conductive feature (LFC) that extends below the depth (~ 10 km) of the inferred décollement beneath central Taiwan. While these MT data do not permit the exact determination of the depth extent of this feature, strong evidence is given that indicates this sub-vertical conductor extends into the mid-crust (i.e. > 10 km). The geometry of the LFC is thus difficult to reconcile with a thin-skinned model and is interpreted as support for the thick-skinned lithospheric deformation model of Wu et al. (1997).

5.3.2 Lateral Resolution of the Lishan Fault Conductor

The anomalous mid-crustal conductor imaged in central Taiwan occurs beneath the surface trace of the Lishan Fault, and has been labeled the Lishan Fault Conductor (LFC in Figure 5-10). While the depth extent of this feature has been shown to extend below ~10 km, the non-uniqueness of the inversion means that all combinations of conductivity and thickness with the same conductance could equally fit these MT data. Thus, the name LFC should not be interpreted to imply that this feature is due to interconnected fluids within a singular narrow fault – the Lishan Fault. Rather, to determine the spatial resolution of these MT data to the observed LFC, sensitivity tests were carried out by the following procedure:

1. A resistivity model was generated by replacing the LFC with a resistive (300 Ωm) background, in the inversion model shown in Figure 5-10.
2. Conductive features that simulate a range of possible geometries for the LFC were added to this starting model (e.g. narrow faults, broad regions of enhanced conductivity).

3. For each model, long-period synthetic MT data were computed with a 2-D forward-modeling algorithm at the same locations where measurements were made in central Taiwan (black triangles in Figure 5-15).
4. 10 % Gaussian noise was added to these synthetic MT data.
5. The synthetic MT data were then inverted using the same 2-D algorithm, starting model and inversion parameters employed in the initial study.

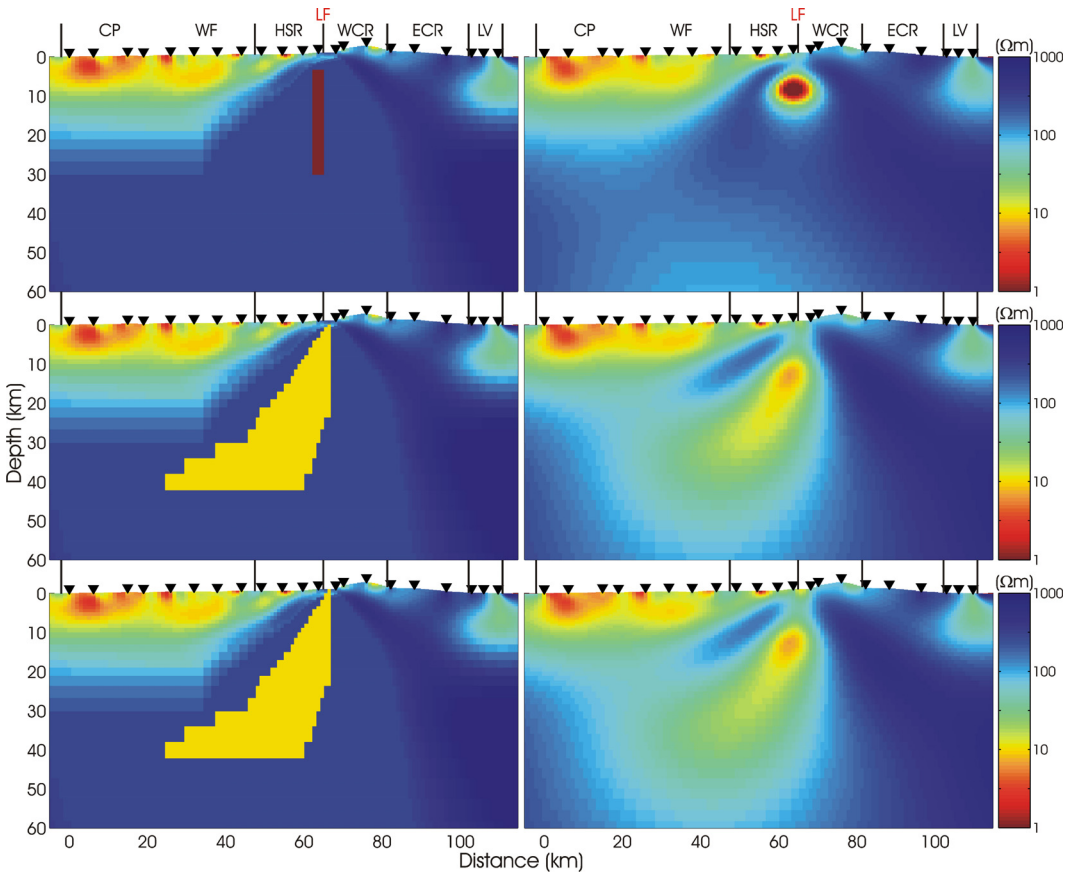

Figure 5-15. Resolution tests of the Lishan Fault Conductor. Left Panels: Starting resistivity models. Right Panels: TE, TM and tipper inversion model results for synthetic MT data computed for the adjacent starting models. Note that 10% Gaussian noise was added to the synthetic MT data prior to inversion.

This process indicates the types of sub-surface structure that result in anomalies that are similar in both conductivity and spatial extent to the LFC (Figure 5-15). The upper row in Figure 5-15 reveals that a narrow conductive fault will not generate a feature similar to the LFC observed in the measured data. In contrast, the middle and bottom rows show that a broad region of distributed conductivity

does yield a feature with similar geometry and conductivity to that observed in the inversion model of the field data. Therefore, these MT data support a 10's of km wide zone of distributed interconnected fluids (i.e. interconnected porosity and/or fluid filled fractures) beneath central Taiwan. Note that while MT data are effective at locating the depth to the top of a conductor, the upper few km of the subsurface are not well resolved with these long-period MT data, as indicated by the similarity between the middle and bottom row models (Figure 5-15).

5.3.3 Correlation of Resistivity and Seismic Velocity

Integration of independent geophysical data was implemented by comparing a seismic velocity model to the resistivity model (Figure 5-16). The tomographic model consists of P-wave velocity estimates on an x = y = 5, z = 2 km grid and includes first arrival data from the TAIGER active seismic transects in 2007–8. The resistivity and velocity models are clearly correlated (e.g. low values occur in the upper 10 km below the CP and WF in both models). However, a quantitative method is required to determine the degree to which these parameters are related.

The method of Bedrosian et al. (2004) was used to determine distinct model domains that are defined by ranges of velocity and resistivity. The resistivity model was first interpolated onto the same grid as the seismic velocity model, and poorly resolved areas of both models were masked to avoid correlating unconstrained parameter estimates. For example, conductors are smeared to depth by the regularized inversion; thus cells beneath conductors were excluded from the analysis. Model edges were also masked where features are poorly resolved. A histogram of the occurrence of resistivity and velocity combinations for each model cell was then generated (Figure 5-17). Distinct domains within this histogram were identified and mapped back onto the resistivity model.

No universal relationship between resistivity and velocity has been reported for crustal scale studies (Bedrosian et al., 2007). In general, porosity provides a link

between electrical resistivity and seismic velocity (Hacikoylu et al., 2006), since as porosity decreases, both resistivity and velocity increase. Metamorphic grade increases eastwards across Taiwan; thus an associated increase in electrical resistivity and seismic velocity is expected as the pore space is reduced. Four distinct domains are observed in the histogram, and three of these (CP/WF, HSR and WCR/ECR) define a trend of increasing velocity and resistivity with metamorphic grade. However, the LFC domain does not lie on this trend.

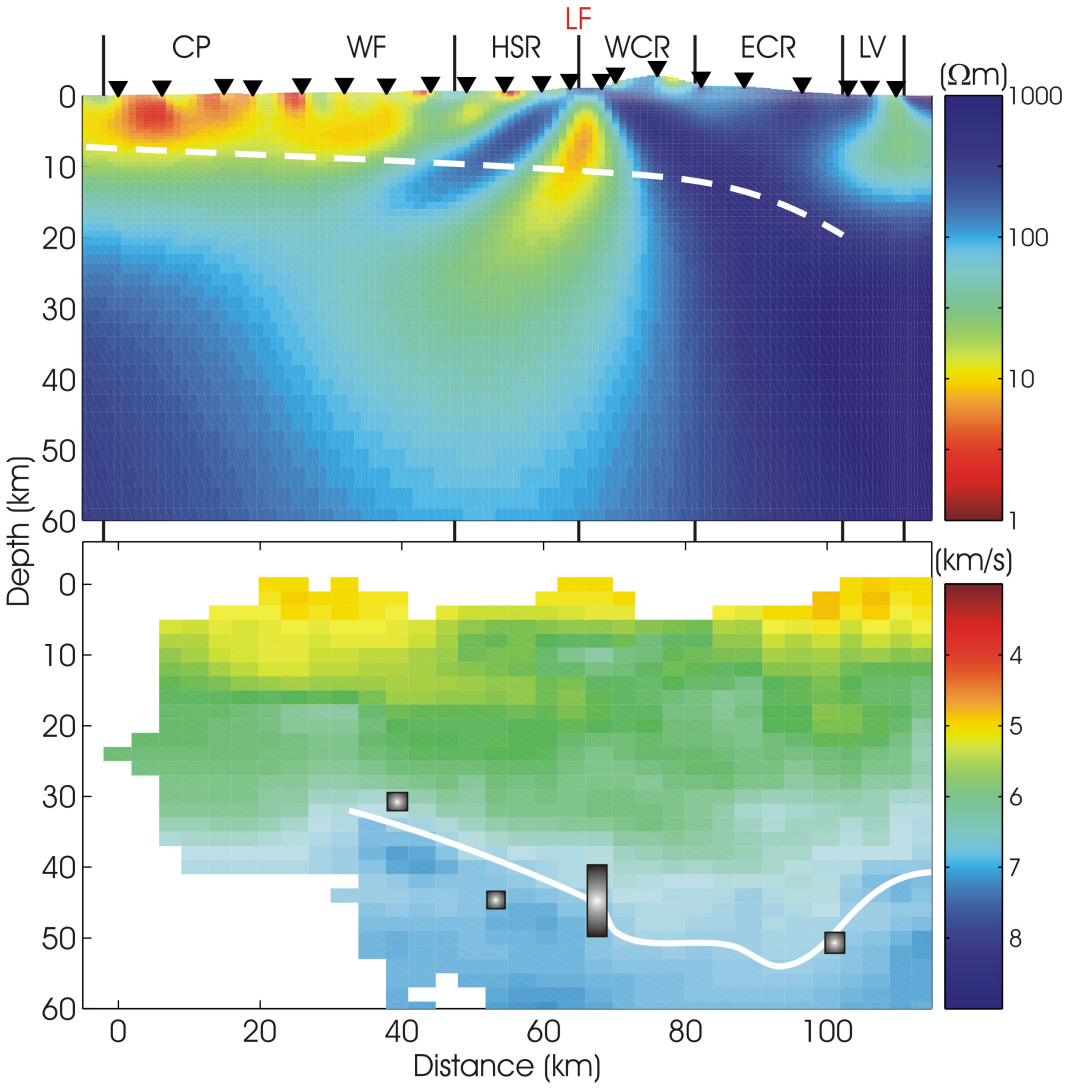

Figure 5-16. Top Panel: TE, TM and tipper resistivity inversion model. White dashed line shows the décollement from Carena et al. (2002). Bottom Panel: Tomographic P-wave velocity model with contour v_p = 7.3 km/s for reference (Wu et al., 2009). Vertical bars show Moho depth from receiver functions (Kim et al., 2004).

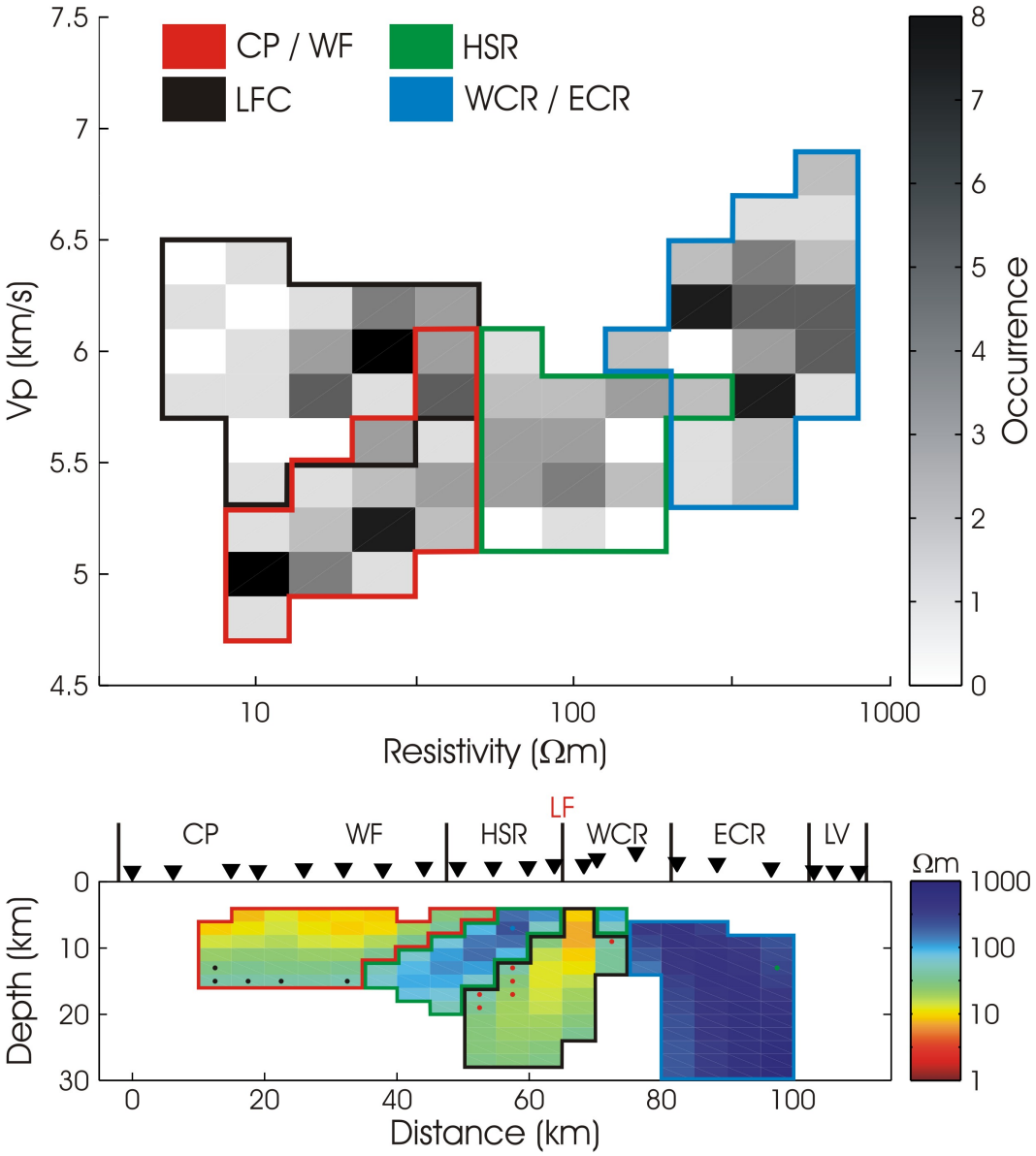

Figure 5-17. Top Panel: Crossplot of P-wave velocity and electrical resistivity for the models shown in Figure 5-16. Bottom Panel: Resistivity model indicating the spatial regions that give rise to the coloured domains in the crossplot. Note that white areas indicate where the resistivity and velocity models were masked. Dots indicate cells that contribute to bins within overlapped domains in the histogram.

The LFC domain is characterized by an area of anomalously low resistivity and only moderately low seismic velocity. Fluids generated by prograde metamorphism within a thickened crust are the most likely explanation for this conductor. Evidence for extensive fluid circulation in this area comes from a number of recent (Pliocene - Pleistocene) Au and Cu deposits that have formed

adjacent to the Lishan Fault (Figure 5-18). In young or active orogens, tectonically driven hydrothermal fluid circulation is often associated with gold mineralization (see table 1 in Craw et al., 2002). In Taiwan, the origin of the fluids that precipitated these deposits is unknown. However, within the Lishan Fault, significant evidence for permeability has been found and isotopic analysis of fluid samples from veins within this fault is currently underway (Phaedra Upton, personal communication). Despite this present uncertainty, it has been suggested that the source fluids arise from dehydration reactions within the crust, rather than circulating meteoric water (Craw et al., 2002). Thus, it is necessary to show that fluids can account for the low resistivities in this domain, without causing a significant decrease in velocity.

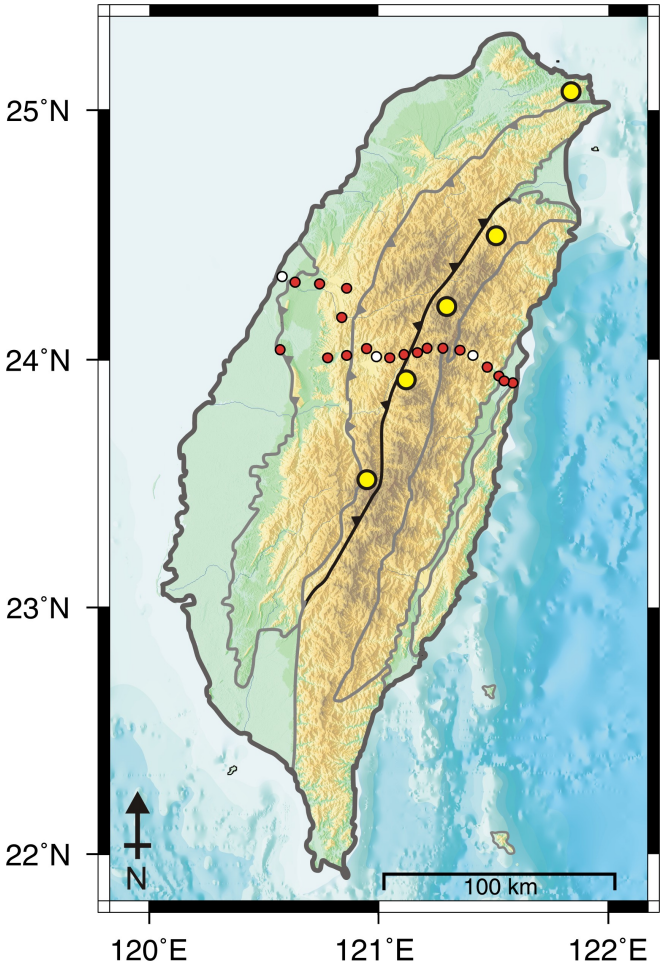

Figure 5-18. Locations of Au and Cu deposits (yellow circles, Lewis et al., 2007) adjacent the Lishan Fault (black line). NIMS data analysed in central Taiwan are shown for reference.

At the pressure-temperature conditions in the middle to lower crust, saline fluid is expected to have a resistivity of ρ_w ~0.01 – 0.05 Ωm (Nesbitt, 1993). This range of resistivity values corresponds to pore fluid salinities in the range 4 - 25% by weight, and with pressure > 3 kbar and temperatures > 250°C. The salinity of lower crustal fluid inclusions has been observed to commonly exceed 20% by weight (Aranovich and Newton, 1996; Shmulovich and Graham, 1996). Note that since no direct sampling of deep crustal fluids has been reported in central Taiwan, values are adopted that have been used to investigate similar conductive features in the middle to lower crust elsewhere (e.g. Nanga Parbat, Northern Pakistan – Park and Mackie, 2000; Southern Alps, New Zealand - Wannamaker et al., 2002; Northeast Japan – Mishina et al., 2009). Assuming a cementation factor of m = 1.5, Archie's law (Archie, 1942) requires porosity values of 1–2% to explain a bulk resistivity of 15 Ωm. Since laboratory measurements indicate little change in P-wave velocity with varying pore-fluid salinity (Jones et al., 1998), it is clear that porosity of a few percent saturated with saline fluid is consistent with both the velocity and resistivity constraints on the Lishan Fault Conductor.

While a range of pore fluid salinity consistent with the pressure-temperature conditions expected in the middle to lower crust beneath central Taiwan has been used in these calculations, it is important to note that the results are not highly sensitive to these chosen values (Figure 5-19). For example, if the estimated pore fluid salinity was 100% greater (i.e. assume an upper limit of ρ_w = 0.1 Ωm), then this value would yield a porosity of 3.5% (using m = 1.5), which is still consistent with our interpretation. In summary, the interpretation does not critically depend upon the specific value of porosity computed. Rather, the key point is that the resistivity of the LFC can be explained by low porosity values that are geologically reasonable. If saturated, the interconnected saline fluids would decrease the observed bulk electrical resistivity more than the seismic velocity and give rise to the distinct LFC domain observed in Figure 5-17.

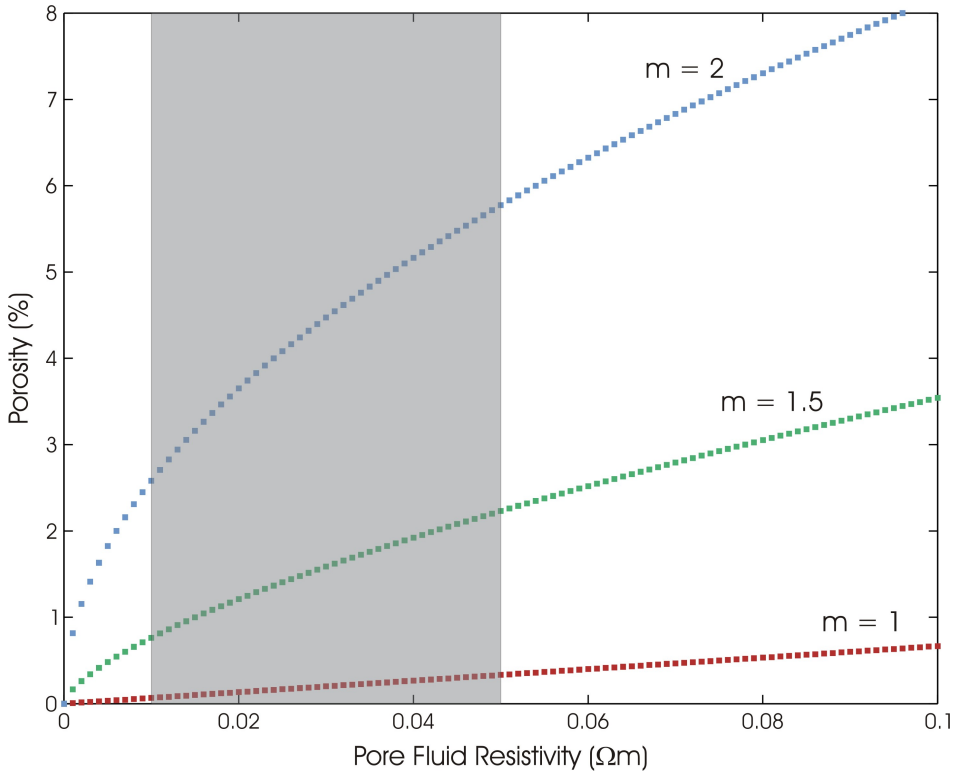

Figure 5-19. Archie's law porosity estimates. The cementation exponent (m) is labeled for each curve. The grey shaded region marks the range of pore fluid resistivity expected in the mid to lower crust beneath central Taiwan (Nesbitt, 1993). Note that calculations assumed a bulk resistivity of 15 Ωm.

5.3.4 Correlation of Resistivity and Hypocentre Locations

Seismic velocity is an intrinsic material property that is sensitive to subsurface structure, and thus lends itself to quantitative correlation with models of electrical resistivity. In contrast, earthquake hypocentres represent an earth response that is sensitive to both material properties and *in situ* conditions of deformation. Links between resistivity and seismicity have been noted in a number of previous studies (e.g. Ogawa et al., 2001; Chen et al., 2007b; Heise et al., 2007; Wannamaker et al., 2009). However, to correlate seismicity and models of electrical resistivity, two scenarios are plausible and must be considered:

1. Fluids cause weakening and control the observed deformation.
2. Deformation enhances the interconnection of fluids and controls the observed resistivity.

Studies of eastern Anatolia using both broadband and long-period MT data suggest that both scenarios are possible in different tectonic settings (Türkoğlu et al., 2009).

In Taiwan, Wu et al. (2004) have derived hypocentre locations for $M_w > 2$ events from 1993 to 2002 using the double-difference relocation method (Waldhauser and Ellsworth, 2000). From this database, events located within 20 km of a sub-vertical plane beneath the MT profile in central Taiwan, have been collapsed and projected onto the resistivity model (top panel in Figure 5-20). Immediately obvious in these hypocentre locations is a sharp decrease in seismicity below ~12 km depth. This apparent horizon reflects the inferred brittle-ductile transition zone that marks the strongest part of the crust, and thus the depth at which many earthquakes naturally occur. Therefore, events with uncertain depth estimates (a difficulty enhanced on a narrow island such as Taiwan) are pinned to this level during the relocation process. For felsic lithology, the brittle-ductile transition occurs within the temperature range 300-500 °C (Bürgmen and Dresen, 2008); the transition from microcracking to dislocation motion within dry Westerly granite occurs at 300-400 °C for quartz and 550-650 °C for feldspathic minerals (Tullis and Yund, 1977). Thus, assuming an average geothermal gradient of 30 °C/km for central Taiwan (Shyu et al., 2005), a depth of 12 km for the brittle-ductile transition is a reasonable estimate. Chen and Molnar (1983) estimate that earthquakes within the crust are generally limited by the 350 ± 100 °C isotherm. Note however, that while occurring near the depth of the inferred brittle-ductile transition, the sharp horizon observed in these relocated events is an artifact of the clustering by the double-difference algorithm. In reality, the transition from brittle to ductile rheology would not occur as a sharp discontinuity.

For comparison, the bottom panel in Figure 5-20 shows events located within 20 km of the MT profile with only the best relocation quality rating (A) by Wu et al. (2008). These hypocentres indicate a pattern where the majority of the seismicity is located within the relatively resistive regions of the MT inversion model. This

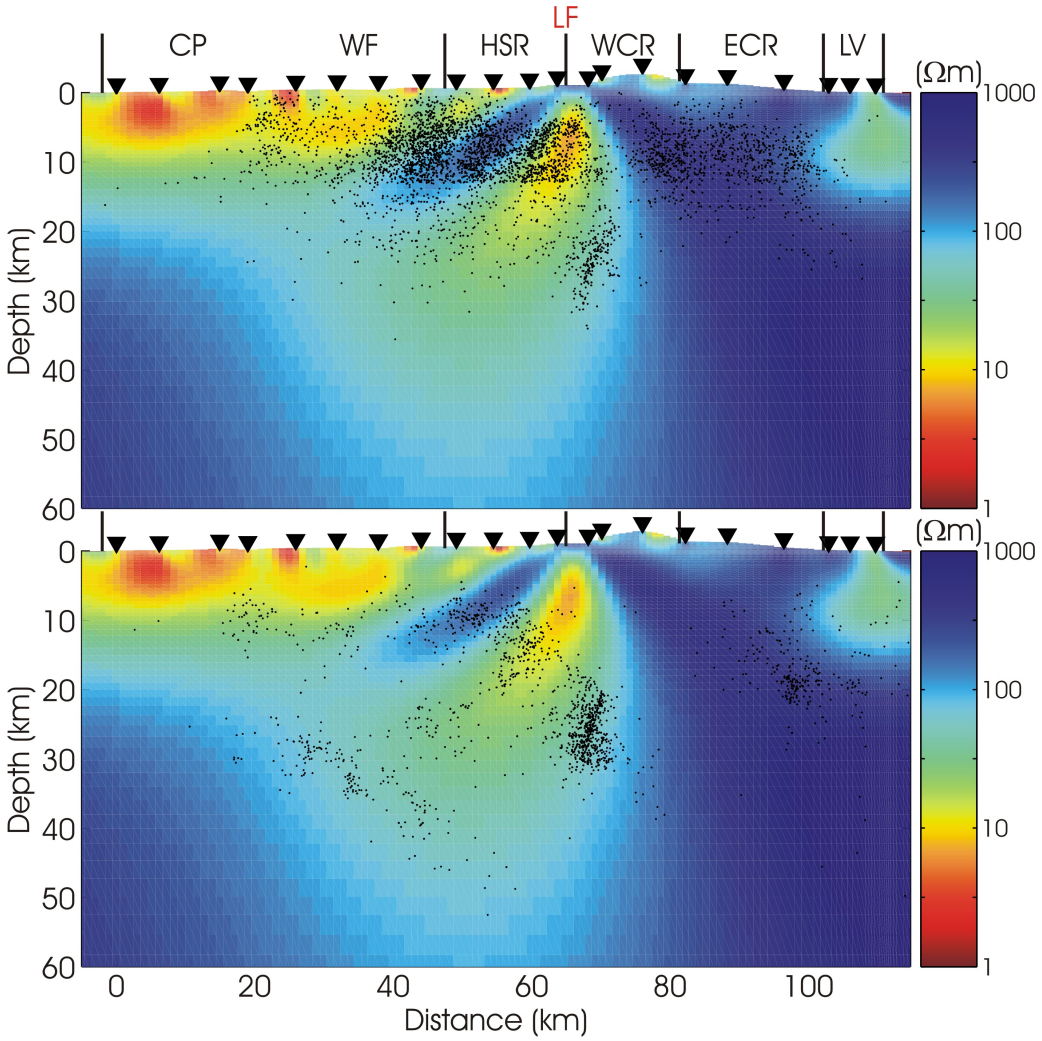

Figure 5-20. TE, TM and tipper resistivity inversion model showing hypocentres located within 20 km of the MT profile. Top Panel: Double-difference relocation by Wu et al., 2004. Bottom Panel: Relocation by Wu et al. 2008.

trend is also clear in the double-difference relocated events. However, in the relocated hypocentres of Wu et al. (2008), a zone of deep (30-50 km) events dipping to the east is shown beneath western Taiwan. These hypocentres do not appear in the double-difference relocations since the algorithm (HypoDD, Waldhauser and Ellsworth, 2000) throws out events that are too sparse and do not cluster (Francis Wu – personal communication). At these depths, it is likely that these earthquakes are occurring within the brittle olivine-rich material below the Moho. The eastward dip towards central Taiwan could result from crustal thickening beneath the Central Ranges and further support the thick-skinned tectonic model.

In both relocations, reduced seismicity in the lower crust and upper mantle is observed beneath the Central Ranges in comparison to western Taiwan. The fewer events at depth beneath the Central Ranges may reflect an increased geothermal gradient in this region. If the geotherm was as high as 50 °C/km, lower crustal and upper mantle seismicity would be suppressed (Wu et al., 1997). Although plagued by uncertainty, the heat flow data across Taiwan do show elevated values beneath the Central Ranges that support this interpretation (Lee and Cheng, 1986).

In a number of MT studies, it has been observed that seismicity occurs at the perimeters of conductors interpreted as zones of fluids (e.g. Wannamaker et al., 2009). For central Taiwan, the overall pattern of seismicity follows this trend; however, a significant number of events overlap the LFC (Figure 5-20) due to the reduced resolution of the large-scale correlation shown. For example, by collapsing seismicity located within 20 km of the MT profile, events occurring on linear structures misaligned to the geoelectric strike will be spatially broadened upon projection to the MT model. In addition, the long-period MT data with a nominal spacing of 5 km cannot resolve near-surface structure as well as tightly spaced broadband measurements (e.g. Unsworth and Bedrosian, 2004; Wannamaker et al., 2009) and correlation cannot be expected to be as compelling.

Despite these effects, of particular interest in central Taiwan is a cluster of deep (20–30 km) seismicity that flanks the eastern edge of the LFC. These events occurred after the Chi-Chi earthquake and focal mechanism solutions suggest that they are associated with a thrust fault[1], with the Central Ranges on the footwall side (Wu et al., 2004). Gourley et al. (2007) have recognized this and other evidence for deep vertical faults within the Central Ranges that would contribute to building a crustal root in a thick-skinned tectonic regime. The high-angle of these epicenters delineate a steeply dipping fault, far from the angle predicted for

[1]A thrust fault with dip >45° is more correctly referred to as a reverse fault, but discussed here as a high-angle thrust fault for clarity.

failure under dry conditions due to maximum horizontal compressive stress (i.e. 30°; Anderson, 1905). Thus, the steep dip and the location adjacent the fluid-based LFC suggests that this fault may act as a conduit for fluid migration toward the surface.

5.4 Summary – Central Taiwan

Both 2-D and 3-D resistivity models of the first long-period MT data collected in central Taiwan reveal a major conductor located beneath the Lishan Fault that extends from the near surface to beyond 10 km depth. The shallow décollement predicted by the thin-skinned tectonic model is consistent with these MT data in western Taiwan, but not with the Lishan Fault Conductor in central Taiwan. Quantitative correlation between the resistivity and a tomographic velocity model indicate aqueous fluids with 1–2% porosity can account for the Lishan Fault Conductor. The thick-skinned lithospheric deformation model is consistent with these observations, with the fluids being produced in the lower crust by prograde metamorphism.

6 INVESTIGATION OF THE YOUNG TAIWAN OROGEN: ANALYSIS OF THE SOUTHERN TAIGER MT DATA

The arc-continent collision in Taiwan has formed a mature orogen in the north where the collision initiated in the late Miocene (Hall, 1997; Byrne and Liu, 2002). However, since the Luzon Volcanic Arc is oblique to the passive margin of Eurasia, the ongoing plate convergence has resulted in a propagating collision that becomes progressively younger to the south. The rate of propagation is estimated at ~60 km/Myr and will eventually close the South China Sea (Tillman and Byrne, 2002). The oblique collision makes it possible to investigate the temporal evolution of the orogen through studies at different latitudes along the island-axis. The TAIGER project took advantage of this opportunity by collecting MT data on linear profiles across southern, central and northern Taiwan. This chapter contains the analysis and interpretation of the long-period MT data collected on a linear profile across southern Taiwan (~23.25°N lattitude). The resistivity model obtained by inverting these data is compared to that obtained from the central Taiwan MT data to investigate along-strike orogen variation. These two parallel profiles are separated by a distance of 105 km along the orogen axis. Using the concept of uniformitarianism (Lyell, 1830), the southern MT profile can be interpreted as a snapshot of central Taiwan ~1.75 Myr before present. Thus, comparison between models of central and southern Taiwan can provide insight on the evolution of the arc-continent collision and associated orogeny.

6.1 MT Data: Collection and Analysis

In total, 14 long-period MT measurements were made on a linear profile across southern Taiwan (Figure 6-1). In general, these stations recorded high-quality MT

data (Appendix A-4) and show a consistent 2-D geoelectric strike direction that is parallel to the orogen structure and coast (Figures 4-8, 4-10 and 4-11). Further, the real induction vector components align perpendicular to the strike azimuths (Figure 4-9), indicating overall 2-D behaviour. However, 3-D effects are expected as these MT data were collected in an area of complex geology that clearly varies along the orogen axis. Specifically, these MT data were located close to the southern extremes of the WF, HSR, LV and CR provinces (Figure 6-1). In addition, this profile crosses the orogen near to where the island tapers towards its southern tip and the surrounding seawater depth is highly variable.

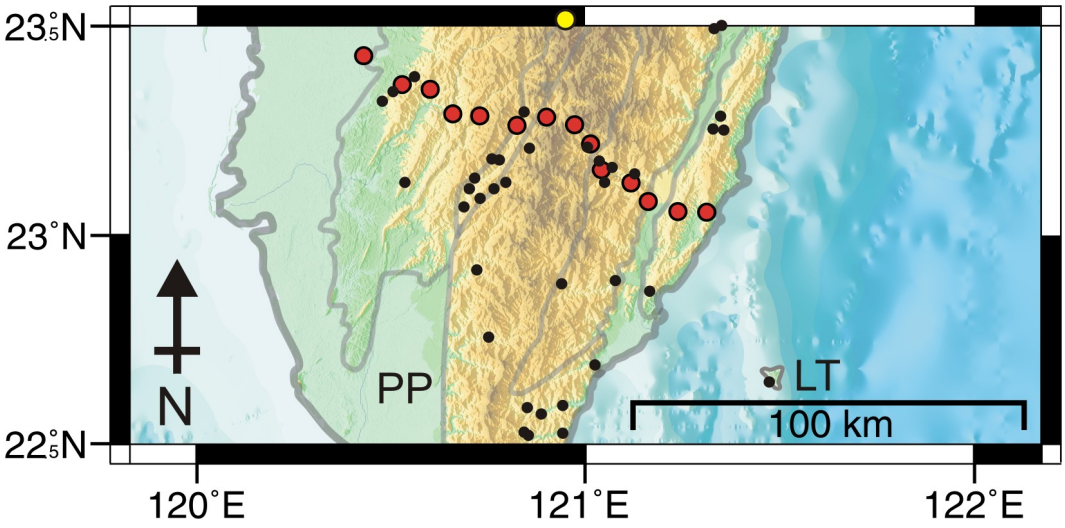

Figure 6-1. Long-period MT stations (red circles) in southern Taiwan. Yellow circle locates an Au-Cu deposit adjacent the Lishan Fault (Lewis et al., 2007). Black dots indicate hot spring locations.

6.1.1 3-D Induction Effects: Out-of-Quadrant Phase

As expected, some of the MT data measured in southern Taiwan display significant 3-D induction effects. In particular, the 6 westernmost MT stations recorded anomalous TM mode phase values that increase with period and exceed 90° (Appendix A-4a). Phase values that exceed 90° are termed out-of-quadrant and cannot be explained by a 2-D resistivity model (Ichihara and Mogi, 2009). The inclusion of out-of-quadrant phase data in conventional 2-D inversion modeling can result in artificial conductive features due to the inability of a 2-D

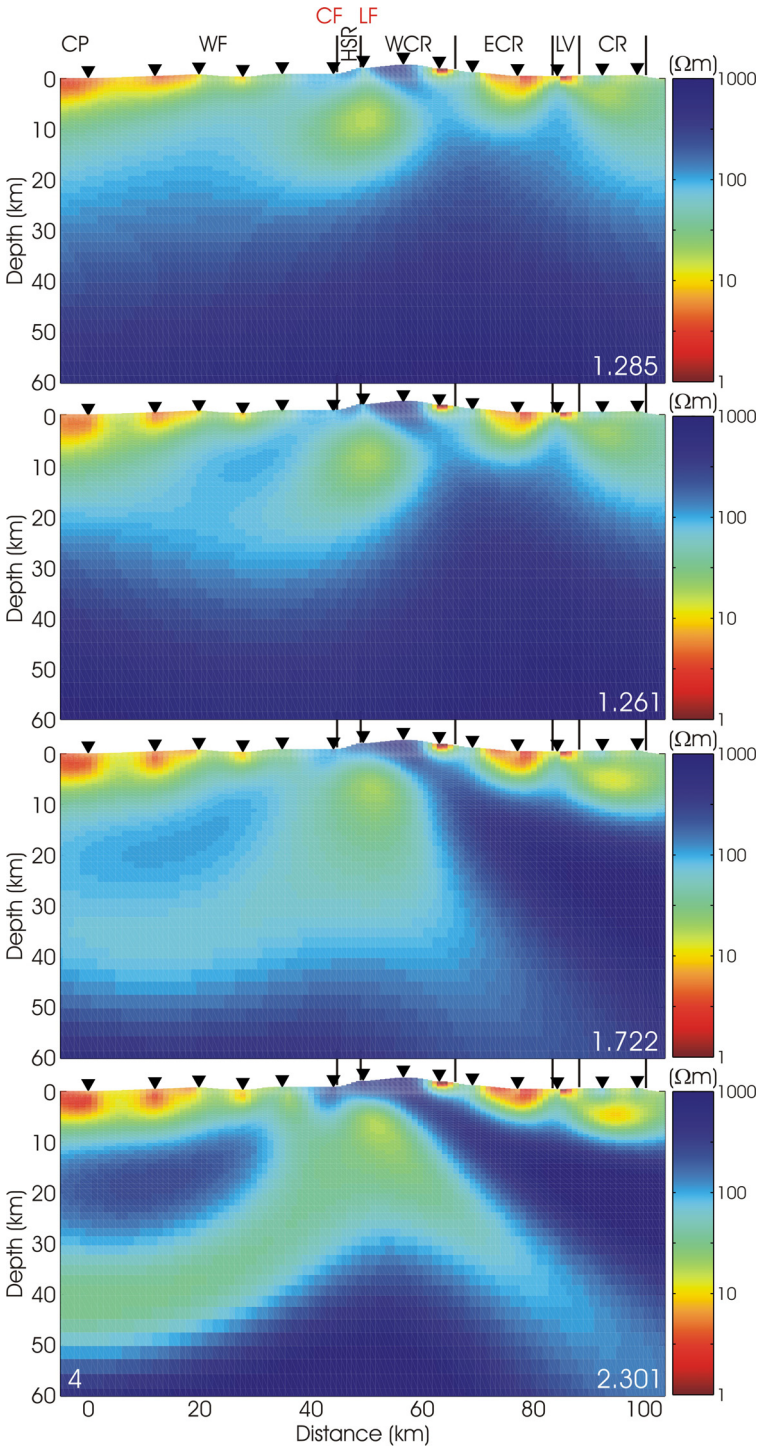

Figure 6-2. 2-D TETMHZ inversion models of southern Taiwan including different period bands of the TM mode data. Top Panel: No TM mode data at the 6 westernmost sites. Second Panel: TM mode data included for periods 10-100 s. Third Panel: TM mode data included for periods 10-1000 s. Bottom Panel: TM mode data included for periods 10-10000 s. All inversions used error floors of 20% and 7.5% for the apparent resistivity and phase, and smoothing values $\alpha = 3$ and $\tau = 3$. R.M.S. data misfit is shown in the bottom right corner of each model.

algorithm to explain these 3-D data (Chiang et al., 2009). For example, Figure 6-2 shows 2-D inversion models of the southern Taiwan MT data that include various period bands of the TM mode data at the 6 westernmost stations. When rotated to geoelectric strike (N30°E – see section 6.2.2), the TM mode apparent resistivity data decrease rapidly at periods greater than 100 s, and the phase exceeds 90°, which is an indication of 3-D behaviour.

The inversion models in Figure 6-2 reveal that the inclusion of the TM mode data at periods greater than 100 s for the 6 westernmost sites (3 and 4 in Figure 6-2) results in a resistivity model that varies significantly compared to that obtained with no TM mode data included at these stations (1 in Figure 6-2). In addition, the r.m.s. data misfit increases considerably and indicates that the 2-D inversion algorithm cannot fit these out-of-quadrant TM mode phase data. In contrast, inclusion of the TM mode data at periods within the range 10–100 s (2 in Figure 6-2) results in a similar model to that obtained with no TM mode data. This similarity indicates that data within this period band can be considered 2-D. Thus, the analysis of these long-period MT data collected in southern Taiwan excluded the TM mode data at periods greater than 100 s for the 6 westernmost stations.

6.1.2 MT Data Dimensionality

After removal of the anomalous TM mode phase data at stations in western Taiwan, the dimensionality and best-fitting geoelectric strike direction were investigated. The tensor decomposition method (McNiece and Jones, 2001) reveal a consistent geoelectric strike direction of N30°E that is parallel to the major geological boundaries in southern Taiwan and the island coast (Figure 6-3). The low r.m.s. misfit values reveal that this estimate is well constrained, despite high values of the shear and twist distortion parameters observed at several sites and periods (Figure 6-4). However, the alpha-beta azimuths from the phase tensor analysis indicate that the greatest inductive response occurs with much greater variation along an average angle of N75°E. Further, the induction vectors align

consistently to N140°E that indicates a strike-perpendicular direction of N50°E. The discrepancy between these estimates of the geoelectric strike can be explained by 3-D distortion effects that are handled differently by these methods. For example, the parameter beta which indicates 3-D effects is inherently set to zero in the tensor decomposition method that seeks to find the best-fitting strike direction for an assumed 2-D earth. However, the high values (i.e. > 30°) of the shear and twist distortion parameters reveal the presence of significant 3-D distortion in the tensor decomposition method. While independent of electric field distortion, the induction vectors are strongly influenced by the coast effect.

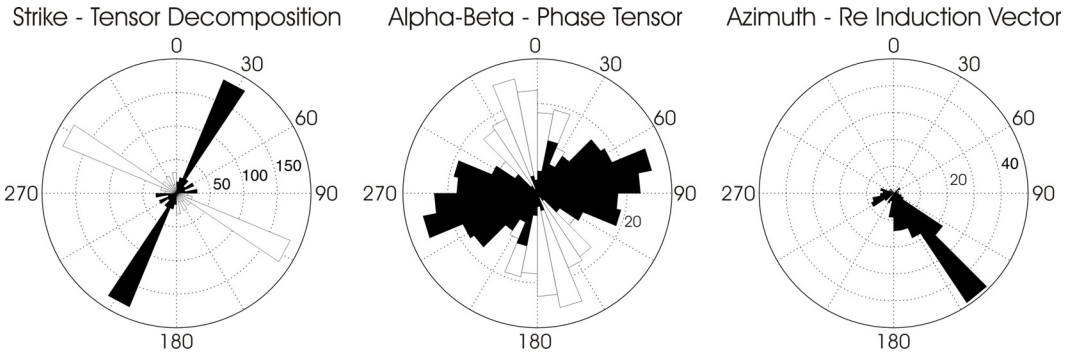

Figure 6-3. Rose diagrams showing results of dimensionality analysis. Results include MT data for the period range 10-10000 s and show variability between estimates of the geoelectric strike direction for the MT data in southern Taiwan.

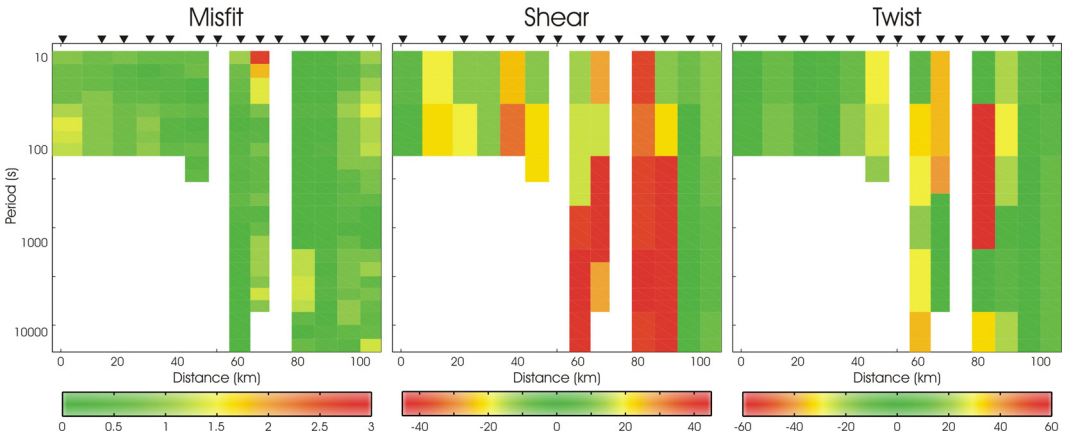

Figure 6-4. Results from tensor decomposition. The low r.m.s. misfit values indicate that the 2-D strike is well constrained. Values of the shear and twist angles greater than ~30° indicate strong galvanic distortion. White areas indicate where electric field data were excluded due to noise and/or strong distortion.

Despite evidence for 3-D effects in these MT data, underlying 2-D behaviour persists. The induction vectors are dominantly perpendicular to the geoelectric strike estimates, and the tensor decomposition algorithm gave a strike direction that is well constrained and parallels both the coast and structure of the orogen. Thus, a geoelectric strike direction of N30°E was chosen for 2-D analysis of these MT data.

6.1.3 MT Data Observations

Given significant indications for 3-D electrical structure in southern Taiwan, inspection of the raw MT data is essential to ensure that conductors/resistors present in 2-D inversion models are associated with features observed in the measured data. Pseudosections of the TE and TM mode phase data and of the ϕ_2 invariant quantity of the phase tensor are shown for the southern MT profile in Figure 6-5. Note that Figure 6-5 shows these MT data after rotation to the geoelectric strike coordinate frame (N30°E). These parameters are all sensitive to the vertical resistivity gradient; values greater than 45° indicate decreasing resistivity with depth, and vice versa.

At long-periods beneath the Lishan Fault, TM mode phase values greater than 45° indicate the presence of a conductor. These high phase values are not observed in the MT data measured to the east of this fault and indicate a significant change in the electrical structure at this location. A similar feature was observed in the TM mode phase data across the LF in the central Taiwan MT data (Figure 5-6). In addition, comparison of the ϕ_2 and TE mode phase data to the central Taiwan measurements show similar patterns exist in these southern measurements. However, while similarity is evident, the magnitude of the high phase values (i.e. > 45°) is lower in the southern MT data in comparison to central Taiwan. These observations indicate that similar resistivity structure is imaged beneath central and southern Taiwan, but suggests that a lower conductance occurs in the south.

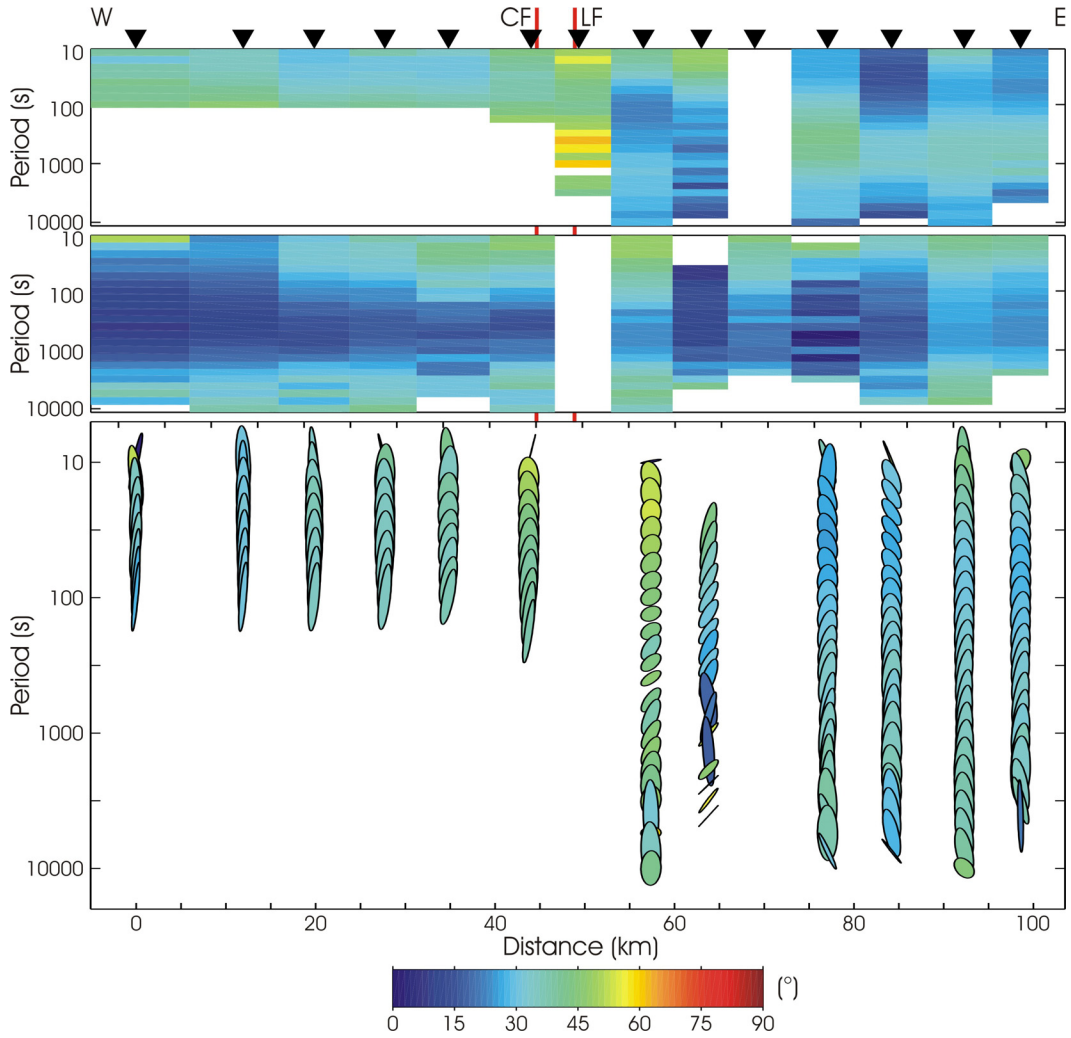

Figure 6-5. Pseudosections of long-period MT phase data in southern Taiwan. Top Panel: TM mode phase. Middle Panel: TE mode phase. Bottom Panel: MT phase tensor invariant ϕ_2. White areas indicate where data has been masked in the following 2-D inversion modeling due to high levels of noise and/or severe distortion. Since ϕ_2 represents an average, results are not shown where either the TM or TE mode phase has been masked. Profiles are oriented perpendicular to the geoelectric strike (N30°E). Faults are: Chuchih Fault CF and Lishan Fault LF.

Due to the removal of the out-of-quadrant TM mode phase data in southwestern Taiwan, and poor-quality TE mode data at station TGR455 recorded nearest to the Lishan Fault (Appendix A4-a), fewer MT impedance data are available in southern Taiwan compared to central Taiwan. However, all stations recorded excellent quality magnetic fields data, and induction vector plots are therefore useful to reveal structural trends in a continuous pattern at all sites and periods.

Figure 6-6 shows the strike-perpendicular components of the real induction vectors plotted at increasing period bands in southern Taiwan. These vectors are sensitive to lateral variations in conductivity and point towards conductors in the Parkinson plotting convention used. A reversal of the induction vector arrows occurs across the Chuchih and Lishan Faults in southern Taiwan, and indicates the presence of a conductor beneath this location (see Figure 3-4). These consistent high-quality magnetic fields data support evidence for a conductor observed in the spatially sparse impedance phase data (Figure 6-5).

6.1.4 2-D Inversion of MT Data

Smooth 2-D resistivity models of the southern Taiwan MT data were generated using the NLCG6 inversion algorithm of Rodi and Mackie (2001). An identical processing sequence was used for both the central (Chapter 5) and the southern MT data presented in this chapter. For example, error floors of 20%, 7.5% and 0.03 were used for the apparent resistivity, phase and tipper data, respectively. In addition, inversion models included the topography and bathymetry along profile and solved in an automated procedure for the static shift coefficients during late-stage iterations. Although not shown, inversion models of southern Taiwan included MT and tipper data measured at the remote reference station on the Penghu archipelago, since this station is located along profile with the southern Taiwan island measurements (Figure 4-2).

As discussed, the southern MT data show some 3-D induction effects and 2-D MT inversion modeling must be applied with caution. Therefore, numerous inversion models were generated for a wide range of control parameters, starting models, error floors and various subsets of these data to ensure that model features are robust (Figure 6-7). The consistent resistivity models resulting from these inversions reveal that the significant resistivity features observed are independent of the choice of regularization parameters (1-6 in Figure 6-7) and starting model resistivity (7-8 in Figure 6-7). Further, as tested in central Taiwan, down-

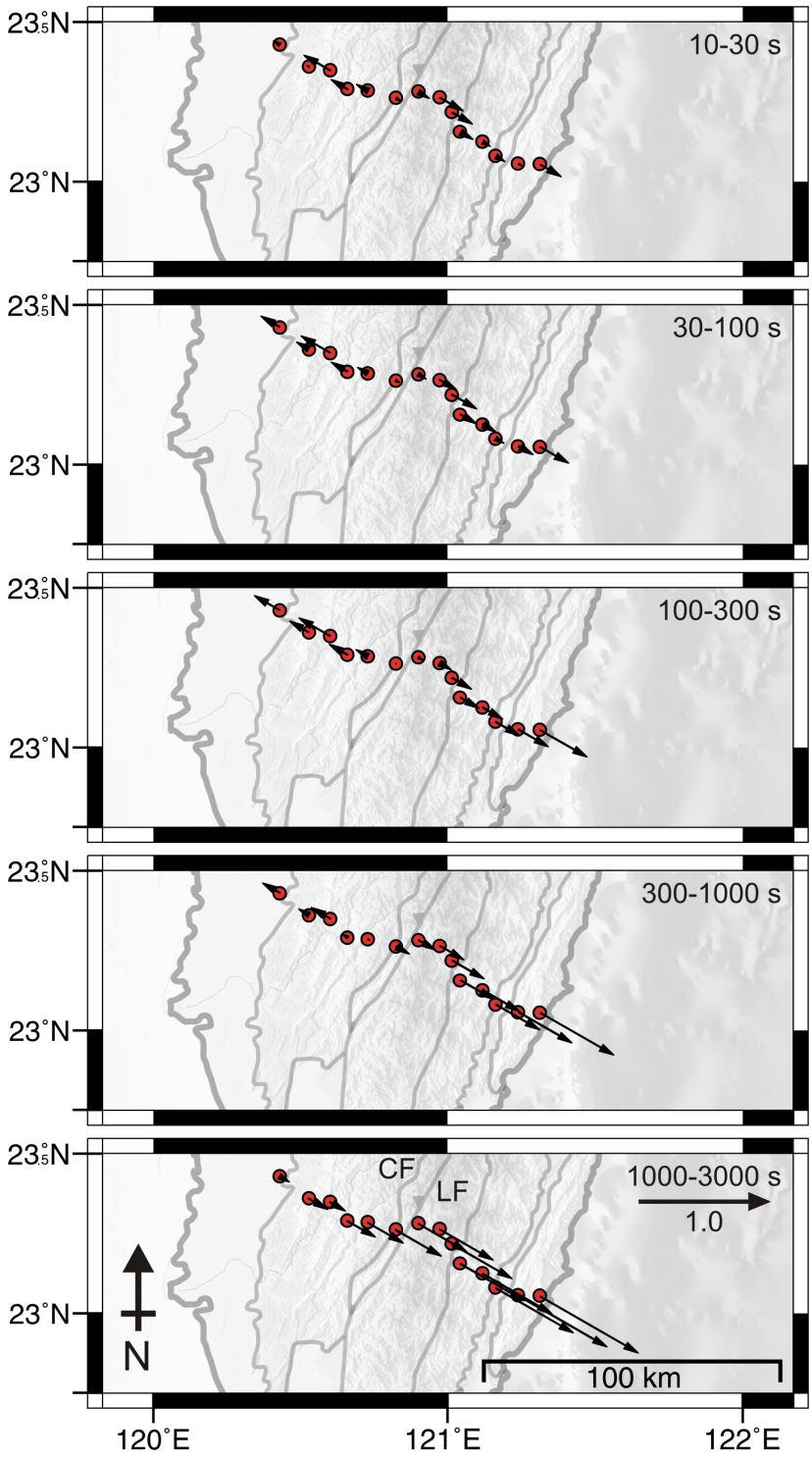

Figure 6-6. Strike-perpendicular components of the real induction vectors averaged over the labeled period decades (Parkinson convention). Scale arrow of magnitude 1.0 is shown. Rotation of the vectors occurs at short periods across the Chuchih and Lishan Faults, locating a conductor in the upper to middle crust. At long periods (1000-3000 s) the induction vectors are influenced by the coast effect from conductive seawater in the deep Philippine Sea offshore eastern Taiwan.

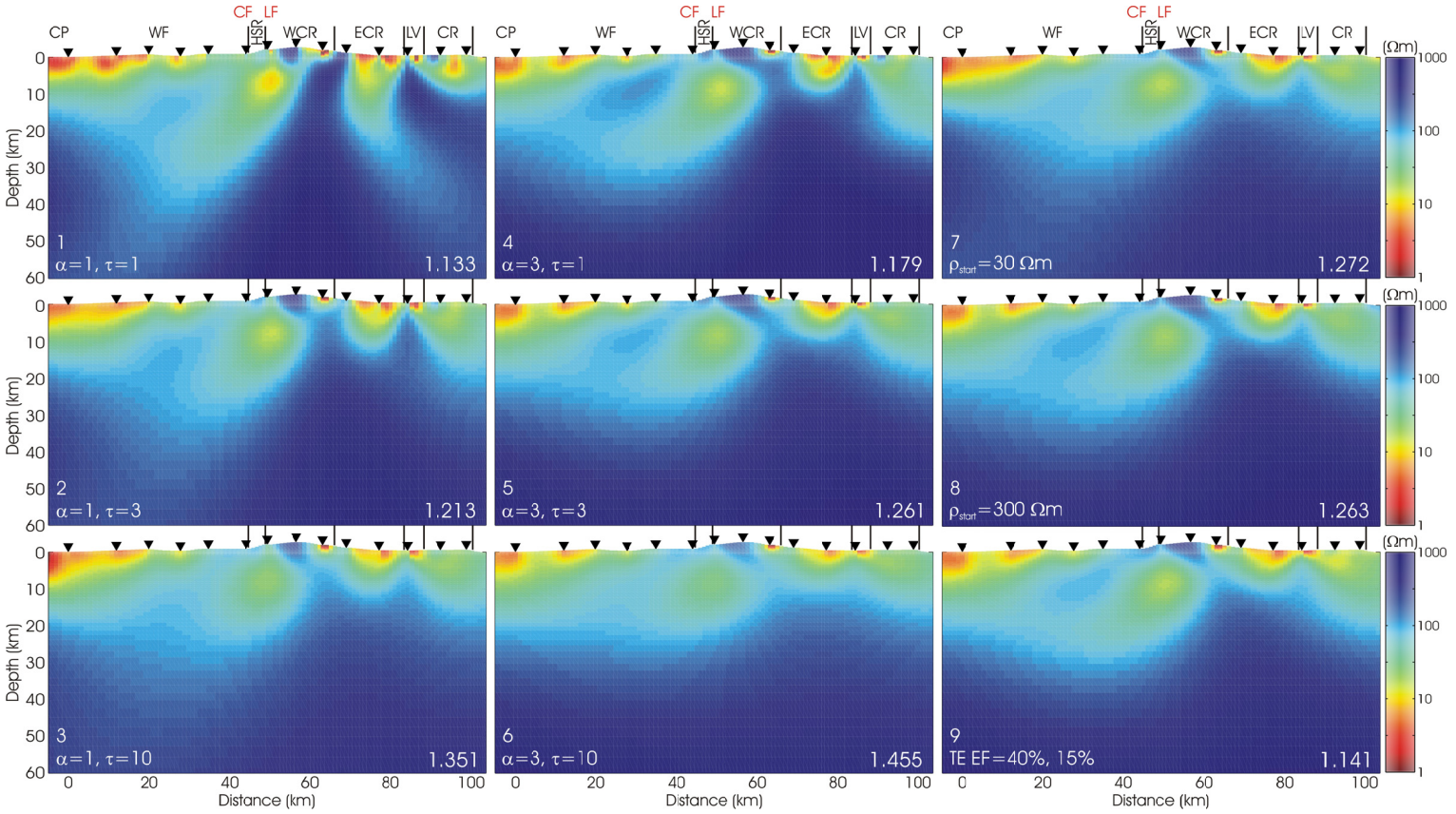

Figure 6-7. 2-D TETMHZ inversion models of southern Taiwan. Inversions solved for the smoothest variations away from an *a priori* starting model that included the Philippine Sea and Taiwan Strait. Models 1-6 and 9 used 100 Ωm as the starting subsurface resistivity. Models 7-9 used smoothing parameters $\alpha = 3$ and $\tau = 3$. Error floors of 20% and 7.5% for the resistivity and phase were used for models 1-8. An absolute error floor of 0.03 was used for the tipper data in all inversion models. R.M.S. data misfit is shown in the bottom right corner of each model.

weighting the TE mode data by doubling the error floors in comparison to the TM mode values does not significantly reduce the r.m.s. misfit value or change the observed model structures (9 in Figure 6-7). This result permits inclusion of the TE mode data, which is most sensitive to off-profile (3-D) structure (Wannamaker et al., 2002).

Note that the consistency of the resistivity structures in the inversion models of Figure 6-7 strongly indicates dominant underlying 2-D behaviour of the MT data in southern Taiwan, after exclusion of the out-of-quadrant TM mode phases. The variability in model structure observed in Figure 6-2 for models including out-of-quadrant phase data is not observed in Figure 6-7. In addition, observation of the raw impedance phase and tipper data supports the significant conductive feature imaged beneath the Chuchih and Lishan Faults.

To choose the optimum 2-D inversion model, a trade-off curve (i.e. L-curve) was generated (Figure 6-8). By plotting roughness against r.m.s. data misfit for models with a range of smoothing parameters, the ideal model can be determined. The location of maximum curvature on an L-curve balances the opposing requirements for a spatially smooth model that honours the measured data by achieving an acceptably low data misfit (Hansen et al., 1992). To emphasize lateral continuity, and to permit a consistent comparison to the central Taiwan model, inversions used a horizontal smoothing factor of $\alpha = 3$. Inspection of the L-curve in Figure 6-8 reveals that the maximum curvature occurs for $\tau = 3$.

The final 2-D inversion model of the MT impedances and induction vector data in southern Taiwan is shown in Figure 6-9. After exclusion of MT data that showed a high level of noise and/or severe distortion, this model fit the observations to within an acceptable r.m.s. data misfit of 1.261. Pseudosections showing the measured MT data and inversion model responses (Figure 6-10) indicate good agreement and support the resistivity structures observed in the inversion model.

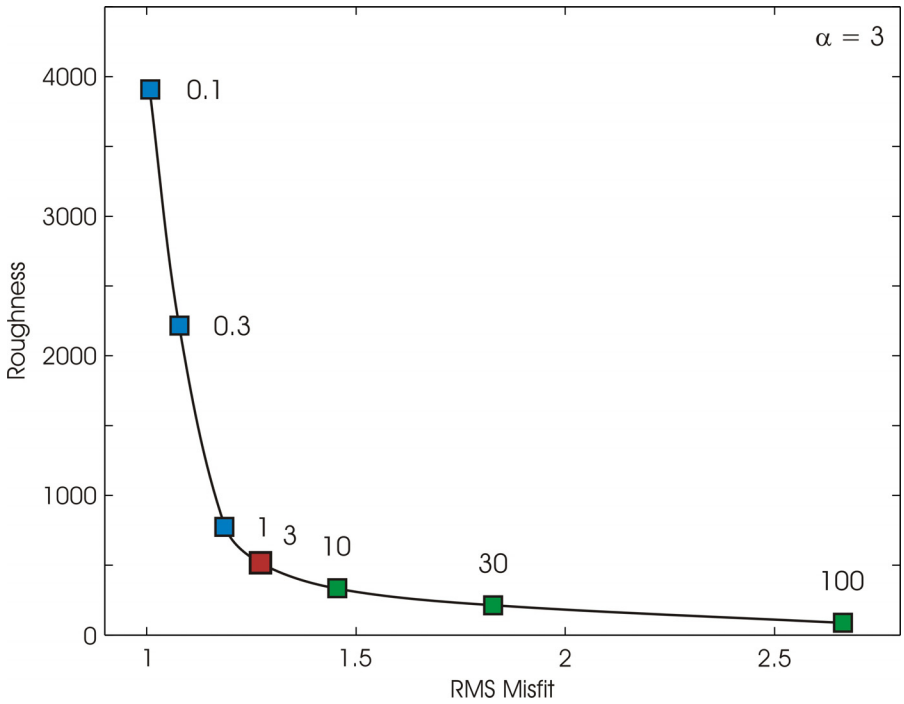

Figure 6-8. L-curve for 2-D TETMHZ inversion models of southern Taiwan. τ for each model is shown, all models used α = 3. The maximum curvature occurs at τ = 3, and balances the tradeoff between data fit (decreasing misfit – blue squares) and obtaining a smooth model (decreasing roughness – green squares).

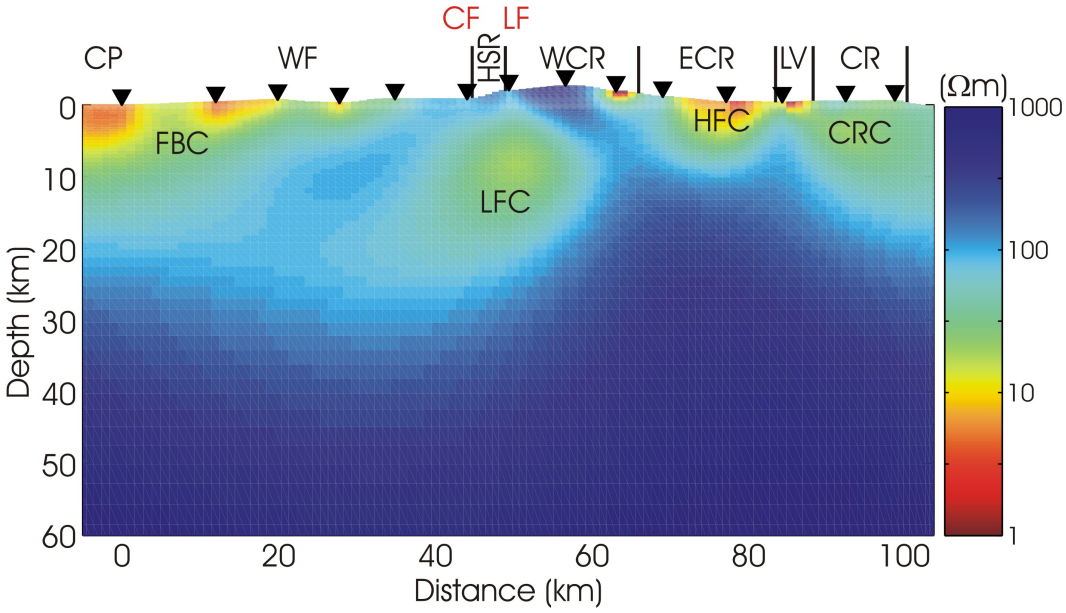

Figure 6-9. TE, TM and tipper, 2-D MT resistivity inversion model of southern Taiwan. Model conductors: FBC – Foreland Basin Conductor; LFC – Lishan Fault Conductor; HFC – Hydrothermal Fluids Conductor; CRC – Coastal Range Conductor. Abbreviations above the model indicate the geological provinces (black), the Chuchih Fault CF and the Lishan Fault LF (red).

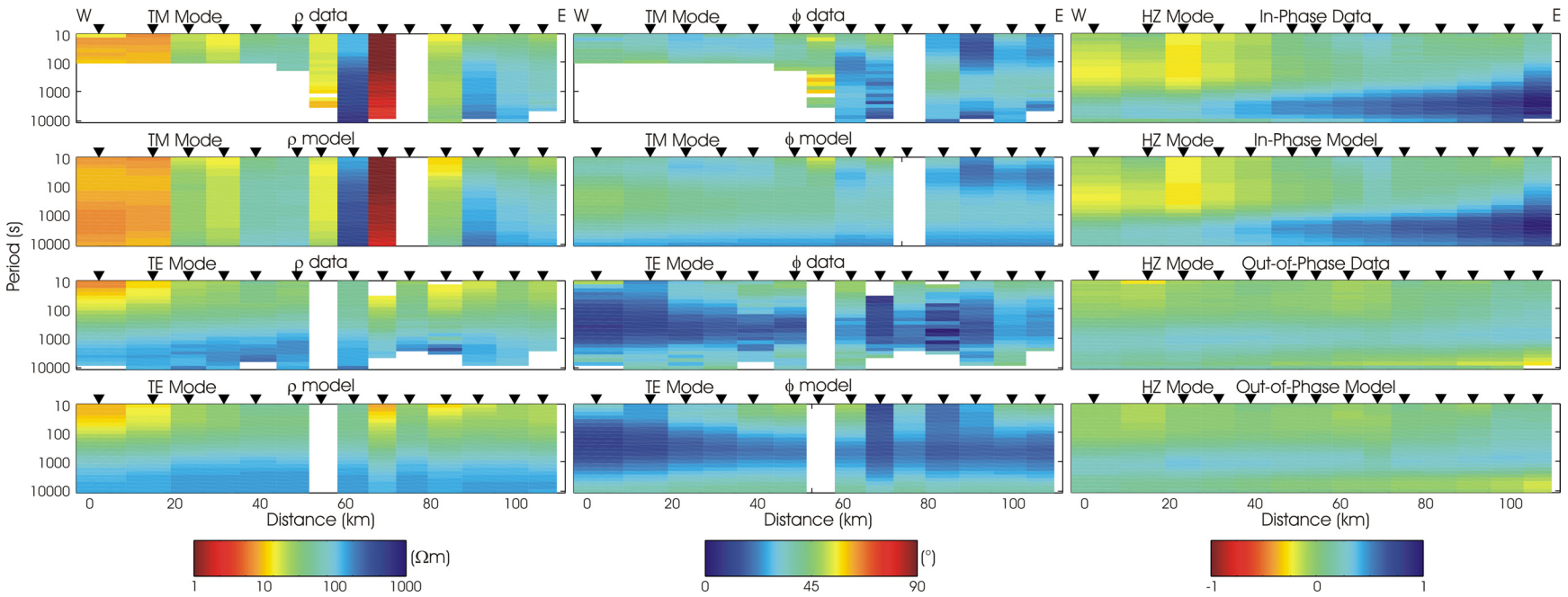

Figure 6-10. Pseudosections of long-period MT data 2-D modeled in southern Taiwan. The left and middle panels display the measured and modeled resistivity and phase data for the TM (Transverse Magnetic) and TE (Transverse Electric) modes. The right panel shows the measured and modeled in-phase (real) and out-of-phase (imaginary) tipper data. White regions indicate data that were excluded from the 2-D inversion modeling because of high levels of noise and/or severe distortion.

Of interest, the effect of the conductive Philippine Sea is observed to decrease the in-phase tipper components at progressively shorter periods at stations collected nearer the east coast of Taiwan. This same phenomenon was observed in the tipper pseudosections of central Taiwan (Figure 5-11). However, large amplitude (i.e. > 0.5) tipper anomalies do not extend west of the Lishan Fault (~45 km from the east coast) in central Taiwan. This reduction in magnitude could be caused by vertical current channeling within the Lishan Fault Conductor in central Taiwan, enhancing the dissipation of electric currents to depth (Park et al., 1991). In contrast, in southern Taiwan large amplitude tipper anomalies extend west of the Lishan Fault to a distance ~65 km from the east coast. This greater extent of the coast effect could be due to a reduction in the conductivity and depth extent of the Lishan Fault Conductor in southern Taiwan. Note that TM mode phase values greater than 45° measured beneath the Lishan Fault are lower in southern Taiwan.

6.2.6 3-D Inversion of MT Data

Strong evidence has been shown that indicates features present in the 2-D inversion model of southern Taiwan are robust. However, the discrepancy in the geoelectric strike results between the tensor decomposition and phase tensor methods (Figure 6-3), and the high values of the shear and twist distortion parameters at some sites and periods (Figure 6-4) reveal that 3-D induction effects are present in these MT data. Therefore, to ultimately ensure that features observed in the 2-D resistivity model are robust, comparison with a 3-D inversion model generated from these same MT data is required.

The full MT impedance tensor data recorded at stations in southern Taiwan were inverted using the 3-D code WSINV3DMT (Siripunvaraporn et al., 2005). Identical to the procedure used in central Taiwan, error floors of 20% and 10% were used for the diagonal and off-diagonal impedance tensor elements, respectively. After 34 days of CPU time, 4 iterations were completed giving a model r.m.s. misfit of 3.222. A 2-D cross-section from this 3-D model that is

oriented perpendicular to N30°E is shown in Figure 6-11. Clearly, very similar resistivity structures appear in Figure 6-11 in comparison to the 2-D model (Figure 6-9). In addition, the key observation that the Lishan Fault Conductor has a reduced conductance in southern Taiwan is evident in comparison of the 3-D models in Figure 5-12 (central Taiwan) and Figure 6-11 (southern Taiwan).

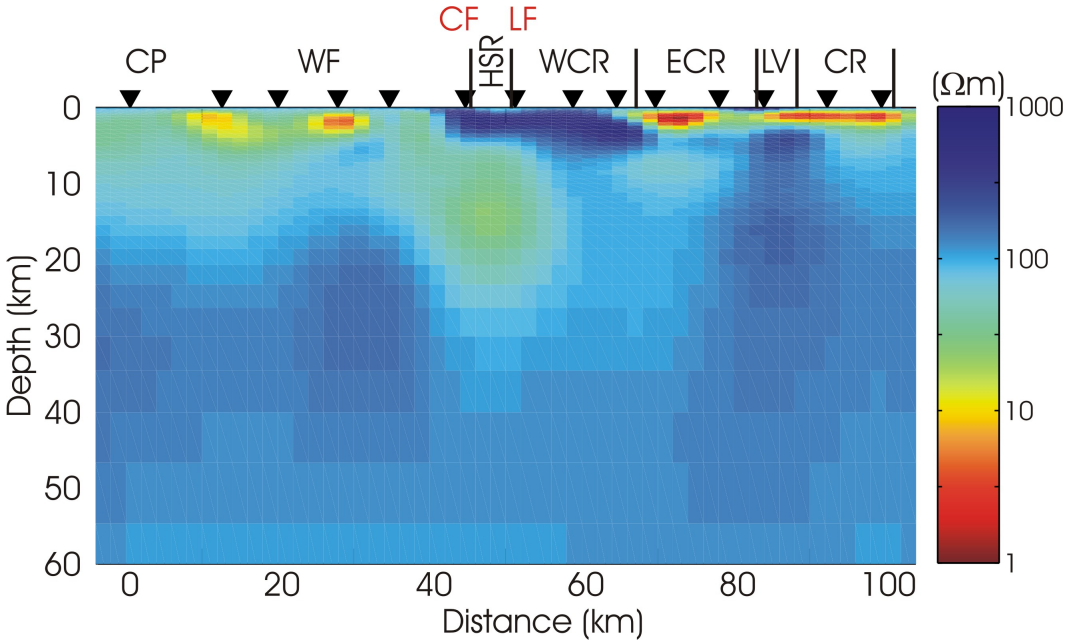

Figure 6-11. 3-D inversion model of the full MT impedance data in southern Taiwan. The r.m.s. data misfit is 3.222 after 4 iterations and 34 days of CPU time.

The similarity between the resistivity features observed in the 2-D (Figure 6-9) and the 3-D (Figure 6-11) inversion models confirms that a 2-D interpretation of the southern TAIGER MT data is valid. The 3-D model is not used for detailed interpretation in the following sections since it is generated on a coarse mesh, resulting in lower resolution in comparison to the 2-D model.

6.2 Interpretation

6.2.1 Resistivity Model Interpretation

Beneath the Coastal Plain and Western Foothills a conductive anomaly occurs in the upper 10 km (FBC in Figure 6-9). This conductor is inferred to be due to

saturated porosity in the sandstones and shales that comprise these geological provinces. In comparison to central Taiwan, the FBC appears thinner in the south, consistent with a thinner sedimentary sequence at this latitude due to these stations being located above the Peikang basement high (Figure 2-2). The Peikang high is comprised of strong pre-Tertiary Eurasian continental lithosphere that resists deformation (Lacombe et al., 2001). This rigid indenter causes the prominent reentrant in the Coastal Plain that leads to increased shortening and the maximum elevation recorded in Taiwan (Yushan – 3952 m; Byrne et al., 2005). In central Taiwan, the MT data collection traversed the deep sediments in the Taichung basin. However, the base of a conductive feature is not well resolved by MT inversion models and this correlation, despite its consistency with the local geology should not be taken too seriously. In contrast, the depth to the top of a conductor is well resolved by MT data, and despite limited lateral resolution (due to the removal of much of the TM mode data in western Taiwan), this model does not support underthrusting of the WF beneath the resistive slates of the Hseuhshan range. As was the case in central Taiwan, a steep contact between these provinces favours deformation by reactivation of a pre-existing structure, possibly a rift-related normal fault (Gourley et al., 2007).

In eastern Taiwan, a near-surface conductor occurs beneath the Coastal Range province (CRC in Figure 6-9). This conductor may be related to fluid filled fractures within the remnant forearc and volcanic arc materials that have been greatly deformed within the Coastal Range. This interpretation is consistent with a zone of high v_p/v_s observed beneath the CR (Wu Y.M. et al., 2007). However, constraints from the MT data on this feature are poor, owing to its location at the end of the profile and adjacent the conductive Philippine Sea.

Beneath the Eastern Central Range a near surface conductor exists (HFC in Figure 6-9) that has been proposed to be due to the circulation of hydrothermal fluids within fractures associated with the Central Range Fault (Chiang et al., 2009). Several hot springs are located in the Eastern Central Range (e.g. Wulu Hot

Springs) directly above this conductive feature (Figure 6-1), and support this interpretation.

Of particular interest is the region of enhanced conductivity that occurs in the mid-crust beneath the Lishan Fault (LFC in Figure 6-9). As discussed for central Taiwan, a distributed zone of saline fluids is the most likely cause of this low resistivity zone.

The resistivity model obtained for the southern Taiwan MT data shows strong similarity in the imaged structures compared to the model of central Taiwan (Figure 6-12). Namely, low resistivity occurs in the foreland basin, the Central Ranges are resistive and a conductor occurs beneath the Lishan Fault in the upper to middle crust. Given this similarity, it is reasonable to propose that the same style of tectonics (i.e. thick-skinned lithospheric deformation) also occurs in southern Taiwan. However, two key elements of the Lishan Fault Conductor were rigorously tested in central Taiwan to provide strong evidence for the thick-skinned tectonic model. These key points include:

1. Quantitative correlation of the resistivity model with a tomographic P-wave velocity model showed that a few percent saline aqueous fluids could explain the observed conductivity of the LFC.
2. Constrained inversions were computed with a resistive basement fixed at depths of 10, 20 and 30 km. Observation of (a) the tipper anomaly at sites adjacent the Lishan Fault, (b) the integrated conductivity (conductance) beneath the profile, and (c) the reduction in r.m.s. misfit for these constrained inversions, were used to show that the LFC extended beyond a depth of 10 km; the inferred level of the thin-skinned décollement in central Taiwan (Carena et al., 2002).

Therefore, this same procedure is required to test whether quantitative evidence to support the thick-skinned lithospheric deformation model exists in these southern MT data.

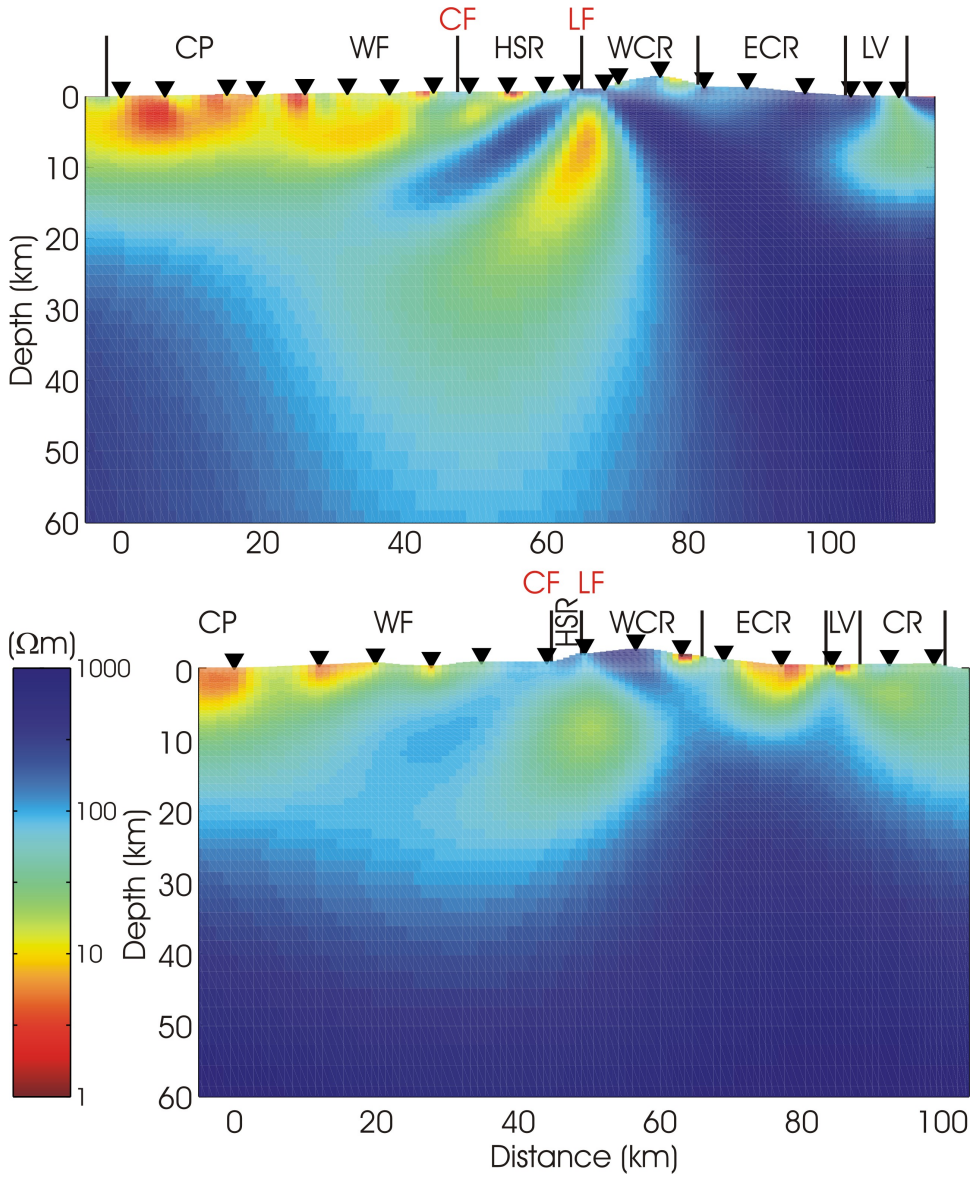

Figure 6-12. 2-D TETMHZ resistivity models of MT data collected in central Taiwan (Top Panel) and southern Taiwan (Bottom Panel). Models used error floors of 20%, 7.5% and 0.03 for the apparent resistivity, phase and tipper data, respectively. Smoothing parameters of $\alpha = 3$ and $\tau = 3$ were used and models achieved acceptable r.m.s. misfit values of 1.304 (central) and 1.261 (south). Models are oriented perpendicular to the determined geoelectric strike directions, (N37°E – central, and N30°E – south) and are aligned to the Lishan Fault, LF.

6.2.2 Correlation of Resistivity and Seismic Velocity

The resistivity model of southern Taiwan was compared with a tomographic model of P-wave velocity estimates on an x = y = 5, z = 2 km grid that included

first arrival data from the TAIGER active seismic transects collected in 2007-8. Visual inspection of these models (Figure 6-13) reveals consistent trends in these independent geophysical data. For example, low values of both parameters are observed beneath the foreland basin in each model, and define a very similar structure. However, to make the analysis more quantitative, the procedure of Bedrosian et al. (2004) that was used in central Taiwan was also applied to the southern Taiwan data to determine if distinct model domains can be identified by ranges of velocity and resistivity.

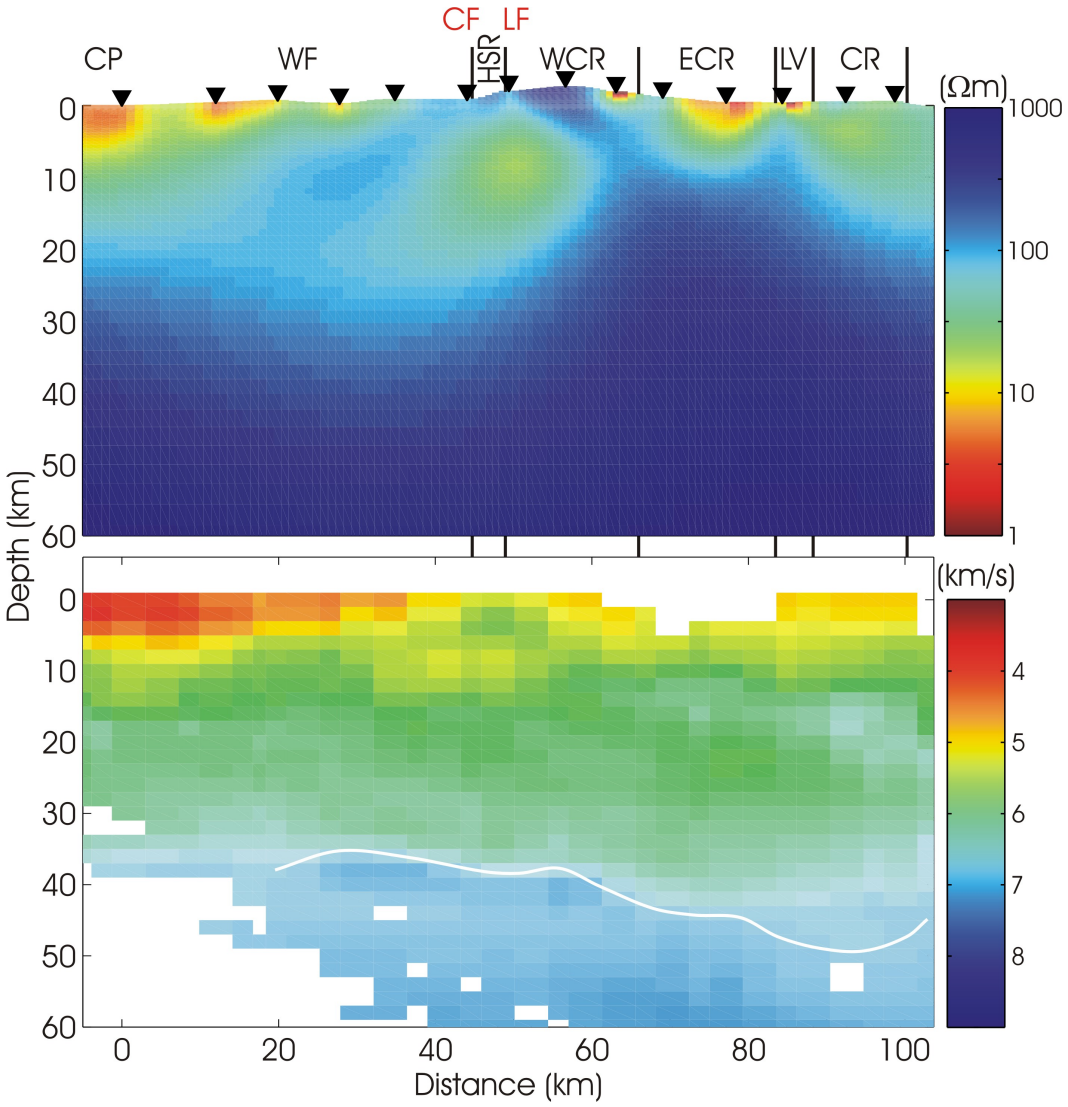

Figure 6-13. Top Panel: TE, TM and tipper resistivity inversion model. Bottom Panel: Tomographic P-wave velocity model with contour v_p = 7.3 km/s for reference (Wu et al., 2009).

After interpolation of the resistivity model onto the same grid as the seismic velocity model, and masking poorly resolved areas of both models to avoid correlation of unconstrained parameter estimates, a histogram of the occurrence of resistivity and velocity combinations for each model cell was generated (Figure 6-14). Cells within the resistivity model were then determined that contributed to the distinct domains identified within this histogram.

Three of these domains (CP/WF, HSR and WCR/ECR) identified in the histogram of Figure 6-14 reveal a general trend that correlates an increase in resistivity with an increase in the seismic velocity. The link between these parameters is the material porosity; as porosity decreases, both resistivity and velocity increase (Hacikoylu et al., 2006). This trend is consistent with the eastwards increase in metamorphic grade across Taiwan that results in a reduction of porosity. However, the majority of cells that comprise the Lishan Fault Conductor do not plot on this trend. Rather, the LFC domain is characterized by low resistivity (largely equal to values observed in the CP/WF domain) but only moderate seismic velocity. A small percent of interconnected porosity, saturated with saline fluid could explain the low resistivities observed, and would not significantly reduce the P-wave velocities (Jones et al., 1998).

Making the same assumptions regarding the fluid composition within the middle crust as for central Taiwan, a saline fluid is expected to have a resistivity within the range ρ_w ~0.01-0.05 Ωm (Nesbitt, 1993). Using Archie's Law (Archie, 1942) with a cementation factor of m = 1.5 requires porosity values of 0.5% - 1.5% to explain a bulk resistivity of 30 Ωm. Note that a recent sulphide deposit is located between the Chuchih and Lishan Faults, not far north of the southern MT profile (Lewis et al., 2007; Figure 6-1). This deposit provides evidence for hydrothermal fluids associated with inferred dehydration reactions within the crust (Craw et al., 2002). Thus, the LFC imaged in southern Taiwan can be explained by a small percent interconnected porosity saturated with saline fluids.

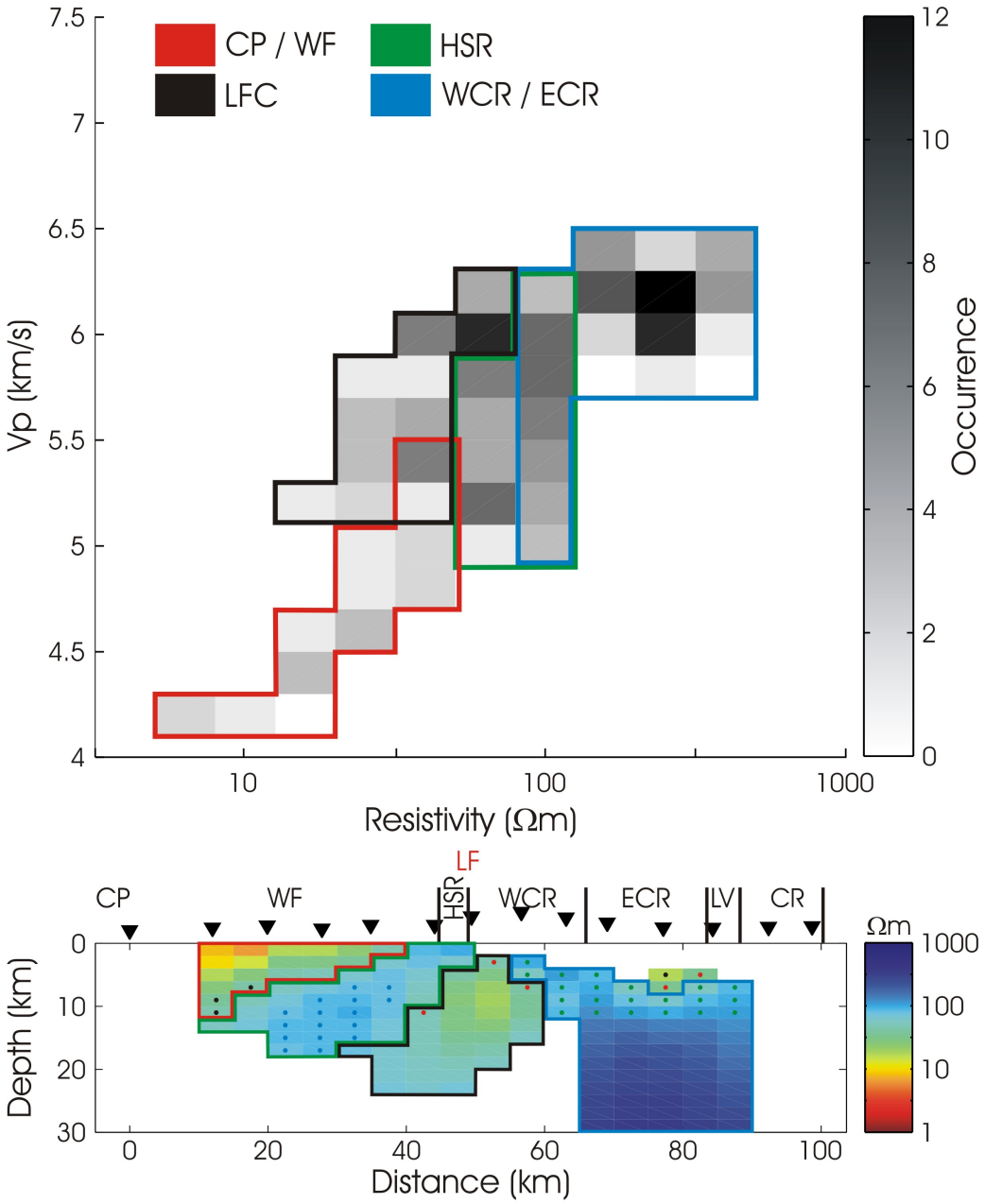

Figure 6-14. Top Panel: Crossplot of P-wave velocity and electrical resistivity for the models shown in Figure 6-12. Bottom Panel: Resistivity model indicating the spatial regions that give rise to the coloured domains in the crossplot. Note that white areas indicate where the resistivity and velocity models were masked. Dots indicate cells that contribute to bins within overlapped domains in the histogram.

6.2.3 Constrained Inversion Results

To support the thick-skinned lithospheric deformation model, it is required to show that the Lishan Fault Conductor extends to mid-crustal depth. Fluids

predicted within the middle to lower crust released by dehydration metamorphic reactions are inconsistent with the thin-skinned tectonic model that restricts collisional deformation to occur within an upper crustal wedge.

Regularization of resistivity models obtained by inversion is typically implemented by seeking spatially smooth models. However, since attenuation of EM fields is strongly dependent on conductivity (equations 3.19 and 3.20) the smoothing constraint can smear structure to depth if the fields do not penetrate through the base of a conductor. Thus, MT data do not reliably resolve the depth extent of conductive features and constrained inversions are required to determine the shallowest conductor consistent with MT data (Li et al., 2003). Constrained inversions were implemented with the resistivity models fixed to be resistive (300 Ωm) below depths of 10, 20 and 30 km. The fit to the observed tipper data at a period of 30 s at stations nearest to the Chuchih and Lishan Faults for these constrained inversions are shown in Figure 6-15. At a period of 30 s, these tipper data correspond to a depth of ~15 km, assuming a resistivity of 30 Ωm (equation 3.24). Note that since the resistivity of the Lishan Fault Conductor beneath central Taiwan is lower (~10 Ωm) the tipper data were analyzed at a period of 100 s (Figure 5-13) in order to be sensitive to a comparable depth.

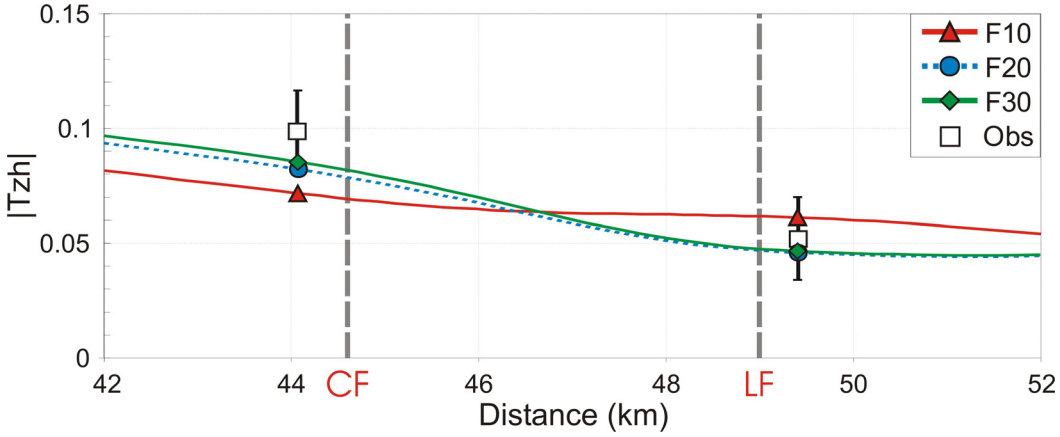

Figure 6-15. Tipper data projected parallel to profile at a period of 30 s for stations near the Chuchih Fault CF, and Lishan Fault LF. Open squares denote measured data with absolute error floor of 0.03. Smooth curves are responses of constrained inversion models with resistive (300 Ωm) basement fixed at depths 10, 20 and 30 km; models F10, F20 and F30, respectively.

Figure 6-15 shows that both the F30 and F20 models fit the observed data to within the errors. In contrast, the F10 model shows a poor fit to the measured data near the CF. The lower quality fit to the observed data by the F10 model provides evidence that the LFC extends beyond a depth of 10 km in southern Taiwan.

Since MT data are sensitive to conductance, plotting the integrated conductivity along profile can also indicate whether the constrained inversion models are able to fit the measured MT data. Figure 6-16 reveals that the conductance for the F20 and F30 models are similar, and suggests that these MT data cannot distinguish between a resistive basement at depths of 20 and 30 km. In contrast, the conductance determined for the F10 model is more variable, with the greatest difference occurring beneath the CF and LF. However, the obvious oscillatory behaviour observed in the F10 model conductance for central Taiwan (Figure 5-14) does not appear in these data. The more subdued difference between the F10 and other constrained inversion models requires a more rigorous approach than simple observation of the conductance along profile for investigating the depth extent of the LFC in southern Taiwan.

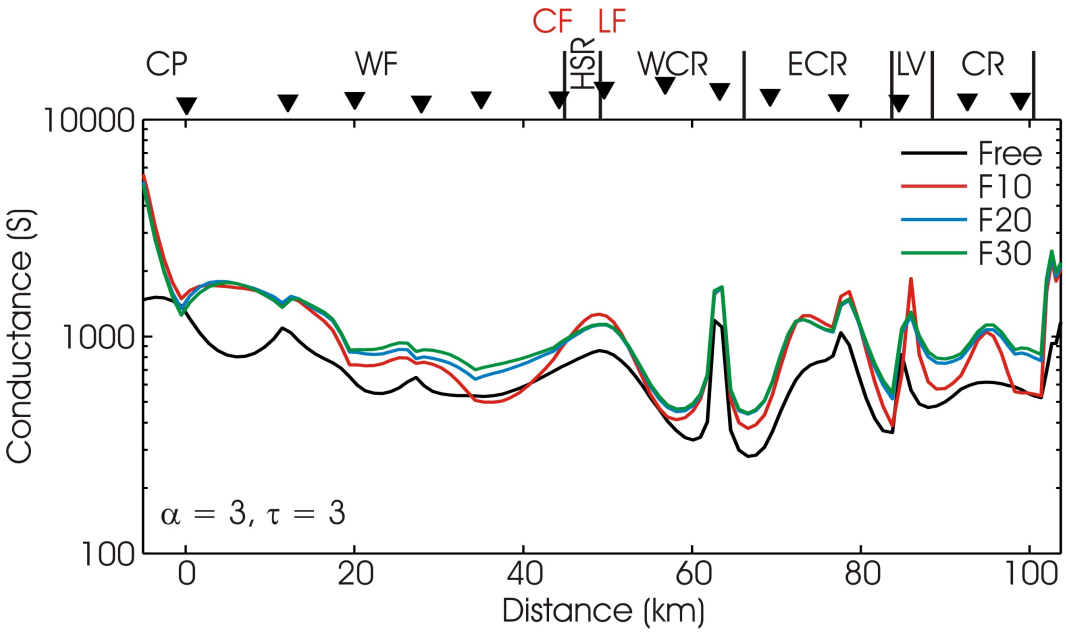

Figure 6-16. Integrated conductance to 60 km depth for the constrained 2-D inversion models of southern Taiwan. Regularization parameters for the inversion models are $\alpha = 3$ and $\tau = 3$.

The r.m.s. data misfit quantifies the ability of the constrained inversions to fit the measured MT data. As expected, Table 6-1 shows that the misfit progressively decreases as the fixed resistive basement is lowered. However, the reduction in r.m.s. misfit between the F20 and F30 models is minimal (0.027). This small reduction is consistent with the observed similarity in these model responses (Figure 6-15 and 6-16) and indicates insensitivity of the southern MT data at these depths. In contrast, a greater reduction in r.m.s. misfit occurs between the F10 and F20 models. However, the magnitude of this reduction (0.096) is equal to that observed between the F20 and F30 models in central Taiwan (0.098 for α =3 and τ = 3; Table 5-1).

Model	r.m.s. Misfit $\alpha = 3, \tau = 3$	Difference
F10	1.632	0.096
F20	1.536	0.027
F30	1.509	

Table 6-1. Normalized r.m.s. misfit for the constrained inversion models of southern Taiwan.

Do the MT data in southern Taiwan require that the Lishan Fault Conductor extend to mid-crustal depths? In central Taiwan, the F10 constrained inversion model was clearly incapable of fitting the measured data. In southern Taiwan, the same analysis suggests that the F10 constrained inversion model does not adequately fit the observed MT data; however, the degree of incompatibility is much less than observed in the central MT data.

6.2.4 Comparison: Southern and Central Taiwan MT Models

The Pingtung Plain is located 45 km southwest of the southern MT profile (Figure 6-1) and marks the northern limit of the Wadati-Benioff zone associated with subduction of the Eurasian Plate at the Manila trench (Kao et al., 2000; Lacombe et al., 2001). At the northern terminus of this basin, initial contact between the WF and Central Ranges occurs and is thought to reflect the elimination of oceanic

lithosphere and initiation of contact between the Eurasian shelf and forearc ridge (Shyu et al., 2005). Assuming steady-state collision at a propagation rate of 60 km/Myr (Byrne and Liu, 2002), the southern MT profile traverses a collision that began ~0.75 Ma. In contrast, the central MT data cross a more mature orogen resulting from mountain building processes that have occurred for ~2.5 Myr. Uncertainty in these age estimates exists; Suppe (1984) estimated a propagation rate of 90 km/Myr and Lee et al. (1991) calculate 40 km/Myr. However, the key point is that the orogen is mature in central Taiwan and developing in the south. Can this difference in the age of collision be related to along-strike variations observed in the MT models between central and southern Taiwan?

The MT inversion models of central and southern Taiwan shown in Figure 6-12 reveal that similar structures occur along the strike of the orogen axis. While elevated conductivity is observed at the near surface beneath the ECR in southern Taiwan, this feature may be attributed to local circulation of hydrothermal fluids (Chiang et al., 2009). At depths of the middle to lower crust, variation between these models occurs in the properties of the Lishan Fault Conductor. The LFC extends over a greater spatial area and shows a lower resistivity in central Taiwan. Saline aqueous fluids occurring within a small percent of interconnected porosity are shown to be consistent with the LFC's in both profiles. In the thick-skinned lithospheric deformation model, fluids are predicted in the middle to lower crust, released by prograde metamorphic reactions in the deforming lithosphere. Bertrand et al. (2009) showed that the TAIGER MT data support the thick-skinned tectonic model for central Taiwan.

The fact that the Lishan Fault Conductor appears in both central and southern Taiwan suggests that the same style of tectonics is occurring in both locations. Further, the lower conductance observed in Southern Taiwan may be linked to the younger age of the orogen at this latitude. As the processes of deformation and metamorphism occur in the thick-skinned model, it is expected that a greater amount of fluids would exist beneath the more mature orogen in central Taiwan.

Approximating the spatial extent of the LFC in central (25 km depth) and southern (15 km depth) Taiwan, and using the porosities computed for the range of fluid salinities expected at mid-crustal depths, the amount of interconnected fluids required by these 2-D inversion models can be estimated. This procedure indicates that twice the quantity of saline fluids is required in central Taiwan (4-8 km^2) in comparison to southern Taiwan (1-4 km^2). The greater quantity of fluids calculated in central Taiwan is consistent with the increased length of time that dehydrating metamorphic reactions have occurred in the mature orogen.

6.2.5 Correlation of Resistivity and Hypocentre Locations

Accurately relocated earthquake hypocentres (Wu et al., 2008) within 20 km of the southern MT profile are plotted on the resistivity model in Figure 6-17. Note that the double-difference catalogue by Wu et al., (2004) only contains events located beneath central Taiwan and cannot be used for comparison with the southern MT model. Earthquake hypocentres provide insight on both the rheology and *in situ* deformation conditions within the Earth. Numerous studies have revealed a general trend where seismicity occurs along the edges of fluid-based conductors (Ogawa et al., 2001; Heise et al., 2007; Wannamaker et al., 2009). The correlation shown in Figure 6-17 reveals a pattern of seismicity that indicates events generally occur within the relatively resistive areas of the MT model. Further, clusters of events are observed along the western margin of the LFC, indicating seismicity along the margin of this inferred fluid-based conductor.

6.3 Summary – Southern Taiwan

A resistivity model obtained by inverting the MT data collected in southern Taiwan revealed strong similarity to the model obtained in central Taiwan. However, the prominent Lishan Fault Conductor showed a lower conductance in the south than observed in central Taiwan. This observation is consistent in comparisons of both the 2-D and 3-D inversion models.

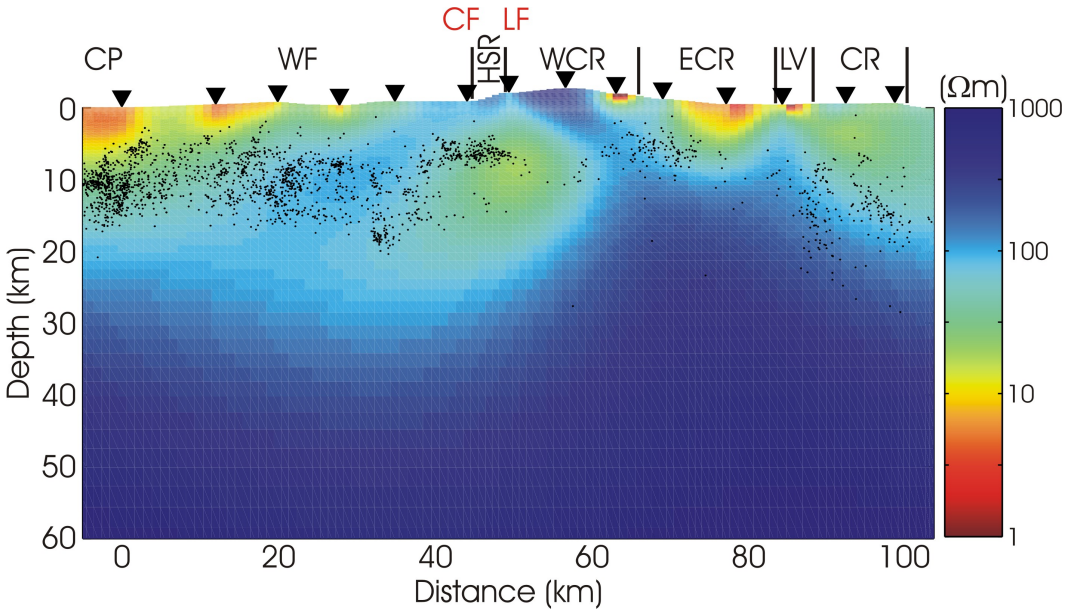

Figure 6-17. TE, TM and tipper resistivity inversion model of southern Taiwan showing hypocentres located within 20 km of the profile.

Comparison of the resistivity model to a seismic P-wave velocity model showed that the LFC is consistent with saline fluids within a small percent porosity. Further, analysis of constrained inversions suggests that this feature extends into the middle crust beyond 10 km depth. However, the depth extent appears less in the south, in comparison with results from central Taiwan. Bertrand et al., (2009) showed that the LFC in central Taiwan was inconsistent with the thin-skinned tectonic model, but could be explained by fluids released from prograde metamorphic reactions within a thickened crust. Thus, this feature was used to support the thick-skinned lithospheric deformation model for central Taiwan.

The existence of the LFC beneath southern Taiwan suggests that the same style of tectonics is occurring in the developing orogen. Further, the lower conductance is consistent with the time-axis of orogen evolution that follows the island strike. Since arc-continent collision has occurred for ~1.75 Myr longer in central Taiwan, the ongoing processes of deformation and dehydrating metamorphism can explain the greater conductance observed beneath central Taiwan. These data are consistent with the concept of uniformitarianism and indicate that the southern MT model yields a snapshot of central Taiwan at ~1.75 Ma.

7 INVESTIGATION OF A SUBDUCTING COLLISION: ANALYSIS OF THE NORTHERN TAIGER MT DATA

Long-period MT data collected at 12 stations in northern Taiwan (Figure 7-1) are analyzed in this chapter. The resulting resistivity models are compared with models from south and central Taiwan, and variations are interpreted in terms of the subducting collision in the north, where contact between the EUP and PSP occurs at progressively greater depth.

The bathymetric expression of the Ryukyu subduction zone is obscured offshore eastern Taiwan due to collisional deformation. While there is consensus that the subduction zone continues westward and terminates against the Taiwan orogen (Wu et al., 2009), several studies suggest different latitudes for this junction (e.g. 24.5°N - Angelier et al., 1990; 24.2°N - Deffontaines et al., 1997; Kao et al., 1998 and Font et al., 2001; 24°N - Lacombe et al., 2001; 23.7°N – Wu et al., 2009). Accurate determination of the plate geometries is necessary for understanding the tectonics of northern Taiwan; as the PSP subducts northwestwards it collides with the EUP at progressively greater depths (the subducting indenter model, Wu et al., 2009). Therefore, in contrast to central and southern Taiwan where the PSP and EUP collide from the surface down, beneath northern Taiwan contact occurs at increasing depth to the north.

A recent detailed investigation by Wu et al. (2009) used seismicity and 3-D seismic velocity structure to locate the western terminus of the Ryukyu trench at 23.7°N, beneath the Coastal Range. A seismically defined Wadati-Benioff zone (Figure 2-12; Wu et al., 2009) places contact between the plates at ~50 km depth beneath northern Taiwan at the latitude of the TAIGER MT stations (~24.7°N).

7.1 MT Data: Collection and Analysis

Time series processing of the northern MT data (Figure 7-1) resulted in relatively smooth apparent resistivity, phase and tipper data curves (Appendix A-1). Only one station (TGR060) showed anomalous out-of-quadrant TM mode phase data after rotation to the geoelectric strike coordinate frame, and these data were excluded from subsequent 2-D analysis. However, these high-quality MT data are expected to reflect the 3-D environment in which they were measured. For example, the bathymetry is highly variable surrounding the northern tip of the island. In addition, the MT stations in eastern Taiwan were located where the Central Ranges terminate at the Ilan Plain, marking the onshore extension of the Okinawa Trough that has been actively opening at ~15 mm/yr since 2 Ma (Sibuet et al., 1998). By modeling the stress regime in northern Taiwan, Hu et al. (2002) predict that a narrow transition zone occurs at the Lishan Fault between compression to the west, and extension to the east. This change reflects the complex interaction of compression forces caused by indentation of the PSP at depth, with tensile forces induced by slab suction at the Ryukyu trench.

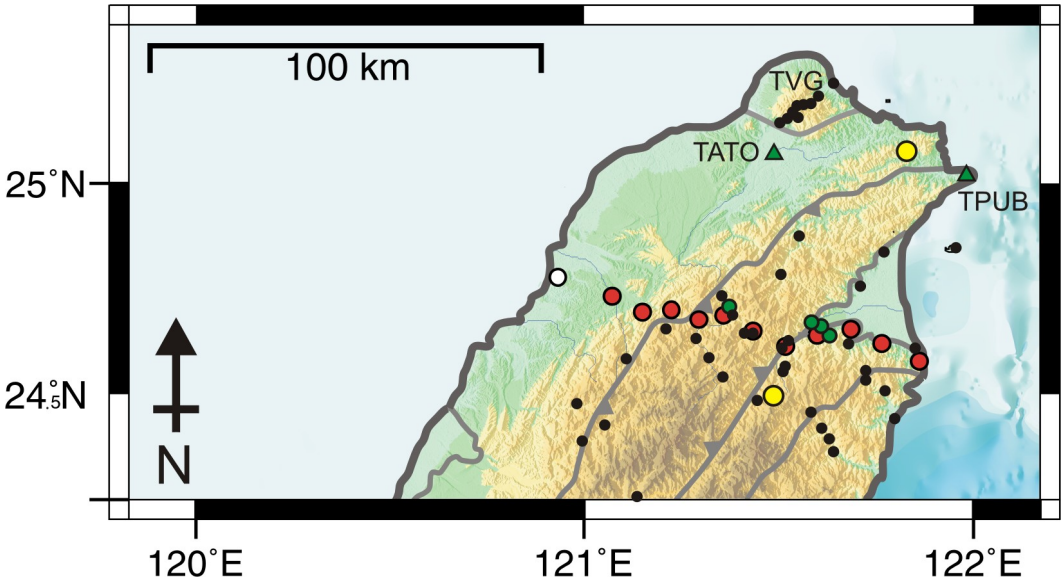

Figure 7-1. Long-period MT stations (red circles) in northern Taiwan. White circle shows where only magnetic field data were used. Green dots show heat flow measurements (Lee and Cheng, 1986). Yellow circles locate Au-Cu deposits (Lewis et al., 2007). Black dots indicate hot spring locations. Green triangles are broadband seismometers, TATO and TPUB. TVG – Tatun Volcanic Group.

7.1.1 MT Data Dimensionality

The tensor decomposition (McNeice and Jones, 2001) and phase tensor (Caldwell et al., 2004) methods were used to investigate the dimensionality of these northern MT data. These methods also provide estimates of the best-fitting 2-D geoelectric strike direction. Despite some scatter, the strike directions show a consistent value of N45°E (left-hand plots in Figure 7-2). This direction aligns with the overall geological strike of the orogen that bends northeastwards in northern Taiwan. In addition, the overall low r.m.s. misfit values at most MT stations and periods indicate that this strike direction is well constrained (Figure 7-3).

However, further analysis reveals a dichotomy in the geoelectric strike direction between stations recorded west and east of the Lishan Fault. The middle plots in Figure 7-2 reveal a geoelectric strike direction of ~N60°E for the 6 MT sites located west of the Lishan Fault. In contrast, both tensor decomposition and phase tensor analysis show a geoelectric strike direction of ~N30°E for the data at the 5 MT sites located east of the Lishan Fault (right-hand plots in Figure 7-2). This dichotomy reflects observed variations in orogen structure that are bounded by the Lishan Fault in northern Taiwan (e.g. the WF and HSR rotate clockwise in northern Taiwan, while the WCR and ECR terminate at the extending Ilan Plain).

While a geoelectric strike of N45°E represents the best-fitting direction for the overall dataset, the variation observed along profile could introduce artifacts in 2-D inversion models since this direction does not ideally represent either the western or eastern measurements. In addition, 2-D inversions require that stations be aligned perpendicular to geoelectric strike. However, since the strike direction is not known precisely prior to data acquisition, and MT station locations are somewhat dictated by local conditions (e.g. land permission, cultural EM noise sources, etc.) the measured impedance tensors are rotated to the strike coordinate frame and projected to a linear profile that is oriented perpendicular to strike. This projection decreases the total profile length in comparison to the actual station locations, and could introduce artifacts in the resulting 2-D resistivity models. The

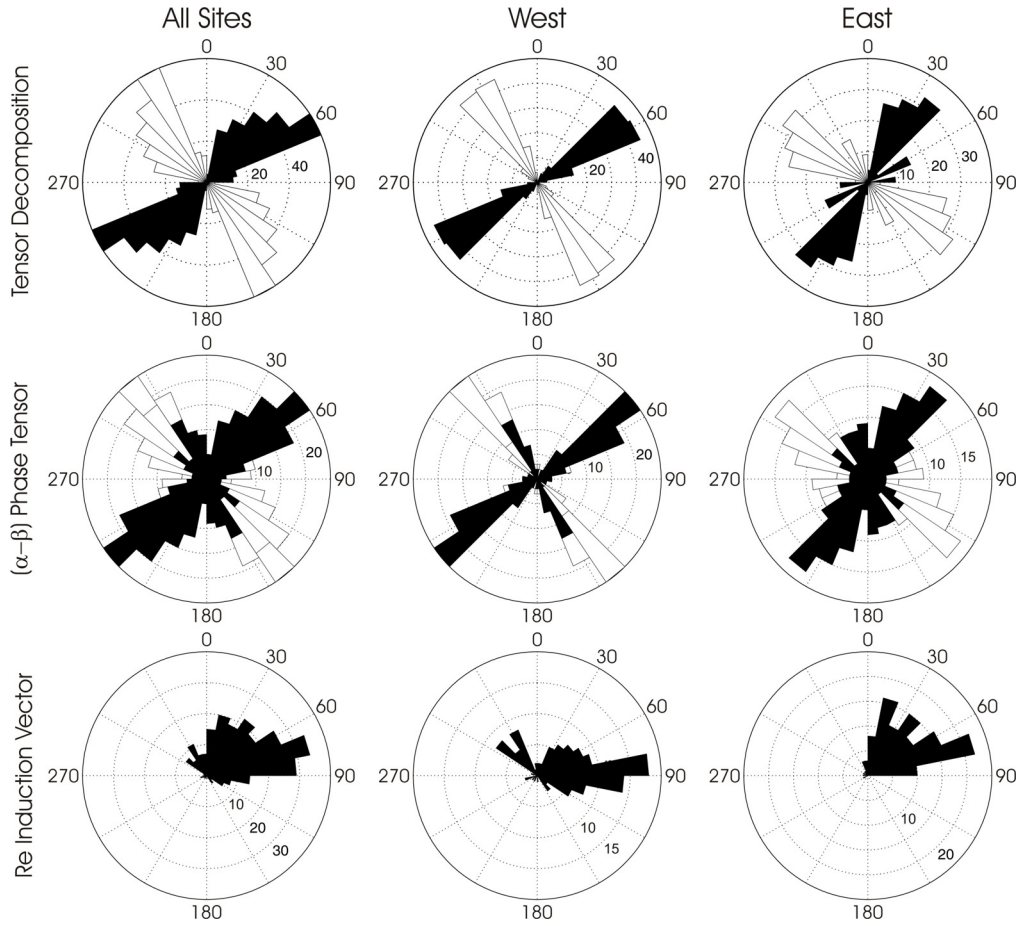

Figure 7-2. Rose diagrams showing results of dimensionality analysis. Results include MT data for the period range 10-10000 s and indicate an overall 2-D orogen-parallel geoelectric strike of ~N45°E. Different strikes are observed for stations west and east of the Lishan Fault, and the real induction vector components show strong along-strike orientation, indicating 3-D effects.

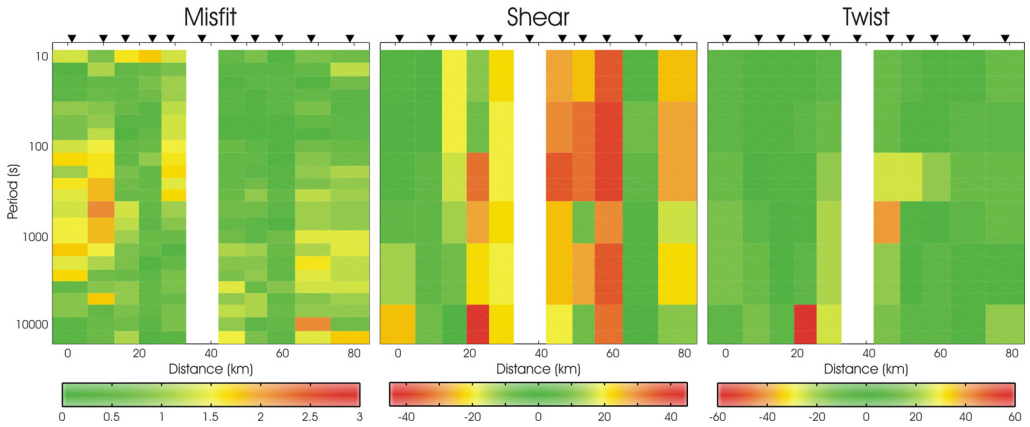

Figure 7-3. Results of tensor decomposition. The generally low r.m.s. misfit values indicate that the 2-D strike is well constrained. High values of shear (>30°) indicate galvanic distortion at some sites and periods. White bands indicate where electric field data were excluded from 2-D analysis due to strong distortion.

sensitivity of 2-D inversion models to variations in the geoelectric strike directions is therefore investigated below (see section 7.1.3).

Despite the first-order agreement between the geoelectric strike directions obtained from tensor decomposition and phase tensor analysis, inspection of the induction vector azimuths shows a strong strike-parallel orientation (bottom plots in Figure 7-2). This effect is seen to be greatest for the MT data measured east of the Lishan Fault (Figure 7-4). If the Earth has a 2-D electrical structure, then both the real and imaginary components of the induction vectors should align perpendicular to the geoelectric strike direction. The induction vectors in northeastern Taiwan that parallel the overall geoelectric strike direction indicate 3-D electrical structure. Therefore, 2-D modeling of these MT data must proceed with caution, and ultimately results must be compared for similarity with structure obtained in a 3-D inversion model to validate detailed analysis in 2-D.

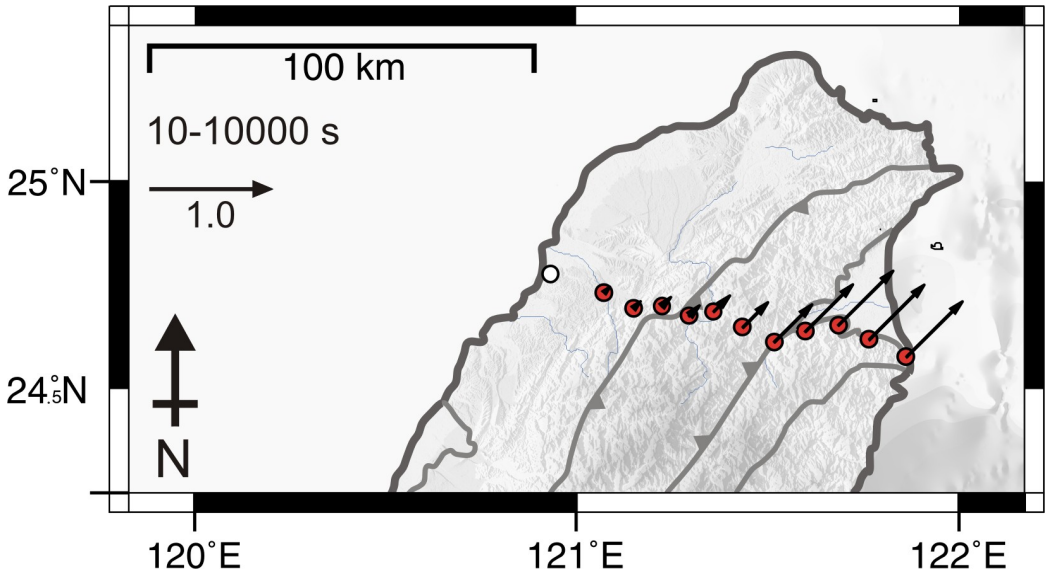

Figure 7-4. Along-strike (N45°E) components of the real induction vectors in northern Taiwan averaged over the period band 10-10000 s. Scale arrow of magnitude 1.0 is shown. Minimal along-strike components in the west indicate 2-D behaviour, while large magnitudes at sites near the Ilan Plain indicate 3-D induction effects.

Note that the Ilan Plain marks the onshore extension of the Okinawa trough – an extending back-arc basin. Plotted in the Parkinson convention (1962) the real

components of the induction vectors in Figures 7-4 and 4-9 indicate that a conductive anomaly occurs beneath this region. Further, a sizeable low-velocity anomaly is observed beneath the Ilan Plain (Wu et al., 2009). Coincident zones of low resistivity and low velocity have been observed elsewhere in back-arc regions (Brasse et al., 2002; Hyndmann et al., 2005; Soyer and Unsworth, 2006) and provide evidence for shallow convecting asthenosphere. Wu et al. (2009) suggest that the asthenosphere beneath northern Taiwan occurs at a shallow depth (~50 km) and permits the continued westward advance of the PSP due to the oblique plate convergence.

7.1.2 MT Data Observations

The differing geoelectric strike directions west and east of the Lishan Fault, and indications of 3-D induction effects near Ilan Plain have already been described. Given these effects, features observed in 2-D inversion models of northern Taiwan must be interpreted with caution and ideally associated with features observed in the actual MT data. Otherwise, model features could be artifacts introduced by non-unique inversions due to the inability of a 2-D algorithm to explain 3-D data.

Observation of the phase data in Figure 7-5 reveals a prominent high phase (>45°) anomaly located beneath the HSR, which is bounded by the Chuchih and Lishan Faults. These data suggest the presence of a major conductor at this location. Note that while the TE mode response occurs over many stations, the ϕ_2 and TM mode data that have more lateral sensitivity display high phase values at stations between the CF and LF in the HSR. In contrast to central and southern Taiwan, the high TM mode phase response terminates westwards of the LF beneath northern Taiwan. However, the exclusion of out-of-quadrant TM mode phase data at station TGR060 (located adjacent the LF) reduces the resolution of the eastern boundary of this low resistivity feature.

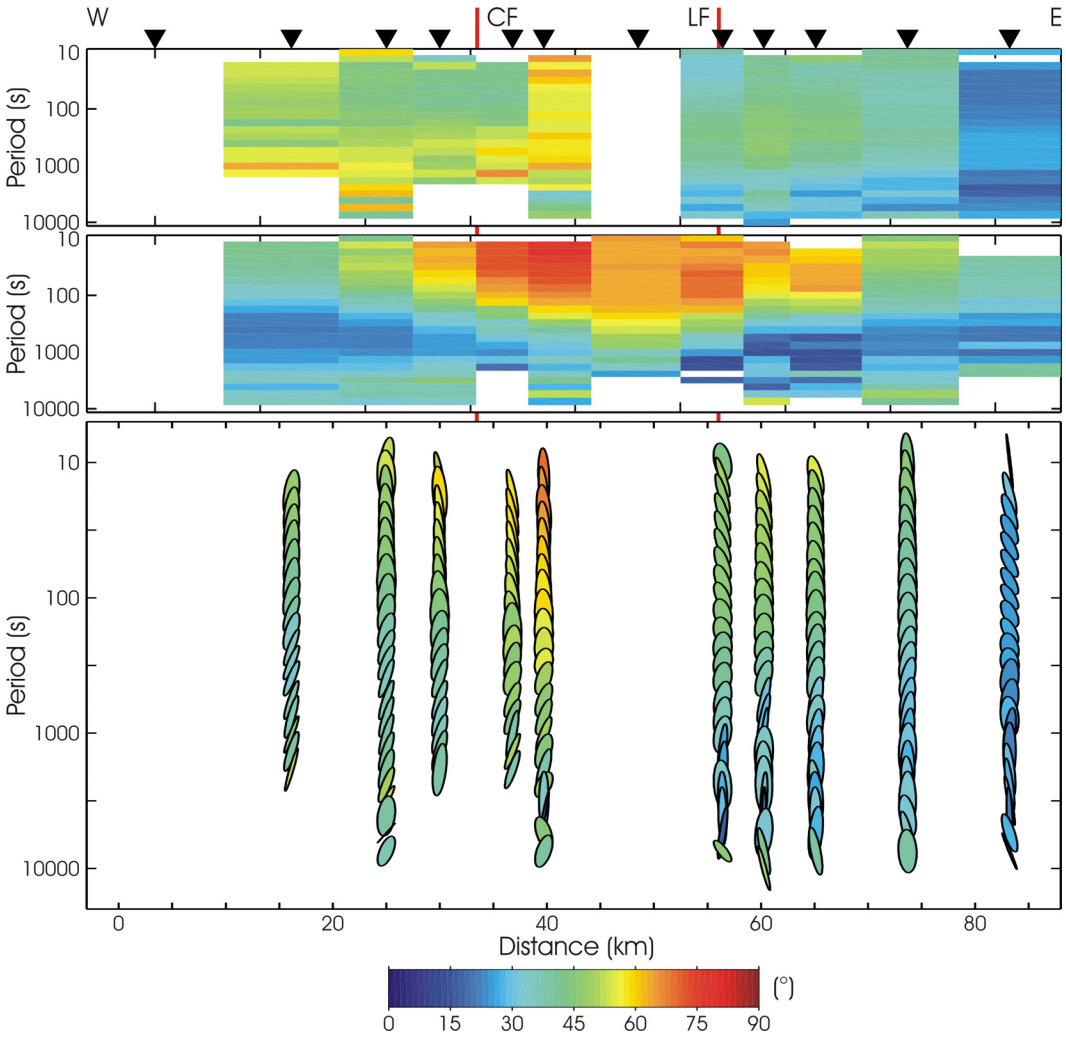

Figure 7-5. Pseudosections of long-period MT phase data in northern Taiwan. Top Panel: TM mode phase. Middle Panel: TE mode phase. Bottom Panel: MT phase tensor invariant ϕ_2. White areas indicate where data has been masked in the following 2-D inversion modeling due to high levels of noise and/or severe distortion. Since ϕ_2 represents an average, results are not shown where either the TM or TE mode phase has been masked. Profiles are oriented perpendicular to the geoelectric strike (N45°E). Faults are: Chuchih Fault CF and Lishan Fault LF.

Of note, these northern MT data display a pattern that is distinct in comparison to the southern (Figure 6-5) and central (Figure 5-6) phase responses that showed strong similarity. The distinct nature of these northern MT data may reflect the change in collisional tectonics from contact between the Eurasian and Philippine Sea Plates from the surface down (central and southern Taiwan), to contact at depth (northern Taiwan).

7.1.3 2-D Sensitivity Tests

Sensitivity tests were performed to investigate the influence that variations in the geoelectric strike and 3-D effects in the TE mode data have on the stability of structures observed in 2-D inversion models of northern Taiwan. These tests are required to validate analysis in 2-D for these northern MT data.

The geoelectric strike direction that provides the best overall fit (N45°E) to the MT data in northern Taiwan does not ideally represent either the data west (strike ~ N60°E) or east (strike ~ N30°E) of the Lishan Fault. Therefore, 2-D inversion models were generated assuming geoelectric strike directions of N30°E, N45°E and N60°E (Figure 7-6). Note that the varying lengths of these models results from projection of the stations onto profiles with a range of azimuths. However, the consistency of the resistivity structures observed in these models, and the similar r.m.s. misfit values obtained, indicate that the variation in geoelectric strike observed along profile does not preclude a 2-D analysis of these data.

The inversion models in Figure 7-6 used the same smoothing parameters and error floors as were used to generate the final 2-D resistivity models for central and southern Taiwan. However, the r.m.s. data misfits are significantly higher for these models of northern Taiwan than models of the central and southern MT data. Inspection of the data misfits for each mode and station for the middle model in Figure 7-6 (geoelectric strike = N45°E) reveals that the TE mode data in northeastern Taiwan are much more poorly fit in comparison to the other components (Figure 7-7). Since the TE mode data are most susceptible to off-profile (3-D) effects, which are clearly shown to occur near the east coast (Figure 7-4), these TE mode data significantly increase the overall misfit. In the presence of 3-D resistivity structure, it is common to down-weight the TE mode data by increasing their error floors in comparison to the TM mode values (Heise et al., 2007; Hill et al., 2009). Inversion models were therefore generated for various levels of inclusion of the TE mode data in northeastern Taiwan (Figure 7-8).

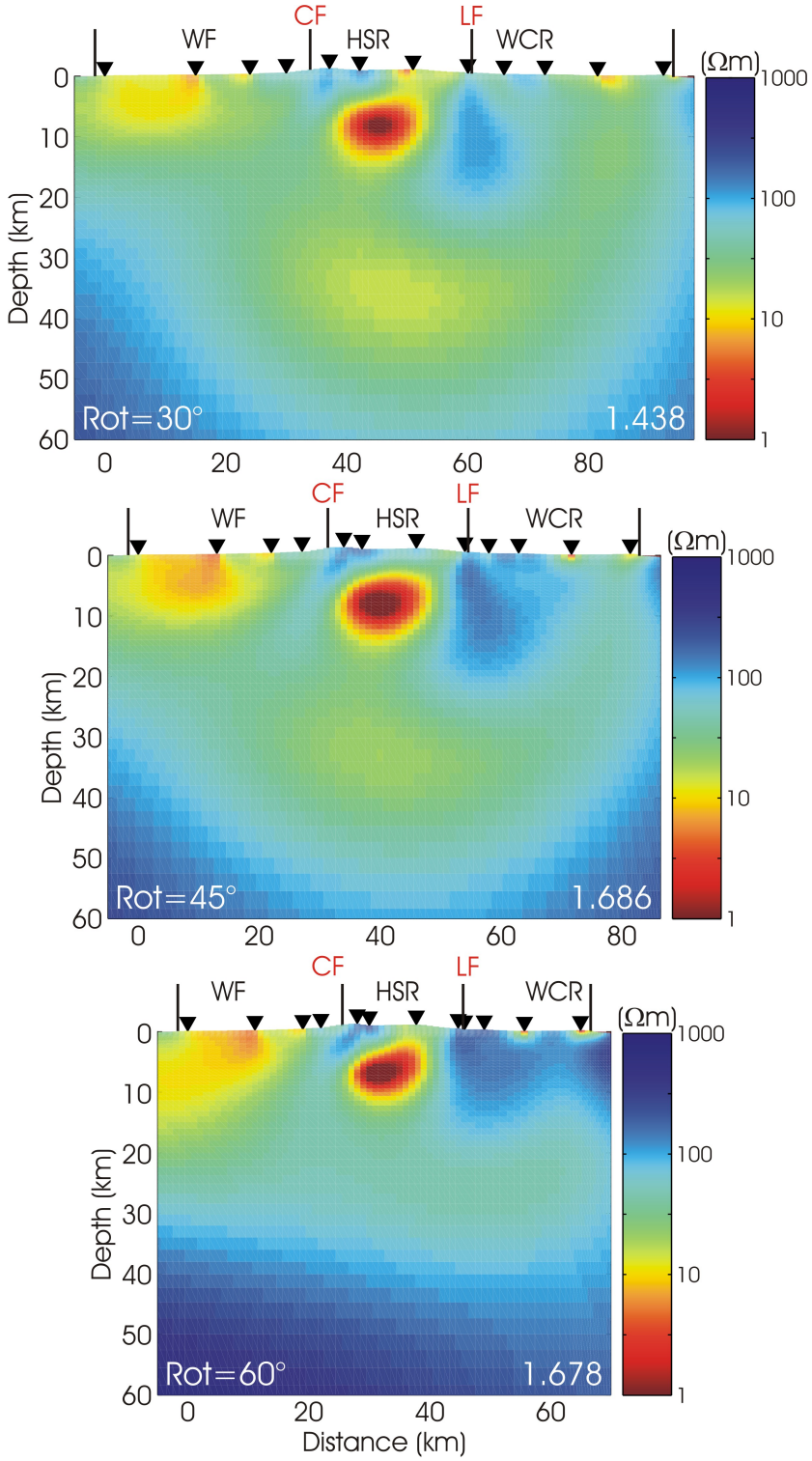

Figure 7-6. 2-D TETMHZ inversion models of northern Taiwan. The geoelectric strike (bottom left corner) and r.m.s. misfit (bottom right corner) are shown for each model. Similar features exist for all rotations with the largest variation in the east where 3-D effects occur. Models used $\alpha = 3$, $\tau = 3$, and error floors of 20%, 7.5% and 0.03 for the apparent resistivity, phase and tipper data, respectively.

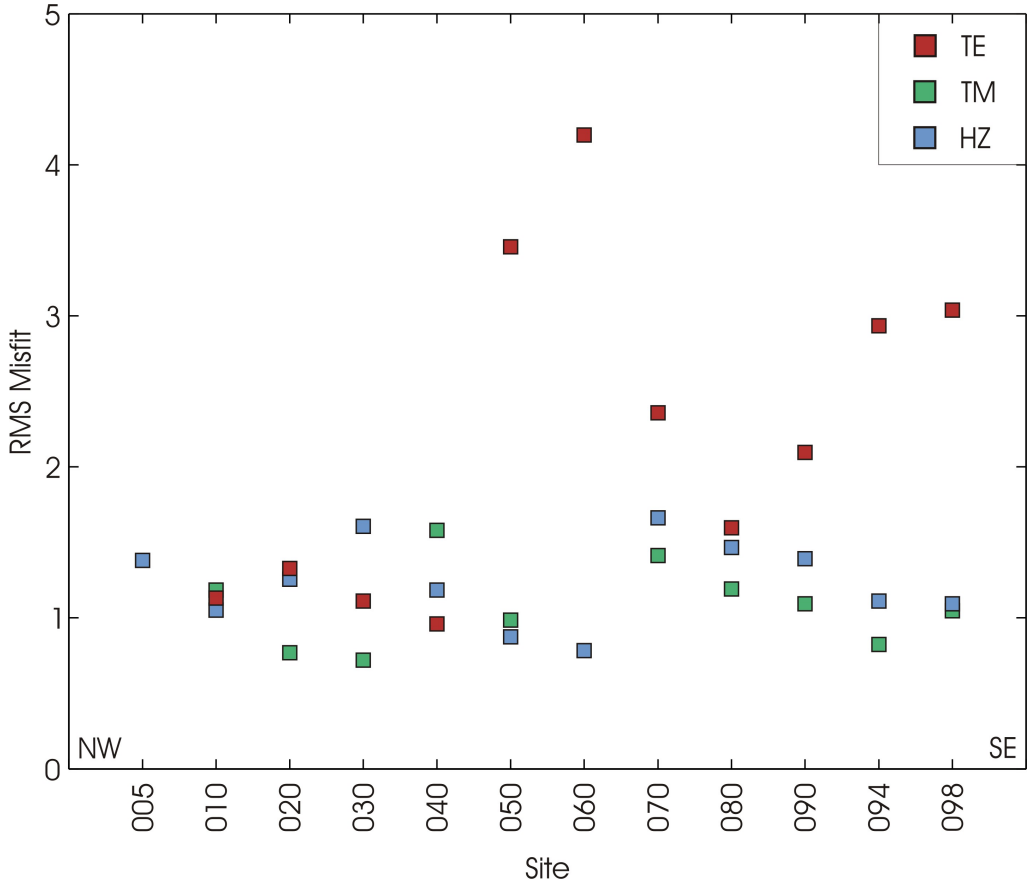

Figure 7-7. R.M.S. data misfit for the 2-D inversion model of northern Taiwan that used a geoelectric strike direction of N45°E (middle panel in Figure 7-4). Smoothing parameters of α =3 and τ = 3, and error floors of 20%, 7.5% and 0.03 for the apparent resistivity, phase and tipper data, respectively were used. Poor fit is achieved to the TE mode data in northeastern Taiwan.

Doubling the TE mode error floors in comparison to the TM mode values resulted in a significant reduction (0.378) in the r.m.s. misfit (middle panel in Figure 7-8). A further reduction (0.227) in data misfit was achieved by completely excluding the northeastern TE mode data. However, since only approximately half the reduction in the misfit occurred by excluding the TE mode data in comparison to that achieved from doubling the error floors, the middle model in Figure 7-8 was chosen as optimum. In addition, despite some variation at lower crustal and upper mantle depths, the observed resistivity structures are very similar in the top two models shown in Figure 7-8. Therefore, error floors of 40% for the TE mode apparent resistivity and 15% for the TE mode phase data were adopted for subsequent 2-D inversion modeling of these MT data in northern Taiwan.

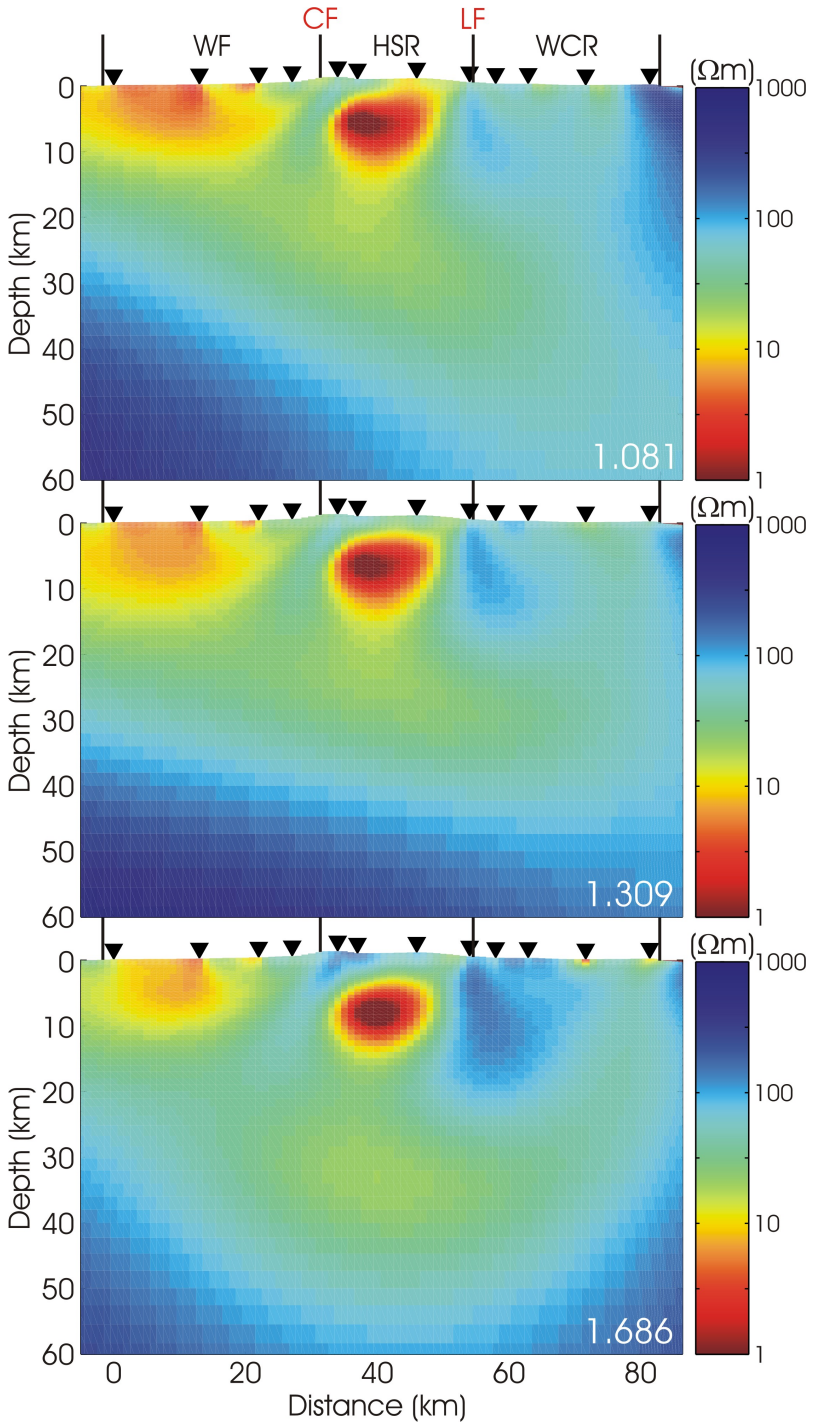

Figure 7-8. 2-D TETMHZ inversion models of northern Taiwan for various levels of inclusion of the TE mode data. Top Panel: No TE mode data for the easternmost 7 sites. Middle Panel: TE mode error floors doubled to 40% and 15% for the apparent resistivity and phase, compared to the TM mode values. Bottom Panel: All TE mode data included with error floors 20% and 7.5% for the apparent resistivity and phase, respectively. All inversion models used $\alpha = 3$, $\tau = 3$ and tipper error floor of 0.03. R.M.S. misfit is shown in the bottom right corner of each model.

7.1.4 2-D Inversion of MT data

Variations in the geoelectric strike and 3-D effects in the TE mode MT data have been shown to not adversely influence features in initial 2-D inversion models of northern Taiwan (Figures 7-6 and 7-8). However, to further ensure the stability of model features, numerous 2-D resistivity models were generated for a range of control parameters using the NLCG6 algorithm (Rodi and Mackie, 2001). All models used the preferred geoelectric strike direction of N45°E, and TE mode error floors of 40% for the apparent resistivity and 15% for the phase. Error floors of 20%, 7.5% and 0.03 were set for the TM mode apparent resistivity and phase, and tipper data, respectively. These values are the same as those used to model the central and southern profiles. All inversions included the profile topography and bathymetry, and solved for the static shift coefficients during late-stage iterations.

Inversion models generated for a range of smoothing parameters and starting models are shown in Figure 7-9. Note that while some variation occurs, significant resistivity features are observed for a wide range of smoothing parameters (1-6 in Figure 7-9) and starting model resistivities (7-8 in Figure 7-9). The similarity of features in these resistivity models further indicates the validity of a 2-D interpretation for these MT data. Recall that for MT data that show 3-D behaviour, if overall 2-D character dominates, the results obtained using 2-D inversion algorithms can be valid (Wannamaker, 1999; Ledo, 2005).

To choose the optimum regularization parameters that find a compromise between minimizing the model roughness and data misfit, an L-curve was generated from models computed over a wide-range of values for the regularization parameter τ (Figure 7-10). To enhance the lateral continuity of resistivity structures, models with $\alpha = 3$ were favoured. The point of maximum curvature on an L-curve indicates the regularization value that gives the best balance between generating a smooth model and fitting the measured MT data to within an acceptable level (Hansen et al., 1992).

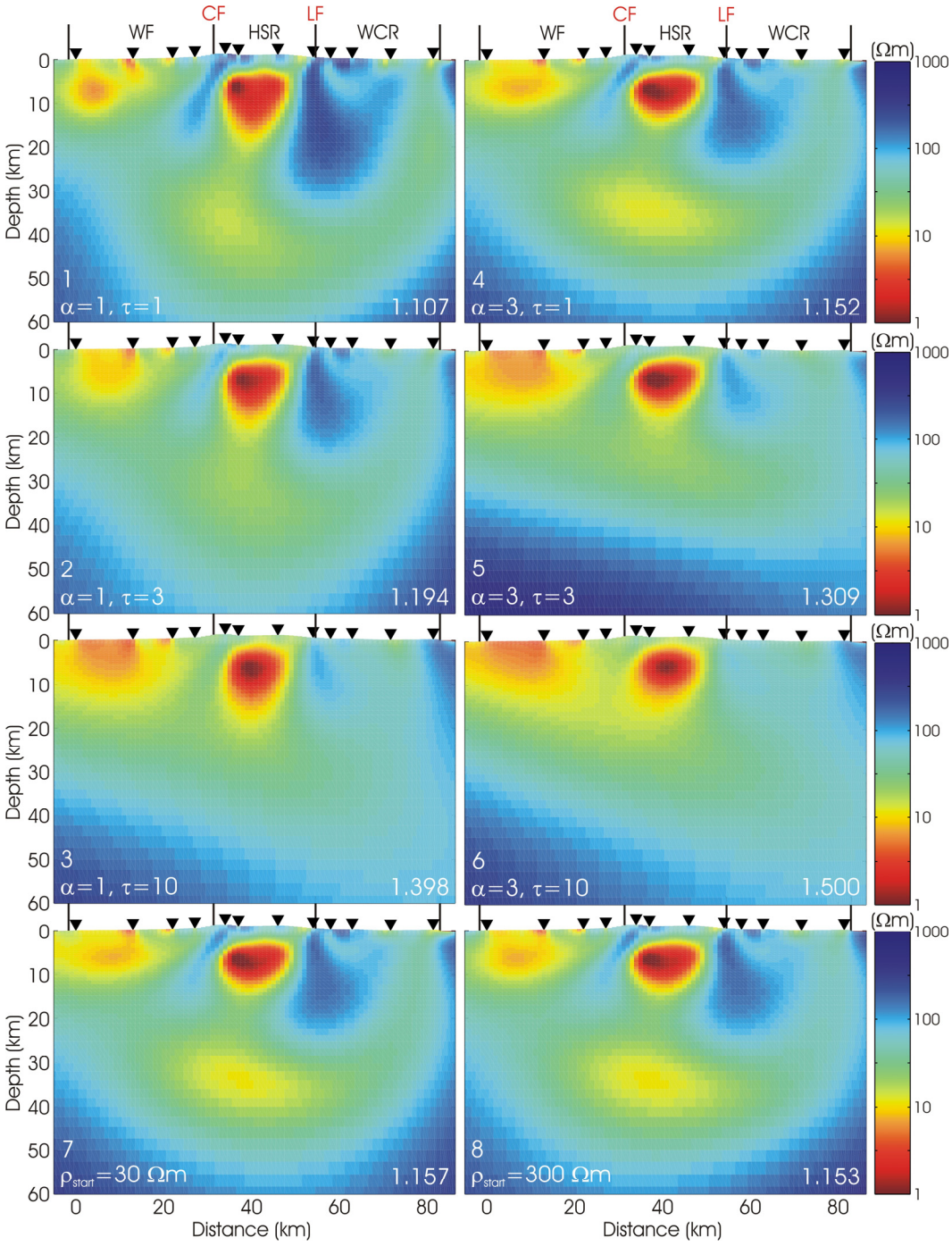

Figure 7-9. 2-D TETMHZ inversion models of northern Taiwan. Inversions solved for the smoothest variations away from an *a priori* starting model that included the Philippine Sea and Taiwan Strait. Models 1-6 used 100 Ωm as the starting subsurface resistivity. Models 7-8 used smoothing parameters $\alpha = 3$ and $\tau = 1$. R.M.S. data misfit is shown in the bottom right corner of each model.

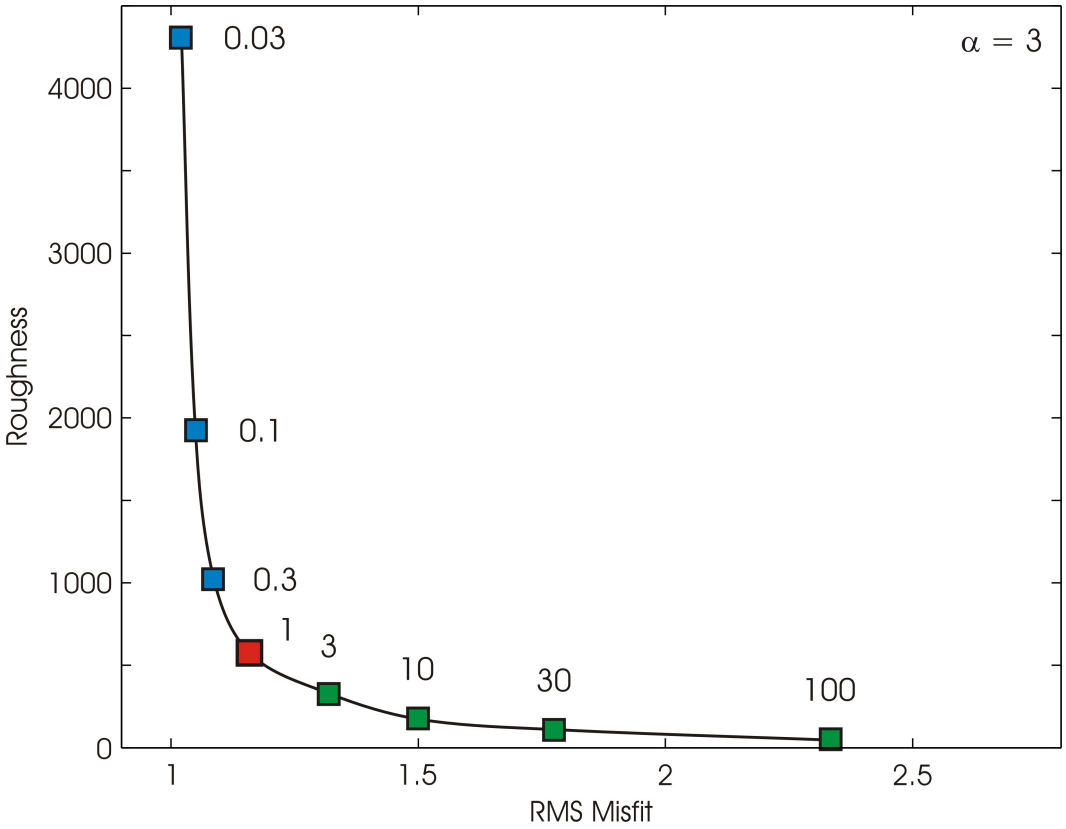

Figure 7-10. L-curve for 2-D TETMHZ inversion models of northern Taiwan. τ for each model is shown, all models used $\alpha = 3$. The maximum curvature occurs at $\tau = 1$, and balances the tradeoff between data fit (decreasing misfit – blue squares) and obtaining a smooth model (decreasing roughness – green squares).

The optimum 2-D inversion model of the northern Taiwan MT impedance and tipper data is shown in Figure 7-11. This model produced an acceptable r.m.s. data misfit of 1.152. Pseudosections displaying the measured data and inversion model responses are shown in Figure 7-12 and indicate the high quality of the fit obtained. Further, as indicated by observation of the MT impedance phase and phase tensor invariant ϕ_2 (Figure 7-5), significant model structures are supported by features observed in the measured MT and tipper data.

The tipper anomaly associated with the coast effect (i.e. observation of the decay of large (> 0.5) in-phase magnitudes at long-periods for stations near the east coast) occurred over a length-scale of ~65 km and ~45 km for southern and central Taiwan, respectively (Figures 6-10 and 5-11). In contrast, this same decay

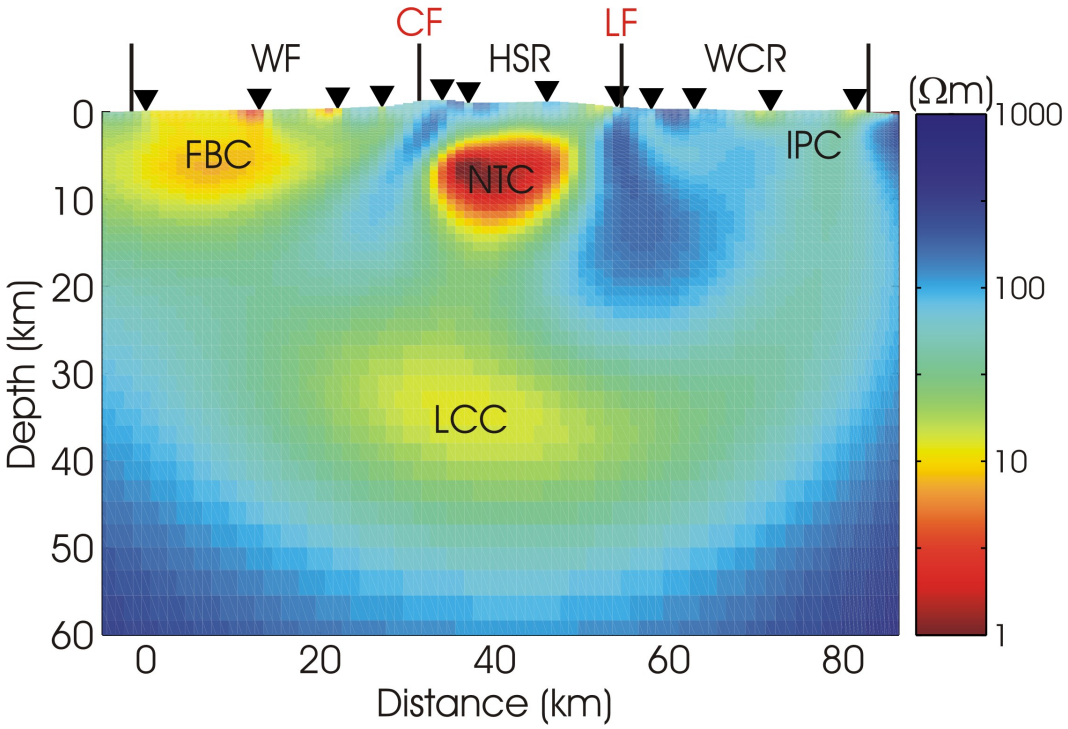

Figure 7-11. TE, TM and tipper resistivity inversion model. Model conductors: FBC – Foreland Basin Conductor; NTC – Northern Taiwan Conductor; IPC – Ilan Plain Conductor; LCC – Lower Crustal Conductor. Abbreviations above the model indicate the geological provinces (black), the Chuchih Fault CF and the Lishan Fault LF (red).

occurs rapidly in the northern MT data; long-period tipper anomalies fall below 0.5 within ~30 km of the Philippine Sea (Figure 7-12). This rapid decay is consistent with the higher conductivity observed beneath northeastern Taiwan, which would decrease the onshore adjustment distance (Figure 3-6) in comparison to that for the highly resistive Central Ranges, imaged in southern and central Taiwan. Also note that the reversal in tipper magnitude that locates the Northern Taiwan Conductor (NTC) in northern Taiwan (Figure 7-11) persists to the longest-periods measured (Figure 7-12). In contrast, the tipper reversal pattern across the LFC in southern Taiwan occurred for the period range 10-100 s (Figure 6-10), and in central Taiwan for periods between 10-1000 s (Figure 5-11). This variation is consistent with the progressive increase in the overall model conductance observed from southern to northern Taiwan.

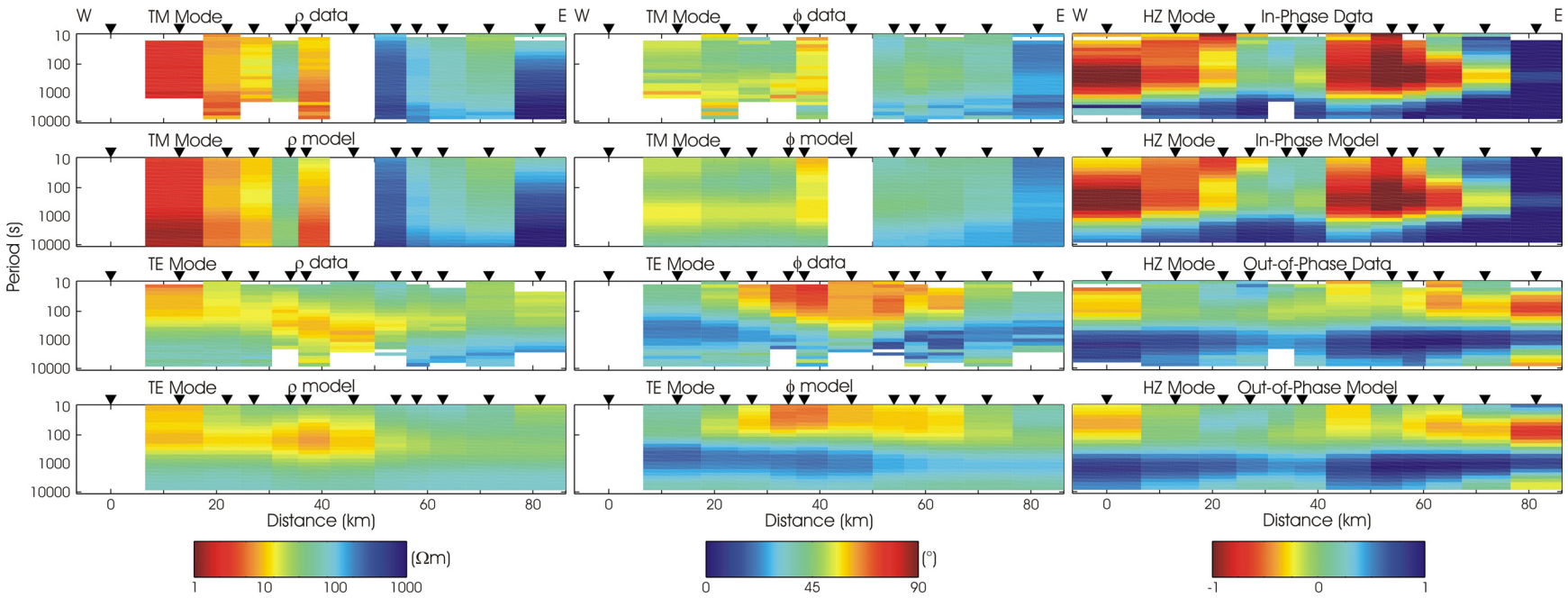

Figure 7-12. Pseudosections of long-period MT data collected in northern Taiwan. The left and middle panels display the measured and modeled resistivity and phase data for the TM (Transverse Magnetic) and TE (Transverse Electric) modes. The right panel shows the measured and modeled in-phase (real) and out-of-phase (imaginary) tipper data. White regions indicate data that were excluded from the 2-D inversion modeling because of high levels of noise and/or severe distortion.

7.1.5 3-D Inversion of MT Data

Rigorous tests have been applied to show that 2-D inversion modeling of the MT data collected in northern Taiwan is appropriate. However, 3-D induction effects are clearly observed in these MT data. For example, the dichotomy observed in the optimum geoelectric strike direction for measurements made to the west and east of the Lishan Fault, and the along-strike real induction vector components in northeastern Taiwan, indicate off-profile (3-D) electrical structure. Therefore, to ensure that structures in the 2-D models are not artifacts from 3-D distortion, the code WSINV3DMT (Siripunvaraporn et al., 2005) was used to invert the full MT impedance tensor data for stations in northern Taiwan. A 2-D slice from this 3-D model, that is oriented perpendicular to N10°E and passes through the actual station locations, is shown in Figure 7-13. The similarity of resistivity features in this 3-D model in comparison to the final 2-D inversion result (Figure 7-11) indicates that 3-D induction effects are not introducing artifacts in the 2-D model.

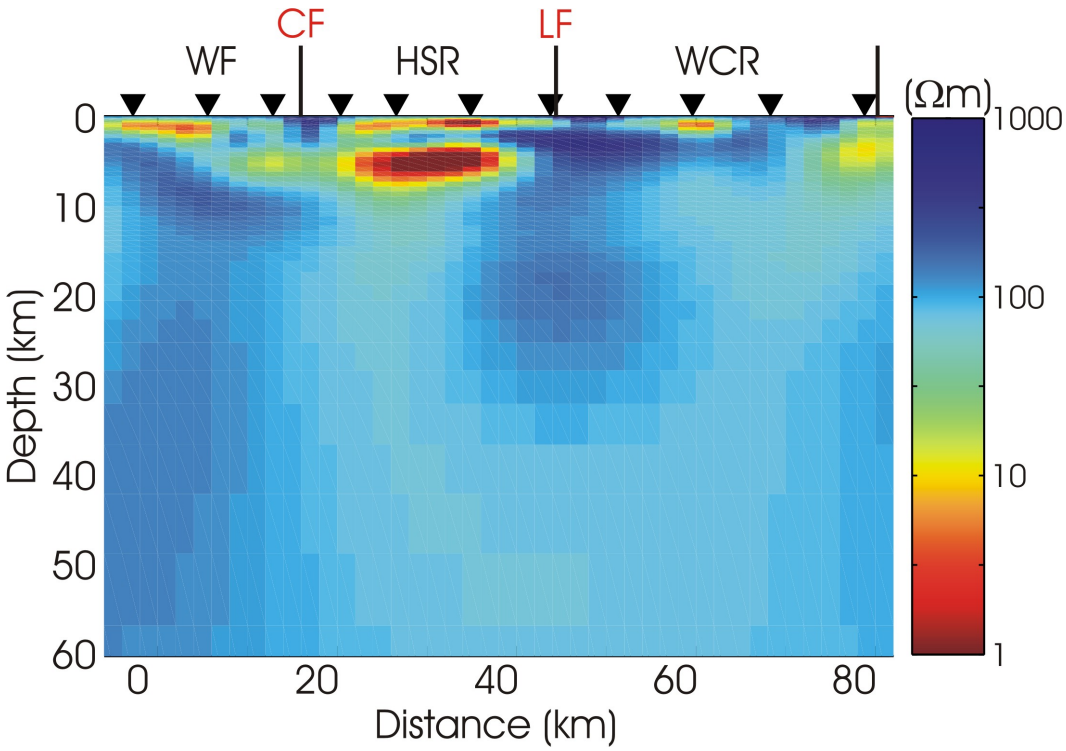

Figure 7-13. 3-D inversion model of the full MT impedance data in northern Taiwan. The r.m.s. data misfit is 1.559 after 4 iterations and 37 days of CPU time.

Note that despite similar structures observed in the 2-D and 3-D models, the depth extent and the absolute resistivity of features is variable. Specifically, conductors in the 3-D model are thinner than their 2-D counterparts. Patterns of variation between models generated for the same MT data with the code WSINV3DMT (Siripunvaraporn et al., 2005), and the 2-D NLCG6 algorithm (Rodi and Mackie, 2001) have been previously reported (Bedrosian, 2008). However, despite these differences, variability is relatively minor and the important observation is that the resistivity structures are similar in both the 2-D and 3-D models.

7.2 Interpretation

7.2.1 Resistivity Model Interpretation

In western Taiwan, low resistivities occur within the upper 10 km beneath the Western Foothills province (FBC in Figure 7-11). Similar features were observed in southern and central Taiwan, and can again be explained by fluid filled porosity within the sedimentary rocks of the foreland basin. East of this zone, the Chuchih Fault marks uplift of the high mountain ranges that expose metamorphic rocks of increasing grade towards the east. A reduction in porosity associated with these crystalline metamorphic materials correlates with the general eastwards increase in resistivity observed in the near-surface.

Near the east coast, low resistivity occurs (IPC in Figure 7-11) that coincides with a low velocity anomaly reported beneath the Ilan Plain (Wu et al., 2009). Located above the Wadati-Benioff zone (profile 10 in Figure 2-12) it is likely that the low resistivity in this zone is due to fluids released from the subducting slab. At this latitude, the subducting Philippine Sea Plate is located at a depth of ~50 km (Wu et al., 2009), and within the stability field for dewatering metamorphic reactions in greenschist and lower amphibolite facies (Wannamaker et al., 2009). However, located at the edge of the profile, and where the measured MT data showed significant 3-D effects, constraints on this diffuse zone of low resistivity are poor.

Below the Hseuhshan range, a significant conductor is imaged in the upper crust (NTC – Northern Taiwan Conductor, in Figure 7-11) that laterally terminates below the surface expressions of the Chuchih and Lishan Faults. This conductor appears to extend upwards towards the trace of the Lishan Fault; however, near surface resolution is poor for these long-period MT data and this aspect of the NTC is not well constrained. The properties of the NTC are best explained by interconnected saline fluids, shown to cause the low resistivities in the similar crustal feature (LFC) imaged in central (Figure 6-9) and southern (Figure 5-10) Taiwan. However, reliable estimates of the geothermal gradient in northern Taiwan do not exist. For example, three measurements made close to the southwestern extent of the Ilan Plain (Figure 7-1) show highly variable surface heat flow estimates (131.4 mW/m^2, 284.6 mW/m^2 and 171.6 mW/m^2; Lee and Cheng, 1986). Further, within the HSR in northern Taiwan (Figure 7-1) a thermal gradient of 36.8 °C/km was predicted from an observed heat flow of 131.4 mW/m^2. This calculation assumes a thermal conductivity of 3.6 W/m°K that is well outside the range commonly used to represent crustal materials (2.25 – 2.5 W/m°K; Claire Currie, personal communication; Clauser and Huenges, 1995). Despite uncertainty in these heat flow data, Song and Ma (2002) determined a preferred geothermal gradient for the Central Ranges of ~17 °C/km. This gradient places the solidus (650 °C) of wet felsic rocks (Vanyan and Gliko, 1999) at a depth of 38 km, eliminating partial melt as an explanation for this low-resistivity feature. Furthermore, even with a thermal gradient of 36.8 °C/km, partial melting would begin at ~18 km depth, still below the depth extent of the NTC in northern Taiwan.

Comparison of the geometry and location of the LFC in southern and central Taiwan with the NTC in northern Taiwan reveals along-strike variations. Namely, the LFC was centred below the Lishan Fault in southern and central Taiwan, while the NTC occurs west of this fault below the northern profile. In addition, while the conductance of the NTC continues the observed trend of increasing conductance associated with the age of collision, a simple extension of the LFC

may not be appropriate for northern Taiwan where plate collision occurs at depth. It may be more reasonable to associate the NTC with fluids in a back-arc region sourced from dewatering of the subducting Philippine slab. For these reasons, the upper crustal conductor beneath northern Taiwan is distinguished as the NTC.

Finally, a broad zone of low resistivity is imaged that dips moderately eastwards at lower crustal depths (LCC – Lower Crustal Conductor, in Figure 7-11). However resolution of this feature is poor owing to its location below the shallower prominent NTC. For MT data to resolve a deeper conductor overlain by a shallow conductor, the conductance of the lower conductor must be greater than that of the upper one. Clearly, the conductance of the NTC (10 km / 3 Ωm ~ 3333 S) is greater than the LCC (15 km / 10 Ωm ~ 1500 S), and the resulting poor sensitivity at depth can explain the lower crustal variability observed in the inversion models shown in Figure 7-9. While characteristics of the LCC are poorly constrained, all inversion models in Figure 7-9 show a broad zone of low resistivity at ~30 km depth that dips to the east. Further, a similar feature was observed in inversion models that completely eliminated the TE mode data in eastern Taiwan (Figure 7-8). Thus, evidence exists to support a broad region of low resistivity in the lower crust. However, constrained inversions are effective to indicate the shallowest conductor permitted by MT data (Li et al., 2003), and must be implemented to resolve whether this low-resistivity zone is required at lower crustal depths.

7.2.2 Constrained Inversion Results

The attenuation of electromagnetic fields is dependent on the conductivity of the medium (equations 3.19 and 3.20). In combination with the smoothing constraint imposed to regularize MT inversions, strong attenuation in conductors results in poor sensitivity to their depth extent. To determine the shallowest conductor permitted by MT data, constrained inversions are commonly implemented that fix a resistive basement at various depth levels (Li et al., 2003).

Constrained inversions were generated for the northern MT profile with the basement forced to be resistive (300 Ωm) beneath various defined depths. The conductances computed for these constrained inversion models are compared to the unconstrained (Free) inversion model in Figure 7-14. Since MT data are sensitive to conductance, these responses can indicate if the inversion algorithm is able to fit the measured MT data subject to the imposed conditions.

Clearly, fixing the basement to be resistive beneath a depth of 10 km (F10) is incompatible with these MT data, since it results in a model with a conductance that varies significantly along the profile. The conductance of the F20 model is broadly similar to the Free model result, but is closer to the F10 response in some parts of the profile. In contrast, the F30 and F40 models show similar conductances to the Free model. Observation of these conductance profiles provides first-order insight to the ability of the constrained inversions to fit the measured MT data. However, a more quantitative method is required to determine the minimum depth extent of the low-resistivity zone (LCC).

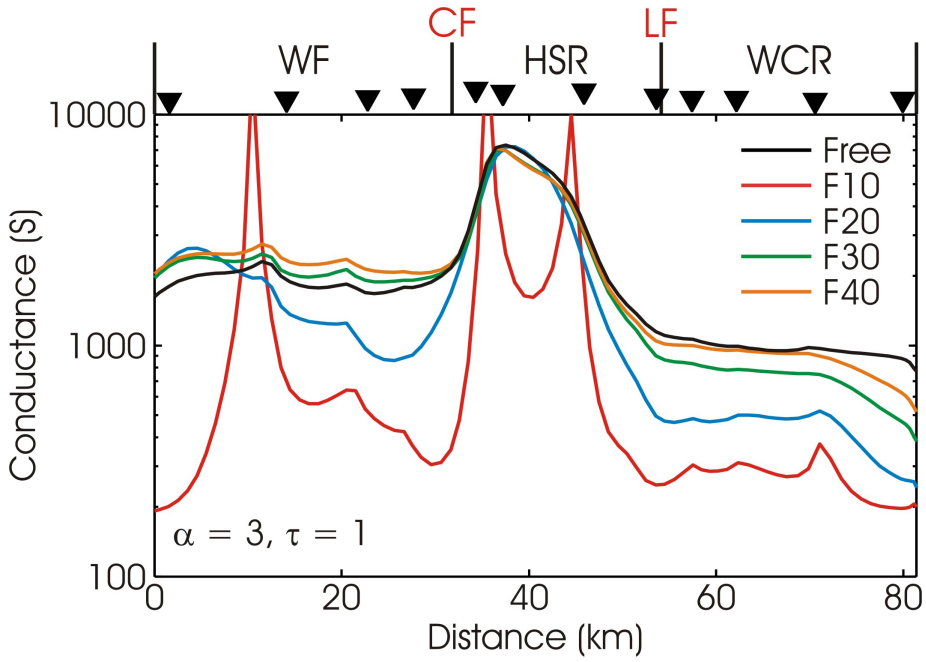

Figure 7-14. Integrated conductance to 60 km depth for the constrained 2-D inversion models of northern Taiwan. Regularization parameters for the inversion models are $\alpha = 3$ and $\tau = 1$.

The r.m.s. data misfit provides a quantitative measure of the degree to which an inversion model fits the observed MT data. Table 7-1 shows the r.m.s. misfit for the constrained inversions, and also the incremental decrease in misfit that results from increasing the depth to the fixed resistive basement. Progressively increasing the depth to the resistive basement causes the r.m.s. data misfit to decrease; the depth at which this decrease becomes negligible indicates the shallowest conductor permitted by these MT data (Li et al., 2003).

Model	r.m.s. Misfit $\alpha = 3, \tau = 1$	Difference
F10	1.577	0.092
F20	1.485	0.144
F30	1.341	0.059
F40	1.282	

Table 7-1. Normalized r.m.s. misfit for the constrained inversion models of northern Taiwan.

Significant reductions in the r.m.s. misfit result from lowering the depth to the resistive basement from 10 to 20 km, and also from 20 to 30 km. In contrast, a change from 30 to 40 km results in a much smaller reduction in the r.m.s. misfit (0.059), indicating that these MT data have little resolution to structure below ~40 km depth. However, the significant reduction in misfit between the F20 and F30 models indicates that these measured data require low model resistivity below ~30 km depth. Therefore, the Lower Crustal Conductor is required at depths in the range 30 – 40 km, and is likely a robust feature of the model.

7.2.3 Correlation of Resistivity and Seismic Velocity

Ore bodies cannot account for large spatial zones of high conductivity as observed beneath northern Taiwan (NTC and LCC in Figure 7-11). Further, graphite is unlikely to maintain a connected network within an active orogen (Katsube and Mareschal, 1993; Wannamaker, 2000). Therefore, two possible sources are left to explain these observed conductors: interconnected saline fluids or partial melt. A

combination of these fluids has been proposed as an explanation of a pervasive crustal conductor beneath the Tibetan plateau (Unsworth et al., 2005).

Temperature is often the key parameter required to discriminate between aqueous fluids and partial melt (Brasse et al 2002). Unfortunately, heat flow data in Taiwan are sparse in the high mountain ranges, and contaminated by the effects of groundwater circulation (Song and Ma, 2002). Therefore, quantitative comparison of the resistivity model of northern Taiwan and a tomographic model of P-wave velocity estimates was implemented to increase constraints on these crustal resistivity anomalies. The integration of independent geophysical data is effective to reduce non-uniqueness inherent in individual techniques.

The northern MT resistivity model is plotted with a coincident tomographic model in Figure 7-15. The P-wave velocity model consists of 5 x 5 x 2 km^3 blocks (in x, y and z directions) and includes first arrival data from the TAIGER active seismic transects collected in 2007-8. As implemented in southern and central Taiwan, these independently derived models were quantitatively correlated with the procedure of Bedrosian et al. (2004). After interpolating the resistivity model onto the same grid as the velocity model and masking poorly constrained areas of both models (e.g. below 40 km depth), distinct domains defined by ranges of resistivity and velocity were identified (Figure 7-16). Cells in the resistivity model that contributed to bins in the histogram domains were then mapped back into the resistivity model.

Implementation of this correlation method for MT data recorded in southern and central Taiwan revealed a consistent trend of eastwards increasing resistivity and velocity across the island. This same trend is repeated for northern Taiwan identified by the WF, HSR and WCR domains in Figure 7-16. Since the grade of metamorphism increases eastwards across Taiwan, an associated reduction in porosity explains this observed trend (Hacikoylu et al., 2006). However, model cells that comprise the NTC plot off this trend in a distinct zone identified by low

resistivity, but only moderate seismic velocity. Note that the velocity ranges (5.25-6.5 km/s) that define the LFC domains in central (Figure 5-17) and southern (Figure 6-14) Taiwan are consistent with the NTC domain in northern Taiwan (Figure 7-16). Bertrand et al. (2009) showed that a small amount of saline fluid

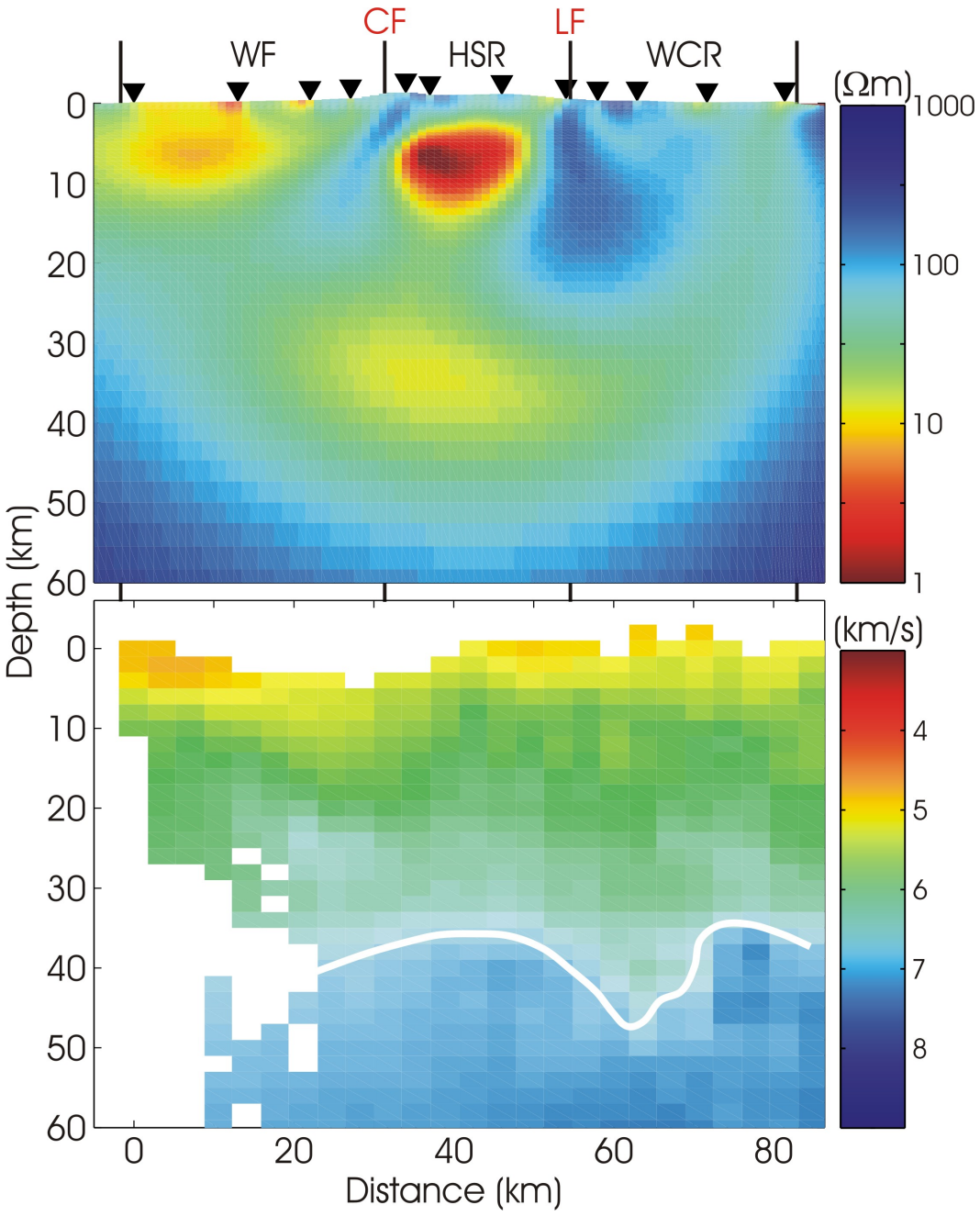

Figure 7-15. Top Panel: TE, TM and tipper resistivity inversion model of northern Taiwan. Bottom Panel: Tomographic P-wave velocity model with contour v_p = 7.3 km/s for reference.

with a small percent porosity was consistent with the LFC in central Taiwan, and would not greatly reduce the observed P-wave velocity (Jones et al., 1998). Using Archie's Law (Archie, 1942), porosities of 2-6 % are required to explain the resistivity (3 Ωm) of the NTC in northern Taiwan, assuming pore fluid salinities within the range ρ_w =0.01-0.05 Ωm (Nesbitt, 1993) and a cementation exponent

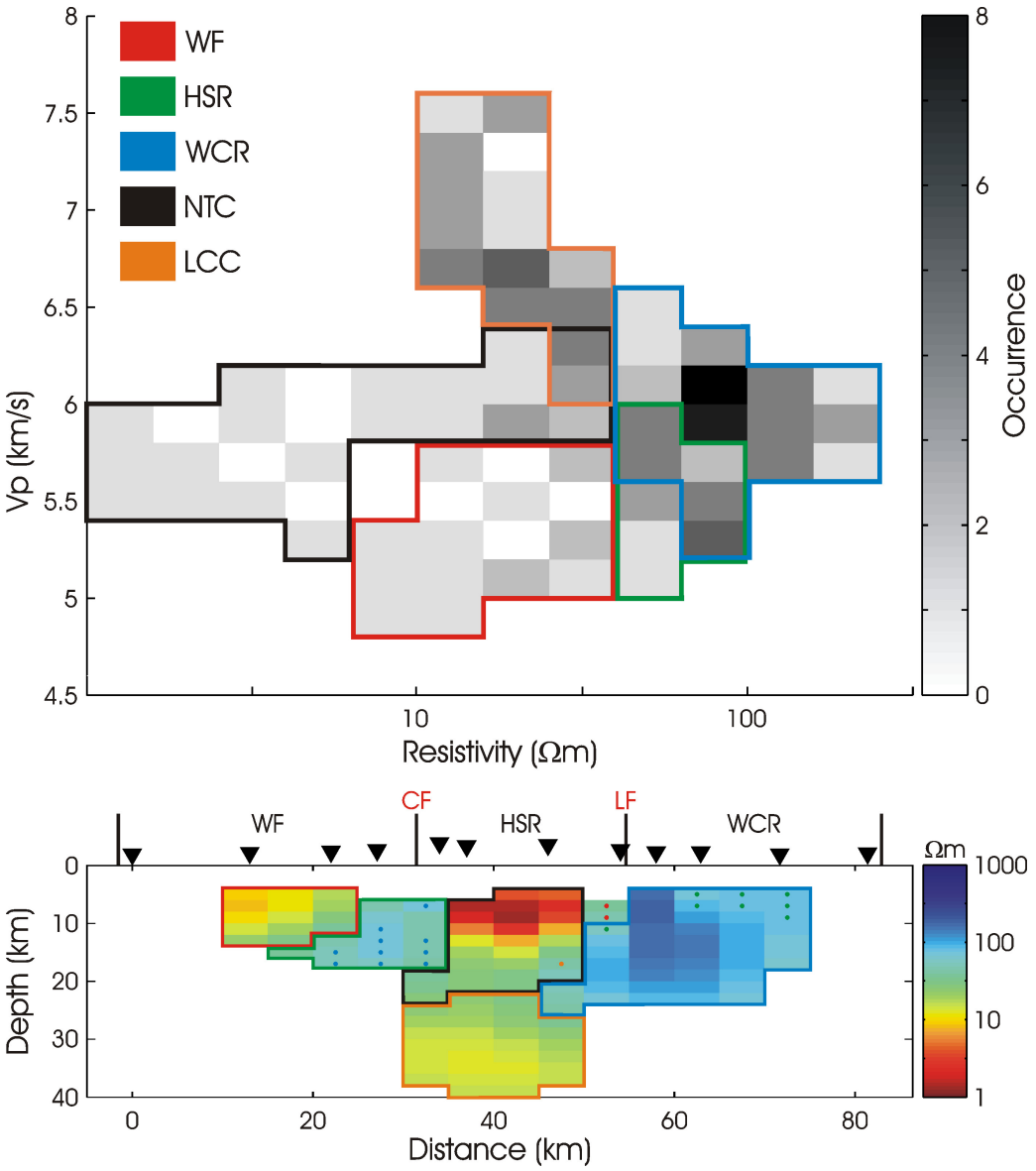

Figure 7-16. Top Panel: Crossplot of P-wave velocity and electrical resistivity for the models shown in Figure 7-15. Bottom Panel: Resistivity model indicating the spatial regions that give rise to the coloured domains in the crossplot. Note that white areas indicate where the resistivity and velocity models were masked to avoid correlation of unconstrained parameter estimates. Dots indicate model cells that contribute to bins within overlapped domains in the histogram.

of m = 1.5. The linear chain of sulphide deposits that occurs along the Lishan Fault (Figure 7-1; Lewis et al., 2007) provides evidence for hydrothermal fluid circulation. The source of the NTC in northern Taiwan is therefore consistent with a small percent interconnected porosity saturated with saline fluids.

Detailed explanation of the Lower Crustal Conductor is difficult due to a lack of high resolution data required to constrain properties of the lower crust beneath northern Taiwan. For example, the change in velocity across the Moho beneath Taiwan is not yet reliably determined, although contours of v_p = 7.5 km/s in tomographic models have been used as a guide (Wu et al., 2009). Therefore, since the LCC domain is characterized by P-wave velocities that are below 7.5 km/s, this supports the location of this feature within the lower crust. Estimates of the Moho depth have been determined from receiver function analysis (TATO: 30-36 km; TPUB: 20-30 km; Figure 7-1); however, significant errors are associated with the nearby subducting Philippine slab – a subsurface dipping interface.

Due to the effects of groundwater circulation, the measured heat flow data are poor. However, the proposed average geothermal gradient (~17 °C/km, Song and Ma, 2002) permits partial melting of wet felsic material at a depth of ~38 km. This estimate defines a lower limit; modeling fission track ages indicates a geothermal gradient of 20-25 °C/km (Willett et al., 2003). These geothermal gradients place the solidus of wet felsic material (650 °C, Vanyan and Gliko, 1999) within the depths of 30-40 km where the LCC is constrained to occur. These data reveal that aqueous fluids are required to explain the low resistivity observed in the LCC. In contrast, partial melt can contribute but is not required. Note that temperatures greater than 1000 °C are required to melt dry crustal materials (Vanyan and Gliko, 1999). Thus, the absence of aqueous fluids would eliminate the possibility of melting at depths of 30-40 km.

Therefore, Regardless of whether partial melt is present, aqueous fluids are necessary to explain the LCC that occurs beneath northern Taiwan.

7.2.4 Correlation of Resistivity and Hypocentre Locations

Do the same mechanisms of prograde metamorphism within a thickening crust that provide the source of crustal aqueous fluids in southern and central Taiwan also operate in the north? Contact between the converging Philippine Sea and Eurasian Plates occurs from the surface down in southern and central Taiwan. In contrast, at the latitude of the northern MT profile, contact occurs at a depth of ~50 km (Wu et al., 2009). Therefore, whole lithosphere-scale convergence does not occur in northern Taiwan. However, subduction of the fluid-rich oceanic crust provides a source of fluids at depth that is not present further south.

Northern Taiwan bears resemblance to the plate boundary that exists in the Marlborough region of the South Island in New Zealand. At this location, subduction of the Pacific Plate beneath the Australian Plate that occurs to the northeast, transitions to oblique continental collision and the formation of the Southern Alps to the southwest (Unsworth, 2009). In comparison, beneath northern Taiwan subduction of the Philippine Sea Plate transitions to collision with the Eurasian continental shelf, and forms the Taiwan orogen. Recently, a detailed MT survey was completed across the Marlborough region (Wannamaker et al., 2009) and revealed a series of fluid-rich zones that occur at progressively greater depths above the descending slab. These zones indicate upward fluid migration sourced from the subducting oceanic plate that is inferred to weaken the crust. This prediction is consistent with a lack of earthquakes in these conductive areas (Wannamaker et al., 2009).

Plotting high-quality relocated hypocentres (Wu et al., 2008) that exist within 20 km of the northern MT profile reveals a strong correlation between model conductors and aseismic zones (Figure 7-17). In addition, a cluster of events occurs along the eastern margin of the LCC at depths of 40-50 km that marks convergence of the subducting Philippine Sea Plate (Wu et al., 2009). The pattern of seismicity occurring at the perimeters of fluid-based conductive zones has been observed elsewhere (Ogawa et al., 2001; Heise et al., 2007; Wannamaker et al.,

2009) and indicates that these events may promote the release of fluids from the downgoing slab, and subsequent migration towards the surface. The subtle eastwards dip of the LCC suggests that the downdip Philippine slab is an important source of fluids beneath northern Taiwan.

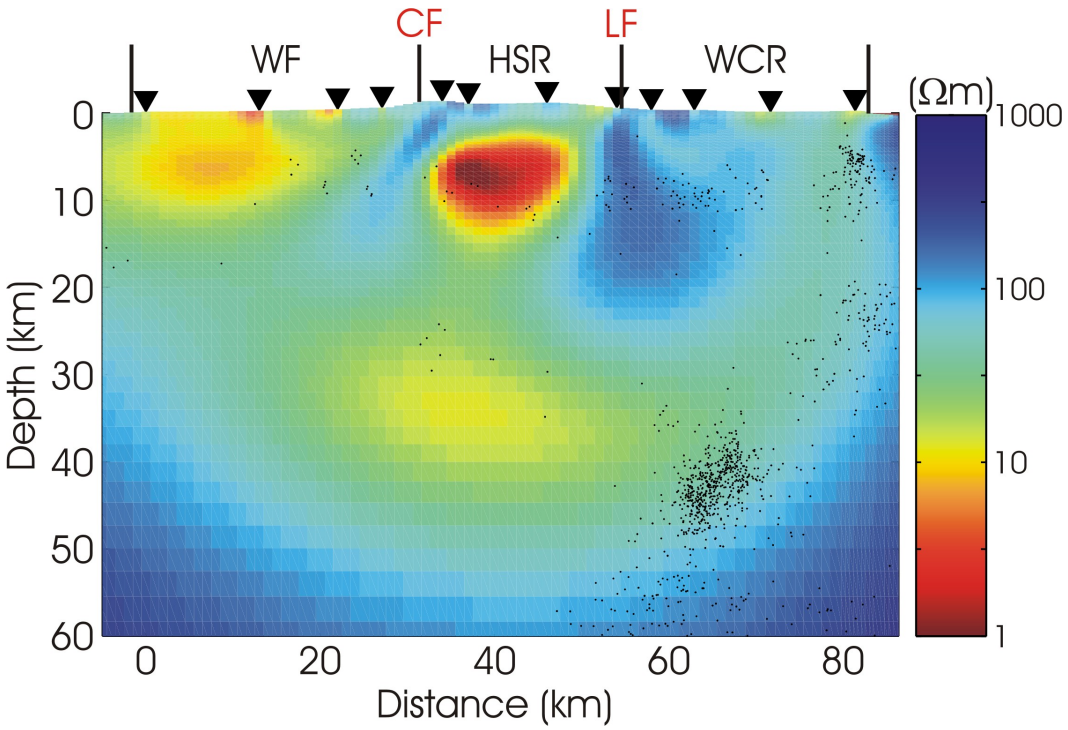

Figure 7-17. TE, TM and tipper resistivity inversion model showing hypocentres located within 20 km of the northern MT profile.

Extensive fluids introduced into the lower crust by dewatering of a subducting slab can permit extensive faulting and widespread deformation (Unsworth, 2009). In addition, fluids significantly lower the solidus of lithospheric materials, promoting melting that leads to further crustal weakening. Beneath the North Island in New Zealand, the Taupo Volcanic Zone defines an extensive region of volcanism and rifting associated with dewatering from Pacific Plate subduction (Heise et al., 2007). At the extreme north in Taiwan, the Tatun Volcanic Group (Figure 7-1) records episodic volcanism during 2.8–0.2 Ma (Kim et al., 2005a) in the extensional back-arc region of the Ryukyu subduction zone. This volcanic zone overlies an area of low v_p and high v_p/v_s anomalies that may indicate a region of magma in the upper crust (Kim et al., 2005b).

7.4 Summary – Northern Taiwan

While the resistivity model of northern Taiwan shares some similarity with the models of central and southern Taiwan, distinct features exist that can be explained by the subducting indenter tectonic model (Wu et al., 2009). Specifically, the conductance of the Northern Taiwan Conductor is much stronger than the Lishan Fault Conductors and occurs entirely west of the Lishan Fault beneath northern Taiwan. In addition, a broad zone of low resistivity is observed at lower crustal depths and dips shallowly to the east. Quantitative comparison of the resistivity model with a seismic P-wave velocity model revealed that aqueous fluids are required to explain both the Northern Taiwan Conductor and the broad conductive region in the lower crust. Further, partial melt may contribute to the Lower Crustal Conductor, but is not required. To determine if partial melt is present in the lower crust would require more accurate control on the thermal gradient, and reveals a need for improved surface heat flow data in Taiwan.

In the subducting indenter model, the Philippine slab contacts the Eurasian lithosphere at progressively greater depths north of 23.7°N (Wu et al., 2009). At the latitude of the northern Taiwan MT profile, contact occurs at ~50 km depth. In general, within a subducting oceanic slab, greenschist and lower amphibolite facies undergo dehydration prograde metamorphic reactions in the range 40-60 km depth (Wannamaker et al., 2009). Therefore, the dewatering Philippine slab provides a source of fluids beneath northern Taiwan that is not present at the latitudes of the central and southern TAIGER MT profiles. These additional fluids can explain the increased conductance observed beneath northern Taiwan, in comparison to central and southern Taiwan where plate contact occurs from the surface down.

8 SYNTHESIS OF THE TAIGER MT INVESTIGATION OF THE TAIWAN OROGEN

8.1 TAIGER MT Data Collection and Analysis

Arc-continent collisions are a fundamental plate tectonic process that controls continental gowth, orogen development and the occurrence of natural hazards and natural resources (Okaya et al., 2007). These processes all impact society and actively occur on the island of Taiwan where the Luzon Volcanic Arc collides with the passive margin of the Eurasian Plate. An important characteristic of the arc-continent collision in Taiwan is the oblique orientation between the LVA and the passive continental margin of Eurasia. Oblique convergence has produced an orogen that decreases in age from north to south. Investigation of the temporal evolution of the orogen is therefore made possible through studies at different latitudes along the island. Further, due to subduction at the Ryukyu trench at 23.7°N (Wu et al., 2009), plate contact occurs at progressively greater depths to the north and compression gives way to extension. Marked by the emergence of coral on elevated beaches in southern Taiwan and the collapse of mature mountains in northern Taiwan, all stages of orogen development, from beginning to end, can be studied in Taiwan.

Substantial previous geoscientific research has defined the geologic framework and plate kinematics of the Taiwan region. However, until recently, insufficient geophysical data existed to determine the lithospheric structure beneath the Central Ranges. These data are needed to unambiguously distinguish between differences in lithospheric structure predicted by a range of tectonic models (Suppe, 1981; Wu et al., 1997). The TAIGER project was initiated in 2004 to collect a data set capable of resolving these questions. This thesis consists of the

analysis and interpretation of the long-period MT data that were collected in Taiwan as a component of TAIGER. This multidisciplinary project has collected extensive active and passive, onshore and offshore seismic surveys. However, due to numerous delays, the seismic data acquisition was not completed until spring 2009 and results are not yet available for integration into this thesis.

MT data yield models of electrical resistivity, a parameter that is particularly sensitive to temperature and small amounts of conductive materials such as saline water, partial melt, graphite and sulphides (Unsworth, 2009). Within the middle and lower crust in active tectonic regions, large zones of low resistivity can be explained by the presence of partial melt and/or saline fluids (Jiracek et al., 2007). Despite occurrence in small quantities (a few percent), these phases can dramatically lower the shear strength of the lithosphere (Cox, 2005; Rosenberg and Handy, 2005). MT data are therefore able to provide constraints on the lithospheric rheology.

In total, 82 long-period MT measurements were recorded on three main profiles across southern (23.25°N), central (24°N) and northern (24.6°N) Taiwan. These data were carefully analysed and converted into models of electrical resistivity. Despite being located in a complex region that straddles a 3-D plate boundary, and surrounded by highly variable seawater depths, these data were shown to exhibit dominant 2-D behaviour. Justification for the detailed analysis of the 2-D resistivity models is provided by the similarity of structures observed in 2-D and 3-D models for each profile (Figure 8-1). Note that the 3-D models were not used for data interpretation since they can only represent the Earth with a coarse mesh.

8.2 MT Evidence for Thick-Skinned Tectonics in Central Taiwan

8.2.1 The Lishan Fault Conductor

Beneath the Lishan Fault in central Taiwan, a prominent vertical conductor was imaged (LFC) that is consistent with a wide zone of distributed interconnected

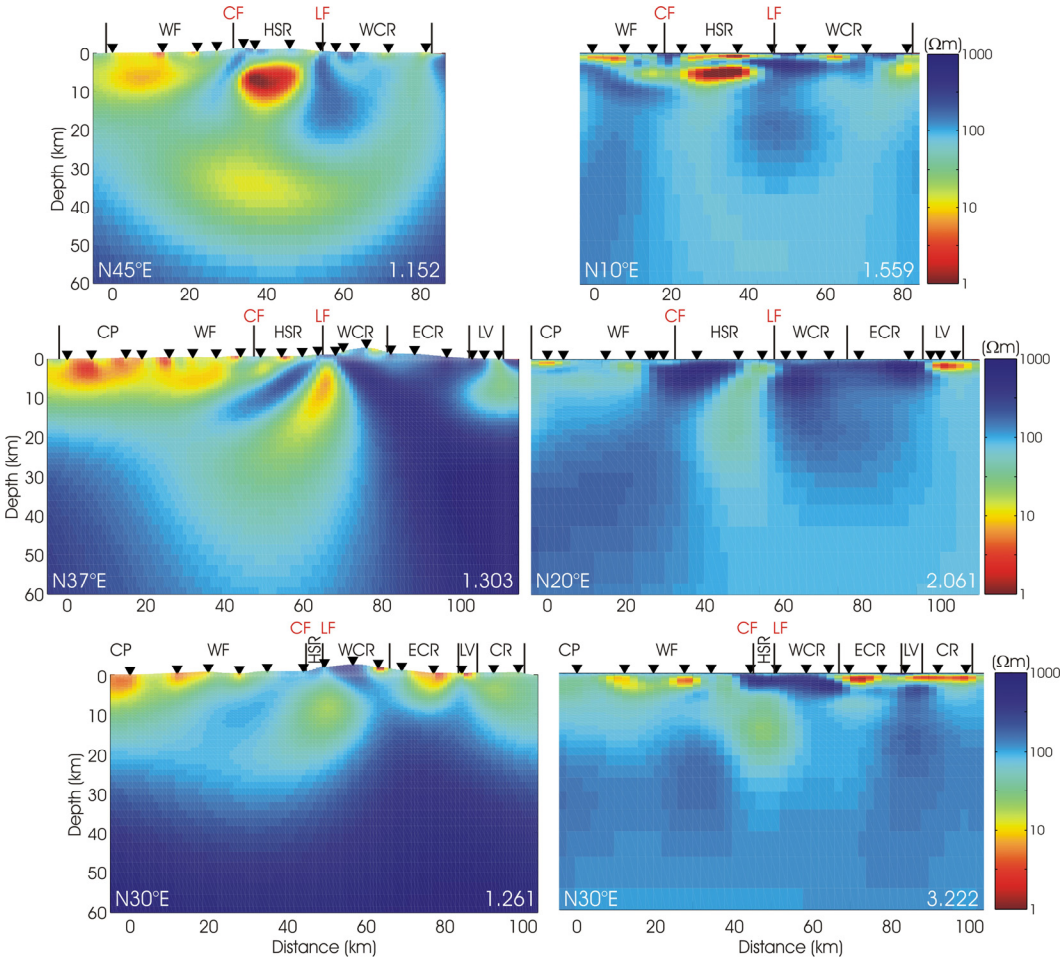

Figure 8-1. Left Panels: 2-D inversion models of the TE, TM and tipper data for north, central and south Taiwan. Right Panels: 3-D inversion models of the full MT impedance tensor data. The orientation of each profile is shown in the bottom left corner of each model, the r.m.s. data misfit is indicated in the bottom right corner. Models are aligned to the Lishan Fault.

saline fluids with a small percent porosity. This interpretation was supported by a quantitative comparison of the resistivity model with a tomographic seismic P-wave velocity model. In addition, the misfit to various data components were studied from a series of constrained inversions with a resistive basement fixed at incremental depths to give evidence that the LFC extended into the mid-crust (Bertrand et al., 2009).

In central Taiwan, by fitting earthquake hypocentres to inferred planar surfaces, a continuous band of seismicity was proposed to extend from the Western Foothills

to the Coastal Range at a depth of ~10 km (Carena et al., 2002). These sub-horizontal events were inferred to mark the basal décollement predicted to occur within the upper crust by the thin-skinned tectonic model (Suppe, 1981). However, other earthquake relocation studies fail to reproduce this pattern and show an aseimic gap beneath the Central Ranges and middle to lower crustal events that support the thick-skinned lithospheric deformation model (Wu et al., 2004; Gourley et al., 2007; Wu et al., 2008). Discrepancy between these earthquake relocation studies is in part due to the difficulty in locating events below islands where the spatial distribution of seismometers is limited (Cheng et al., 2002; Gourley et al., 2007).

The debate over which end-member tectonic model is applicable in central Taiwan was advanced by analysis of the LFC imaged with the TAIGER MT data (Figure 8-2). Bertrand et al. (2009) showed that this feature was inconsistent with the thin-skinned model, since thin-skinned deformation is inconsistent with a zone of interconnected aqueous fluids that crosses the inferred décollement. In contrast, the thick-skinned tectonic model predicts deformation to occur on the lithospheric scale and leads to the development of a crustal root beneath the Central Ranges. Dehydrating prograde metamorphic reactions would occur as the crust is thickened (Wannamaker et al., 2002) and can account for the source of fluids required in the middle and lower crust to explain the LFC (Figure 8-2).

8.2.2 Reactivation of Existing Structure

The resistivity models of central and southern Taiwan indicate that there is a steep contact between the Western Foothills fold-and-thrust belt and the slate belt of the Hseuhshan Range (Figure 8-3). Further, these resistivity models do not indicate that the sedimentary rocks of the Western Foothills underthrust the Hseuhshan Range. Low-angle thrust faults associated with regional shortening are predicted by thin-skinned tectonic models (Lee et al., 2002).

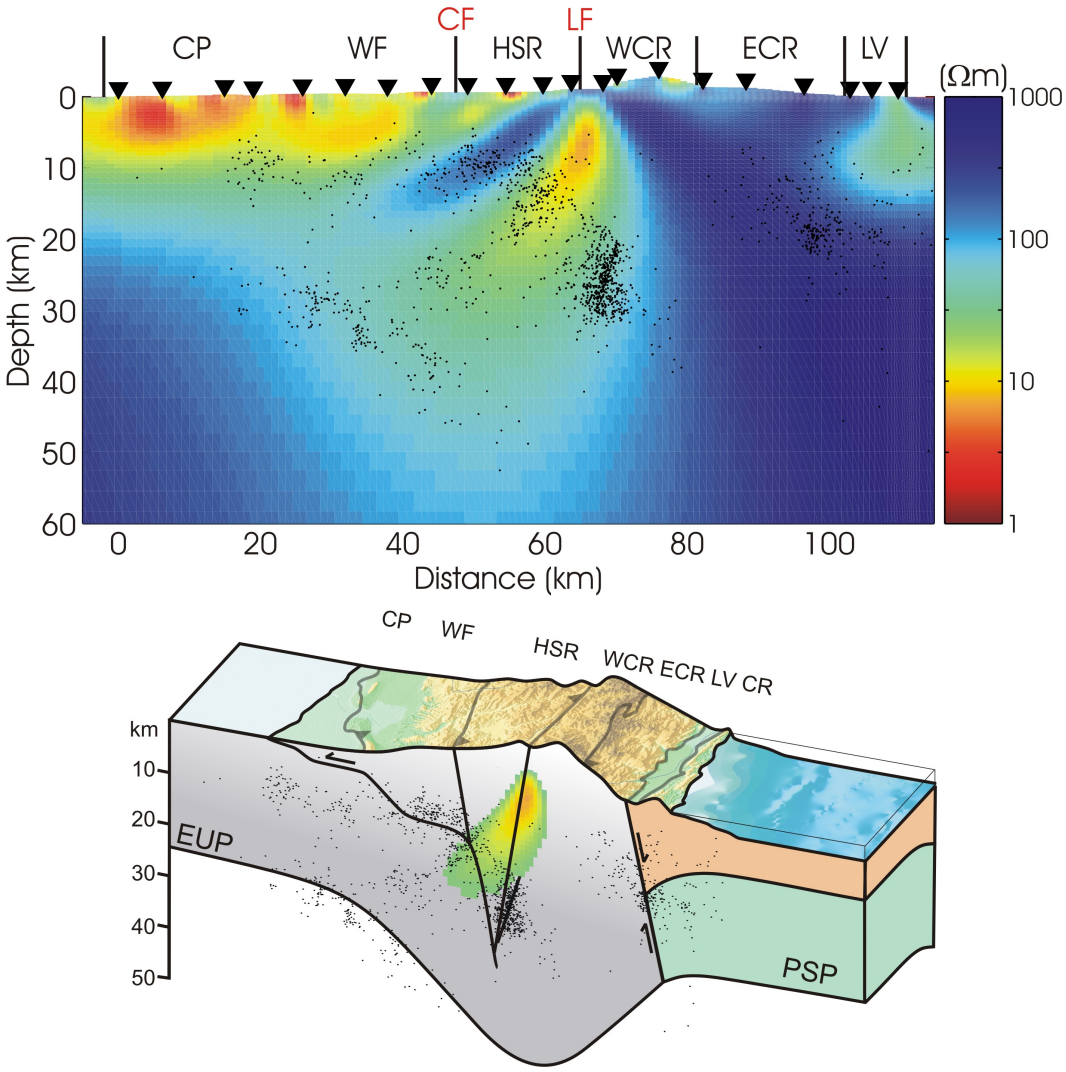

Figure 8-2. Top Panels: TE, TM and tipper 2-D inversion model of central Taiwan showing high quality relocated hypocentres occurring within 20 km of the profile (Wu et al., 2008). Bottom Panel: Schematic diagram showing relocated hypocentres from Wu et al. (2008) with fault interpretations. The Lishan Fault Conductor is overlayed, and a crustal root is shown below the Central Ranges to a depth of ~50 km.

Unfortunately, resolution of this contact is poor for these long-period MT data that are spaced ~5 km apart. Further, in central Taiwan the MT profile passed through the Puli basin that is located just east of the Chuchih Fault, marking the boundary between the WF and HSR. The low resistivity of the sedimentary deposits in this basin reduced the amplitudes of the measured electric fields. Coupled with the high level of cultural electromagnetic noise from the city of Puli and surrounding developments resulted in poor quality MT impedance data. In

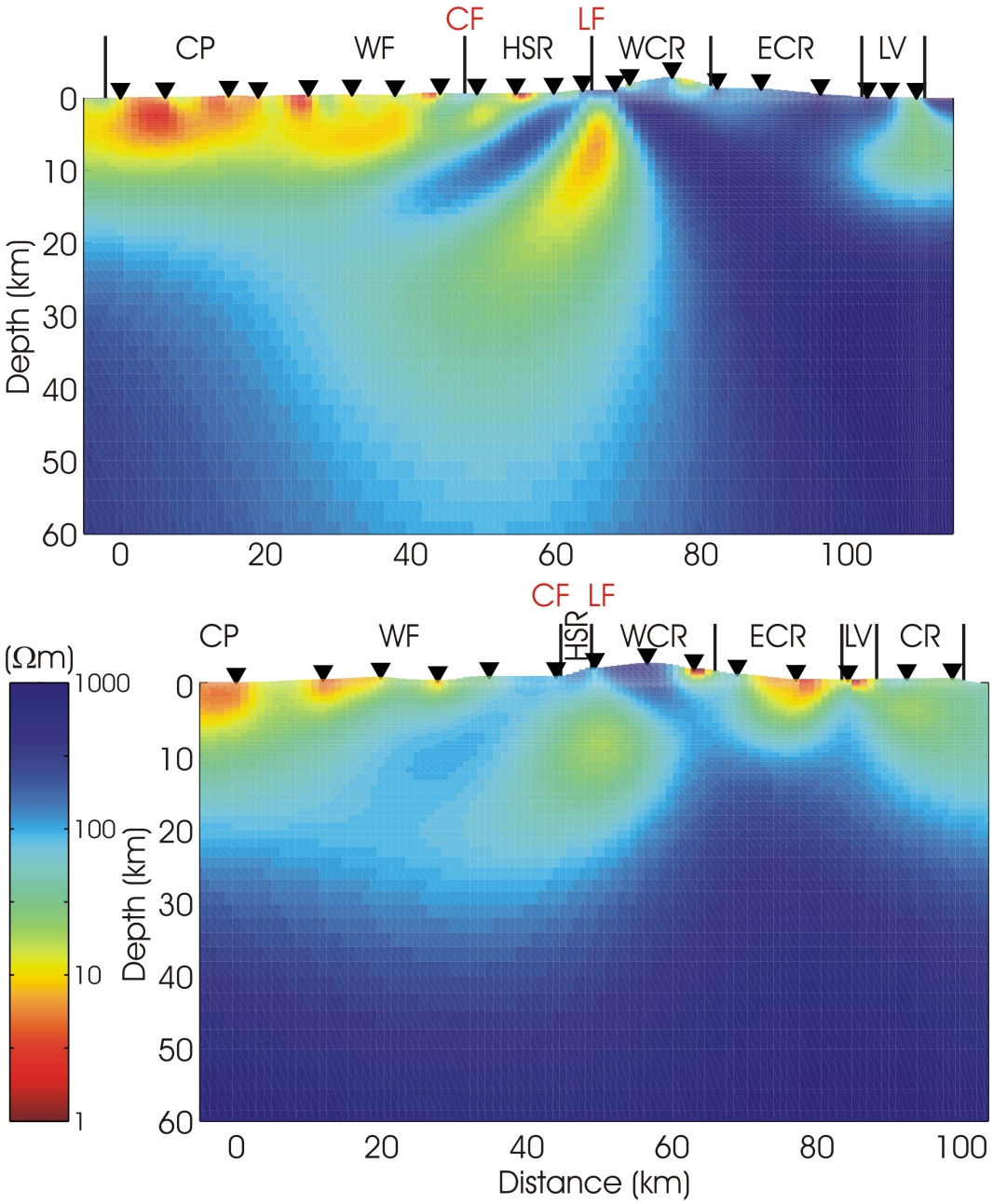

Figure 8-3. Top Panels: TE, TM and tipper 2-D inversion model of central Taiwan. Bottom Panel: TE, TM and tipper 2-D inversion model of southern Taiwan. Note that similar structures are imaged in both models, but that the conductance of the LFC is greater in central Taiwan.

southern Taiwan, the TM mode data across the Chuchih Fault, which are sensitive to lateral variations in structure, showed 3-D induction effects and were largely excluded from 2-D analysis. However, if the sedimentary material of the WF does underthrust the HSR, this configuration (resistor-over-conductor) would be

favourable for structural imaging by MT (Christopherson 1991). Therefore, the consistent evidence for a steep contact in both the central and southern resistivity models is compelling evidence for thick-skinned tectonics.

The Anderson (1905) theory of faulting predicts that thrust faults should form with a dip angle of 30° for maximum horizontal compressive stress. However, this theory is not universally applicable; if conditions are favourable, a pre-existing fault may be reactivated rather than initiation of a new fault. In Taiwan, Cenozoic rifting has left a legacy of normal faults in the passive margin of Eurasia that are now largely obscured by Pliocene-Pleistocene sediment from the adjacent orogen (Lee et al., 2002). For example, the Lishan Fault is interpreted as an inverted passive margin growth fault that shows oblique thrust movement (Angelier et al., 1990; Clark et al., 1993; Lee et al., 1997). Inversion of rift-related high-angle faults highlights the importance of pre-existing features in the development of the Taiwan orogen. In general, inversion can result in thick-skinned tectonics. Steeply dipping clusters of seismicity beneath the Central Ranges that show thrust fault focal mechanisms provide further evidence for deep collision-related deformation that supports the thick-skinned tectonic model (Lee et al., 2002; Gourley et al., 2007).

8.3 Orogen Evolution: Comparison of South and Central Taiwan

The Lishan Fault Conductor was also observed in the resistivity model of southern Taiwan (Figure 8-3). Note that an additional MT profile located between the southern and central TAIGER transects would be very useful for mapping the along-strike continuity of this feature. However, the strong similarity between the resistivity model in central and southern Taiwan suggests that the same style of tectonics is occurring in both locations. Data analysis in both locations was used to determine the depth extent of the LFC and showed that the LFC was required to extend below 10 km depth. In both locations the conductivity of the LFC was consistent with interconnected saline fluids with a small percent (0.5 - 2 %)

porosity. The consistent explanation for these similar along-strike features supports the thick-skinned lithospheric deformation model for the Taiwan orogen between ~23-24°N latitude.

While similar structure occurs in resistivity models of southern and central Taiwan, the conductance of the LFC is lesser in the south. This variation correlates with the time-axis of orogen evolution that follows the island strike. The fundamental geological concept of uniformitarianism (Lyell, 1830) provides the simple explanation that the southern MT model represents a glimpse of central Taiwan at ~1.75 Ma. The ongoing processes of deformation and dehyration metamorphism within a developing crustal root have occurred longer in central Taiwan, and result in the greater present day conductance observed in the middle and lower crust. These results are supported by tomographic seismic velocity models which indicate that the crustal root beneath central Taiwan (inferred by the 7.5 km/s contour) becomes shallower to the south (Rau and Wu, 1995).

8.4 The Subducting Indenter: Dewatering of the Philippine Slab

Beneath northern Taiwan at the latitude of the TAIGER MT profile (~24.7°N), the obliquely subducting Philippine Sea Plate contacts the Eurasian Plate at a depth of ~50 km and beneath the Lishan Fault (Wu et al., 2009). At this location, deformation due to the converging plates significantly differs in comparison to locations south of 23.7° N, where contact occurs from the surface down (Figure 8-4). The subducting indenter causes compression west of the plate contact (within the HSR), but permits extension to develop in the overlying Eurasian wedge, clearly expressed at the surface by the Ilan Plain. While the resistivity model of northern Taiwan shares some similarity with the models of central and southern Taiwan (e.g. low resistivity beneath the western foreland basin and high resistivity in the Central Ranges), significant variations occur that can be explained by the subducting indenter tectonic model (Figure 8-4).

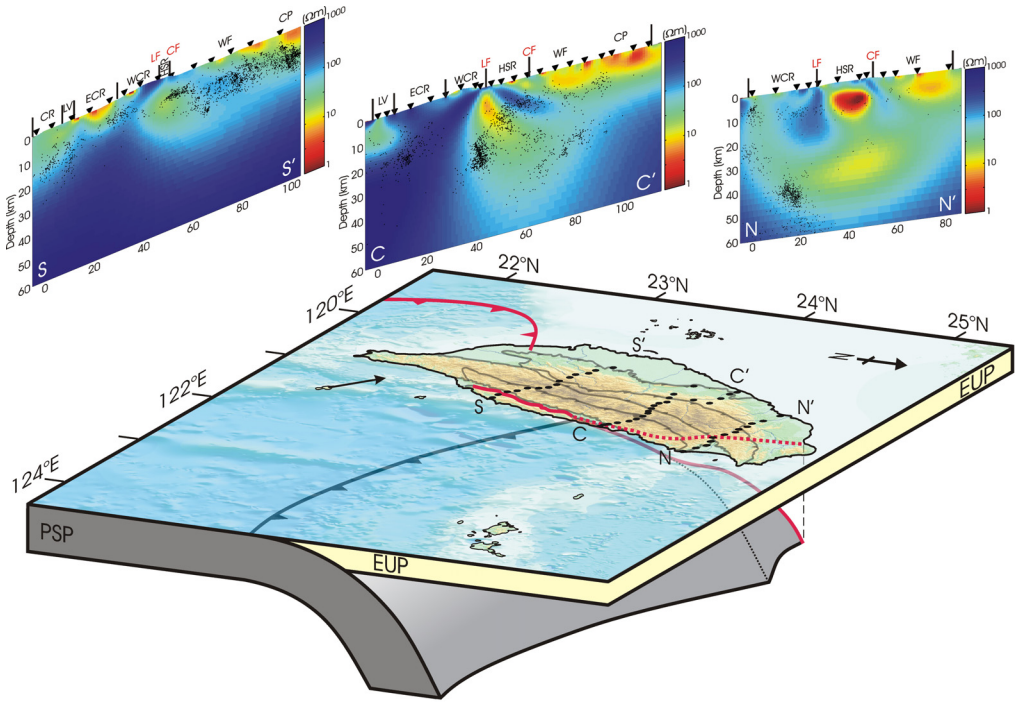

Figure 8-4. 3-D schematic of plate convergence in the region of Taiwan. The solid red line defines the western boundary of the Philippine Sea Plate. The 2-D resistivity models from the TAIGER MT data are shown above for comparison. Beneath northern Taiwan, the EUP is absent and likely removed by slab break-off.

8.4.1 The Lower Crustal Conductor

Most notably, a distributed zone of conductivity with down-to-the-east dip occurs in the lower crust beneath northern Taiwan. The diffuse eastern boundary of this zone coincides with a cluster of seismicity that marks the subducting PSP slab. While the uncertain temperature regime may permit partial melt to contribute to the low resistivities in this zone, saline aqueous fluids are required. The pattern of seismicity occurring at the perimeter of this conductor suggests that these events promote dewatering of the slab and fluid mobilization towards the surface. At depths of 40-60 km, greenschist and lower amphibolite facies within a subducting slab undergo dehydration metamorphic reactions (Wannamaker et al., 2009).

Note that the crust is also thickened beneath northern Taiwan at the latitude of the TAIGER MT profile. Although not yet constrained, the 7.5 km/s P-wave velocity contour in seismic tomography models has been used as a proxy for the depth to

the Moho beneath Taiwan (Wu et al., 2009). This contour indicates that the Moho depth is ~40-50 km beneath the centre of the northern MT profile.

Near to Taiwan, the subduction obliquity and rollback rate of the Ryukyu trench increases (Long and van der Hilst, 2006). Offshore northeastern Taiwan, opening of the Okinawa trough is estimated at ~1.5 cm/yr for the past 2 Ma (Sibuet et al., 1998), but may be as high as 5-6 cm/yr (Yu et al., 1997; Nakamura, 2004). At any rate, southwards propagation of the Ryukyu trench implies that contact between the Philippine Sea and Eurasian Plates occurred at progressively shallower depths in the past, for any fixed latitude beneath northern Taiwan (i.e. north of 23.7°N). Therefore, since a thickened crust exists beneath northern Taiwan and plate convergence would have occurred at shallower depths in the past, remnant fluids released by prograde metamorphic reactions due to deformation within the thickening crust would also contribute to the zones of low resistivity observed beneath northern Taiwan. In summary, two sources of fluids are possible in northern Taiwan to account for the low resistivity structures observed.

8.4.2 The Northern Taiwan Conductor

Is the NTC the along-strike continuation of the LFC identified in central and southern Taiwan? Spatially, the NTC occurs just west of the Lishan Fault beneath the HSR. In contrast, in central and southern Taiwan, the LFC was centred below the surface trace of the Lishan Fault. Further, the LFC was attributed to fluids released by prograde metamorphism within a thickening crust due to deformation caused by plate convergence. Does this same mechanism cause the NTC?

Unfortunately, additional MT data between the northern and central TAIGER profiles are required to unequivocally resolve these questions. However, two potential sources of fluids in the crust beneath northern Taiwan have been identified. In addition, the NTC is located ~60 km south of the Tatun Volcanic Group, which recorded episodic volcanism during 2.8–0.2 Ma (Kim et al., 2005a)

within the extensional back-arc region of the Ryukyu subduction zone. Given that the Tatun volcanoes have been dormant for 0.2 Ma and that the Ryukyu trench is propagating southwards, the NTC may be related more to extension within the back-arc region of the Ryukyu subduction zone, rather than crustal deformation processes below. That this zone of high conductivity is explained by fluids suggests significant weakening of the crust may be occurring – perhaps foreshawdowing the location of future Ryukyu back-arc volcanism.

8.5 Crustal Fluids

Small quantities of saline fluids (~0.5-2 % saturated porosity) have been proposed to explain the presence of major crustal conductive features imaged beneath Taiwan. However, to lower the resistivity below a few 100 Ωm requires that these fluids are interconnected through fracture networks, and/or grain edge wetting (Jiracek, 2007). Within ductile shear zones, saline fluids are likely to interconnect through grain-edge wetting (Holness, 1993; Tullis et al., 1996) since salts significantly lower the dihedral angle to ~40° (Watson and Brenan, 1987), which is below that required for interconnection (60°) in low porosity (< 1%) rocks (Watson et al., 1990). In addition, extensional fracture networks can initiate perpendicular to the minimum principal stress direction for elevated fluid pressures (Cox, 2005). Thus, in compressional tectonic environments, extensional cracks form horizontally and can cause widespread zones of low resistivity.

Clearly, to explain the large regions of crustal conductivity beneath Taiwan requires pervasive shear to promote fluid interconnection. Observation of outcrops along the Lishan Fault shows evidence for pure shear deformation in exposures of mid-crustal rocks (Dennis Brown, personal communication). These results support the interpretation that small quantities of saline fluids can explain the crustal conductors observed in the resistivity models of Taiwan. Further, that deformation is required to promote fluid interconnection supports the lithospheric-scale deformation predicted by the thick-skinned tectonic model.

8.6 Global Context: Comparison to Similar Tectonic Environments

The TAIGER MT data have provided constraints on the deformation processes that are related to the arc-continent collision in Taiwan. However, to determine if the tectonic style operating beneath the Taiwan orogen is unique or ubiquitous in a global context requires comparisons be made with studies from other areas that display similar tectonic characteristics.

8.6.1 East Timor: Active Arc-Continent Collision

In the late Miocene to early Pliocene, the westernmost Banda Arc collided with the continental shelf of the Indo-Australian Plate and ensuing deformation has formed the island of East Timor (Figure 8-5; Charlton, 1991). However, at present no Plio-Pleistocene andesitic volcanics of the Banda Arc have been accreted to the emergent island of Timor (Huang et al., 2000). Therefore, arc-continent collision is in the initial stages of development and comparable to southeastern Taiwan where the offshore volcanic islands of Lutao and Lanhsu mark the oceanward Luzon Volcanic Arc. Since no TAIGER MT data were collected south of the contact between the LVA and Eurasian margin (i.e. south of ~23.6°N, or south of the Longitudinal Valley) a direct comparison to initial arc-continent collision in East Timor is not possible.

8.6.2 Papua New Guinea: Active Arc-Continent Collision

Oblique arc-continent collision between the Bismarck Arc and the Indo-Australian Plate has occurred since the Pliocene (~3.5 Ma; Abbott et al., 1994) and formed Papua New Guinea (Figure 8-5). This collision has propagated southeastwards along the Ramu-Markham Fault, which is analogous to the Longitudinal Valley Fault in Taiwan (Huang et al., 2000). In fact, the geology of Papua New Guinea and Taiwan share many similarities. The Finisterre Range northeast of the Ramu-Markham Fault is comprised of volcanic arc and forearc materials unconformably overlain by younger limestones, and is the equivalent of

the Coastal Range province in Taiwan. To the southwest of the Ramu-Markham Fault, lies the New Guinea Highlands comprised of Mesozoic – Cenozoic crystalline rocks, and the Papuan fold-and-thrust belt; equivalent to the Central Ranges and Western Foothills in Taiwan, respectively (Huang et al., 2000).

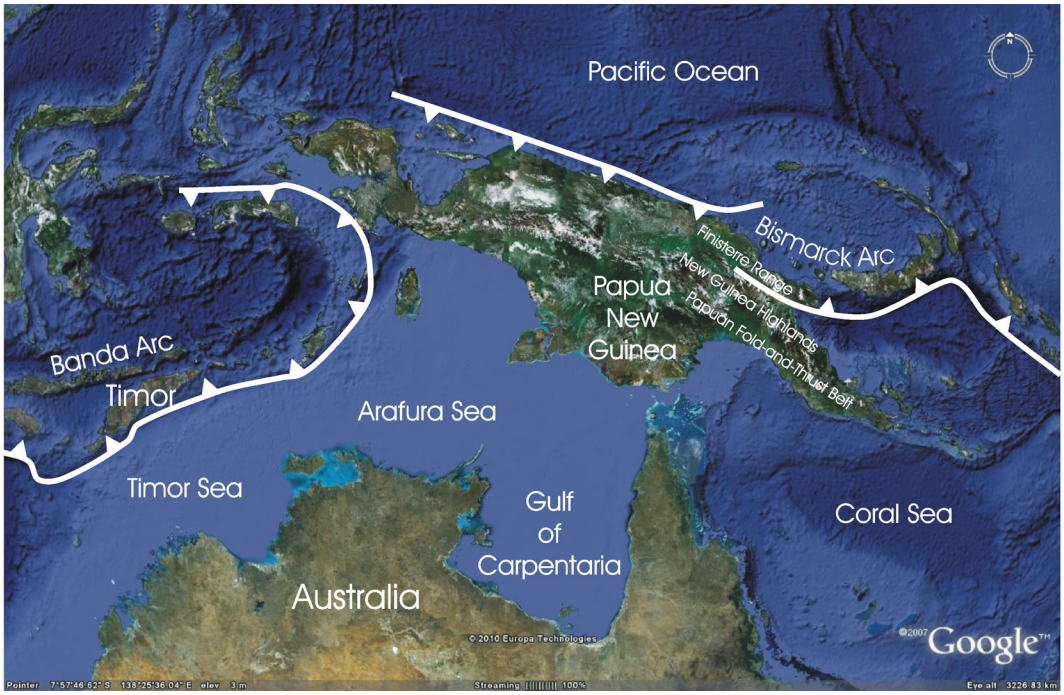

Figure 8-5. Regional map of southeast Asia showing plate boundaries that result in arc-continent collisions at Timor and Papua New Guinea.

Is deformation beneath the New Guinea Highlands lithospheric in scale as inferred beneath the Central Ranges in Taiwan? Models of offshore gravity data across the submerged Finisterre Range indicate a doubling of the crustal thickness to ~52 km beneath the collision zone (Abbott et al., 1994). In addition, both seismicity and seismic velocity models provide evidence for crustal thickening (Abers and Roecker, 1991). Notably, a northwards dipping Wadati-Benioff zone that marks the offshore subduction of the Indo-Australian Plate is absent beneath the Finisterre Range (Huang et al., 2000). While these data favour deformation by thick-skinned tectonics, higher resolution data are required to constrain this interpretation. Unfortunately, like early data acquisition in Taiwan, present geophysical surveys are largely focused in the Papuan fold-and-thrust belt motivated by hydrocarbon exploration. Owing to karstic limestone at the surface

that scatters seismic waves, MT has been used effectively to map the depth to the conductive sandstone layers below (Christopherson, 1991; Hoversten, 1996), but no island wide survey is available for comparison to the TAIGER MT data across the Taiwan orogen.

8.6.3 Southern Alps, New Zealand: Transpressional Collision

Both the South Island of New Zealand and the island of Taiwan lie on a transpressive plate boundary between oppositely dipping subduction zones (Wu F.T. et al., 2007a). In the South Island, the transpressional Alpine Fault marks the boundary between two continental fragments of Gondwanaland that have had a component of convergence since 5-10 Ma, and formed the Southern Alps (Walcott, 1998). These recent oblique collisions at the South Island and Taiwan are complementary and provide an ideal opportunity for comparative study. Further, a multidisciplinary geophysical investigation of the South Island orogeny (SIGHT – South Island Geophysical Transect) included coincident active source seismic and magnetotelluric data collected on a profile across the Southern Alps (Stern et al., 1997; Davey et al., 1998; Wannamaker et al., 2002). The SIGHT profile provides the orogen-scale MT data required for placing the TAIGER MT models in a global context.

A resistivity model derived from the SIGHT MT data revealed a widespread zone of low resistivity in the middle to lower crust. This conductive zone was interpreted to be caused by saline fluids (~1 %) released from prograde metamorphism and interconnected via shear deformation within a thickened crust (Wannamaker et al., 2002). This resistivity model bears strong resemblance to the TAIGER resistivity models of central and south Taiwan where the EUP and PSP are in contact from the surface down (Figure 8-6). Specifically, both locations show a pervasive region of low resistivity in the middle and lower crust that arc towards the surface near a major fault – the Alpine Fault in the South Island, and the Lishan Fault in Taiwan. The strong similarity of these resistivity models and

their support for thick-skinned tectonic models (Wu et al., 1997; Molnar et al., 1999) give strong indication for the common occurrence of lithospheric-scale deformation associated with orogeny. In addition, shear wave splitting delay times (Klosko et al., 1999; Savage et al., 2007) and the observation of a crustal root in active source seismic data (Davey et al., 2007; Stern et al., 2007) also provide strong evidence for thick-skinned tectonics in the Southern Alps.

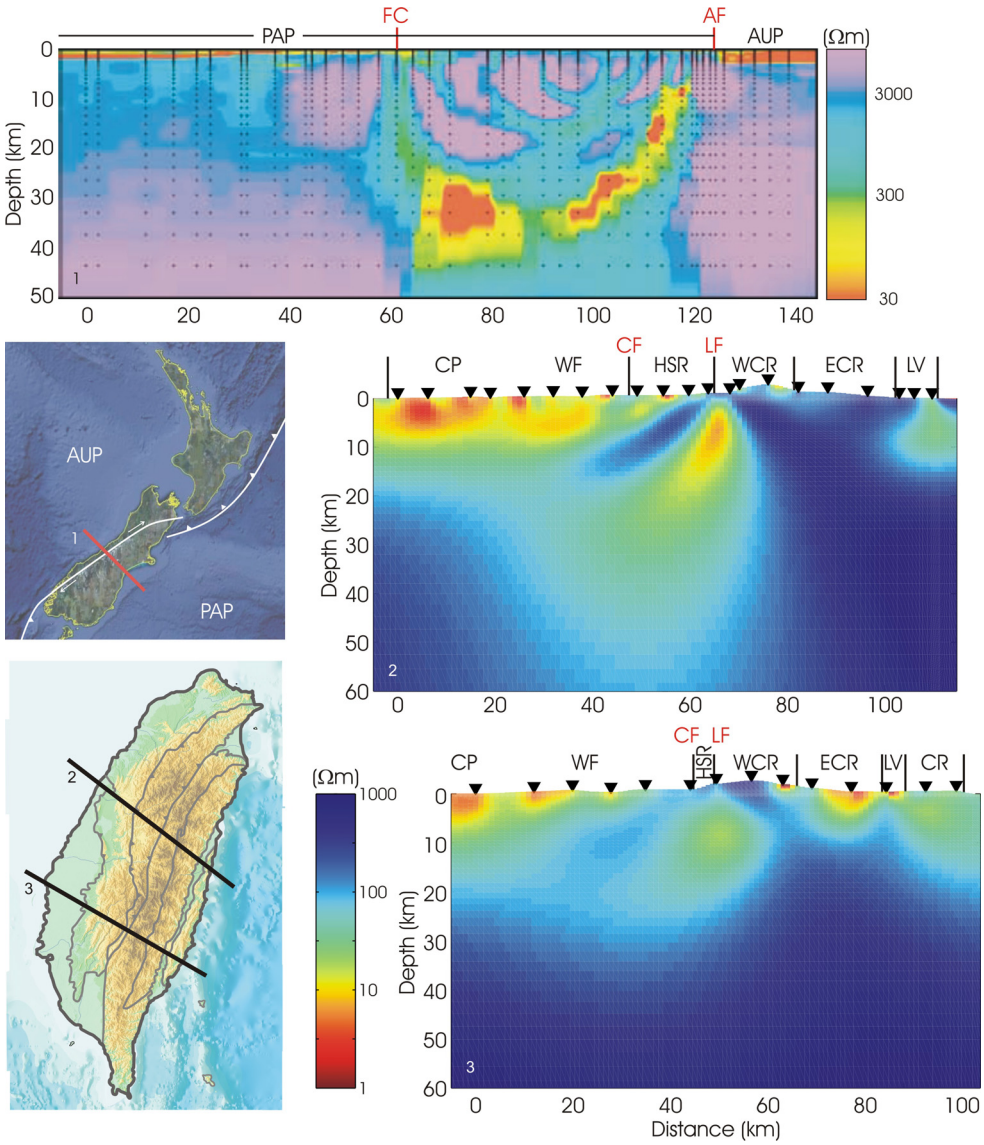

Figure 8-6. 1: 2-D resistivity model across the Southern Alps, New Zealand (Wannamaker et al., 2002). 2. 2-D resistivity model of central Taiwan (Bertrand et al., 2009). 3. 2-D resistivity model of southern Taiwan. Profile locations are shown in the maps and identified by number. Profiles are aligned to the Lishan (Taiwan) and Alpine (New Zealand) Faults. Pacific Plate PAP, Australian Plate AUP, Alpine Fault AF, Forest Creek Fault Zone FC.

8.6.4 Marlborough Region, New Zealand: Oblique Subduction System

In the north of the South Island, the Marlborough region contains a series of sub-parallel strike-slip faults that mark the transition from the Hikurangi subduction zone to the Alpine Fault (Figure 8-7 and 8-8; Wannmaker et al. 2009).

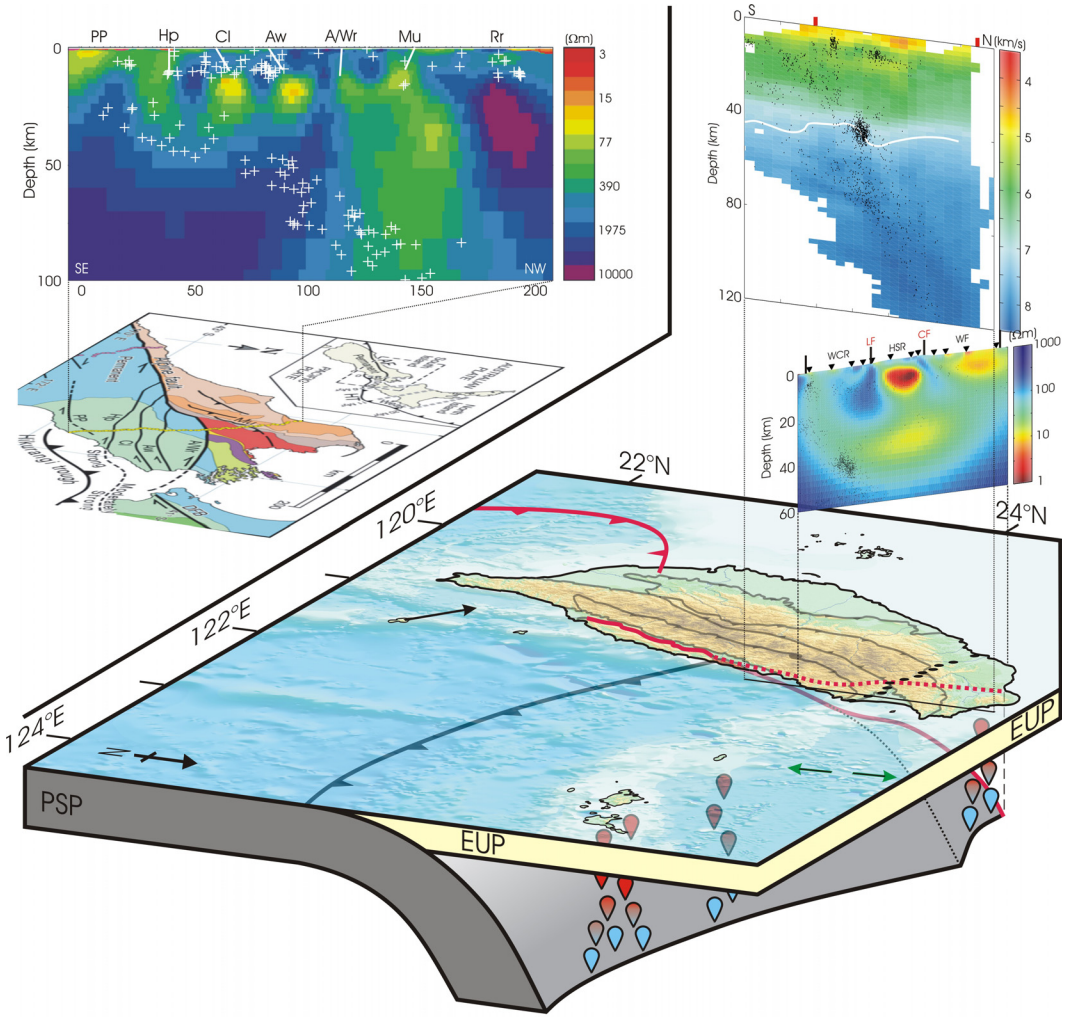

Figure 8-7. 3-D schematic of plate convergence in the region of Taiwan and comparison with the Marlborough region on the South Island of New Zealand. The map and 2-D resistivity model of Marlborough are from Wannamaker et al., 2009. The solid red line defines the western boundary of the Philippine Sea Plate. Blobs represent the dewatering (blue) of the subducting Philippine slab that promotes melting (red) of the overlying Eurasian wedge and leads to volcanism along the Ryukyu Arc. Green arrows indicate extension in the Okinawa trough, and the black arrow shows the relative plate convergence vector between the EUP and PSP (82 mm/yr, N54°W; Yu et al., 1997). Note that for clarity the inset map of Marlborough is shown enlarged in Figure 8-8.

The Marlborough region therefore shares some similarity with northern Taiwan, where subduction at the Ryukyu trench transitions to collision with the Eurasian continental margin. Note however, that oblique subduction along the Hikurangi trough is oriented nearly parallel to the South Island, while the Ryukyu trough rotates offshore eastern Taiwan and intersects the island nearly perpendicularly. The relative plate motion components in Taiwan (80 mm/yr convergence and 27 mm/yr transcurrent) and in the South Island (10 mm/yr convergence and 38 mm/yr transcurrent) reflect this variation in plate geoemtery (Wu F.T. et al., 2007a). Despite these differences in plate orientation and kinematics, a recent high-quality transect of MT soundings across the Marlborough advancing subduction system (Wannamaker et al., 2009) can be compared with the TAIGER MT profile across north Taiwan (Figure 8-7).

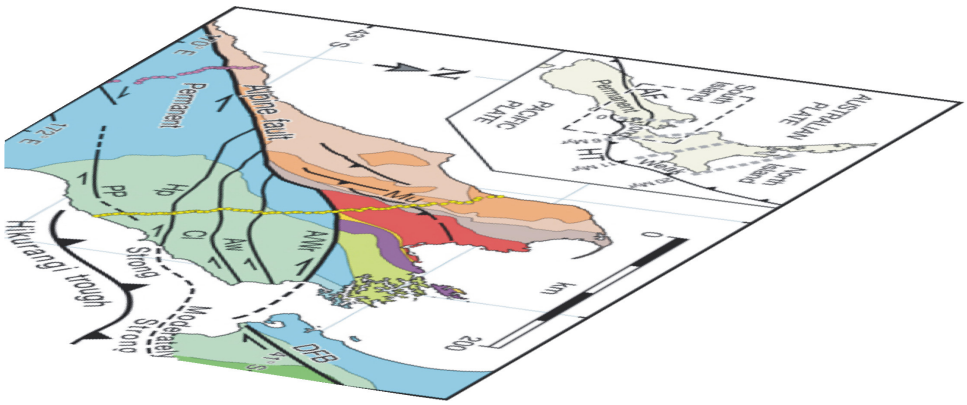

Figure 8-8. Geological terrane map of central New Zealand (Marlborough), modified from Wannamaker et al. 2009.

The resistivity model of the Marlborough region reveals a series of low resistivity zones that lie above the descending Pacific slab. These zones are inferred to be fluid-rich and indicate the upward migration of fluids from dehydration metamorphism of the Pacific slab (Wannamaker et al., 2009). Further, these low-resistivity zones coincide with some of the strike-slip faults in this region and may indicate zones of crustal weakening (Unsworth, 2009). In comparison to the north Taiwan MT model, these results support the interpretation that the pervasive zone of low resistivity in the lower crust beneath Taiwan is in part sourced from dewatering of the subducting Philippine Sea Plate.

8.7 Conclusions

The TAIGER MT data have provided information that was used to successfully constrain the style of tectonics operating beneath central Taiwan (Bertrand et al., 2009). In addition, comparison of the MT profiles collected in southern and central Taiwan provide a guide to the evolution of the arc-continent collision and indicate that the young orogen is developing through the same manner of thick-skinned lithospheric deformation. Finally, the TAIGER MT data collected in northern Taiwan indicate along-strike variations in the electrical resistivity structures that have been linked with the subducting indentation of the Philippine Sea Plate on the Eurasian Plate at progressively greater depths to the north.

Throughout Taiwan, saline fluids have been shown to explain key crustal low resistivity features. Fluids, even in small quantities, strongly lower both the electrical resistivity and the strength of lithospheric materials. Therefore, the MT technique is a particulary useful tool in active tectonic environments to map the location of fluids, and by extension, zones of weakness where deformation is localized.

In Taiwan, the crustal conductance observed beneath the TAIGER MT profiles increases progressively towards the north. The greatest conductance recorded beneath northern Taiwan indicates a widespread concentration of fluids within the lower crust sourced from deformation during crustal thickening and from dewatering of the subducting PSP slab. This widespread zone of fluids could facilitate the reorganization of this plate boundary. Extension in northern Taiwan, due to slab suction and rollback of the Ryukyu trench, is propagating onland and chasing the convergence to the south. Beneath central and southern Taiwan, fluids map a pervasive zone of collisional deformation that is lithospheric in scale.

BIBLIOGRAPHY

Abbott, L.D., E.A. Silver and J. Galewsky, Structural evolution of a modern arc-continent collision in Papua New Guinea: *Tectonics*, 13, 1007-1034, 1994.

Abers, G.A. and S.W. Roecker, Deep Structure of an Arc-Continent Collision: Earthquake Relocation and Inversion for Upper Mantle P and S Wave Velocities Beneath Papua New Guinea: *Journal of Geophysical Research*, 96, 6379-6401, 1991.

Ague, J.J., J. Park and D.M. Rye, Regional metamorphic dehydration and seismic hazard: *Geophysical Research Letters*, 25, 4221-4224, 1998.

Anderson, E.M., The Dynamics of Faulting: Oliver and Boyd, London, 206p, 1905.

Angelier, J., H.T. Chu and J.C. Lee, Shear concentration in a collision zone: kinematics of the Chihshang fault as revealed by outcrop-scale quantification of active faulting, Longitudinal Valley, eastern Taiwan, *Tectonophysics*, 274, 117-143, 1997.

Angelier, J., F. Bergerat, H.T. Chu and T.Q. Lee, Tectonic analysis and the evolution of a curved collision belt: The Hsüehshan range, northern Taiwan: *Tectonophysics*, 183, 77-96, 1990.

Aranovich, L.Ya. and R.C. Newton, H_2O activity in concentrated NaCl solutions at high pressures and temperatures measured by the brucite-periclase equilibrium: *Contributions to Mineralogy and Petrology*, 125, 200-212, 1996.

Archie, G.E., The electrical resistivity log as an aid in determining some reservoir characteristics: *Transactions of the American Institute of Mining and Metallurgical Engineers*, 146, 54-62, 1942.

Bahr, K., Interpretation of the Magnetotelluric impedance tensor: regional induction and local telluric distortion: *Journal of Geophysics*, 62, 119-127, 1988.

Barr, T.D. and F.A. Dahlen, Constraints on friction and stress in the Taiwan fold-and-thrust belt from heat flow and geochronology: *Geology,* 18, 111-115, 1990.

Barr, T.D. and F.A. Dahlen, Brittle frictional mountain building 2: Thermal structure and heat budget: *Journal of Geophysical Research*, 94, 3923-3947, 1989.

Barrier E. and J. Angelier, Active collision in eastern Taiwan: The Coastal range: *Tectonophysics*, 125, 39-72, 1986.

Bedrosian, P.A., A tale of two-inversions – a comparison of 3-D magnetotelluric inversion in a mineralized region: 19th Workshop on Electromagnetic Induction in the Earth: Beijing, China, Abstract S1.1_S30, 2008.

Bedrosian, P.A., N. Maercklin, U. Weckmann, Y. Bartov, T. Ryberg and O. Ritter, Lithology-derived structure classification from the joint interpretation of Magnetotelluric and seismic models: *Geophysical Journal International*, 170, 737-748, 2007.

Bedrosian, P.A., M.J. Unsworth, G.D. Egbert and C.H. Thurber, Geophysical images of the creeping segment of the San Andreas Fault: Implications for the role of crustal fluids in the earthquake process: *Tectonophysics*, 385, 137-158, 2004.

Berdichevsky, M.N. and M.S. Zhdanov, Advanced theory of deep geomagnetic sounding: Amsterdam, Elsevier, 408 p, 1984.

Bertrand, E.A., M.J. Unsworth, C.W. Chiang, C.S. Chen, C.C. Chen, F.T. Wu, E. Türkoğlu, H.L. Hsu and G.J., Hill, Magnetotelluric evidence for thick-skinned tectonics in central Taiwan: *Geology*, 37, 711-714, 2009.

Bibby, H.M., T.G. Caldwell and C. Brown, Determinable and non-determinable parameters of galvanic distortion in Magnetotellurics: *Geophysical Journal International*, 163, 915-930, 2005.

Bijwaard, H., W. Spakman and E.R. Engdahl, Closing the gap between regional and global travel time tomography: *Journal of Geophysical Research*, 103, 30055-30078, 1998.

Bos, A.G., W. Spakman and M.C.J. Nyst, Surface deformation and tectonics setting of Taiwan inferred from a GPS velocity field, *Journal of Geophysical Research*, 108, 2458, 2003.

Brasse, H., P. Lazeta, V. Rath, K. Schwalenberg, W. Soyer and V. Haak, The Bolivian Altiplano conductivity anomaly: *Journal of Geophysical Research*, 107, doi:10.1029/2001JB000391, 2002.

Brown, D., Personal Communication: *Email Correspondence*, Sept. 15, 2009.

Bürgmann, R. and G. Dresen, Rheology of the lower crust and upper mantle: Evidence from rock mechanics, geodesy, and field observations: *Annual Review of Earth and Planetary Science*, 36, 531-567, 2008.

Byerlee, J., Friction of Rocks: *Pure and Applied Geophysics*, 116, 615-626, 1978.

Byrne, T.B., J.R. Gourley and Y.C. Chan, Double indenters and oblique extrusion and extension in Taiwan: The colliding seamount analogy, 2005 Fall Meeting, American Geophysical Union, San Francisco, abs. Eos, Transactions, American Geophysical Union, Fall Meeting Supplement, Abstract T11B-0372, 2005.

Byrne, T.B. and C.S. Liu, eds., Geology and Geophysics of an Arc-Continent Collision, Taiwan: Boulder, Colorado, *Geological Society of America Special Paper 358*, 211 p, 2002.

Cagniard, L., Basic theory of the Magneto-Telluric method of geophysical prospecting: *Geophysics*, 8, 605-635, 1953.

Caldwell, T.G., H.M. Bibby and C. Brown, The magnetotelluric phase tensor: *Geophysical Journal International*, 158, 457-469, 2004.

Carena, S., J. Suppe and H. Kao, Active detachment of Taiwan illuminated by small earthquakes and its control of first-order topography, *Geology*, 30, 935-938, 2002.

Chai, B.H.T., Structure and tectonic evolution of Taiwan: *American Journal of Science*, 272, 389-422, 1972.

Chang, S.L. and C.C. Hu, Gravity and magnetic anomalies of Taiwan and their tectonic implication: *Memoirs of the Geological Society of China*, 4, 121-142, 1981.

Chapple, W.M., Mechanics of thin-skinned fold-and-thrust belts: *Geological Society of America Bulletin,* 89, 1189-1198, 1978.

Charlton, T.R., Postcollision extension in arc-continent collision zones, eastern Indonesia: *Geology*, 19, 28-31, 1991.

Chave, A.D. and J.T. Smith, On electric and magnetic galvanic distortion tensor decomposition: *Journal of Geophysical Research*, 99, 4669-4682, 1994.

Chemenda, A.I., R.K. Yang, J.F. Stephan, E.A. Konstantinovskaya and G.M. Ivanov, New results from physical modeling of arc-continent collision in Taiwan: Evolutionary model: *Tectonophysics*, 333, 159-178, 2001.

Chemenda, A.I., R.K. Yang, C.H. Hsieh and A.L. Groholsky, Evolutionary model for the Taiwan collision based on physical modeling: *Tectonophysics*, 274, 253-274, 1997.

Chen, C.C., S.C. Chi, C.S. Chen and C.H. Yang, Electrical structures of the source area of the 1999 Chi-Chi, Taiwan, earthquake: Spatial correlation between crustal conductors and aftershocks: *Tectonophysics*, 443, 280-288, 2007b.

Chen, C.C. and C.S. Chen, Sanyi-Puli conductivity anomaly in NW Taiwan and its implication for the tectonics of the 1999 Chi-Chi earthquake: *Geophysical Research Letters*, 29, 1166, 2002.

Chen, C.C., C.S. Chen and C.F. Shieh, Crustal electrical conductors, crustal fluids and 1999 Chi-Chi, Taiwan, Earthquake: *Terrestrial Atmospheric and Oceanic Sciences*, 13, 367-374, 2002.

Chen, C.C. and C.S. Chen, Preliminary report on the Sanyi-Puli seismic zone conductivity anomaly and its correlation with velocity structure and seismicity in the northwestern Taiwan: *Earth Planets and Space*, 52, 377-381, 2000a.

Chen, C.S., C.C. Chen, C.W. Chiang, H.L. Hsu, W.H. Chiu, M.J. Unsworth and E.A. Bertrand, Crustal resistivity anomalies beneath central Taiwan imaged by a broadband Magnetotelluric transect: *Terrestrial Atmospheric and Oceanic Sciences*, 18, 19-30, 2007a.

Chen, C.S. and C.C. Chen, Magnetotelluric soundings of the source area of the 1999 Chi-Chi earthquake in Taiwan: Evidence of fluids at the hypocentre: *Terrestrial Atmospheric and Oceanic Sciences*, 11, 679-688, 2000b.

Chen, C.S., Mapping plate boundaries using TEM method along the longitudinal valley, Taiwan: *Geophysics*, 63, 868-879, 1998a.

Chen, C.S., The subsurface structure of Taiwan: Preliminary results of a Magnetotelluric study: *The Leading Edge*, 17, 683-685, 1998b.

Chen, C.S., Deep electrical structure of Taiwan as inferred from Magnetotelluric observations: *Terrestrial Atmospheric and Oceanic Sciences*, 9, 51-68, 1998c.

Chen, J.S., A comparative study of the refraction and reflection seismic data obtained on the Changhua Plain to the Peikang Shelf, Taiwan: *Petroleum Geology of Taiwan*, 15, 199-217, 1978.

Chen, W.P. and P. Molnar, Focal depths of intracontinental and intraplate earthquakes and their implications for the thermal and mechanical properties of the lithosphere: *Journal of Geophysical Research*, 88, 4183-4214, 1983.

Cheng, W.B., Tomographic imaging of the convergent zone in Eastern Taiwan – A subducting forearc sliver revealed? *Tectonophysics*, 466, 170-183, 2009.

Cheng, W.B., C. Wang, C.T. Shyu and T.C. Shin, Crustal structure of the convergent plate-boundary zone, eastern Taiwan, assessed by seismic tomography: *in* Byrne, T.B. and C.S. Liu, eds., Geology and Geophysics of an Arc-Continent Collision, Taiwan: Boulder, Colorado, *Geological Society of America Special Paper 358*, 161-176, 2002.

Chi, W.R., J. Namson and J. Suppe, Stratigraphic record of plate interactions in the Coastal Range of eastern Taiwan: *Geological Society of China Memoir 4*, 155-194, 1981.

Chiang, C.W., C.C. Chen, M.J. Unsworth, E.A. Bertrand, C.S. Chen and H.L. Hsu, Deep electrical structure of southern Taiwan and its tectonic implications: *Terrestrial Atmospheric and Oceanic Sciences*, in review, 2009.

Chou, Y.W. and H.S. Yu, Structural expressions of flexural extension in the arc-continent collisional foredeep of western Taiwan, *in* Byrne, T.B. and C.S. Liu, eds., Geology and Geophysics of an Arc-Continent Collision, Taiwan: Boulder, Colorado, *Geological Society of America Special Paper 358*, 1-12, 2002.

Christensen, N.I. and W.D. Mooney, Seismic velocity structure and composition of the continental crust: A global view: *Journal of Geophysical Research*, 100, 9761-9768, 1995.

Christopherson, K.R., Applications of magnetotellurics to petroleum exploration in Papua New Guinea: A model for frontier areas: *Geophysics: The Leading Edge of Exploration*, April, 21-27, 1991.

Clark, M.B., D.M. Fisher, C.Y. Lu and C.H. Chen, Kinematic analysis of the Hseuhshan range, Taiwan: A large scale pop-up structure, *Tectonics*, 12, 205-207, 1993.

Clauser, C. and E. Huenges, Thermal conductivity of rocks and minerals, *in* T. Ahrens, ed. Rock physics and phase relations: A handbook of physical constants: *American Geophysical Union*, Washington D.C., 105-126, 1995.

Cloos, M., Lithospheric buoyancy and collisional orogenesis: Subduction of oceanic plateaus, continental margins, island arc, spreading ridges, and seamounts: *Geological Society of America Bulletin 105*, 715-737, 1993.

Condie, K.C., Plate tectonics and crustal evolution, 4th Edition: Oxford, Butterworth-Heinemann, 282 p, 1997.

Constable, C.S., R.L. Parker and C.G. Constable, Occam's inversion: A practical algorithm for generating smooth models from electromagnetic sounding data: *Geophysics*, 52, 289-300, 1987.

Cox, S. F., Coupling between deformation, fluid pressures, and fluid flow in ore-producing hydrothermal systems at depth in the crust, *in* Hedenquist, J.W., J.F.H. Thompson, R.J. Goldfarb and J.P. Richards, eds., Economic Geology 100th Anniversary Volume, *Economic Geology*, 39–76, 2005.

Craw, D., P.O. Koons, T. Horton and C.P. Chamberlain, Tectonically driven fluid flow and gold mineralization in active collisional orogenic belts: Comparison between New Zealand and western Himalaya: *Tectonophysics*, 348, 135–153, 2002.

Crespi, J.M., Y.C. Chan and M.S. Swaim, Synorogenic extension and exhumation of the Taiwan hinterland: *Geology*, 24, 247-250, 1996.

Currie, C., Personal Communication: *Email Correspondence*, Nov 13, 2009.

Dahlen F.A. and T.D. Barr, Brittle frictional mountain building 1. Deformation and mechanical energy budget: *Journal of Geophysical Research*, 94, 3906-3922, 1989.

Dahlen, F.A. and J. Suppe, Mechanics, growth, and erosion of mountain belts: *Geological Society of America*, Special Paper 218, 161-178, 1988.

Davey, F.J., T. Henyey, W.S. Holbrook, D. Okaya, T.A. Stern. A. Melhuish, S. Henrys, H. Anderson, D. Eberhart-Phillips, T. McEvilly, R. Uhrhammer, F. Wu, G.R. Jiracek, P.E. Wannamaker, G. Caldwell and N. Christensen, Preliminary results from a geophysical study across a modern continent-

continent collision plate boundary – The southern Alps, New Zealand: *Tectonophysics*, 288, 221-235, 1998.

Davis, D., J. Suppe and F.A. Dahlen, Mechanics of fold-and-thrust belts and accretionary wedges: *Journal of Geophysical Research,* 88, 1153-1172, 1983.

Deffontaines, B., O. Lacombe, J. Angelier, H.T. Chu, F. Mouthereau, C.T. Lee, J. Deramond, J.F. Lee, M.S. Yu and P.M. Liew, Quaternary transfer faulting in the Taiwan foothills: Evidence from a multi-source approach: *Tectonophysics*, 274, 61-82, 1997.

Dominguez, S., J.P. Avouac and M. Michel, Horizontal coseismic deformation of the 1999 Chi-Chi earthquake measured from SPOT satellite images: Implications for the seismic cycle along the western foothills of central Taiwan: *Journal of Geophysical Research*, 108, 2083, 2003.

Dorsey, R.J., Collapse of the Luzon volcanic arc during onset of the arc-continent collision: Evidence from a Miocene-Pliocene unconformity, eastern Taiwan: *Tectonics*, 11, 177-191, 1992.

Egbert, G.D., Processing and interpretation of electromagnetic induction array data: *Surveys in Geophysics*, 23, 207-249, 2002.

Egbert, G.D., Robust multiple-station Magnetotelluric data processing: *Geophysical Journal International*, 130, 475-496, 1997.

Egbert, G.D. and J.R. Booker, Robust estimation of geomagnetic transfer functions: *Geophysical Journal of the Royal Astronomical Society*, 87, 173-194, 1986.

Ernst, W. G., C.S. Ho, and J.G. Liou, Rifting, drifting, and crustal accretion in the Taiwan sector of the Asiatic continental margin, *in* Howell, D.G., ed., *Tectonostratigraphic terranes of the Circum-Pacific region*, 375-389, 1985.

Fischer, G., Electromagnetic induction effects at an ocean coast: Proceedings of the Institute of Electrical and Electronics Engineers, 67, 1050-1060, 1979.

Fisher, D.M., S. Willet, E.C. Yeh and M. Brooks Clark, Clevage fronts and fans as reflections of orogen stress and kinematics in Taiwan: *Geology*, 35, 65-68, 2007.

Fisher, D.M., C.Y. Lu and H.T. Chu, Taiwan slate belt: Insights into the ductile interior of an arc-continent collision: *in* Byrne, T.B. and C.S. Liu, eds., Geology and Geophysics of an Arc-Continent Collision, Taiwan: Boulder, Colorado, *Geological Society of America Special Paper 358*, 93-106, 2002.

Font, Y., C.S. Liu, P. Schnurle and S. Lallemand, Constraints on backstop geometry of the southwest Ryukyu subduction based on reflection seismic data: *Tectonophysics*, 333, 135-158, 2001.

Fowler, C.M.R., The Solid Earth, An Introduction to Global Geophysics, 2nd Edition: Cambridge, Cambridge University Press, 685 p, 2005.

Fuller, C.W., S.D. Willett, D.M. Fisher and C.Y. Lu, A thermomechanical wedge model of Taiwan constrained by fission-track thermochronometry: *Tectonophysics*, 425, 1-24, 2006.

Fuller, C.W., S.D. Willet, N. Hoivus and R. Slingerland, Erosion rate for Taiwan mountain basins: New determinations from suspended sediment records and a stochastic model of their temporal variation: *The Journal of Geology*, 111, 71-87, 2003.

Fuller C.W., S.D. Willett and D.M. Fisher, Exhumational steady state in Taiwan: Quantification through thermomechanical modeling: *Eos Transactions of the American Geophysical Union*, 83, 47, T71A-1151, 2002.

Gallardo, L.A., and M.A. Meju, Joint two-dimensional cross-gradient imaging of Magnetotelluric and seismic traveltime data for structural and lithological classification: *Geophysical Journal International*, 169, 1261-1272, 2007.

Gamble, T.D., W.M. Goubeau and J. Clarke, Magnetotellurics with a remote reference: *Geophysics*, 44, 53-68, 1979.

Gourley, J.R., T. Byrne, Y.C. Chan, F. Wu and R.J. Rau, Fault geometries illuminated from seismicity in central Taiwan: Implications for crustal scale structural boundaries in the northern central range: *Tectonophysics*, 445, 168-185, 2007.

Grevemeyer, I. and V.M. Tiwari, Overriding plate controls spatial distribution of megathrust earthquakes in the Sunda-Andaman subduction zone: *Earth and Planetary Science Letters*, 251, 199-208, 2006.

Griffiths, D.J., Introduction to Electrodynamics, 3rd Edition: Prentice Hall, 576 p, 1999.

Groom, R.W. and K. Bahr, Correction for near-surface effects: decomposition of the Magnetotelluric impedance tensor in the presence of local three-dimensional galvanic distortion: *Surveys in Geophysics*, 13, 341-379, 1992.

Groom, R.W. and R.C. Bailey, Decomposition of the Magnetotelluric impedance tensor in the presence of local three-dimensional galvanic distortion: *Journal of Geophysical Research*, 94, 1913-1925, 1989.

de Groot-Hedlin, C., Removal of static shift in two-dimensions by regularized inversion: *Geophysics*, 56, 2102-2106, 1991.

de Groot-Hedlin, C. and S. Constable, Occam's inversion to generate smooth, two-dimensional model from Magnetotelluric data: *Geophysics*, 55, 1613-1624, 1990.

Hacikoylu, P., J. Dvorkin, J. and Mavko, G., Resistivity-velocity transforms revisited: *The Leading Edge*, 25, 1006-1009, 2006.

Hall, R., Cenozoic geological and plate tectonic evolution of SE Asia and the SW Pacific: Computer-based reconstructions and animations: *Journal of Asian Earth Sciences,* 20, 353-434, 2002.

Hall, R., Cenozoic plate tectonics reconstructions of SE Asia: *Geological Society of London Special Publication*, 126, 11-23, 1997.

Hansen, P.C., Analysis of discrete ill-posed problems by means of the L-curve: *Society for Industrial and Applied Mathematics*, 34, 561-580, 1992.

Hao, K.C., F.T. Wu, D. Okaya, B.S. Huang and W.T. Liang, SKS/SKKS splitting and Taiwan orogeny: *Geophysical Research Letters*, 36, L12303, 2009.

Hartshorn, K., N. Hovius, W.B. Dade and R.L. Slingerland, Climate-driven bedrock incision in an active mountain belt: *Science*, 297, 2036, 2002.

Heise, W., T.G. Caldwell, H.M. Bibby and S.C. Bannister, Three-dimensional modeling of Magnetotelluric data from the Rotokawa geothermal field, Taupo volcanic zone, New Zealand: *Geophysical Journal International*, 173, 740-750, 2008.

Heise, W., H.M. Bibby, T.G. Caldwell, S.C. Bannister, Y. Ogawa, S. Takakura and T. Uchida, Melt distribution beneath a young continental rift: The Taupo volcanic zone, New Zealand: *Geophysical Research Letters*, 34, L14313, 2007.

Heise, W., T.G. Caldwell, H.M. Bibby and C. Brown, Anisotropy and phase splits in magnetotellurics: *Physics of the Earth and Planetary Interiors*: 158, 107-121, 2006.

Hetland, E.A. and F.T. Wu, Deformation of the Philippine Sea plate under the coastal range, Taiwan: Results from an offshore-onshore seismic experiment: *Terrestrial Atmospheric and Oceanic Sciences*, 9, 363-378, 1998.

Hickman, J.B., D.V. Wiltschko, J.H. Hung, P. Fang and Y. Bock, Structure and evolution of the active fold-and-thrust belt of southwestern Taiwan from global positioning system analysis, *in* Byrne, T.B. and C.S. Liu, eds., Geology and Geophysics of an Arc-Continent Collision, Taiwan: Boulder, Colorado, *Geological Society of America Special Paper 358*, 75-92, 2002.

Hill, G.J, T.G. Caldwell, W. Heise, D.G. Chertkoff, H.M. Bibby, M.K. Burgess, J.P. Cull and R.A.F. Cas, Distribution of melt beneath Mount St Helens and Mount Adams inferred from magnetotelluric data: *Nature Geoscience*, 2, 785-789, 2009.

Ho, C.S., An introduction to the geology of Taiwan, explanatory text of the geologic map of Taiwan: Taipei, Taiwan, 192 p, 1988.

Ho, C.S., Geologic map of Taiwan: Central Geological Survey, Ministry of Economic Affairs: Taipei, Taiwan, scale 1:500,000, 1986.

Holness, M.B., Temperature and pressure dependence of quartz-aqueous fluid dihedral angles: the control of adsorbed H_2O on the permeability of quartzites: *Earth and Planetary Science Letters*, 117, 363-377, 1993.

Hoversten, G. M., Papua New Guinea MT: Looking where Seismic is Blind: *Geophysical Prospecting*, 44, 935-961, 1996.

Hsieh, M.L. and P.K. Kneupfer, Synchroneity and morphology of Holocene river terraces in the southern Western Foothills, Taiwan: a guide to interpreting and correlating erosional river terraces across growing anticlines, *in* Byrne, T.B. and C.S. Liu, eds., Geology and Geophysics of an Arc-Continent Collision, Taiwan: Boulder, Colorado, *Geological Society of America Special Paper 358*, 55-74, 2002.

Hsieh, S.H. and C.C. Hu, Gravity and magnetic studies of Taiwan: *Petroleum Geology of Taiwan*, 10, 283-321, 1972.

Hsu, Y.J., S.B. Yu, M Simmons, L.C. Kuo and H.Y. Chen, Interseismic crustal deformation in the Taiwan plate boundary zone revealed by GPS observations, seismicity, and earthquake focal mechanisms: *Tectonophysics*, in press, 2009.

Hsu, Y.J., M. Simons, S.B. Yu, L.C. Kuo and H.Y. Chen, A two-dimensional dislocation model for interseismic deformation of the Taiwan mountain belt: *Earth and Planetary Science Letters*, 211, 287-294, 2003.

Hsu, S.K., C.S. Liu, C.T. Shyu, S.Y. Liu, J.C. Sibuet, S. Lallemand, C. Wang and D. Reed, New gravity and magnetic anomaly maps in the Taiwan-Luzon region and their preliminary interpretation: *Terrestrial Atmospheric and Oceanic Sciences*, 9, 509-532, 1998.

Hu, J.C., S.B. Yu, H.T. Chu and J. Angelier, Transition tectonics of northern Taiwan induced by convergence and trench retreat, *in* Byrne, T.B. and C.S. Liu, eds., Geology and Geophysics of an Arc-Continent Collision, Taiwan: Boulder, Colorado, *Geological Society of America Special Paper 358*, 147-160, 2002.

Huang, B.S., W.G. Huang, W.T. Liang, R.J. Rau and N. Hirata, Anisotropy beneath an active collision orogen of Taiwan: results from across islands array observations: *Geophysical Research Letters*, 33, L24302, 2006.

Huang, C.Y., P.B. Yuan and S.J. Tsao, Temporal and spatial records of active arc-continent collision in Taiwan: A synthesis: *GSA Bulletin*, 118, 274-288, 2006.

Huang, C.Y., P.B. Yuan, C.W. Lin, T.K. Wang and C.P. Chang, Geodynamic processes of Taiwan arc-continent collision and comparison with analogs in Timor, Papua New Guinea, Urals and Corsica: *Tectonophysics*, 320, 1-21, 2000.

Huang, C.Y., C.W. Lin, W.C. Chen, Y.G. Chen, S.B. Yu, I.P. Chia, M.D. Lu, C.S. Hou and S.Y. Wang, Seismic geology of the Chi-Chi earthquake, *in* International workshop on Chi-Chi, Taiwan, Earthquake of September 21, 1999: *National Science Council Report*, 3.1-3.8, 1999.

Huang, T., Significant new look on the Tertiary stratigraphy of Taiwan: *Petroleum Geology of Taiwan*, 15, 167-179, 1978.

Hubbard, J. and J.H. Shaw, Uplift of the Longmen Shan and Tibetan plateau, and the 2008 Wenchuan (M=7.9) earthquake, *Nature*, 458, 194-197, 2009.

Hung, J.H., D.V. Wiltschko, H.C. Huang, J.H. Hickman, P. Fang and Y. Bock, Structure and motion of the southwestern Taiwan fold and thrust belt: *Terrestrial Atmospheric and Oceanic Sciences*, 10, 543-568, 1999.

Hung, J.H. and D.V. Wiltschko, Structure and kinematics of arcuate thrust faults in the Miaoli-Cholan area of western Taiwan: *Petroleum Geology of Taiwan*, 28, 59-96, 1993.

Hwang, C., Y.S. Hsiao, H.S. Shih, M. Yang, K.H. Chen, R. Forsberg and A.V. Olesen, Geodetic and geophysical results from a Taiwan airborne gravity survey: Data reduction and accuracy assessment: *Journal of Geophysical Research*, 112, B04407, 2007.

Hwang, W.T. and C.Y. Wang, Sequential thrusting model for mountain building: Constraints from geology and heat flow of Taiwan: *Journal of Geophysical Research*, 98, 9963-9973, 1994.

Hyndman, R.D., C.A. Currie and S.P. Mazzotti, Subduction zone backarcs, mobile belts, and orogenic heat: *Geological Society of America Today*, 15, 4-10, 2005.

Ichihara, H. and T. Mogi, A realistic 3-D resistivity model explaining anomalous large Magnetotelluric phases: the L-shaped conductor model: *Geophysical Journal International*, 179, 14-17, 2009.

Jiracek, G.R., V.M. Gonzalez, T.G. Caldwell, P.E. Wannamaker and D. Kilb, Seismogenic, electrically conductive, and fluid zones at continental plate boundaries in New Zealand, Himalaya, and California-USA, *in* Okaya, D., T. Stern and F. Davey, A continental plate boundary: tectonics of South Island, New Zealand: *AGU Geophysical Monograph 175,* 347-369, 2007.

Jiracek, G.R., Near-surface and topographic distortions in electromagnetic induction: *Surveys in Geophysics*, 11, 163-203, 1990.

Jones, A.G., Electrical conductivity of the continental lower crust, *in* Fountain, D.M., R. Arculus and R.W. Kay, Continental lower crust, Developments in Geotectonics, 23: New York, Elsevier, 81-43, 1992.

Jones, F.W. and A.T. Price, The perturbations of alternating geomagnetic fields by conductivity anomalies: *Geophysical Journal of the Royal Astronomical Society*, 20, 317-334, 1970.

Jones, S.M., C. McCann, T.R. Astin and J. Sothcott, The effects of pore-fluid salinity on ultrasonic wave propagation in sandstones: *Geophysics*, 63, 928-934, 1998.

Kao, H. and W.P. Chen, The Chi-Chi earthquake sequence: Active, out-of-sequence thrust faulting in Taiwan: *Science*, 288, 2346-2349, 2000.

Kao, H., G.C. Huang and C.S. Liu, Transition from oblique subduction to collision in the northern Luzon arc-Taiwan region: Constraints from

bathymetry and seismic observations: *Journal of Geophysical Research,* 105, 3059-3079, 2000.

Kao, H., S.S.J. Shen and K.F. Ma, Transition from oblique subduction to collision: Earthquakes in the southernmost Ryukyu arc-Taiwan region: *Journal of Geophysical Research*, 103, 7211-7229, 1998.

Karato, S.I. and H.R. Wenk, Plastic deformation of minerals and rocks: *Reviews in Mineralogy and Geochemistry*, Mineralogical Society of America, 420 p, 2002.

Katsube, T.J. and M. Mareschal, Petrophysical modeling of deep electrical conductors: Graphite lining as a source and its disconnection due to uplift: *Journal of Geophysical Research*, 98, 8019-8030, 1993.

Kaufman, A.A. and G.V. Keller, The Magnetotelluric Sounding Method: Amsterdam, Elsevier, 595 p, 1981.

Kim, K.H., C.H. Chang, K.F. Ma, J.M. Chiu, and K.C. Chen, Modern seismic observations in the Tatun volcano region of northern Taiwan: seismic/ volcanic hazard adjacent to the Taipei metropolitan area, *Terrestrial Atmospheric and Oceanic Sciences*, 16, 579-594, 2005a.

Kim, K.H., J.M. Chiu, J. Pujpl, K.C. Chen, B.S. Huang, Y.H. Yeh and P. Shen, Three-dimensional Vp and Vs structural model associated with the active subduction and collision tectonics in the Taiwan region: *Geophysical Journal International*, 162, 204-220, 2005b.

Kim, K.H., J.M. Chiu, H. Konn, Q. Liu and Y.H. Yeh, A preliminary study of crustal structure in Taiwan region using receiver function analysis: *Geophysical Journal International*, 156, 146-164, 2004.

Klosko, E. R., F. T. Wu, H. J. Anderson, D. Eberhart-Phillips, T. V. McEvilly, E. Audoine, M. K. Savage and K. R. Gledhill, Upper mantle anisotropy in the New Zealand Region: *Geophysical Research Letters*, 26, 1497-1500, 1999.

Kuo, B.Y., C.C. Chen and T.C. Shin, Split S-wave forms observed in northern Taiwan; implications for crustal anisotropy: *Geophysical Research Letters*, 21, 1491-1494, 1994.

Lachenbruch, A.H., J.H. Sass, G.D. Clow and R. Weldon, Heat flow at Cajon Pass: California, revisited: *Journal of Geophysical Research*, 100, 2005-2012, 1995.

Lacombe, O., F. Mouthereau, J. Angelier and B. Deffontaines, Structural, geodetic and seismological evidence for tectonic escape in SW Taiwan: *Tectonophysics,* 333, 323-345, 2001.

Lacombe, O., F. Mouthereau, B. Deffontaines, J. Angelier, H.T. Chu and C.T. Lee, Geometry and Quaternary kinematics of fold-and-thrust units of southwestern Taiwan: *Tectonics*, 18, 1198-1223, 1999.

Lallemand, S.E., Y. Font, H. Bijwaard and H. Kao, New insights on 3-D plates interaction near Taiwan from tomography and tectonic implications: *Tectonophysics*, 335, 229-253, 2001.

Lallemand, S.E. and C.S. Liu, Geodynamic implications of present-day kinematics in the southern Ryukyus: *Journal of the Geological Society of China*, 41, 551-564, 1998.

Lallemand, S.E., C.S. Liu and Y. Font, A tear fault boundary between the Taiwan orogen and the Ryukyu subduction zone: *Tectonophysics*, 274, 171-190, 1997.

Lan, C.Y., B.M. Jahn, A.S. Mertzman and T.W. Wu, Subduction-related granitic rocks of Taiwan: *Journal of Southeast Asian Earth Sciences*, 14, 11-28, 1996.

Ledo, J., 2-D versus 3-D magnetotelluric data interpretation: *Surveys in Geophysics*, 26, 671-806, 2005.

Lee, C.R. and W.T. Cheng, Preliminary heat flow measurements in Taiwan: *Fourth Circum-Pacific Energy and Mineral Resources Conference*, Singapore, 1986.

Lee, C.I., Y.L. Chang and M.P. Coward, Inversion tectonics of the fold-and-thrust belt western Taiwan: *in* Byrne, T.B. and C.S. Liu, eds., Geology and Geophysics of an Arc-Continent Collision, Taiwan: Boulder, Colorado, *Geological Society of America Special Paper 358*, 13-30, 2002.

Lee, J.C., J. Angelier, H.T. Chu, J.C. Hu and F.S. Jeng, Continuous monitoring of an active fault in a plate suture zone: A creepmeter study of the Chihsang fault, eastern Taiwan: *Tectonophysics*, 333, 219-240, 2001.

Lee, J.C., J. Angelier and H.T. Chu, Polyphase history and kinematics of a complex major fault zone in the northern Taiwan mountain belt: The Lishan fault: *Tectonophysics*, 274, 97-115, 1997.

Lee, T.Q., C. Kissel, E. Barrier, C. Laj and W.R. Chi, Paleomagnetic evidence for a diachronous clockwise rotation of the Coastal Range, Eastern Taiwan: *Earth and Planetary Science Letters*, 105, 245-257, 1991.

Letouzey, J. and M. Kimura, Okinawa trough genesis: Structure and evolution of a backarc basin developed in a continent: *Marine and Petroleum Geology*, 2, 111-130, 1985.

Lewis, C., D. Ray and K.K. Chiu, Primary Geologic Sources of Arsenic in the Chianan Plain (Blackfoot Disease Area) and the Lanyang Plain of Taiwan: *International Geology Review*, 49, 947-961, 2007.

Li, S., M.J. Unsworth, J.R. Booker, W. Wei, H. Tan and A.G. Jones, Partial melt and or aqueous fluid in the mid-crust of southern Tibet? Constraints from INDEPTH Magnetotelluric data: *Geophysical Journal International*: 153, 289-340, 2003.

Li, Y.H., Denudation of Taiwan island since the Pliocene epoch: *Geology,* 4, 105-107, 1976.

Liew, P.M., P.A. Pirazzoli, M.L. Hsieh, M. Arnold, J.P. Barusseau, M. Fontugne and P. Giresse, Holocene tectonic uplift deduced from elevated shorelines, eastern coastal range of Taiwan: *Tectonophysics*, 222, 55-68, 1993.

Lilley, T., Coast effect of induced currents: *in* Gubbins, D. and E. Herrero-Bervera, eds., Encyclopedia of Geomagnetism and Paleomagnetism: *Encyclopedia of Earth Sciences Series*, Springer, 61-65, 2007.

Lin, A.T. and A.B. Watts, Orogen of the west Taiwan basin by orogenic loading ad flexure of a rifted continental margin: *Journal of Geophysical Research*, 107, 2185, 2002.

Lin, C.H., Identification of mantle reflections from a dense linear seismic array: Tectonic implications to the Taiwan orogeny: *Geophysical Research Letters*, 32, L06315, 2005.

Lin, C.H., Thermal modeling of continental subduction and exhumation constrained by heat flow and seismicity in Taiwan: *Tectonophysics*, 324, 189-201, 2000.

Lin, C.H., Y.H. Yeh, H.Y. Yen, K.C. Chen and B.S. Huang, Three-dimensional elastic wave velocity structure of the Hualien region of Taiwan: Evidence of active crustal exhumation: *Tectonics*, 17, 89-103, 1998.

Liu, C.C. and S.B. Yu, Vertical crustal movements in eastern Taiwan and their tectonic implications: *Tectonophysics,* 183, 111-119, 1990.

Liu, T.K., S. Hsieh, Y.G. Chen and W.S. Chen, Thermo-kinematic evolution of the Taiwan oblique-collision mountain belt as revealed by zircon fission track dating: *Earth and Planetary Science Letters*, 186, 45-56, 2001.

Lo, C.H., T.C. Onstott, C.C. Chen and T. Lee, An assessment of $^{40}Ar/^{39}Ar$ dating for the whole-rock volcanic samples from the Luzon arc near Taiwan: *Chemical Geology*, 114, 157-178, 1994.

Loevenbruck, A., R. Cattin, X.L. Pichon, M.L. Courty and S.B. Yu, Seismic cycle in Taiwan derived from GPS measurements: *Earth and Planetary Sciences*, 333, 57-64, 2001.

Long, M.D. and R.D. van der Hilst, Shear wave splitting from local events beneath the Ryukyu arc: Trench-parallel anisotropy in the mantle wedge: *Physics of the Earth and Planetary Interiors*, 155, 300-312, 2006.

Lu, C.Y. and J. Malavieille, Oblique convergence, indentation and rotation tectonics in the Taiwan mountain belt: Insights from experimental modeling: *Earth and Planetary Science Letters,* 121, 477-494, 1994.

Lundberg, N. and R.J. Dorsey, Rapid quaternary emergence, uplift and denudation of the coastal range: *Geology*, 18, 638-641, 1990.

Lyell, C., Principles of geology, being an attempt to explain the former changes of the Earth's surface, by reference to causes now in operation: London, Volume 1, 346 p, 1830.

Ma, K.F., M.H. Tanaka, S.R. Song, C.Y. Wang, J.H. Hung, Y.B. Tsai, J. Mori, Y.F. Song, E.C. Yeh, W. Soh, H. Sone, L.W. Kuo and H.Y. Wu, Slip zone and energetics of a large earthquake from the Taiwan Chelungpu-fault drilling project: *Nature*, 444, 473-476, 2006.

Ma, K.F. and D.R. Song, Pn velocity and Moho depth in Taiwan: *Journal of the Geological Society of China*, 40, 167-184, 1997.

Ma, K.F., J.H. Wang and D. Zhao, Three-dimensional seismic velocity structure of the crust and uppermost mantle beneath Taiwan: *Journal of Physics of the Earth*, 44, 85-105, 1996.

Mackie, R., Users manual and software documentation for two-dimensional inversion of Magnetotelluric data: GSY-USA, Inc., 18 p, 2001.

Madden, T., P. Nelson, A defense of Cagniard's magnetotelluric method: Project NR-371-401, Geophysical Lab, Massachusetts Institute of Technology, 41p, 1964. Reprinted, in K. Vozoff ed., Society of Exploration Geophysics, Geophysics Reprint Series No. 5, 1986.

Malavieille, J., Lallemand, S.E., Dominguez, A.D., Lu, C.Y., Liu, C.S., Schnurle, P. and the ACT scientific crew, Arc-continent collision in Taiwan: New marine observations and tectonic evolution, *in* Byrne, T.B. and C.S. Liu, eds., Geology and Geophysics of an Arc-Continent Collision, Taiwan: Boulder, Colorado, *Geological Society of America Special Paper 358*, 187-211, 2002.

Marquis, G., A.G. Jones and R.D. Hyndman, Coincident conductive and reflective middle and lower crust in southern British Columbia, *Geophysical Journal International*, 120, 111-131, 1995.

Marquis, G. and R.D. Hyndman, Geophysical support for aqueous fluids in the deep crust: seismic and electrical relationships: *Geophysical Journal International*, 110, 91-105, 1992.

Maxwell, J.C., A treatise on electricity and magnetism: Dover Publication Inc., 452 p, 1873.

McIntosh, K., Y. Nakamura, T.K. Wang, R.C. Shih, A. Chen and C.S. Liu, Crustal-scale seismic profiles across Taiwan and the western Philippine Sea: *Tectonophysics*, 401, 23-54, 2005.

McNeice, G.W. and A.G. Jones, Multisite, multifrequency tensor decomposition of Magnetotelluric data, *Geophysics*, 66, 158-173, 2001.

Meju, M.A. and L.A. Gallardo, Evidence for correlation of electrical resistivity and seismic velocity in heterogeneous near-surface materials: *Geophysical Research Letters*, 30, 1373, 2003.

Mishina, M., Distribution of crustal fluids in Northeast Japan as inferred from resistivity surveys: *Gondwana Research*, 16, 563-571, 2009.

Molnar, P., H.J. Anderson, E. Audoine, D. Eberhart-Phillips, K.R. Gledhill, E.R. Klosko, T.V. MvEvilly, D. Okaya, M.K. Savage, T. Stern and F.T. Wu, Continuous deformation versus faulting through the continental lithosphere on New Zealand: *Science*, 286, 516-519, 1999.

Moorkamp, M., A.G. Jones and D.W. Eaton, Joint inversion of teleseismic receiver functions and Magnetotelluric data using a genetic algorithm: Are seismic velocities and electrical conductivities compatible? *Geophysical Research Letters*, 34, doi:10.1029/2007GL030519, 2007.

Mouthereau, F., B. Deffontaines, O. Lacombe and J. Angelier, Variations along the strike of the Taiwan thrust belt: Basement control on structural style, wedge geometry and kinematics, *in* Byrne, T.B. and C.S. Liu, eds., Geology and Geophysics of an Arc-Continent Collision, Taiwan: Boulder, Colorado, *Geological Society of America Special Paper 358*, 31-54, 2002.

Mouthereau, F., O. Lacombe, B. Deffontaines, J. Angelier and S. Brusset, Deformation history of the southwestern Taiwan foreland thrust belt: Insights from tectono-sedimentary analyses and balanced cross-sections: *Tectonophysics,* 333, 293-322, 2001.

Mueller, K., Y. Chen and L. Powell, Modern strain and structural architecture of the central Taiwanese orogen – evidence for active backstepping in response to erosion?: 2002 Fall Meeting, American Geophysical Union, San Francisco, abs. Eos, Transactions, American Geophysical Union, Fall Meeting Supplement, Abstract T61B-1279, 2002.

Nakamura, M., Crustal deformation in the central and southern Ryukyu arc estimated from GPS data: *Earth and Planetary Science Letters*, 217, 389-398, 2004.

Narod, B., Personal Communication: *Email Correspondence*, Jan 8, 2009.

Negi, J. G., P.K. Agrawal and O.P. Pandey, Large variation of Curie depth and lithospheric thickness beneath the Indian subcontinent and a case for magnetothermometry: *Geophysical Journal of the Royal Astronomical Society*, 88, 763-775, 1987.

Nelson, K.D., W. Zhao, L.D. Brown, J. Kuo, J. Che, X. Liu, S.L. Klemperer, Y. Makovsky, R. Meissner, J. Mechie, R. Kind, F. Wenzel, J. Ni, J. Nabalek, C. Leshou, H. Tan, W. Wei, A.G. Jones, J. Booker, M. Unsworth, W.S.F. Kidd, M. Hauck, D. Alsdorf, A. Ross, M. Cogan, C. Wu, E. Sandvol and M. Edwards, Partially molten middle crust beneath southern Tibet: Synthesis of project INDEPTH results: *Science*, 274, 1684-1688, 1996.

Nesbitt, B., Electrical resistivities of crustal fluids: *Journal of Geophysical Research*, 98, 4301-4310, 1993.

Nezat, C.A., The geochemistry of dissolved load and sediments in high sediment-yielding rivers of Taiwan: *Geological Society of America*, 33, 282, 2001.

Ng, S.M., J. Angelier and C.P. Chang, Earthquake cycle in western Taiwan: Insights from historical seismicity: *Geophysical Journal International*, 178, 753-774, 2009.

Ogawa, Y., M. Mishina, T. Goto, H. Satoh, N. Oshiman, T. Kasaya, Y. Takahashi, T. Nishitani, S. Sakanaka, M. Uyeshima, Y. Takahashi, Y. Honkura and M. Matsushima, Magnetotelluric imaging of fluids in intraplate earthquake zones, NE Japan back arc: *Geophysical Research Letters*, 28, 3741-3744, 2001.

Okaya, D., T. Stern, F. Davey, S. Henrys and S. Cox, Continent-continent collision at the Pacific/Indo-Australian plate boundary: background, motivation, and principal results, *in* Okaya, D., T. Stern and F. Davey, eds., A continental plate boundary: tectonics of South Island, New Zealand: *AGU Geophysical Monograph 175,* 1-18, 2007.

Oldenburg, D.W. and R.G. Ellis, Efficient inversion of Magnetotelluric data in two dimensions: *Physics of the Earth and Planetary Interiors*, 81, 177-200, 1993.

Park, S.K., R.L. Mackie, Resistive (dry?) lower crust in an active orogen, Nanga Parbat, northern Pakistan: *Tectonophysics*, 316, 359-380, 2000.

Park, S.K., G.P. Biasi, R.L. Mackie and T.R. Madden, Magnetotelluric evidence for crustal suture zones bounding the southern great valley, California: *Journal of Geophysical Research*, 96, 353-376, 1991.

Parker, R.L., The inverse problem of electromagnetic induction: Existence and construction of solutions based on incomplete data: *Journal of Geophysical Research*, 85, 4421-4428, 1980.

Parkinson, W.D., The influence of continents and oceans on geomagnetic variations: *The Geophysical Journal of the Royal Astronomical Society*, 6, 411-449, 1962.

Parkinson, W.D., Directions of rapid geomagnetic fluctuations: *The Geophysical Journal of the Royal Astronomical Society*, 2, 1-14, 1959.

Partzsch, G. M., F.R. Schilling and J. Arndt, The influence of partial melting on the electrical behaviour of crustal rocks: laboratory examinations, model calculations and geological interpretations: *Tectonophysics*, 317, 189-203, 2000.

Patro, P.K. and G.D. Egbert, Regional conductivity structure of Cascadia: Preliminary results from 3D inversion of USArray transportable array Magnetotelluric data: *Geophysical Research Letters*, 35, L20311, 2008.

Petiau, G. Second generation of lead-lead chloride electrodes for geophysical applications: *Pure and Applied Geophysics*, 157, 357-382, 2000.

Powell, L., K. Mueller and Y. Chen, Geomorphic constraints on patterns of shortening and erosion in the Puli basin: Hinterland of the central Taiwan thrust belt: 2002 Fall Meeting, American Geophysical Union, San Francisco, abs. Eos, Transactions, American Geophysical Union, Fall Meeting Supplement, Abstract T61B-1270, 2002.

Price, A.T., The theory of geomagnetic induction: *Physics of the Earth and Planetary Interiors*, 7, 227-233, 1973.

Price, A.T., The theory of Magnetotelluric methods when the source field is considered: *Journal of Geophysical Research*, 67, 1907-1918, 1962.

Primdahl, F. and P. Anker Jensen, Noise in the tuned fluxgate: *Journal of Physics E: Scientific Instruments*, 20, 637-642, 1987.

Primdahl, F., The fluxgate magnetometer, Review Article: *Journal of Physics E: Scientific Instruments*, 12, 241-253, 1979.

Pulver, M.H., J.M. Crespi and T.B. Byrne, Lateral extrusion in a transpressional collision zone: An example from the pre-Tertiary metamorphic basement of Taiwan, *in* Byrne, T.B. and C.S. Liu, eds., Geology and Geophysics of an Arc-Continent Collision, Taiwan: Boulder, Colorado, *Geological Society of America Special Paper 358*, 107-120, 2002.

Pysklywec, R.N., Evolution of subducting mantle lithosphere at a continental plate boundary: *Geophysical Research Letters*, 28, 4399-4402, 2001.

Ranganayaki, R.P. and T.R. Madden, Generalized thin sheet analysis in Magnetotellurics: An extension of Price's analysis: *Geophysical Journal of the Royal Astronomical Society*, 60, 445-457, 1980.

Rankin, D. and I.K. Reddy, A magnetotelluric study of resistivity anisotropy: *Geophysics*, 34, 438-449, 1969.

Rau, R.J., W.T. Liang, H. Kao and B.S. Huang, Shear wave anisotropy beneath the Taiwan orogen: *Earth and Planetary Science Letters*, 177, 177-192, 2000.

Rau, R.J. and F.T. Wu, Tomographic imaging of lithospheric structures under Taiwan: *Earth and Planetary Science Letters*, 133, 517-532, 1995.

Reed, D.L., N. Lundberg, C.S. Liu and B.Y. Kuo, Structural relations along the margins of the offshore Taiwan accretionary wedge: Implications for accretion and crustal kinematics: *Acta Geologica Taiwanica*, 30, 105-122, 1992.

Reynolds, J.M., An introduction to applied and environmental geophysics: New York, John Wiley and Sons, 796 p, 1997.

Rodi, W. and R.L. Mackie, Nonlinear conjugate gradients algorithm for 2-D Magnetotelluric inversion: *Geophysics*, 66, 174-187, 2001.

Roecker, S.W., Y.H. Yeh and Y.B. Tsai, Three-dimensional P and S wave velocity structures beneath Taiwan; deep structure beneath an arc-continent collision: *Journal of Geophysical Research*, 92, 10547-10570, 1987.

Rosenberg C.L. and M.R. Handy, Experimental deformation of partially melted granite revisited: implications for the continental crust: *Journal of Metamorphic Geology*, 23, 19-28, 2005.

Savage, M.K., A. Tommasi, S. Ellis and J. Chery, Modeling strain and anisotropy along the Alpine Fault, South Island, New Zealand, *in* Okaya, D., T. Stern and F. Davey, eds., A continental plate boundary: tectonics of South Island, New Zealand: *AGU Geophysical Monograph 175,* 291-308, 2007.

Schiff, A.J., Introduction, *in* Schiff, A.J. and A.K. Tang, eds., Chi-Chi, Taiwan, Earthquake of September 21, 1999 Lifeline Performance: *Technical Council on Lifeline Earthquake Engineering*, 18, 1-10, 2000.

Seno, T., S. Stein and A.E. Gripp, A model for the motion of the Philippine Sea Plate consistent with NUVEL-1 and geological data: *Journal of Geophysical Research*, 98, 17941-17948, 1993.

Shmulovich, K.I. and C.M. Graham, Melting of albite and dehydration of brucite in H_2O-NaCl fluids to 9 kbars and 700-900 °C: Implications for partial melting and water activities during high pressure metamorphism: *Contributions to Mineralogy and Petrology*, 124, 370-382, 1996.

Shyu, J.B.H., K. Sieh, Y.G. Chen, R.Y. Chuang and Y. Wang, Geomorphology of the southernmost Longitudinal Valley fault: Implications for evolution of the active suture of eastern Taiwan: *Tectonics*, 27, TC1019, 2008.

Shyu, J.B.H., K. Sieh, Y.G. Chen and C.S. Liu, Neotectonic architecture of Taiwan and its implications for future large earthquakes: *Journal of Geophysical Research,* 110, B08402, 2005.

Sibuet, J.C., S.K. Hsu, X. Le Pichon, J.P. Le Formal, D. Reed, G. Moore and C.S. Liu, East Asia plate tectonics since 15 Ma: constraints from the Taiwan region: *Tectonophysics*, 344, 103-134, 2002.

Sibuet, J.C., B. Deffontaines, S.K. Hsu, N. Thareau, J.P. Formal, C.S. Liu and ACT party, Okinawa trough backarc basin: Early tectonic and magmatic evolution: *Journal of Geophysical Research*, 103, 30245-30267, 1998.

Silver, P.G., Seismic anisotropy beneath the continents: Probing the depths of geology: *Annual Reviews of Earth and Planetary Sciences*, 24, 385-432, 1996.

Simoes, M., J.P. Avouac, O. Beyssac, B. Goffe, K. Farley and Y.G. Chen, Mountain building in Taiwan: a thermokinematic model: *Journal of Geophysical Research*, 112, B11405, 2007.

Simoes, M. and J.P. Avouac, Investigating the kinematics of mountain building in Taiwan from the spatiotemporal evolution of the foreland basin and western foothills: *Journal of Geophysical Research*, 111, B10401, 2006.

Simpson, F. and K. Bahr, Practical Magnetotellurics: Cambridge University Press, Cambridge, 254 p, 2005.

Sims, W.E., F.X. Bostick Jr. and H.W. Smith, The estimation of Magnetotelluric impedance tensor elements from measured data: *Geophysics*, 36, 938-942, 1971.

Siripunvaraporn, W., G. Egbert, Y. Lenbury and M. Uyeshima, Three-dimensional Magnetotelluric inversion: data-space method: *Physics of the Earth and Planetary Interiors*, 150, 3-14, 2005.

Siripunvaraporn, W. and G. Egbert, An efficient data-subspace inversion method for 2-D Magnetotelluric data: *Geophysics*, 65, 791-803, 2000.

Smith, J.T., Understanding telluric distortion matrices: *Geophysical Journal International*, 122, 219-226, 1995.

Smith, J.T. and J.R. Booker, Rapid inversion of two- and three-dimensional Magnetotelluric data: *Journal of Geophysical Research*, 96, 3905-3922, 1991.

Song, T.R.A. and K.F. Ma, Estimation of thermal structure of a young orogenic belt according to a model of whole-crust thickening: *in* Byrne, T.B. and C.S. Liu, eds., Geology and Geophysics of an Arc-Continent Collision, Taiwan: Boulder, Colorado, *Geological Society of America Special Paper 358*, 121-136, 2002.

Soyer, W. and M.J. Unsworth, Deep electrical structure of the northern Cascadia (British Columbia, Canada) subduction zone: Implications for the distribution of fluids: *Geology, 34, 53-56, 2006.*

Spichak, V., Electromagnetic sounding of the Earth's interior: Amsterdam, Elsevier, 404 p, 2006.

Stern, T.A., P.E. Wannamaker, D. Eberhart-Phillips, D. Okaya, F.J. Davey and South Island Project Working Group, Mountain building and active deformation studied in New Zealand: *Eos Transactions of the American Geophysical Union*, 78, 335-336, 1997.

Sternberg, B.K., J.C. Washburne and L. Pellerin, Correction for the static shift in Magnetotellurics using transient electromagnetic soundings: *Geophysics*, 53, 1459-1468, 1988.

Stratton, J.A., Electromagnetic Theory: McGraw-Hill Book Company Inc., 631 p, 1941.

Sun, S.C., The Cenozoic tectonic evolution of offshore Taiwan: *Energy*, 10, 421-432, 1985.

Suppe, J., The active Taiwan mountain belt, *in* Shear, J.P. and J. Rodgers, eds., Anatomy of mountain chains: Princeton University Press, 277-293, 1987.

Suppe, J., Kinematics of arc-continent collision, flipping of subduction, and back-arc spreading near Taiwan: *Memoirs of the Geological Society of China*, 6, 21-33, 1984.

Suppe, J., Geometry and kinematics of fault-bend folding: *American Journal of Science*, 283, 684-721, 1983.

Suppe, J., Mechanics of mountain building and metamorphism in Taiwan, *Memoir of the Geological Society of China*, 4, 67-89, 1981.

Suppe, J., Imbricated structure of western foothills belt, south-central Taiwan: *Petroleum Geology Taiwan*, 17, 1-16, 1980.

Suppe, J., Decollement folding in southwestern Taiwan: *Petroleum Geology Taiwan*, 13, 25-35, 1976.

Suppe, J. and D.A. Medwedeff, Fault-propagation folding: *Geological Society of America, Abstracts with Programs*, 16, 670, 1984.

Suppe, J. and J. Namson, Fault-bend origin of frontal folds of the western Taiwan fold-and-thrust belt: *Petroleum Geology of Taiwan*, 16, 1-18, 1979.

Swift, C.M., A Magnetotelluric investigation of an electrical conductivity anomaly in the south western United States: *in* K. Vozoff ed., Magnetotelluric methods: Tulsa, Oklahoma, *Society of Exploration Geophysicists*, 156-166, 1986.

Swift, C.M., A Magnetotelluric investigation of an electrical conductivity anomaly in the south western United States: Ph.D. Thesis, *Massachusetts Institute of Technology*, Cambridge, Massachusetts, 230 p, 1967.

Tang, J.C., A.I. Chemenda, J. Chéry, S. Lallemand and R. Hassani, Compressional subduction regime and initial arc-continent collision: Numerical modeling: *in* Byrne, T.B. and C.S. Liu, eds., Geology and Geophysics of an Arc-Continent Collision, Taiwan: Boulder, Colorado, *Geological Society of America Special Paper 358*, 177-186, 2002.

Tapponnier, P., G. Peltzer, A.Y. Le Dain, R. Armijo and P. Cobbold, Propagating extrusion tectonics in Asia: New insights from simple experiments with plasticine: *Geology*, 10, 610-616, 1982.

Telford, W.M., L.P. Geldart and R.E. Sheriff, Applied Geophysics, 2nd Edition, Cambridge, Cambridge University Press, 770 p, 1990.

Teng, L.S., C.T. Lee, Y.B. Tsai and L.Y. Hsiao, Slab breakoff as a mechanism for flipping of subduction polarity in Taiwan, *Geology*, 28, 155-158, 2000.

Teng, L.S., Extensional collapse of the northern Taiwan mountain belt, *Geology*, 24, 949-952, 1996.

Teng, L.S., Geotectonic evolution of late Cenozoic arc-continent collision in Taiwan: *Tectonophysics,* 183, 57-76, 1990.

Teng, L.S., Stratigraphic records of the late Cenozoic Penglai orogeny of Taiwan, *Acta Geologica Taiwanica*, 25, 205-224, 1987.

Tikhonov, A.N., The determination of the electrical properties of deep layers of the Earth's crust: *Doklady*, SSR, 73, 295-297, 1950. Reprinted, On determining electrical characteristics of the deep layers of the Earth's crust, *in* K. Vozoff ed., Magnetotelluric methods: Tulsa, Oklahoma, *Society of Exploration Geophysicists*, 2-3, 1986.

Tikhonov, A. N. and V.Y. Arsenin, Solutions of Ill-Posed Problems: V.H. Winston and Sons, Washington, D.C., 272 p, 1977.

Tillman, K.S. and T.B. Byrne, Kinematic analysis of the Taiwan slate belt: *Tectonics*, 14, 322-341, 1995.

Tomfohrde, D.A. and R.L. Nowack, Crustal structure beneath Taiwan using frequency-band inversion of receiver function waveforms: *Pure and Applied Geophysics*, 157, 737-767, 2000.

Tsai, Y.B., Y.M. Hsiung, H.B. Liaw, H.P. Lueng, T.H. Yao and Y.T. Yeh, A Seismic refraction study of eastern Taiwan: *Petroleum Geology of Taiwan*, 11, 115-182, 1974.

Tsao, S.H., T.C. Li, J.L. Tien, C.H. Chen, T.K. Liu, and C.H. Chen, Illite crystallinity and fission-track ages along east central cross-island highway of Taiwan: *Acta Geologica Taiwanica*, 30, 45–64, 1992.

Tullis, J., A. Yund and J. Farver, Deformation-enhanced fluid distribution in feldspar aggregates and implications for ductile shear zones: *Geology*, 24, 63-66, 1996.

Tullis, J. and R.A. Yund, Experimental deformation of dry Westerly granite: *Journal of Geophysical Research*, 82, 5705-5718, 1977.

Tuncer, V., M.J. Unsworth, W. Siripunvaraporn and J.A. Craven, Case History, Exploration for unconformity-type uranium deposits with audiomagnetotellurics data: A case study from the McArthur River mine, Saskatchewan, Canada: *Geophysics*, 71, B201-B209, 2006.

Türkoğlu, E., M. Unsworth and D. Pana, Deep electrical structure of northern Alberta (Canada): Implications for diamond exploration: *Canadian Journal of Earth Sciences*, 46, 139-154, 2009.

Türkoğlu, E., M. Unsworth, I. Çağlar, V. Tuncer and Ü. Avşar, Lithospheric structure of the Arabia-Eurasia collision zone in eastern Anatolia: Magnetotelluric evidence for widespread weakening by fluids?: *Geology*, 36, 619-622, 2008.

Türkoğlu, E. and E.A. Bertrand, Book Review: K. Bahr and F. Simpson, Practical Magnetotellurics, 2005, Cambridge University Press, 270 p, ISBN 978-0521817271 £45.00., Surveys in Geophysics, DOI 10.1007/s10712-007-9025-8, 325-327, 2007.

Twiss, R.J. and E.M. Moores, Structural geology, 2nd edition: New York, W.H. Freeman and Company, 736 p, 2007.

Uchida, T., Smooth 2-D inversion for Magnetotelluric data based on statistical criterion ABIC: *Journal of Geomagnetism and Geoelectricity*, 45, 841-858, 1993.

Unsworth, M.J., A plate boundary in flux: *Nature Geoscience*, 2, 605-606, 2009.

Unsworth, M.J., Magnetotellurics: *in* D. Gubbins and E. Herrero-Bervera, eds., Encyclopedia of Geomagnetism and Paleomagnetism: Springer, 670-673, 2007.

Unsworth, M.J., New developments in conventional hydrocarbon exploration with electromagnetic methods: *Canadian Society of Exploration Geophysicists Recorder*, April, 34-38, 2005.

Unsworth, M.J., Magnetotellurics, *in* McGraw-Hill 2000, Yearbook of Science and Technology: McGraw-Hill, New York, 240-242, 1999.

Unsworth, M.J. W. Soyer, V. Tuncer, A. Wagner and D. Barnes, Case History, Hydrologic assessment of the Amchitka Island test site (Alaska) with magnetotellurics: *Geophysics*, 72, B47-B57, 2007.

Unsworth, M.J., A.G. Jones, W. Wei, G. Marquis, S.G. Gokarn, J.E. Spratt and the INDEPTH-MT team, Crustal rheology of the Himalaya and Southern Tibet inferred from magnetotelluric data: *Nature*, 438, 78-81, 2005.

Unsworth, M.J. and P.A. Bedrosian, Electrical resistivity structure at the SAFOD site from Magnetotelluric exploration: *Geophysical Research Letters*, 31, L12S05, 2004.

Unsworth, M.J., P. Bedrosian, M. Eisel, G. Egbert and W. Siripunvaraporn, Along strike variations in the electrical structure of the San Andreas Fault at Parkfield, California: *Geophysical Research Letters*, 27, 3021-3024, 2000.

Upton, P., Personal Communication: *Email Correspondence*, June 18, 2009.

Vanyan, L. and A.O. Gliko, Seismic and electromagnetic evidence of dehydration as a free water source in the reactivated crust: *Geophysical Journal International*, 137, 159-162, 1999.

Vozoff, K., The magnetotelluric method, in M.N. Nabighian ed., Electromagnetic methods in applied geophysics, vol.2: Tulsa, Oklahoma, *Society of Exploration Geophysicists*, 641-711, 1991.

Vozoff, K., Magnetotellurics: Principals and Practice: *Proceedings of the Indian Academy of Sciences, Earth and Planetary Sciences*, 99, 441-471, 1990.

Wait, J.R., On the relation between telluric currents and the Earth's magnetic field: *Geophysics*, 19, 281-289, 1954.

Walcott, R.I., Modes of oblique compression: Late Cenozoic tectonics of the South Island of New Zealand: *Reviews of Geophysics*, 36, 1-26, 1998.

Waldhauser, F. and W.L. Ellsworth, A double-difference earthquake location algorithm: Method and application to the northern Hayward fault, California: *Bulletin of the Seismological Society of America*, 90, 1353-1368, 2000.

Wannamaker, P.E., T.G. Caldwell, G.R. Jiracek, V. Maris, G.J. Hill, Y. Ogawa, H.M. Bibby, S.L. Bennie and W. Heise, Fluid and deformation regime of an advancing subduction system at Marlborough, New Zealand: *Nature*, 460, 733-737, 2009.

Wannamaker, P.E., Comment on "The petrologic case for a dry lower crust" by B.W. D. Yardley and J.W. Valley: *Journal of Geophysical Research*, 105, 6057-6064, 2000.

Wannamaker, P.E., Affordable magnetotellurics: interpretation in natural environments: *in* M. Oristaglio and B. Spies, eds., Three-dimensional Electromagnetics: Geophysical Development Series, *Society of Exploration Geophysics*, Tulsa, Oklahoma, 7, 349-374, 1999.

Wannamaker, P.E., D.P. Hasterok, J.M. Johnston, J.A. Stodt, D.B. Hall, T.L. Sodergren, L. Pellerin, V. Maris, W.M. Doerner, K.A. Groenewold and M.J. Unsworth, Lithospheric dismemberment and magmatic processes of the Great Basin-Colorado Plateau transition, Utah, implied form Magnetotellurics: *Geochemistry Geophysics Geosystems*, 9, Q05019, 2008.

Wannamaker, P.E., G.R. Jiracek, J.A. Stodt, T.G. Caldwell, V.M. Gonzalez, J.D. McKnight and A.D. Porter, Fluid generation and pathways beneath an active compressional orogen, the New Zealand Southern Alps, inferred from magnetotelluric data: *Journal of Geophysical Research*, 107, JB000186, 2002.

Wannamaker, P.E. J.A. Stodt and L. Rijo, A stable finite element solution for two-dimensional Magnetotelluric modeling: *Geophysical Journal of the Royal Astronomical Society*, 88, 277-296, 1987.

Wannamaker, P.E., J.A. Stodt and L. Rijo, Two-dimensional topographic responses in Magnetotellurics modeled using finite elements: *Geophysics*, 51, 2131-2134, 1986.

Wannamaker, P.E., G.W. Hohmann and S.H. Ward, Magnetotelluric responses of three-dimensional bodies in layered earths: *Geophysics*, 49, 1517-1533, 1984.

Watson, E.B., J.M. Brenan and D.R. Baker, Distribution of fluids in the continental mantle, *in* M.A. Menzies, ed., Continental Mantle: Clarendon Press, Oxford, 111-125, 1990.

Watson, E.B. and J.M. Brenan, Fluids in the lithosphere, 1, Experimentally determined wetting characteristics of CO_2-H_2O fluids and their implications for fluid transport, host rock physical properties, and fluid inclusion formation: *Earth and Planetary Science Letters*, 85, 497-515, 1987.

Weaver, J.T. and T.W. Dawson, Adjustment distance in TM mode electromagnetic induction: *Geophysical Journal International*, 108, 291-300, 1992.

Wei, W., M.J. Unsworth, A. Jones, J. Booker, H. Tan, D. Nelson, L. Chen, S. Li, K. Solon, P. Bedrosian, S. Jin, M. Deng, J. Ledo, D. Kay and B. Roberts, Detection of widespread fluids in the Tibetan crust by Magnetotelluric studies: Science, 292, 716-718, 2001.

Wiese, H., Geomagnetische tiefentellurik: *Pure and Applied Geophysics*, 57, 31-46, 1962.

Willett, S.D., D. Fisher, C. Fuller, E.C. Yeh and C.Y. Lu, Erosion rates and orogenic-wedge kinematics in Taiwan inferred from fission track thermochronometry: *Geology,* 31, 945-948, 2003.

Wilett, S.D. and M.T. Brandon, On steady states in mountain belts: *Geology*, 30, 175-178, 2002.

Willett, S.D., Rheological dependence of extension in wedge models of convergent orogens: *Tectonophysics*, 305, 419-435, 1999.

Wu, F.T., Personal Communication: *Email Correspondence*, Oct 26, 2009.

Wu, F.T., Recent tectonics in Taiwan: *Journal of Physics of the Earth*, 26, s265-s299, 1978.

Wu, F.T., W.T. Liang, J.C. Lee, H. Benz and A. Villasenor, A model for the termination of the Ryukyu subduction zone against Taiwan: A junction of collision, subduction/separation, and subduction boundaries: *Journal of Geophysical Research*, 114, B07404, doi:10.1029/2008JB0058950, 2009.

Wu, F.T., F.J. Davey and D.A. Okaya, Taiwan and South Island, New Zealand: A comparison of continental collisional orogenies: *in* Okaya, D., T. Stern and F. Davey, eds., A continental plate boundary: tectonics of South Island, New Zealand: *AGU Geophysical Monograph 175,* 329-346, 2007a.

Wu, F.T., L. Kuo and H. Kuo-Chen, Deformation of Taiwan from continuous GPS monitoring: *American Geophysical Union*, Fall Meeting, Abstract T42A-01, 2007b.

Wu, F.T., Chang, C.S. and Y.M. Wu, Precisely relocated hypocentres, focal mechanisms and active orogeny in central Taiwan: *in* Malpas, J., C.J.N. Fletcher, J.R. Ali and J.C. Aitchison, eds., Aspects of the tectonic evolution of China: *The Geological Society of London,* 226, 333-354, 2004.

Wu, F.T., R. Rau and D. Slazberg, Taiwan orogeny: thin-skinned or Lithospheric collision: *Tectonophysics*, 274, 191-220, 1997.

Wu, Y.M., C.H. Chang, L. Zhao, T.L. Teng and M. Nakamura: A Comprehensive Relocation of Earthquakes in Taiwan from 1991 to 2005: *Bulletin of the Seismological Society of America*, 98, 1471-1481, 2008.

Wu, Y.M., C.H. Chang, L. Zhao, J.B.H. Shyu, Y.G. Chen, K. Sieh and J.P. Avouac, Seismic tomography of Taiwan: Improved constraints from a dense network of strong motion stations: *Journal of Geophysical Research*, 112, B08312, 2007.

Yang, T.Y., J.L. Tien, C.H. Chen, T. Lee and R.S. Punongbayan, Fission-track dating of volcanics in the northern part of the Taiwan-Luzon Arc: eruption ages and evidence for crustal contamination: *Journal of Southeast Asian Earth Sciences*, 11, 81-93, 1995.

Yang, T.Y., T.K. Liu and C.H. Chen, Thermal event records on the Chimei igneous complex: Constraint on the ages of magma activities and the structural implications based on fission track dating: *Acta Geologica Taiwanica*, 26, 237-246, 1988.

Yen, H.Y., C.H. Chen, H.H. Hsieh, C.R. Lin, Y.H. Yeh, Y.B. Tsai, J.Y. Liu, G.K. Yu and Y.R. Chen, Magnetic survey of Taiwan and its preliminary implications: *Terrestrial Atmospheric and Oceanic Sciences*, 20, 309-314, 2009.

Yen, H.Y., Y.H. Yeh and F.T. Wu, Two-dimensional crustal structures of Taiwan from gravity data: *Tectonics*, 17, 104-111, 1998.

Yu, S.B. and L.C. Kuo, Present-day crustal motion along the Longitudinal Valley Fault, eastern Taiwan: *Tectonophysics*, 333, 199-217, 2001.

Yu, S.B., L.C. Kuo, R.S. Punongbayan and E.G. Ramos, GPS observation of crustal deformation in the Taiwan-Luzon region: *Geophysical Research Letters*, 26, 923-926, 1999.

Yu, S.B., H.Y. Chen and L.C. Kuo, Velocity field of GPS stations in the Taiwan area: *Tectonophysics*, 274, 41-59, 1997.

Yu, S.B. and H.Y. Chen, Global positioning system measurements of crustal deformation in the Taiwan arc-continent collision zone: *Terrestrial Atmospheric and Oceanic Sciences*, 5, 477-498, 1994.

Yue, L.F., J. Suppe and J.H. Hung, Structural Geology of a classic thrust belt earthquake: the 1999 Chi-Chi earthquake Taiwan (Mw=7.6): *Journal of Structural Geology*, 27, 2058-2083, 2005.

Zhang, J., C.Y. Wang, Y. Shi, Y. Cai, W.C. Chi, D. Dreger, W.B. Cheng and Y.H. Yuan, Three-dimensional crustal structure in central Taiwan from gravity inversion with a parallel genetic algorithm: *Geophysics*, 69, 917-924, 2004.

Zhang, P., R.G. Roberts and L.B. Pedersen, Magnetotelluric strike rules: *Geophysics*, 52, 267-278, 1987.

Zhang, W. and Z. Huang, Geomorphological effects of plate movement during Quaternary in China's tropics: *Journal of Geographical Sciences*, 14, 215-256, 2004.

Zhao, D., H. Kanamori, H. Negishi and D. Wiens, Tomography of the source area of the 1995 Kobe earthquake: Evidence for fluids at the hypocentre? *Science*, 274, 1891-1894, 1996.

Zhao, W., K.D. Nelson and Project INDEPTH Team, Deep seismic reflection evidence for continental underthrusting beneath southern Tibet: *Nature*, 366, 557-559, 1993.

Zhdanov, M.S. and G.V. Keller, The geoelectrical methods in geophysical exploration: Amsterdam, Elsevier, 873 p, 1994.

Zill, D.G., A first course in differential equation with modeling applications, 6th edition: Brooks/Cole Publishing Company, 440 p, 1997.

APPENDIX A – Long-Period TAIGER MT Data

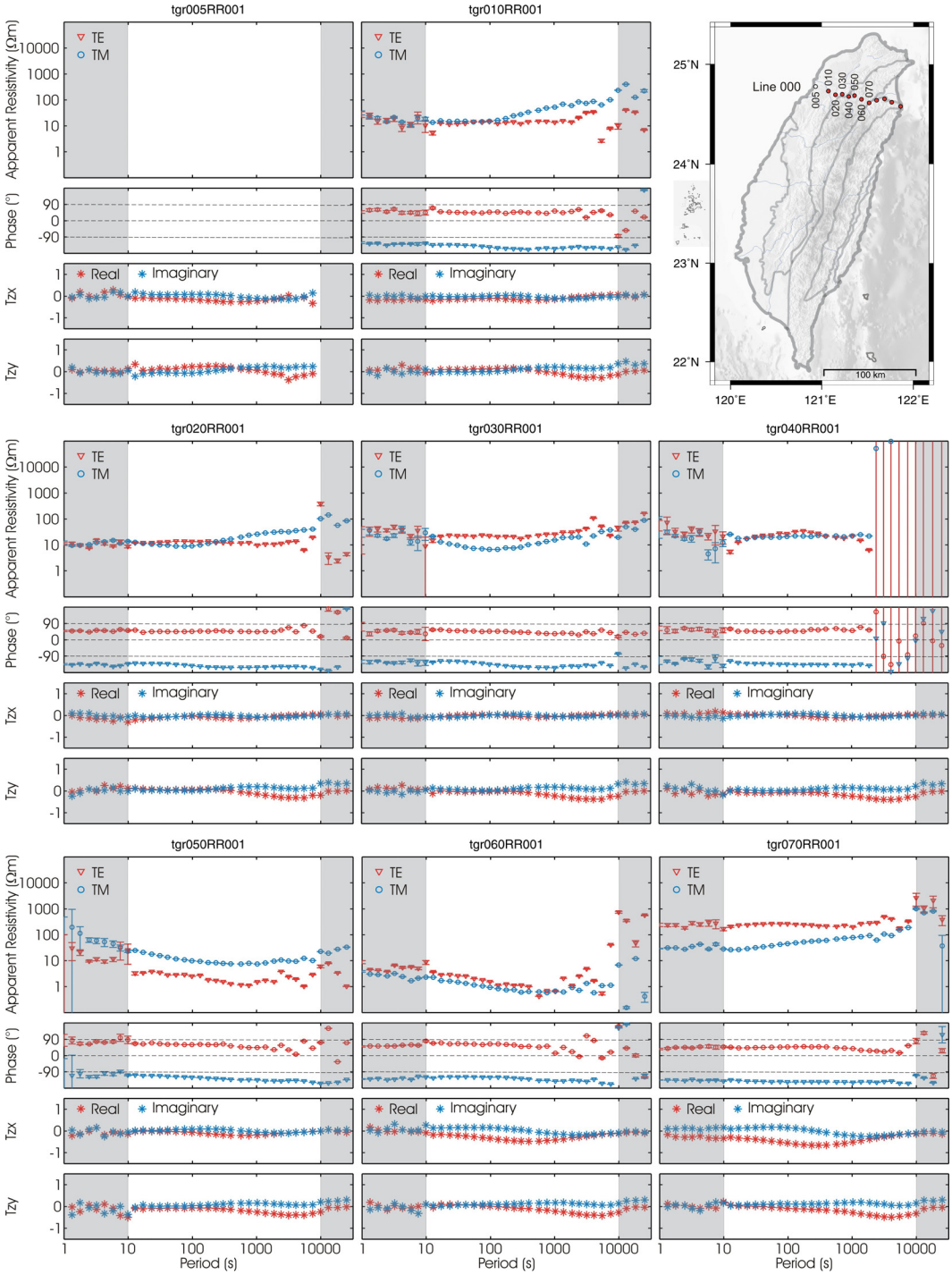

Figure A-0a: Long-period TAIGER MT data collected in northern Taiwan on Line 000. Note that only magnetic fields data were recorded at station TGR005.

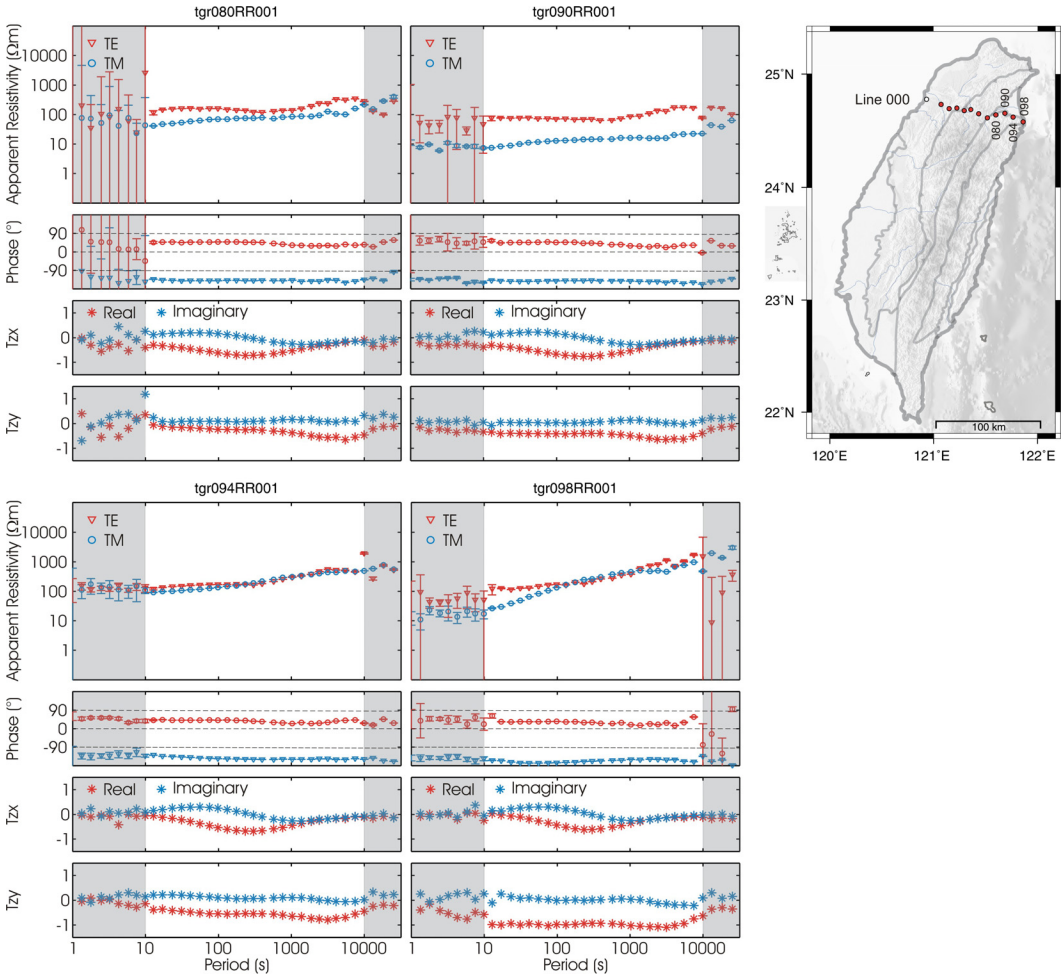

Figure A-0b: Long-period TAIGER MT data collected in northern Taiwan on Line 000.

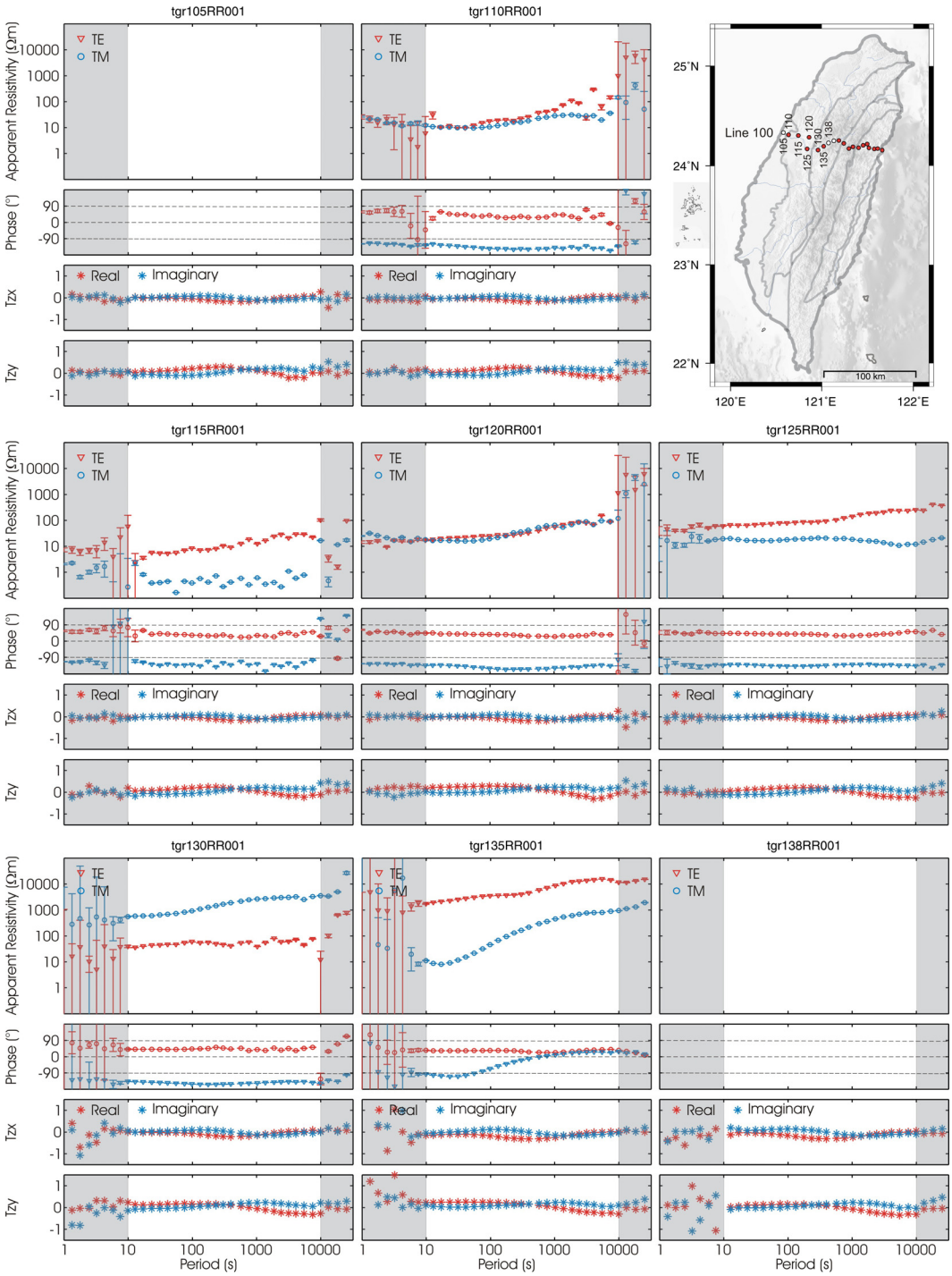

Figure A-1a: Long-period TAIGER MT data collected in north-central Taiwan on Line 100. Note that only magnetic fields data were recorded at stations TGR105 and TGR138.

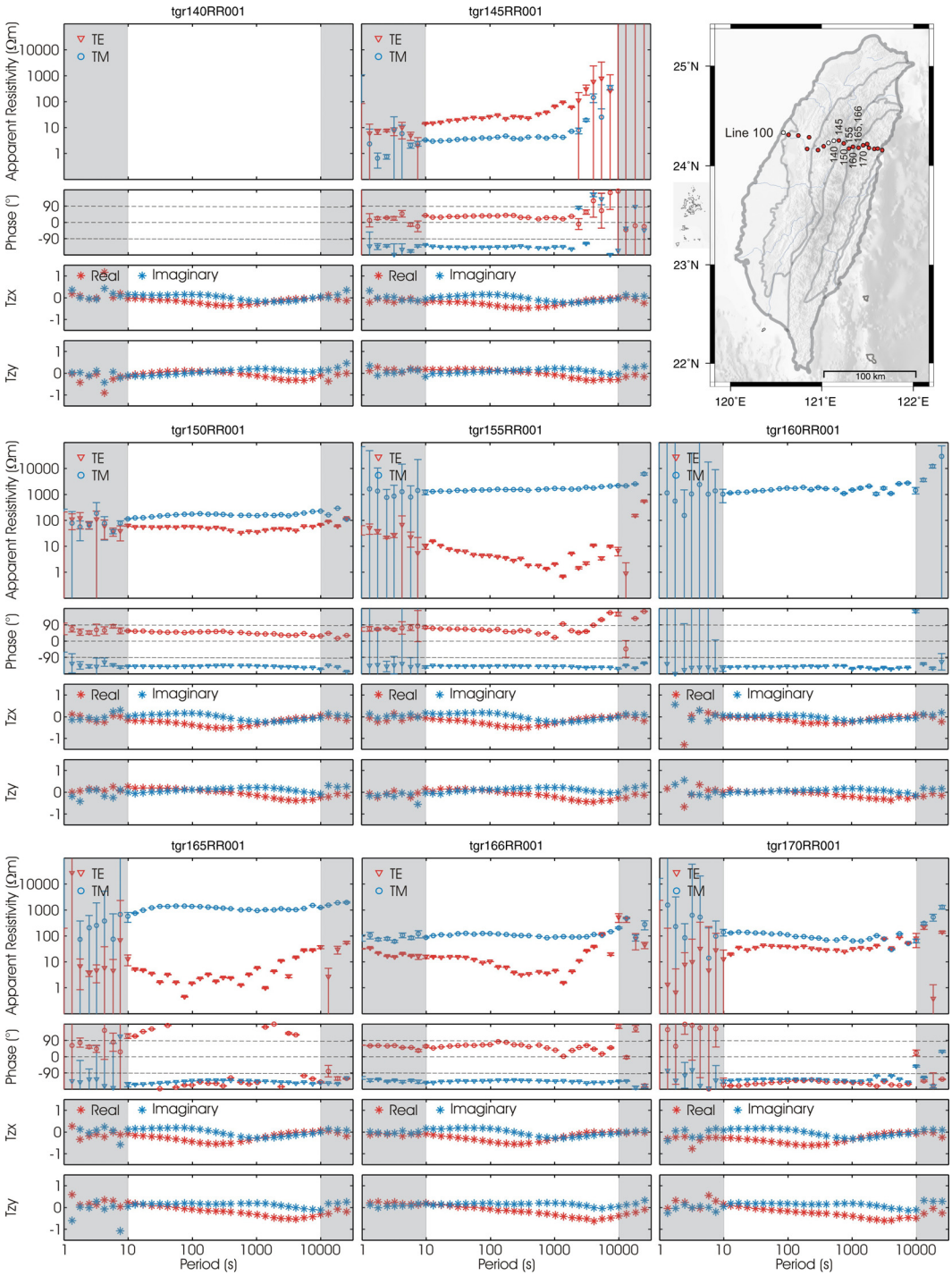

Figure A-1b: Long-period TAIGER MT data collected in north-central Taiwan on Line 100. Note that only magnetic fields data were recorded at station TGR140. At station TGR160, Ex was damaged and no TE data was recorded

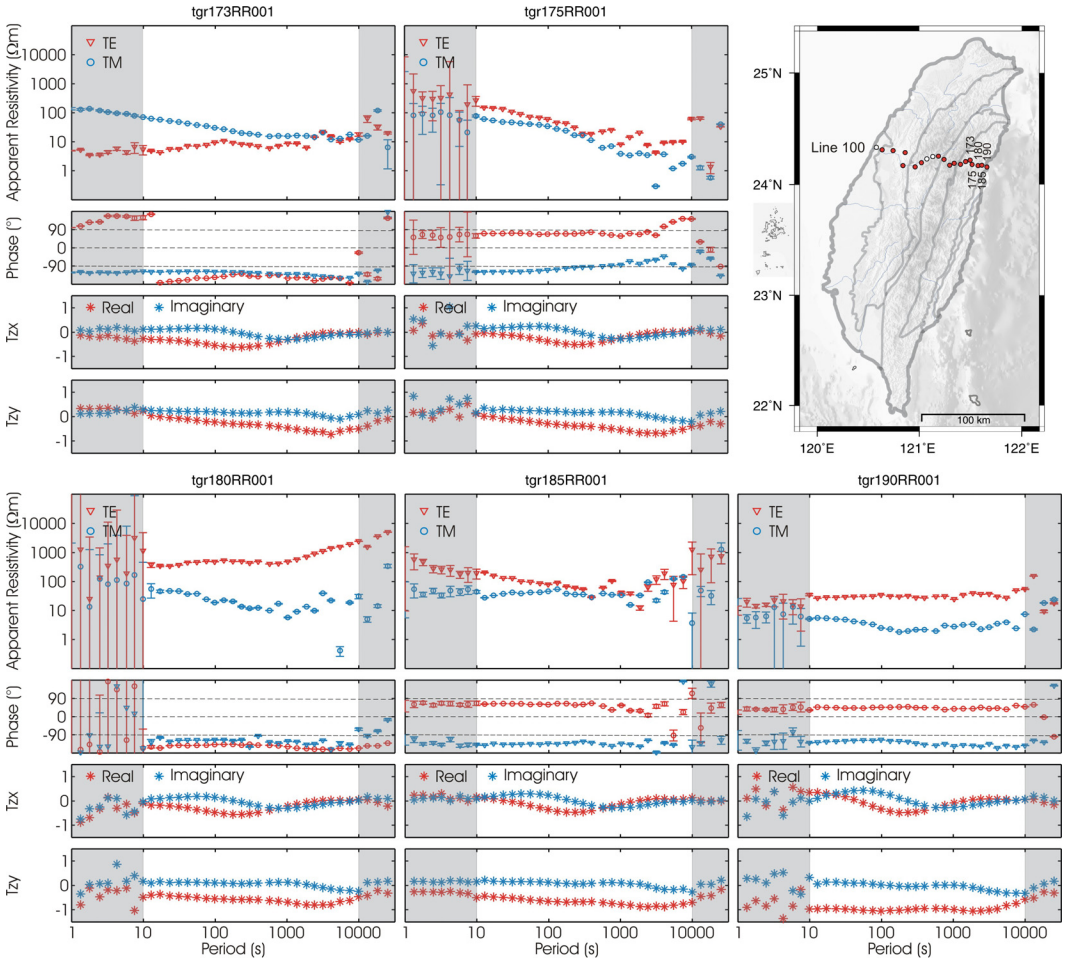

Figure A-1c: Long-period TAIGER MT data collected in north-central Taiwan on Line 100.

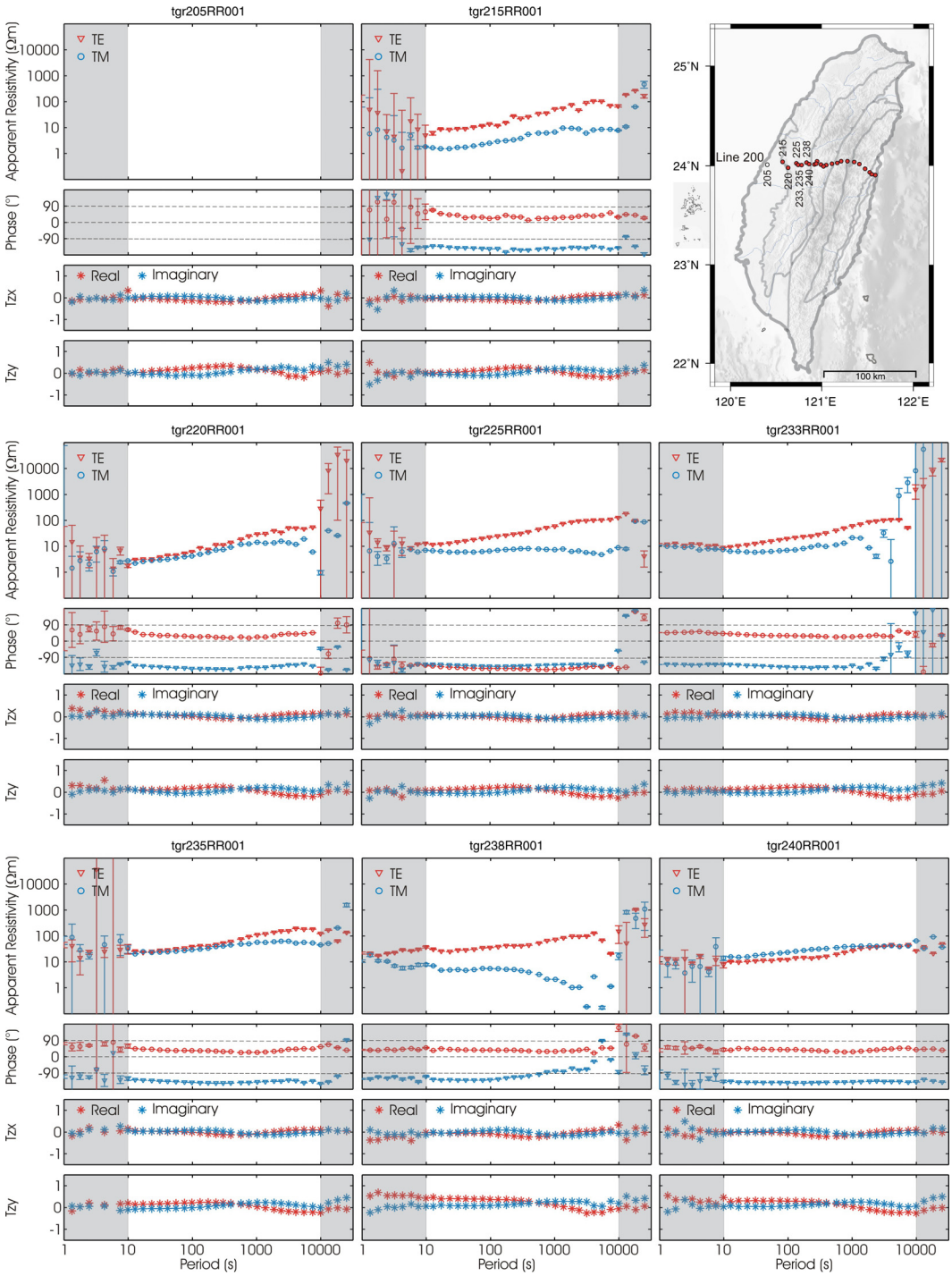

Figure A-2a: Long-period TAIGER MT data collected in south-central Taiwan on Line 200. Note that only magnetic fields data were recorded at station TGR205.

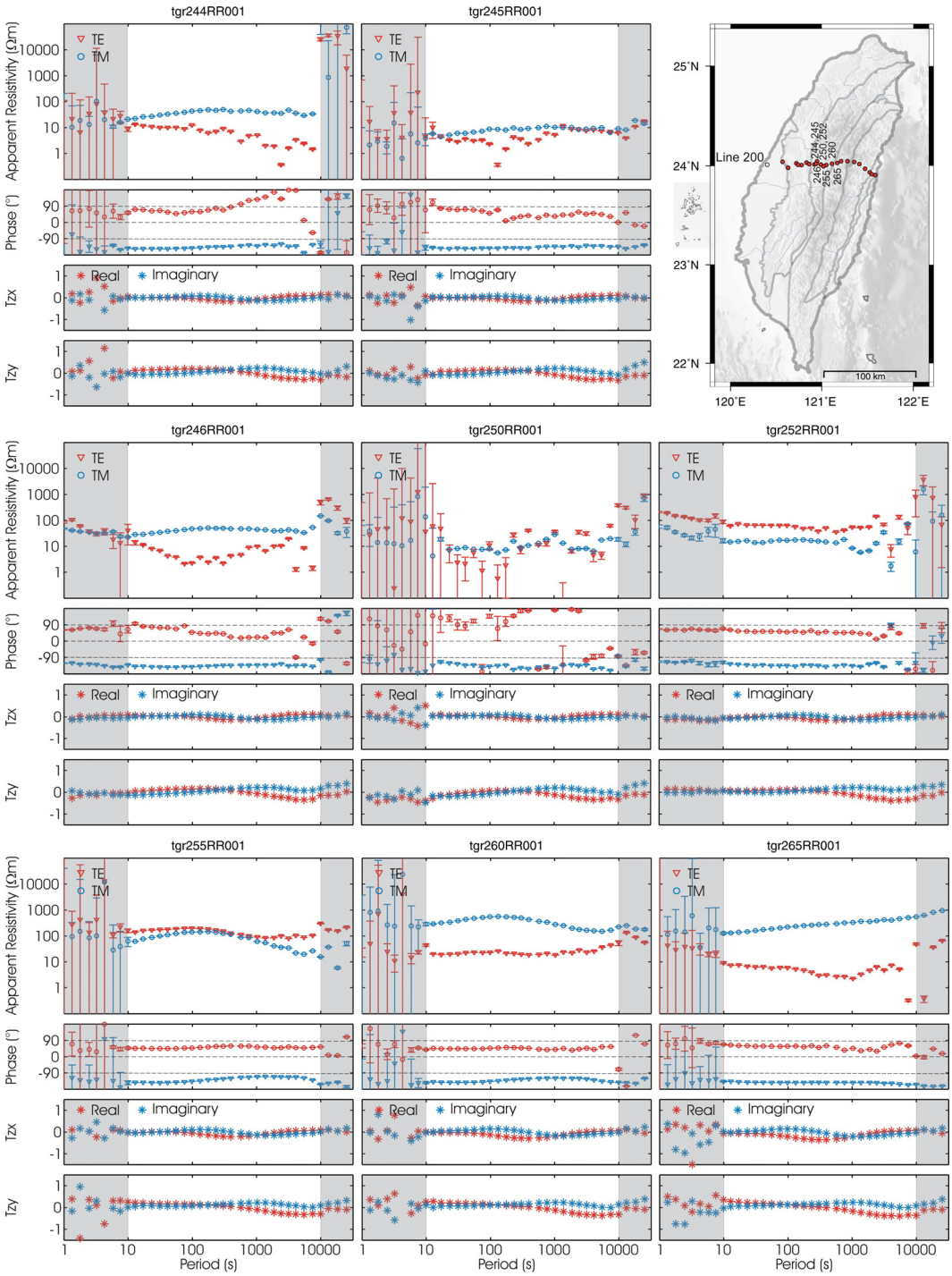

Figure A-2b: Long-period TAIGER MT data collected in south-central Taiwan on Line 200.

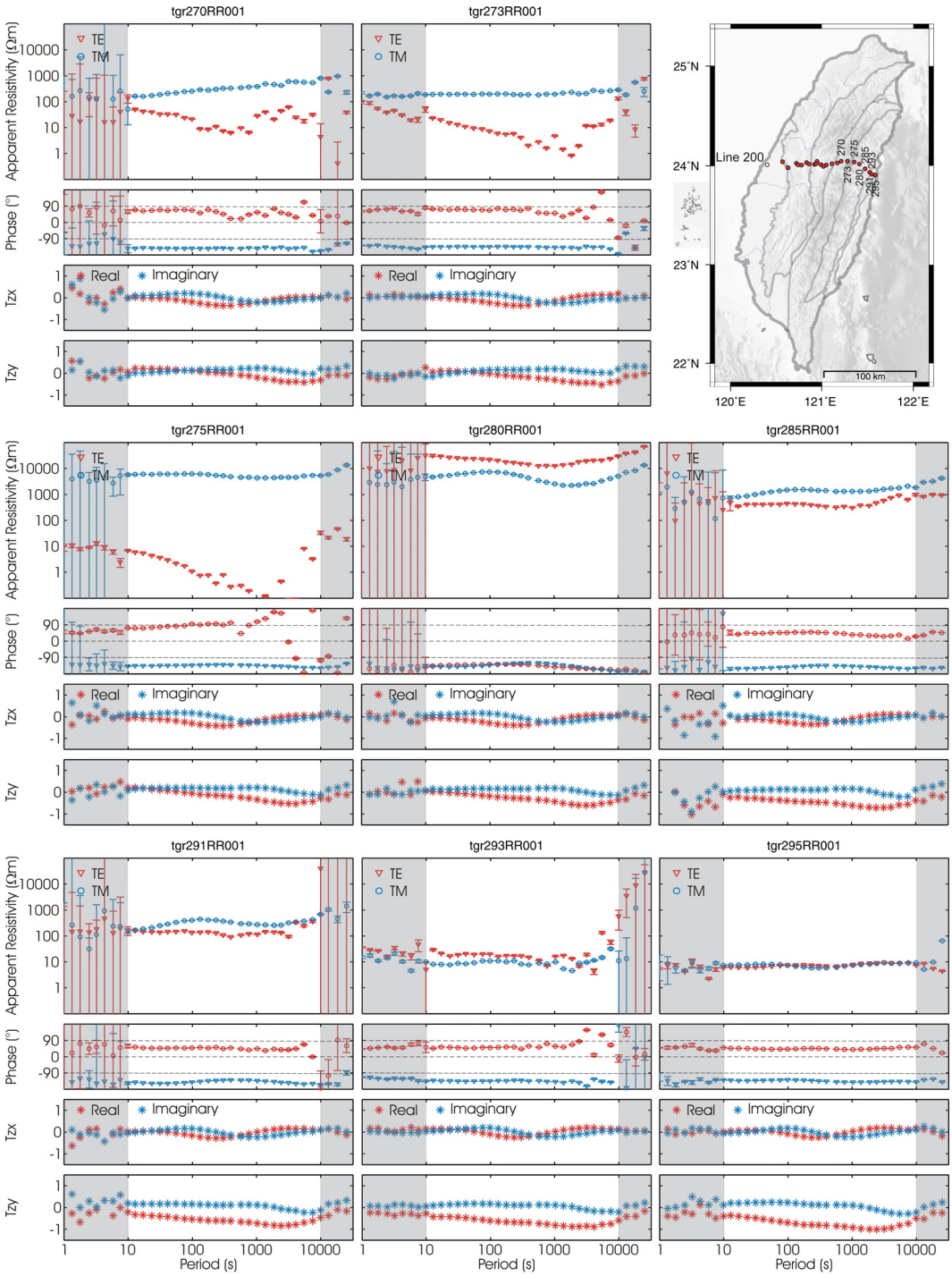

Figure A-2c: Long-period TAIGER MT data collected in south-central Taiwan on Line 200.

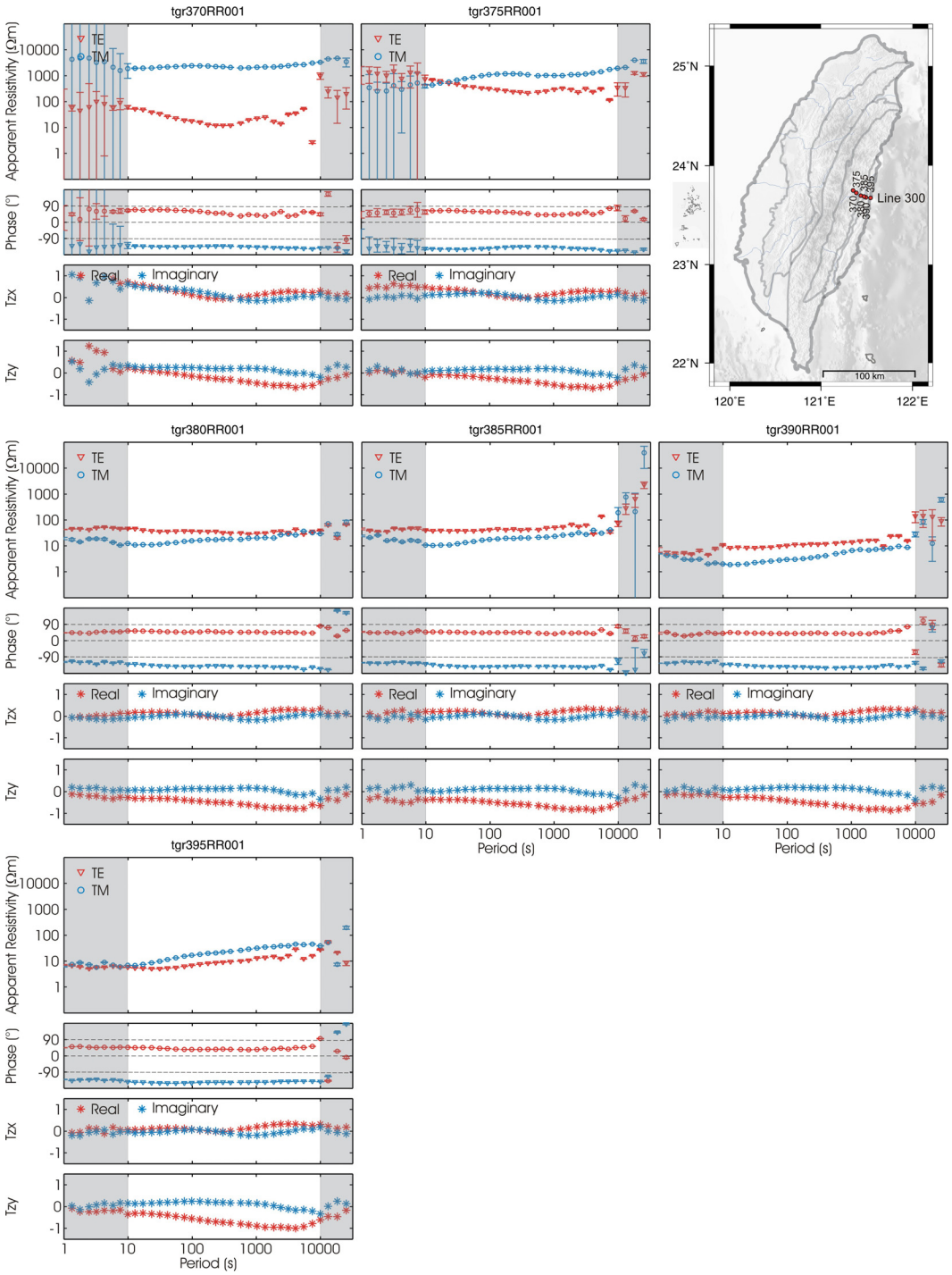

Figure A-3: Long-period TAIGER MT data collected across the central Longitudinal Valley on Line 300.

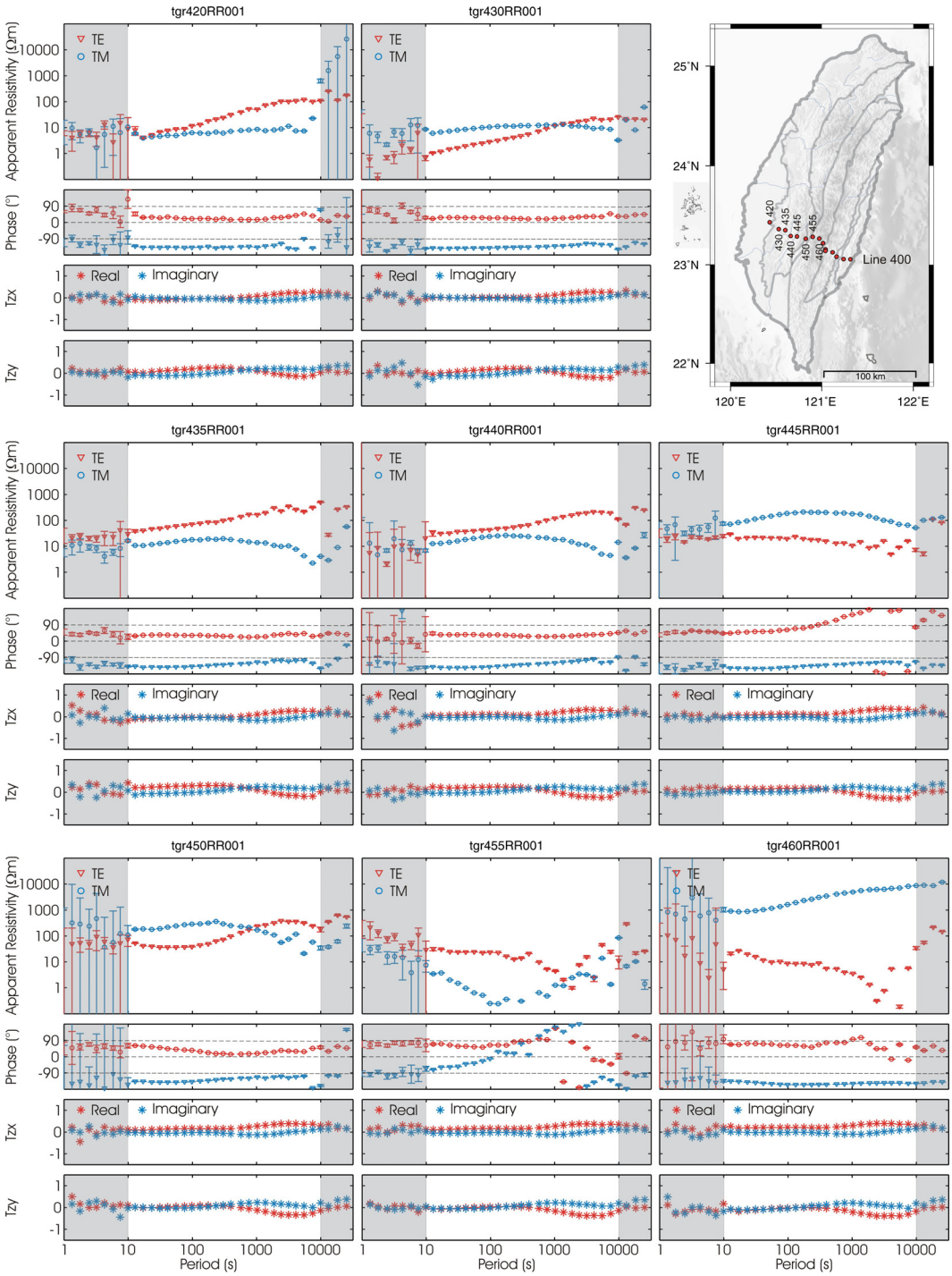

Figure A-4a: Long-period TAIGER MT data collected in southern Taiwan on Line 400.

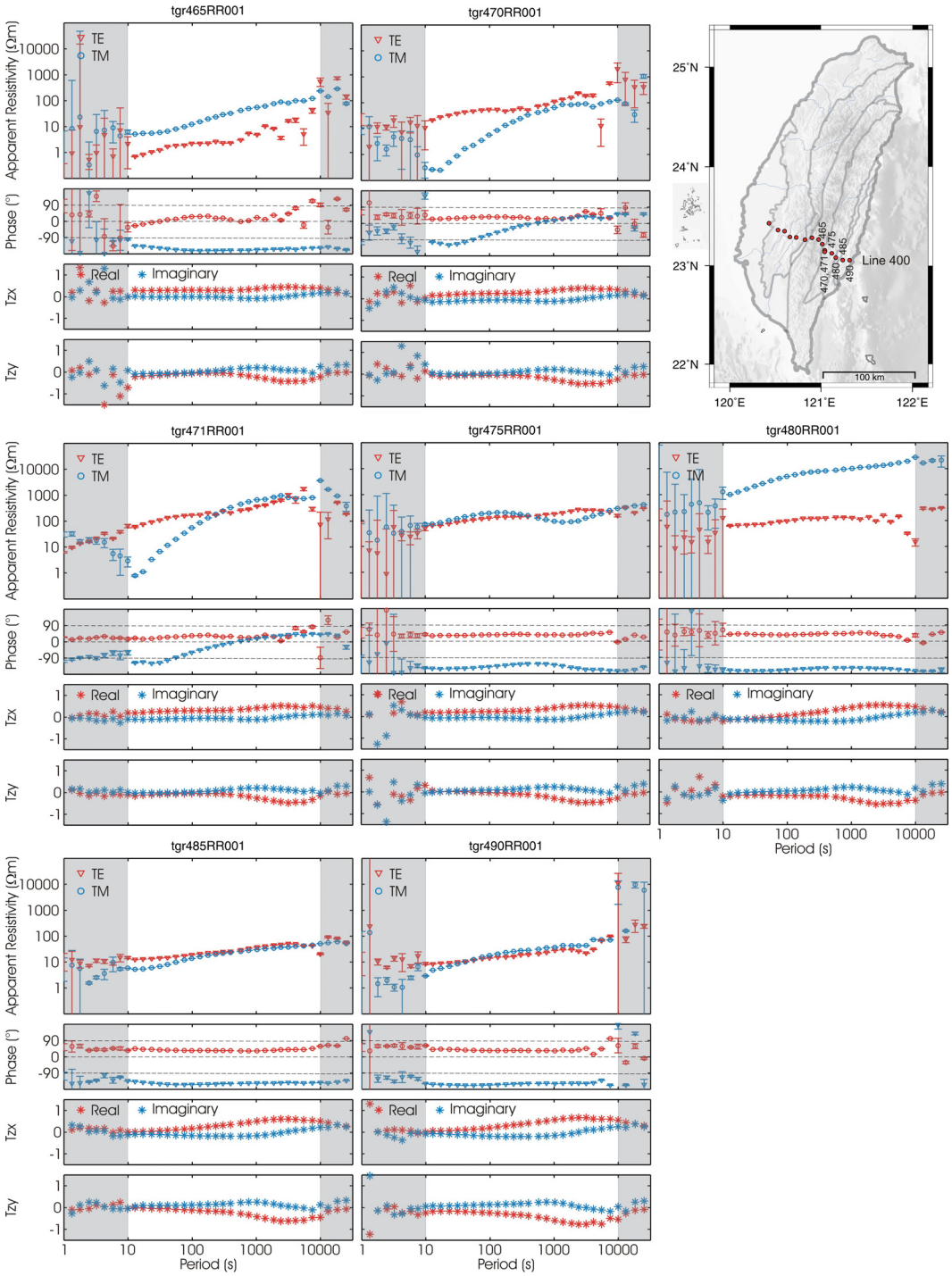

Figure A-4b: Long-period TAIGER MT data collected in southern Taiwan on Line 400.

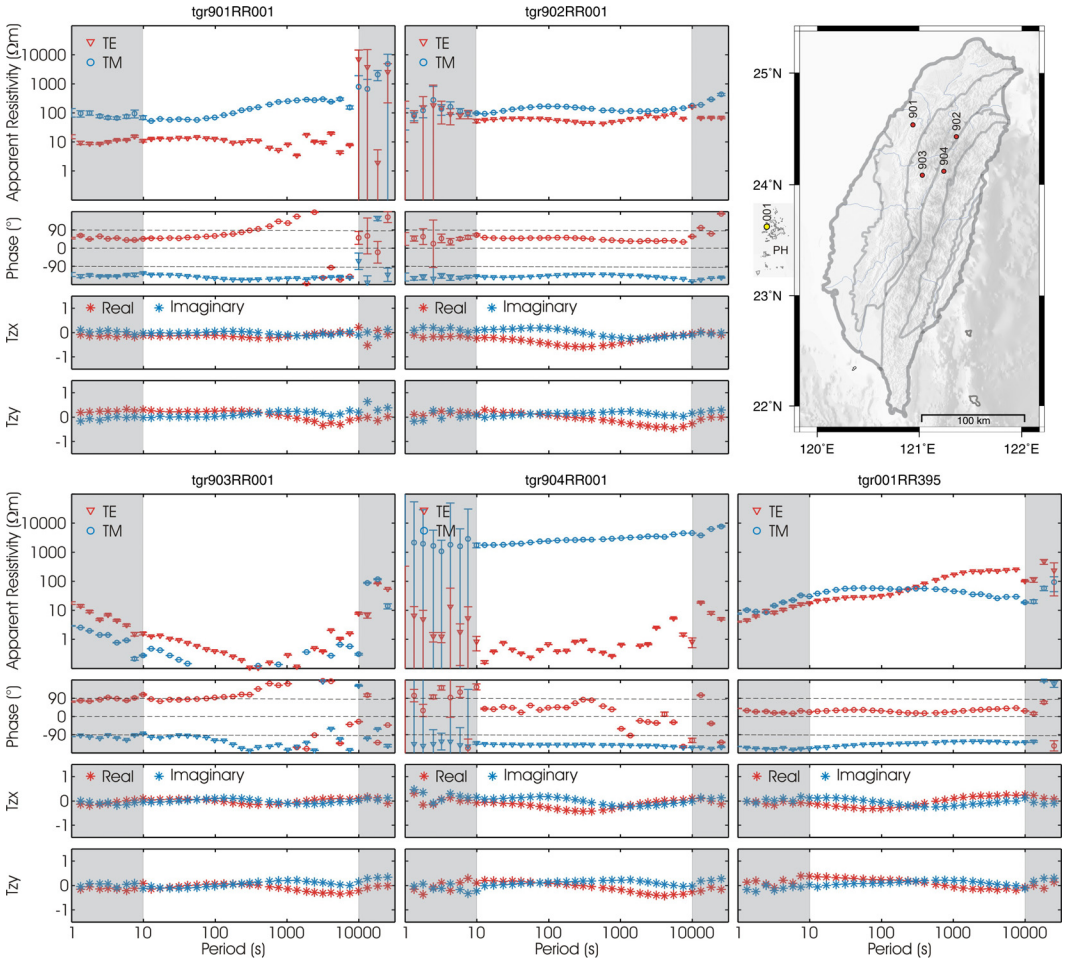

Figure A-5: Long-period TAIGER MT data collected between main profiles in north and central Taiwan (900 series stations). Remote reference station on the Penghu archipelago (TGR001).